



Developing Electrocatalysts (Precious and Non-precious) for PEM Fuel Cells Applying Metal Organic Frameworks

Thèse

Foroughazam Afsahi

Doctorat en génie chimique
Philosophiae Doctor (Ph.D.)

Québec, Canada

© Foroughazam Afsahi, 2015

Developing Electrocatalysts (Precious and Non-precious) for PEM Fuel Cells Applying Metal Organic Frameworks

Thèse

Foroughazam Afsahi

Sous la direction de :

Prof. Serge Kaliaguine

Résumé

Les piles à combustible ont un grand potentiel pour une utilisation en tant que dispositifs alternatifs de conversion d'énergie pour de nombreuses applications. Les piles à combustible PEM sont considérées comme des remplaçants potentiels du moteur à combustion interne des véhicules automobiles, en raison de leurs émissions réduites et d'une meilleure efficacité. Un catalyseur à base de Pt est nécessaire pour faciliter à la fois la réaction d'oxydation de l'hydrogène (HOR) et la réaction de réduction de l'oxygène (ORR) qui se produisent à l'anode et à la cathode d'une PEMFC, respectivement. La vitesse d'ORR est intrinsèquement très lente et est considérée comme le facteur limitant de la performance des PEMFCs. Afin de produire de l'énergie à un rythme acceptable pour les applications du monde réel, une quantité importante de catalyseur au Pt est nécessaire. Celui-ci est habituellement sous la forme de nanoparticules de platine uniformément réparties sur un matériau de support en carbone poreux (Pt/C). Le Pt est un métal noble extrêmement coûteux avec une abondance naturelle très limitée. Ainsi, la commercialisation à grande échelle de PEMFC nécessite des progrès importants dans le développement de catalyseurs à la fois pour réduire la quantité de platine et renforcer la durabilité du catalyseur.

Dans ce travail de recherche, nous avons utilisé des réseaux de coordination hybrides métal composé organique (MOF) comme seul précurseur pour préparer des électrocatalyseurs pour PEMFC. En raison de leur cristallinité, de leur porosité et de leur structure hybride, ces matériaux ont un potentiel pour être appliqués comme précurseur d'électrocatalyseurs de PEMFC. La structure tridimensionnelle bien définie de ces matériaux peut produire une forte densité de sites métalliques actifs distribués uniformément à travers leur structure et disposés régulièrement. Ainsi, ils peuvent améliorer l'utilisation du catalyseur. Les groupes de liaison organiques du précurseur à base de MOF sont convertis en carbone lors de l'activation thermique, tout en maintenant le réseau poreux, ce qui conduit à des catalyseurs ayant une grande surface spécifique et des sites actifs uniformément distribués sans la nécessité d'un autre support de carbone. Des précurseurs MOF contenant du Pt et du Fe ont été synthétisés et utilisés comme le précurseur exclusif pour développer à la fois des électrocatalyseurs à base de Pt et de métaux non précieux (Fe) pour PEMFC. L'expérience construite avec des

électrocatalyseurs à base de Pt a été le premier essai de mise en œuvre de métaux précieux à base de MOFs pour développer des électrocatalyseurs PEMFC. L'électrocatalyseur à base de Pt dérivé de ce précurseur contenant du Pt MOF a démontré une performance catalytique comparable à celle disponible dans le commerce Pt/C en particulier pour les HOR du côté de l'anode.

Pour préparer un électrocatalyseur non-précieux, un MOF contenant du Fe appartenant à une nouvelle classe de matériaux MOF, autre que les ZIFs, a été synthétisé et utilisé comme le précurseur unique d'électrocatalyseurs. Ce fut le premier rapport sur l'utilisation d'un précurseur MOF non-ZIF pour le développement d'électrocatalyseurs ORR. Cet électrocatalyseur à base de Fe a révélé une activité prometteuse en ORR et les performances de pile à combustible PEM lorsqu'il est appliqué à la couche de catalyseur cathodique de la MEA correspondante.

En outre, l'effet de la composition de l'encre de catalyseur préparée à partir du dérivé MOF électrocatalyseur à base de Pt, en termes de teneur en ionomère Nafion, a été étudiée sur la performance globale du PEMFC via un modèle CFD macroscopique. La tendance prédite à partir des calculs de modélisation a ensuite été examinée expérimentalement à la recherche de la teneur optimale en ionomère Nafion.

De plus, les électrocatalyseurs produits par la transformation thermique des MOFs à base de Pt sur noir de carbone, ont été étudiés par spectroscopie d'impédance. Les précurseurs (MOF-253) et leurs produits de thermolyse ont été pris en compte dans cette étude. Il a été observé que les matériaux soumis à la thermolyse à différentes températures passaient par différents états de conductibilité, depuis des isolants jusqu'à des matériaux de conductance voisine de celle des métaux. Ces données présentaient une augmentation de conductance avec la température et des valeurs élevées à température ambiante.

Abstract

Fuel cells have great potential for use as alternative energy conversion devices for a wide variety of applications. Proton exchange membrane fuel cells (PEMFCs) are considered to be potential replacements for internal combustion engines in automobiles, owing to their reduced emissions and better efficiency. A platinum (Pt)-based catalyst is required to facilitate both hydrogen oxidation reaction (HOR) and oxygen reduction reaction (ORR) which occur at the anode and cathode of PEMFCs, respectively. The ORR kinetic is inherently very sluggish and is considered the limiting factor facing the performance of PEMFCs. In order to generate power at an acceptable rate for real world applications, a significant amount of Pt catalyst is required. This is traditionally in the form of Pt nanoparticles evenly distributed on a porous carbon support material (Pt/C). Pt is an extremely expensive noble metal with very limited natural abundance. Thus, large-scale commercialization of PEMFCs requires significant advances in catalyst development in order both to reduce the amount of Pt metal and to enhance catalyst durability.

In this research work, we employed Metal-Organic Frameworks (MOFs) as a sole precursor for preparing PEMFC electrocatalysts. Owing to their crystalline, porous, hybrid structure, these materials have potential to be applied as PEMFCs electrocatalyst precursor. The clearly-defined three-dimensional structure of these materials can produce a high density of metal active sites evenly distributed through their regularly arranged structure. They can therefore enhance catalyst utilization. The organic linkers of the MOF-based precursor would be converted to carbon during thermal activation while maintaining the porous framework, leading to catalysts with high surface area and uniformly distributed active sites without the need for a carbon support. Pt and Fe containing MOF precursors were synthesized and used as the sole precursor to develop both Pt and non-precious (Fe)-based electrocatalysts for PEMFCs. A Pt-based electrocatalyst was the first reported on implementation of precious metal containing MOFs for developing PEMFC electrocatalyst. The Pt-based electrocatalyst derived from this Pt-containing MOF precursor demonstrated catalytic performance comparable to the commercially available Pt/C especially for HOR at the anode side.

To prepare a non-precious electrocatalyst, Fe containing MOF belonging to a different class of MOF materials other than ZIFs was synthesized and used as the sole electrocatalyst precursor. This was the first report on using non-ZIF MOF precursor for ORR electrocatalyst development. This Fe-based electrocatalyst revealed promising ORR activity and PEM fuel cell performance when applied at the cathodic catalytic layer of the corresponding membrane electrode assembly (MEA).

In addition, the effect of catalyst ink composition prepared from the MOF derived Pt-based electrocatalyst, in terms of Nafion ionomer content, on the overall performance of PEMFC was investigated via a macroscopic CFD model. The trend predicted from the model calculations was then surveyed experimentally in search for the optimum Nafion ionomer content.

Furthermore, the products of thermal transformation of Pt-based MOF into carbon-black based electrocatalyst were studied using a.c. impedance spectroscopy. Along with the electrocatalyst precursor, thermolysis products of parent MOF-253 (Al-containing) were considered in these studies. The materials subjected to thermolysis at increasing temperatures were found to pass through different conduction states starting from insulator and ending up with a particular metal-like conductance with positive temperature dependence and high ambient conductivity.

Table of Content

Résumé	iii
Abstract.....	v
Table of Content	vii
List of Tables	x
List of Figures.....	xi
Acknowledgments	xviii
Foreword.....	xx
Chapter 1 PEM Fuel cell Fundamentals	1
1.1 A Brief History of fuel cells	1
1.2 PEM fuel cells (principles and main components)	3
1.2.1 Flow field (bipolar) plates.....	5
1.2.2 Gas-diffusion electrode	6
1.2.3 Polymer electrolyte membrane.....	8
1.3 Thermodynamics of fuel cells	8
1.3.1 Fuel cell efficiency	12
1.4 Kinetics of fuel cells.....	14
1.5 Polarization curve and voltage losses	18
1.6 PEMFC issues and challenges.....	22
Chapter 2 PEM Fuel Cell Electrocatalysts.....	27
2.1 Platinum alloys.....	27
2.1.1 Pt alloy nanoparticles: Effects of composition, structure, morphology and particle size on ORR electrocatalysis	32
2.1.2 Nanotextured Pt alloys: surface modification routes.....	35
2.2 Non-platinum electrocatalysts for ORR	37
2.2.1 Non-pyrolyzed/pyrolyzed transition-metal-containing macrocycles.....	37
2.2.2 Non-macrocyclic heat treated catalysts (M/N/C type of catalysts).....	42
2.3 Support enhancement	57
2.3.1 Carbon nanotubes.....	58
2.3.1.1 Carbon nanotubes as support for Pt-based catalysts.....	58
2.3.1.2 Carbon nanotubes as support for non-precious catalysts.....	65
2.3.2 Ordered mesoporous carbon.....	66
2.3.2.1 OMC as support for Pt-based catalysts.....	67
2.3.2.2 OMC as support for non-precious catalysts.....	69
2.3.3 Graphene.....	71
2.3.3.1 Graphene as support for Pt-based catalysts	71
2.3.3.2 Graphene as support for non-precious catalysts	74
2.4 Conclusion.....	74
Chapter 3 Metal Organic Frameworks.....	90
3.1 Introduction	90
3.1.1 Node and Spacer Approach.....	90

3.1.2	Building Block Approach	91
3.2	Porosity.....	94
3.3	Electrocatalyst derived from non-pyrolyzed MOFs (preserved MOF structure).....	95
3.4	Metal free electrocatalyst derived from pyrolyzed MOFs.....	102
3.5	Metal containing electrocatalyst derived from pyrolyzed MOFs	109
Chapter 4	Electrocatalyst synthesized from metal organic frameworks.....	125
	Résumé	125
	Abstract.....	126
4.1	Introduction	127
4.2	Experimental	129
4.2.1	Synthesis of Pt-based MOF.....	129
4.2.2	Pyrolytic transformation of the Pt-based MOF into electrocatalysts	130
4.2.3	Characterization of the synthesized Pt-MOF and electrocatalysts.....	130
4.2.4	Performance tests of membrane-electrode assemblies (MEAs)	131
4.3	Results and discussion	132
4.3.1	Characteristic properties.....	132
4.3.2	Single cell polarization test	142
4.4	Conclusion.....	146
4.5	Acknowledgments	147
Chapter 5	Non-precious electrocatalyst synthesized from metal organic frameworks.....	151
	Résumé	151
	Abstract.....	152
5.1	Introduction	153
5.2	Experimental	155
5.2.1	Synthesis of the Fe-based MOF	155
5.2.2	Preparation of electrocatalysts	155
5.2.3	Characterization of the synthesized Fe-MOF and electrocatalysts.....	156
5.2.4	Rotating disk electrode (RDE) measurements.....	156
5.2.5	Performance tests of membrane-electrode assemblies (MEAs)	157
5.3	Results and discussion.....	158
5.3.1	Characteristic properties.....	158
5.3.2	ORR activity measured with the RDE.....	167
5.3.3	Performance in a fuel cell	170
5.4	Conclusions	174
5.5	Acknowledgments	174
Chapter 6	Impact of ionomer content on proton exchange membrane fuel cell performance .	179
	Résumé	179
	Abstract.....	180
6.1	Introduction	181
6.2	Description of the fuel cell device.....	183
6.2.1	Description of the three designs of interest	185
6.2.2	Description of the MEAs	186
6.2.3	Description of the operating condition.....	187
6.3	Mathematical modeling and numerical strategy	188
6.3.1	Mathematical model.....	188

6.3.2	Numerical methodology	192
6.4	Sensitivity analysis	193
6.4.1	Description of the parameters	193
6.4.2	Parametric analysis	195
6.5	Fuel cell model calibration	199
6.5.1	Commercial/Commercial fuel cell model calibration.....	200
6.5.2	Home-made/Commercial fuel cell model calibration.....	202
6.5.3	Commercial/Home-made fuel cell model calibration.....	205
6.6	Predicted impact of Nafion content	207
6.6.1	Home-made/Commercial fuel cell numerical optimization.....	207
6.6.2	Commercial/Home-made fuel cell numerical optimization.....	208
6.7	Experimental measurement of Nafion content impact	209
6.7.1	Home-made/Commercial fuel cell experimental measurement.....	210
6.7.2	Commercial/homemade fuel cell experimental measurement.....	211
6.7.3	Discussion of the results.....	213
6.8	Conclusions	214
6.9	Nomenclature	215
6.10	Acknowledgments	217
Chapter 7	Complex impedance spectroscopy study of the thermolysis products of metal organic frameworks	221
	Résumé	221
	Abstract.....	222
7.1	Introduction	223
7.2	Experimental	224
7.3	Results and discussion	225
7.3.1	Unthermolized Pt-MOF (sample C0)	225
7.3.2	Pt-MOF and Al-MOF thermolyzed at 700 °C (sample C700 and A700)	226
7.3.3	Pt-MOF thermolyzed at 800 °C (sample C800)	230
7.3.4	MOF pyrolyzed at 950 °C (sample C950 compared with A700).....	231
7.3.5	Pt-MOF and Al-MOF pyrolyzed at 1050 °C (samples C1050 and A1050).....	232
7.3.6	Temperature dependence of the conductivity.....	235
7.3.7	MOF shelf stability	240
7.4	Conclusion.....	242
7.5	Acknowledgments	242
Chapter 8	Conclusions and outlook	244
8.1	Conclusions	244
8.2	Outlook.....	248

List of Tables

Table 1.1 Characteristics of Fuel Cells.....	3
Table 3.1 Specific surface area (SSA), onset potential (E_0), half-wave potential ($E_{1/2}$), volumetric current density (I_v), and peak power density (P_{max}) of electrocatalysts [45].....	115
Table 4.1 Average Pt particle size of the carbonized C ₁ -C ₄ samples	134
Table 4.2 BET specific surface areas and pore volumes of the MOF materials and carbonized C ₁ -C ₄ samples.....	135
Table 4.3 Pt dispersion and average particle size of carbonized C ₁ -C ₄ samples determined by H ₂ chemisorption	142
Table 4.4 Electrochemical parameters of the resulting MEAs for oxygen reduction reaction	146
Table 5.1 BET specific surface area (S_{BET}), microporous surface area and pore volumes of the Fe-MOF and the samples thermolyzed under Ar, C700-C1000 and the final electrocatalyst samples C700/700-C1000/1000, C700/950, C900/950.....	163
Table 5.2 Carbon, nitrogen, oxygen and Fe contents and relative ratio of N species.....	164
Table 5.3 Comparison of onset, half-wave potentials ($E_{1/2}$), kinetic currents (j_F), and mass activities ($j_{k,m}$) at 0.8 V vs. RHE of the electrocatalysts prepared in this work and the catalyst previously reported using Fe-containing ZIF as the electrocatalyst precursor [32].....	168
Table 5.4 Electrochemical parameters of the prepared electrocatalysts for the ORR in H ₂ SO ₄ solution (pH=1).....	170
Table 6.1 Operating conditions of the fuel cell	187
Table 6.2 Physical and electrochemical parameters with well-determined values used in the PEM fuel cell model	192
Table 6.3 Geometrical parameters of the fuel cell.....	195
Table 6.4 Undetermined model parameters used in the sensitivity analysis.....	195
Table 6.5 Four series of adjusted parameters	202
Table 7.1 Parameters of equivalent circuits evaluated from simulation of a.c. impedance data.	234

List of Figures

Figure 1.1 Simplified representation of PEMFC single cell (adopted from http://www.fuelcells.org/base.cgim?template=fuel_cells_and_hydrogen)	4
Figure 1.2 PEMFC stack (adopted from http://www.deskeng.com/de/designing-fuel-cells-for-the-future/)	5
Figure 1.3 Schematic view of reaction pathway at PEMFC cathode (adopted from http://rsta.royalsocietypublishing.org/content/364/1838/147)	7
Figure 1.4 Chemical structure of Nafion (adopted from http://www.doitpoms.ac.uk/tlplib/fuel-cells/pem_membrane.php)	8
Figure 1.5 A typical polarization curve for a PEM fuel cell (adopted from http://www.altenergymag.com/content.php?issue_number=07.02.01&article=solar_polymer)	19
Figure 1.6 Cost analysis of a PEMFC stack	23
Figure 2.1 iR-corrected Tafel plots for ORR in PEMFCs at 95 °C and 5 atm pressure for Pt and Pt alloy electrocatalysts, Pt loading on electrodes 0.3 mg cm ⁻² [3].	27
Figure 2.2 Relationships between the catalytic properties and electronic structure of Pt ₃ M alloys [11].	29
Figure 2.3 Volcano plot over the ORR activity as a function of atomic oxygen chemisorptions energy [13].	30
Figure 2.4 In situ characterization of the Pt ₃ Ni(111) surface in HClO ₄ (0.1 M) at 333 K [21].	32
Figure 2.5 The dependence of specific activity (top), and mass activity (bottom, columns, left axis) and specific surface area (bottom, filled squares, right axis) on the types of alloys [24].	34
Figure 2.6 Examples of N ₄ - metallomacrocycles used as catalysts for ORR	38
Figure 2.7 Molecular structure of (a) FePc and (b, c and d) various substituted FePc molecules [62].	39
Figure 2.8 Schematic illustration of the micropore hosted active site structure present in ammonia-treated non-PGM electrocatalyst, consisting of Fe ion bridged between two adjacent nitrogen-doped graphitic crystallites [113].	43
Figure 2.9 Schematic depicting (left) metal-centered active site structure in proximity to a surface nitrogen species, (center) protonation of the surface nitrogen species with the active site having a high turnover frequency, and (right) anion binding to protonated surface nitrogen species dramatically reducing active site turnover frequency [114].	44
Figure 2.10 Schematic illustration of the fabrication of highly active PANI-based NPMCs. (a) Mixing carbon support particles with aniline monomer and transition metal precursors, (b) polymerization of aniline with ammonium persulfate, (c) heat treatment in nitrogen, and (d) acid leaching and second heat treatment [106].	45
Figure 2.11 The radial distribution functions (RDFs) of (a) PANI-Fe-C and PANI-Co-C, (b) PANI-Co-C and (c) PANI-Fe-C catalysts [86].	46
Figure 2.12 Depiction of the types of nitrogen species commonly present in pyrolyzed nitrogen-containing carbon.	48
Figure 2.13 Initially proposed catalytically active FeN ₂ /C and FeN ₄ /C structures, a and b, respectively [113].	49
Figure 2.14 Deconvoluted Mössbauer spectra of the Fe/N/C-catalysts. The iron content of the original catalyst is given as an inset in each spectrum [130].	50
Figure 2.15 Side and top views of the proposed structures of: (A) the FeN ₄ /C catalytic site in heat-treated, macrocycle-based catalysts assigned to Mössbauer doublet D1, (B) the FeN ₂₊₂ -like micropore-hosted site found in the catalyst prepared with iron acetate and heat-treated in NH ₃ assigned to doublet D2, and (C) the N-FeN ₂₊₂ -like composite site, where N-FeN ₂₊₂ is assigned to doublet D3. In all side views, graphene planes are drawn as lines. In (B), the distance between the two nitrogen atoms belonging to the graphene planes above and below the FeN ₂₊₂ -plane is similar to that in crystalline iron phthalocyanine, thus similarly influencing the lattice contribution to the quadrupole splitting. In (C), the iron (II) ion in N-FeN ₂₊₂ is coordinated by five pyridinic nitrogen atoms, one of them belonging to a plane located at the vertical below the N ₄ -plane. This axial nitrogen coordination moves the iron (II) ion out of the N ₄ -plane towards the fifth coordinating nitrogen atom. Doublet 3 may exist as N-FeN ₂₊₂ /C or as a composite site N-FeN ₂₊₂ ...N _{prot} /C, where N _{prot} is a protonable pyridinic nitrogen atom appearing at the edge of the upper	

plane in the side view of D3 [114]. N_{prot} is too far from N-FeN ₂₊₂ to have an influence on the Mössbauer spectrum of D3, but it is close enough to drastically improve the turn-over frequency of the composite site proposed in (C) [130].	51
Figure 2.16 Optimized structures (top and side views) of (a and b) two FeN ₂₊₂ /C-type structures without (left) and with axial pyridine group (right), and (c) a structure resulting from the FeN ₄ moiety embedded in an extended graphene sheet without (left) and with axial pyridine group (right) [151].	56
Figure 2.17 Structure of a single wall carbon nanotube (SWNT) and multi wall carbon nanotube (MWNT).	58
Figure 2.18 High-resolution TEM bright-field images of supported Pt catalysts prepared by SB12-stabilized method: (a) Pt/MWNTs-m, (b) Pt/MWNTs-m, (c) Pt/C, and (d) Pt/C [188].	62
Figure 2.19 Catalytic performance of PANI-Fe catalysts supported on various carbon materials. (a) Steady-state RDE polarization plots, (b) hydrogen peroxide yield plots; (c) initial fuel cell polarization plots, and (d) fuel cell life test, cell temperature: 80 °C [205].	66
Figure 2.20 TEM images of the Pt/graphene-PDDA nanocomposites synthesized at different mass ratios of PDDA-GO to H2PtCl6: (a) 1:1, (b) 1:1.5, (c) 1:2.5, (d) 1:3.5, (e) 1:6.0, and (f) 1:8.5 [236].	73
Figure 3.1 Formation of square grid (4,4) network by square planar metal nodes and 4,4'-bipyridine [4] (b) Formation of diamondoid network by tetrahedral nodes and 4,4'-bipyridine [5].	91
Figure 3.2 Three common MOF SBUs (a) Metal carboxylate paddle-wheel M ₂ (OOC) ₄ (M= Cu ²⁺ , Zn ²⁺ , Ni ²⁺ , Fe ²⁺ and Co ²⁺) [9,10]; (b) Octahedral zinc carboxylate Zn ₄ O(OOC) ₆ [11,12]; (c) Trigonal prismatic building units Fe ₃ O(COO) ₆ [13,14].	92
Figure 3.3 Structure of the zinc acetate SBU and its use in the construction of representative IRMOFs [11].	93
Figure 3.4 (a) Coordination geometry of Cu atoms in Cu-bipy-btc, (b) Typical CVs obtained at the Cu-bipy btc modified GC electrodes in 0.1 M phosphate buffer (pH 6) saturated with N ₂ (dotted curve) or O ₂ (solid curve). Scan rate, 20 mV s ⁻¹ , (c) Typical RRDE voltammograms obtained with bare (black curves) and Cu-bipy-btc-modified (red curves) GC electrodes as disk electrodes (solid curves) and platinum ring electrode (dotted curves) in 0.1 M phosphate buffer (pH 6) under air-saturated O ₂ . Electrode rotation rate: 400 rpm, Scan rate: 10 mV s ⁻¹ [31].	96
Figure 3.5 (a) Crystal structure of NPC-4, (b) CVs of as-prepared NPC-4 and activated NPC-4 modified onto the GCE in 0.1 mol L ⁻¹ phosphate buffer (pH 6.0) solution. Dash line represents CV of activated NPC-4 after tens of CV cycles. Scan rate: 20 mV s ⁻¹ , (C) CVs of as-prepared NPC-4 (a) and activated NPC-4 (b) modified onto the GCE in 0.1 mol L ⁻¹ phosphate buffer (pH 6.0) solution saturated with N ₂ (solid curves) and O ₂ (dot curves). The inset represents the CVs obtained at bare GCE. Scan rate: 20 mV s ⁻¹ [32].	98
Figure 3.6 (a) Schematic of the chemical structures of Cu-MOF, (b) the paddle-wheel SBUs of pure Cu-MOF, (c) Cyclic voltammograms of catalysts drop casted on GC electrode; GO, Cu-MOF, (GO 2 wt%) Cu-MOF, and (GO 8 wt%) Cu-MOF in 0.5 M H ₂ SO ₄ ; scan rate: 50 mV s ⁻¹ , (d) Comparing ORR current density of: 1) GO, 2) (graphene 2 wt%) Cu-MOF, 3) Cu-MOF, 4) (GO 4 wt%) Cu-MOF, 5) (GO 6 wt%) Cu-MOF, and 6) (GO 8 wt%) Cu-MOF. The inset shows the corresponding ORR RDE voltammograms at a rotation rate of 3500 rpm; scan rate: 2 mV s ⁻¹ [33].	100
Figure 3.7 PEMFC study of the (GO X wt%) Cu-MOF composite compared with Pt/C for the H ₂ /O ₂ fuel cell MEAs operating at 80 °C with different cathodes catalysts: 1) 20 wt.% Pt/C, 2) (GO 8 wt%) Cu-MOF, 3) (GO 6 wt%) Cu-MOF, 4) (GO 4 wt%) Cu-MOF, and (5) Cu-MOF [33].	100
Figure 3.8 (a) Synthetic routes to make Graphene-Porphyrin MOF, (b) Cyclic voltammograms of oxygen reduction on the (1) (Fe-P) _n MOF, (2) (G-dye 5 wt % -FeP) _n MOF, (3) (G-dye 10 wt %-FeP) _n MOF, (4) (G-dye 25 wt %-FeP) _n MOF, (5) (G-dye 50 wt %-FeP) _n MOF electrodes obtained in O ₂ -saturated 0.1 M KOH, scan rate: 50 mV s ⁻¹ [34].	101
Figure 3.9 (a) Schematic illustration of the NMOFs-driven template synthesis of highly graphitized nitrogen-doped porous carbon nanopolyhedra, (b) TEM images of typical ZIF-8 and NGPC polyhedron nanoparticle, (c) CV curves of different NGPC samples, GPC-1000-5 and commercial 20 wt.% Pt/C sample (red line, N ₂ ; blue line, O ₂) in 0.1 M KOH solution (scan rate: 10 mV s ⁻¹) [37].	104
Figure 3.10 (a) LSVs of different samples at a rotation rate of 1600 rpm; (b) K-L plots of different samples at 20.6 V; (c) Electron-transfer numbers of different samples from 20.4 to 20.9 V; (d) Kinetic limiting current densities of different samples and the corresponding electron-transfer numbers at 20.6 V [42].	108
Figure 3.11 Structures, CVs and LSVs of different samples in O ₂ saturated 0.1 M KOH solution [42].	109



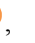




Figure 3.12 (a) Coordination geometry in CoIm framework, (b) ORR polarization curves for CoIm samples pyrolyzed at different temperatures [43].	110
Figure 3.13 (a) Coordination geometry in FeIm framework, (b) ORR polarization curve measured by RRDE, (c) Polarization and power density curves of the single cell using FeIm/ZIF-8 as the cathode catalyst (Nafion® 211 membrane) operated with H ₂ -air at the cell temperature of 80 °C and the active area of the 5 cm ² [44].	112
Figure 3.14 (a) Chemical structures of ligands and iron additive along with crystal structure of different ZIFs, (b) ORR polarization curve measured by RRDE, (c) The current-voltage polarizations (solid symbols) and power densities (hollow symbols) from single cell tests, membrane = Nafion 211, cathode catalyst loading = 2.2 mg cm ⁻² , anode catalyst = Pt/C @ 0.25 mg _{Pt} cm ⁻² , cell area = 5 cm ² , T = 80 °C, P _{O₂} = P _{H₂} = 1.5 bar, flow-rates @ 400 ml min ⁻¹ [45].	114
Figure 3.15 (a) Polarization and (b) power density curves for MEAs comprising a cathode made with the most active Fe/Phen/Z8-derived catalyst (blue stars), previously reported most active iron-based catalyst [47] in a similar manner using carbon black as catalyst support (red circles) and a state-of-the-art Pt-based cathode with a loading of 0.3 mg _{Pt} cm ⁻² (green squares) For the two MEAs made with iron-based cathodes, the catalyst loading was 3.9 mg cm ⁻² . For all MEAs, NRE 211 membranes were used [46].	116
Figure 3.16 Flowchart of the synthesis approaches and steps [49].	117
Figure 3.17 Schematic representation of synthesizing ZIF-67 with various sizes, (b) Structure information of the ZIF-67 crystal [52].	119
Figure 3.18 (a) Coordination geometry in MIL-88B-NH ₃ , (b) LSV curves of MIL-88B-NH ₃ nanoparticles, CNPs, and Pt/C at a rotation rate of 1600 rpm, (c) ADMFC single-cell performance constructed with CNPs and Pt/C catalysts at 60 °C under the same condition [53].	120
Figure 3.19 (a) SEM image of MIL-88B-NH ₃ nanoparticles, (b) SEM image of pyrolyzed MIL-88B-NH ₃ nanoparticles, (c) SEM image of MIL-88B-NH ₃ microparticles, (d) SEM image of pyrolyzed MIL-88B-NH ₃ microparticles [53].	120
Figure 4.1 Synthesis and structure of Pt-MOF. Al atoms (cyan octahedra), yellow, green, red, blue, and gray spheres stand for Pt, Cl, O, N, and C atoms, respectively; H atoms are omitted for simplicity.	129
Figure 4.2 (001) view of MOF-253 crystal	132
Figure 4.3 XRD patterns of (a) MOF-253 and Pt-MOF (b) carbonized C ₁ -C ₄ samples	133
Figure 4.4 N ₂ adsorption-desorption isotherms of (a) MOF-253 and Pt-MOF (b) carbonized C ₁ -C ₄ samples (closed: adsorption; open: desorption)	136
Figure 4.5 TEM images and their corresponding histograms of particle size distribution of C ₁ -C ₄ (the length of the bar in each photograph is 20nm)	137
Figure 4.6 Pt 4f XPS spectra of (a) C ₁ and (b) C ₄ , C 1s XPS spectra of (c) C ₁ and (d) C ₄ , and N 1s XPS spectra of (e) C ₁ and (f) C ₄	139
Figure 4.7 Re (Z) vs. frequency for (a) C ₁ and C ₂ (b) C ₃ and C ₄ samples	141
Figure 4.8 Polarization and power curves of PEMFCs with anode: commercial (BASF) electrode, C ₃ and C ₄ based electrode, cathode: commercial (BASF) electrode. Polymer electrolyte membrane: Nafion®NRE-212. Pt loading on both the cathode and the anode: 0.5 mg cm ⁻² , Test conditions: cell temperature at 80 °C, H ₂ and air flow rate of 120 and 250 ml min ⁻¹ , respectively, and 100% humidified gases at 30 psig. (solid lines are based on equation (4.5)).	144
Figure 4.9 Polarization and power curves of PEMFCs with anode: commercial (BASF) electrode, cathode: commercial (BASF) electrode, C ₃ and C ₄ based electrode. Polymer electrolyte membrane: Nafion®NRE-212. Pt loading on both the cathode and the anode: 0.5 mg cm ⁻² , Test conditions: cell temperature at 80 °C, H ₂ and air flow rate of 120 and 250 ml min ⁻¹ , respectively, and 100% humidified gases at 30 psig. (solid lines are based on equation (4.5))	144
Figure 5.1 The crystal structure of Fe-MOF, A cube of eight sodalite-like truncated-octahedral cages sharing square faces. ³⁵ Fe yellow, C gray, N blue and Cl green.	159
Figure 5.2 XRD patterns of (a) Fe-MOF (b) thermolized C700-C1000 samples and (c) electrocatalysts prepared upon acid leaching and NH ₃ thermolysis (C700/700-C1000/1000, C700/950 and C900/950),  ,  ,  ,  ,  ,  ,  stand for metallic Fe, Fe ₃ C, FeN _{0.0324} , Fe ₇ S ₈ , Fe ₃ O ₄ , Fe ₂ N, FeN _{0.056} , respectively...	160

Figure 5.3 N ₂ adsorption–desorption isotherms of (a) Fe-MOF (b) thermolized C700-C1000 samples and (c) electrocatalysts prepared upon acid leaching and NH ₃ thermolysis (C700/700-C1000/1000, C700/950 and C900/950), closed: adsorption; open: desorption.....	162
Figure 5.4 TEM images of C700/700-C1000/1000.....	163
Figure 5.5 N 1s XPS spectra of (a) C700/700 and (b) C900/900, (c) C700/950 and (d) C900/950.....	165
Figure 5.6 C 1s XPS spectra of (a) C700/700 and (b) C900/900, (c) C700/950 and (d) C900/950.....	166
Figure 5.7 Faradaic current potential curves recorded on a rotating disk electrode coated with prepared electrocatalysts (a), Corresponding Tafel plot (b). Electrolyte: O ₂ (N ₂) saturated H ₂ SO ₄ solution (pH=1); electrode rotation rate: 1500 rpm; potential scan rate: 10 mV s ⁻¹ ; catalyst loading 0.8 mg cm ⁻²	169
Figure 5.8 Polarization (a) and power density (b) curves at 80 °C for H ₂ and air PEMFC with C700/950, C900/950, C900/900 and C ⁹⁰⁰ /900 as the cathode catalysts. MEA active area 1 cm ² , cathode catalyst loading 4 mg cm ² , anode catalyst loading 0.5 mg cm ² 47wt % Pt/C, membrane was NRE 211. Hydrogen and air flow rate 0.3 slpm. Fuel cell operated at 100% relative humidity and 15 psig backpressure.....	171
Figure 6.1 Schematic representation of the fuel cell device: (a) three dimensional exploded view, (b) channels pathways, and (c) two dimensional cross section of MEA and bipolar plates.....	185
Figure 6.2 Illustration of the three fuel cell design: (a) commercial electrodes on both anode and cathode sides, (b) homemade electrode on the anode side, and (c) homemade electrode on the cathode side.....	186
Figure 6.3 Two dimensional (along the channel) domain of the mathematical and numerical model.....	189
Figure 6.4 Polarization curves obtained from numerical simulations (solid lines) and experimental results, for the fuel cell design using the homemade electrode on the anode side.....	198
Figure 6.5 Polarization curves obtained from numerical simulations (solid lines) and experimental results, for the fuel cell design using commercial electrodes.....	201
Figure 6.6 Polarization curves obtained from numerical simulations (solid lines) and experimental results, for the fuel cell design using the homemade electrode on the anode side.....	204
Figure 6.7 Polarization curves obtained from numerical simulations (solid lines) and experimental results, for the fuel cell design using the homemade electrode on the cathode side.....	206
Figure 6.8 Numerical prediction of the impact of Nafion content on the current density, for the fuel cell design using home-made electrode on the anode side. (a) Fixed electrical potential of 0.6 V, (b) 0.4 V, and (c) 0.2 V.....	208
Figure 6.9 Numerical prediction of the impact of Nafion content on the current density, for the fuel cell design using home-made electrode on the cathode side. (a) Fixed electrical potential of 0.6 V, (b) 0.4 V, and (c) 0.2 V.....	209
Figure 6.10 Measured polarization curves of the fuel cell design using homemade electrode on the anode side, for various Nafion content.....	210
Figure 6.11 Measurement of the impact of Nafion content on the current density, for the fuel cell design using home-made electrode on the anode side. (a) Fixed electrical potential of 0.6 V, (b) 0.4 V, and (c) 0.2 V.....	211
Figure 6.12 Measured polarization curves of the fuel cell design using homemade electrode on the cathode side, for various Nafion content.....	212
Figure 6.13 Measurement of the impact of Nafion content on the current density, for the fuel cell design using home-made electrode on the cathode side. (a) Fixed electrical potential of 0.6 V, (b) 0.4 V, and (c) 0.2 V.....	213
Figure 7.1 A.c. impedance responses obtained at different temperatures for untreated Pt-MOF sample (C0); (a) Nyquist plot, the signal below 100 Hz is not shown, (b) Phase angle as a function of frequency. Conductivity evaluation is $\sigma_{25}=1.3\times 10^{-11}$ S cm ⁻¹ and $\sigma_{200}=4.9\times 10^{-10}$ S cm ⁻¹	225
Figure 7.2 Fitting of impedance response for C0 sample acquired at 200 °C with an –RC- circuit.....	226
Figure 7.3 Room temperature a.c. impedance spectra of C700, a) Nyquist plot with a model circuit; b) High frequency part of the same plot; c) Real part of conductance vs. frequency; d) Phase angle vs. frequency. Symbols – experimental data, dotted line – fitting results.....	227
Figure 7.4 A.c. impedance spectra of C700 acquired at 25-200 °C. a) Nyquist plot; b) real part conductance vs. frequency.....	228

Figure 7.5 A.c. impedance spectra of C700 acquired at 150 and 200 °C. a) Nyquist plot, 150 °C; b) Phase angle vs. frequency, 150 °C. c) Nyquist plot, 200 °C; d) Phase angle vs. frequency, 200 °C. Symbols – experimental data, dotted line – fitting results.	229
Figure 7.6 A.c. impedance spectra of A700 (Al-MOF sample) acquired at 25-200 °C. a) Nyquist plot; b) Phase angle vs. frequency.	230
Figure 7.7 A.c. impedance spectra of C800 acquired at 25-200 °C. a) Nyquist plot; b) Phase angle vs. frequency.	231
Figure 7.8 A.c. impedance spectra of C950 acquired at 25-200 °C. a) Nyquist plot; b) Phase angle vs. frequency.	232
Figure 7.9 Complex impedance representation of the responses obtained at 25-200 °C from MOF pyrolyzed at 1050 °C. a) Nyquist plot acquired at selected temperatures for C1050; b) same as a), enlarged; c) Nyquist plot for A1050.	233
Figure 7.10 Conductivity of thermolysis products of Pt-MOF (C700-C1050) and Al-MOF (A700-A1050) as a function of temperature.	235
Figure 7.11 TGA and DTG plots of Al-MOF and Pt-MOF samples.	237
Figure 7.12 Arrhenius plot of conductivity of Pt-MOF pyrolysis products.	239
Figure 7.13 (a) XRD patterns of freshly prepared Pt-MOF and (b) Pt-MOF after storage for 3 months.	241

*“If a little dreaming is dangerous, the cure for it is not to dream less, but to dream more, to
dream all the time.”*

Marcel Proust: Remembrance of Things Past.

DEDICATED TO MY PARENTS: TAHEME & ABBAS,

AND MY HUSBAND NIMA,

YOUR LOVE AND SUPPORT MADE THIS DISSERTATION POSSIBLE

Acknowledgments

It has been a long journey, since I started my PhD here in Québec City. My life changed in different ways during this mission and I passed many long days of hard work to accomplish this chapter of my life. It has not been easy, but it has been a fun ride and an amazing experience.

I would like to acknowledge every one who helped me out during my studies. First and foremost, I would like to express my deepest appreciation to my supervisor Prof. Serge Kaliaguine for the opportunity to work on such an interesting and challenging subject and for being an excellent source of direction, support and encouragement. His dedication and diligent work ethic is inspirational to me.

I would like to thank Professors Jean-Pol Dodelet, Edward Ghali and Francois Mathieu-Potvin for serving in my defense committee. Moreover, I wish to acknowledge Prof. Jean-Pol Dodelet for providing me the great opportunity to test some of my catalysts at his Lab at INRS, Varennes (Québec) and for his insightful comments. I also would like to acknowledge Prof. Francois Mathieu-Potvin for his very valuable contribution and assistance in numerical modeling.

I am also thankful to Dr. Serguei Mikhailenko and Dr. Hoang Vinh-Thang for their expertises and support and for the informative lessons which they have shared with me. I owe much gratitude to Mr. Gilles Lemay for helping me out with experimental procedures.

I am indebted to many of my colleagues for their friendship over the years: Dr. Omid Ghaffari Nik, Dr. Zahra Sarshar, Dr. Zhen Kun Sun, Lin Chen, Thanh Binh Nguyen, Tien Binh Nguyen, Luc Charbonneau and Dominique Jean. It has been a real pleasure working with you all.

I would like to thank my wonderful family who has been a continuous source of strength and inspiration for me throughout the life. Without their love, support and understanding, I would not be here today. I would like to thank my Parents for their willingness to sacrifice everything for the sake of their children. To my siblings, I love you dearly and am so glad that you are in my life.

I would also like to thank my wonderful husband and best friend Nima Masoumifard. You have been a blessing in my life. Thank you for your continuous support and encouragement. I am really looking forward to starting a new chapter in our lives together.

Foreword

This dissertation is composed of eight chapters. The first chapter provides a brief review of PEMFCs operation, components and the importance of the catalyst layer (CL) regarding to its contribution to fuel cell cost. In the second chapter, a complete review of different approaches employed widely in the literature toward improving the CL performance and cost reduction will be discussed. The third chapter includes a general overview of MOFs and their characteristics along with their applications as ORR electrocatalysts. Chapters four, five, six and seven report the results of this dissertation in the form of four scientific articles as follows:

Chapter four,

Electrocatalyst Synthesized from Metal Organic Frameworks

Foroughazam Afsahi, Hoang Vinh-Thang, Serguei Mikhailenko, Serge Kaliaguine*

Department of Chemical Engineering, Laval University, Québec, G1V 0A6, Canada

Published in Journal of Power Sources, 2013, 239, 415-423.

Pt-based electrocatalysts for PEMFCs were prepared for the first time through pyrolytic transformation of Pt containing MOF which was used as the sole precursor. The synthesis and several characterization analyses along with MEA preparation and fuel cell performance tests of these electrocatalysts were all carried out by the submitter of this dissertation who is also the first author of the paper.

Chapter five,

Non-precious Electrocatalyst Synthesized from Metal Organic Frameworks

Foroughazam Afsahi, and Serge Kaliaguine*

Department of Chemical Engineering, Laval University, Québec, G1V 0A6, Canada

Published in Journal of Materials Chemistry A, 2014, 2, 12270-12279.

An Fe containing MOF material was synthesized and submitted to thermolysis process under inert gas condition to produce a non-precious electrocatalyst for ORR in PEMFC cathodic

electrode. The synthesis of Fe-based MOF and preparation of final ORR electrocatalyst along with all the characterization tests were performed by the submitter of this thesis. The Rotating Disk Electrode (RDE) measurements along with performance tests of MEAs were performed by the first author of this paper at Institut National de la Recherche Scientifique (INRS), Varennes.

Chapter six,

Impact of Ionomer Content on Proton Exchange Membrane Fuel Cell Performance

Foroughazam Afsahi¹, Francois Mathieu-Potvin² and Serge Kaliaguine^{1*}

¹*Department of Chemical Engineering, Laval University, Québec, GIV 0A6, Canada*

²*Department of Mechanical Engineering, Laval University, Québec, GIV 0A6, Canada*

Submitted to Journal of Fuel Cells, September (2015).

In this chapter, a macroscopic CFD PEMFC model previously developed by the second author of this paper was modified and used by the submitter of this thesis who is also the principal author of the paper to study the effect of Nafion ionomer in the ink composition. All the experimental work reported in this paper was also done by the first author of this paper.

Chapter seven,

Complex Impedance Spectroscopy Study of the Thermolysis Products of Metal–Organic Frameworks

Serguei D. Mikhailenko, **Foroughazam Afsahi**, and Serge Kaliaguine^{*}

Department of Chemical Engineering, Laval University, Québec, GIV 0A6, Canada

Published in Physical Chemistry C, 2014, 118, 9165-9175.

In this paper the author of this thesis, who was the second author of the paper, conducted all the experiments including impedance spectroscopy measurements as well as contributing to discussions presented in the paper.

Finally, chapter eight completes this dissertation by providing the overall conclusions along with some recommendations for future work.

Chapter 1 PEM Fuel cell Fundamentals

1.1 A Brief History of fuel cells

The very first fuel cells were demonstrated as early as 1839, while the British physicist and lawyer, Sir William R. Grove (often referred to as the “Father of the Fuel Cell”) produced an electric current by reversing the electrolysis of water [1]. He was probably the first who built the real fuel cell but a few years before a German scientist, Christian Friedrich Schoenbein, had discovered the fuel cell effect [2]. The fuel cell of Grove, which he called “gaseous voltaic battery”, proved that the chemical energy of hydrogen and oxygen can directly be converted into dc electricity at a platinum black anode and cathode immersed in sulphuric acid. 50 years later, two researchers Ludwig Mond and Charles Langer used the term “fuel cell” as they were attempting to engineer the first practical fuel cell using air and coal gas [3]. In their design, a porous non-conducting diaphragm impregnated with dilute sulphuric acid is used as the electrolyte. The perforated leaves of platinum coated with a thin film of platinum black are used as electrodes. With this cell they obtained a current density of 6.5 mA cm^{-2} at a voltage of 0.73 V. The invention of the combustion engines caused further development of fuel cells to be postponed.

The Mond/Langer fuel cell concept of 1889 was later reconsidered by Francis Bacon at Cambridge University during 1930s. He applied a number of changes to this design, such as using alkaline solution of potassium hydroxide as the electrolyte and nickel gauze as electrodes. Thirty more years of efforts led Bacon to develop a 40-cell stack fuel cell that could generate 5 kW of energy capable of powering a welding machine [4].

The sulfonated polystyrene membranes forerunner of the polymer electrolyte membrane fuel cells (PEMFCs) were first used as the solid electrolytes in the early 1960s at General Electric. They were soon replaced by Nafion® membranes that have been proved to be superior in performance and durability. Nafion® membranes are still the most popular membranes in use. The first commercial use of PEMFCs was planned to be in NASA’s Gemini V space project, however later on they were replaced by alkaline fuel cells (due to their better performances) in the Apollo missions to supply the electric power when the USA landed on the moon in 1969 [5].

Oil crisis and increased environmental awareness over 1970s led to huge step forward in further development of the fuel cells. German, Japanese and USA automobile manufacturers and their partners began developing fuel cell electric vehicle by increasing the power density of PEMFC stacks and generating hydrogen fuel storage systems. By the end of the century, most automobile manufacturers had demonstration models of hydrogen-fueled fuel cell vehicles. During the 1980s and 1990s, automobile manufacturers continued into the use of fuel cells for transport applications. The world's first demonstration of fuel cell vehicle was a 10-metre transit bus developed in 1993 by the Canadian company Ballard Power Systems. As in the 21st century fuel cell technology is being used by many different manufacturers for various applications. For instance, vending machines and vacuum cleaners are operating with fuel cells. They also are being used for cell phones, laptops and portable electric devices. At larger scale, fuel cell systems are generating electrical power for hospitals, banks and police stations at their facilities. Automotive industry is also replacing the internal combustion engines by fuel cells. Thus, the widespread fuel cell application can be categorized in four main areas: a) stationary application, b) portable usage, c) backup power and d) application for transport [6].

As it is obvious from their very vast area of application, there are different types of fuel cells. Each type is suitable for a special kind of application; however, all types of fuel cells consist of two electrodes with an electrolyte sandwiched between them. The fuel and oxidant fed into anode and cathode respectively are oxidized and reduced electrochemically. In operation of fuel cells, the ions produced at anode or cathode transport from one electrode to the other through the ionically conducting while electronically insulating electrolyte. Electrons generated at the anode pass through the external circuit (hence generating electricity) to the cathode, where they complete the reduction reaction.

Fuel cells are mainly classified according to the type of the electrolyte employed. The electrolyte in turn dictates the temperature of operation, the choice of fuel, fuel processing equipments, and choice of materials for device components (current collectors, electrodes, etc.). Naming fuel cells in order of increasing operating temperature, they are Polymer Electrolyte Membrane Fuel Cells (PEMFCs) (60-140°C), Alkaline Fuel Cells (AFCs) (150-200°C), Phosphoric Acid Fuel Cells (PAFCs) (180-200°C), Molten Carbonate Fuel Cells

(MCFCs) (650°C) and Solid Oxide Fuel Cells (SOFCs) (1000°C). Of the five, only PEMFCs with great potential to replace currently used internal combustion engines in automobiles will be discussed in more details later. Application for low-power devices, such as cell phones and portable computers, might utilize methanol as fuel. This type of PEMFCs that employs methanol as a fuel is known as direct methanol fuel cells (DMFCs). They can be considered as a sub-type of PEMFCs with the advantage of convenient liquid fuel handling, opposed to compressed H₂ gas. The operational characteristics of different types of fuel cells are listed in Table 1.1.

Table 1.1 Characteristics of Fuel Cells

Types of Fuel Cells	Fuel	Power Level (kW)	Efficiency (chemical to electrical)	Lifetime (hours)	Areas of Application
AFC	H ₂	10-100	40-60	>10,000	Space, mobile
PAFC	H ₂	100-5000	55	>40,000	Power stations
PEMFC	H ₂	0.01-1000	45-60	>40,000	Space, mobile portable, stationary
MCFC	H ₂ , CO, CH ₄	1000-100,000	60-65	>40,000	Power stations
SOFC	H ₂ , CO, CH ₄	100-100,000	55-65	>40,000	Power stations
DMFC	CH ₃ OH	0.001-100	34	>10,000	Portable applications

1.2 PEM fuel cells (principles and main components)

Figure 1.1 illustrates schematic of a single cell PEMFC running on H₂ and O₂ fuels. It consists of an electrolyte membrane sandwiched between two gas diffusion electrodes (GDEs), the anode and cathode, to form the so called membrane electrode assembly (MEA). Each GDE layer is made of a catalyst layer (CL) deposited on a gas diffusion layer (GDL), usually a carbon paper or carbon cloth, which is followed by the flow field plates. Flow field (bipolar) plates contain flow channels where H₂ and O₂ are directed through the fuel cell. H₂ from an external source enters the anodic half of the fuel cell and gets dissociated into protons and electrons. The protons diffuse through the membrane electrolyte to the cathodic side while the electrons flow through an external circuit before reaching the cathode. At the cathode, the circuit is completed when O₂ combines with protons and electrons to produce water. Heat

is produced and removed as by-product of the system. The reactions at the anode and the cathode can be summarized as:

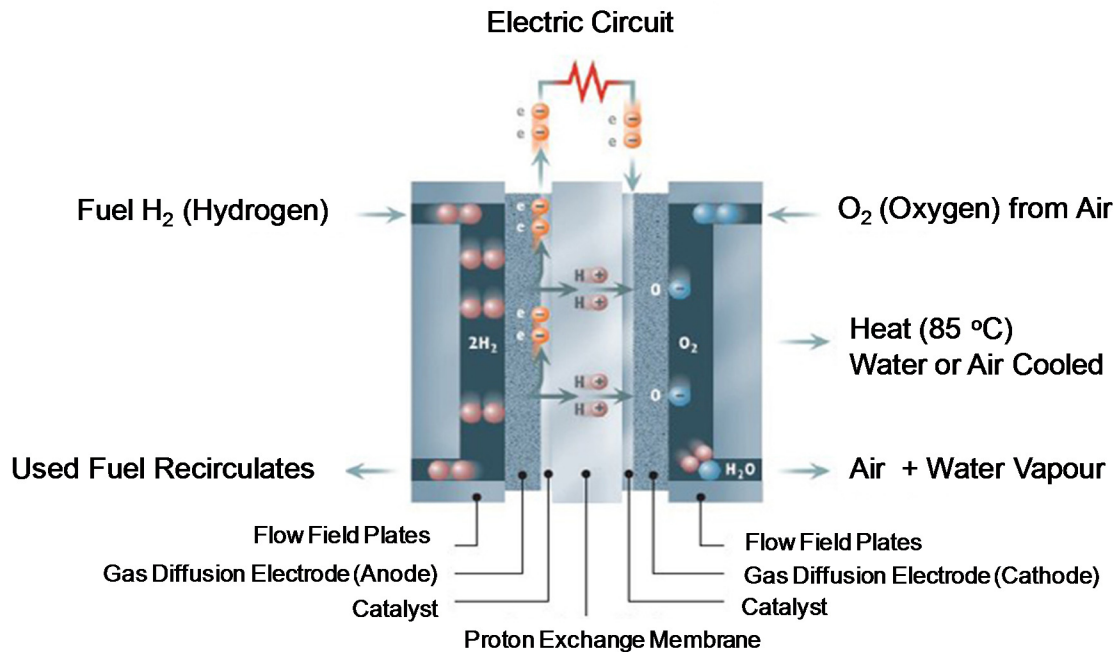
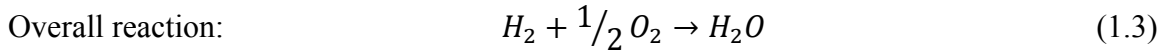
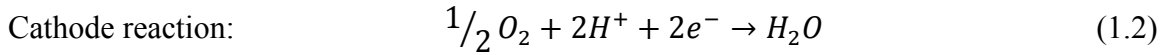
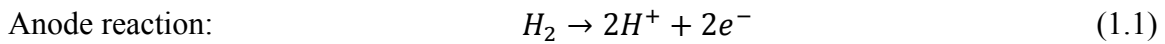


Figure 1.1 Simplified representation of PEMFC single cell (adopted from http://www.fuelcells.org/base.cgim?template=fuel_cells_and_hydrogen)

Electricity produced by a single cell (less than 1 V) is not sufficient to power a vehicle therefore, in practice several cells must be assembled into a fuel cell stack. A typical PEMFC stack is shown in Figure 1.2.

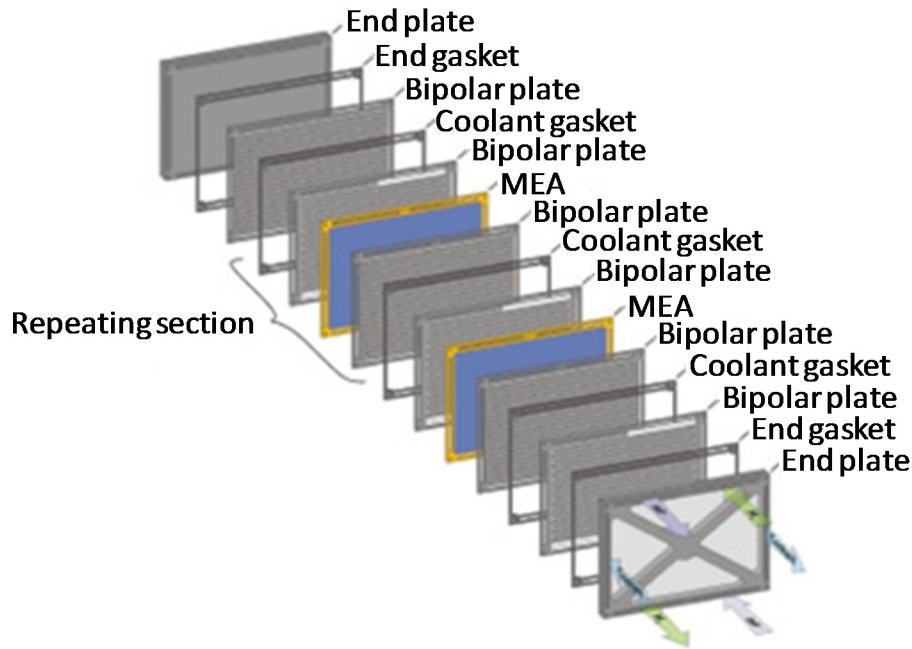


Figure 1.2 PEMFC stack (adopted from <http://www.deskeng.com/de/designing-fuel-cells-for-the-future/>)

1.2.1 Flow field (bipolar) plates

The bipolar plates act as current collectors and electrical connectors between MEAs in a PEMFC stack. Flow field plates are multi-functional components and their main task is to provide the flow pattern for reactant gases to distribute and diffuse evenly through the gas diffusion electrode to the catalyst layer. The flow field geometry has a dominant effect on gas distribution as well as water management. Different flow field designs e.g. parallel, serpentine, radial or complicated zigzag and various gas flow directions e.g. parallel, counter-current or 90° is applied to maximize H_2 , O_2 and water transport within the fuel cell.

The bipolar plate is also known as separator plate since it physically separates H_2 and O_2 flow within the fuel cell. Bipolar plates need to be chemically stable to the corrosive conditions in a fuel cell. The raw materials of bipolar plates should be widely available at reasonable cost well-suited for high volume manufacturing. Usually graphite composites are considered as the main material for PEM bipolar plates because of their excellent chemical stability and electrical conductivity. However, their low mechanical strength and high manufacture cost block their application in the commercial market [7]. Therefore, metallic bipolar plates [8] have attracted much attention as potential bipolar plates. The problem with typical metals

such as aluminum, steel, titanium or nickel as bipolar plate is related to their dissolution in corrosive environment inside PEM fuel cells [9,10]. The dissolved metal ions would diffuse into the ionomer membrane and cause their poisoning and lead to considerable power degradation. In addition, a corrosion layer on the surface of a bipolar plate would increase electrical resistance and decrease the output of the cell. Because of these issues, metallic plates must be adequately coated with a non-corrosive and electrically conductive layer, such as graphite [11], noble metals [12] conductive polymer [13], metal nitrides [14], metal carbides [15], etc.

1.2.2 Gas-diffusion electrode

The gas-diffusion electrode (GDE) of a PEMFC consists of the gas-diffusion layer (GDL) and the catalyst layer (CL). The GDL, usually made of either carbon paper or carbon cloth, is a highly porous structure that allows gaseous reactants reach the catalyst layer on both anode and cathode side of the cell and facilitate the excess water removal from the cathode electrode. Therefore, GDL provides both hydrophobic and hydrophilic pores [16], the former allows gas diffusion from the flow field to the catalyst layer while the later eases the water transportation. Water transport is an important issue in fuel cells; if the cathodic GDE becomes saturated with water, flooding may occur. This fills the GDL pores with water and severely reduces O₂ supply to the catalyst, causing irreversible voltage losses [17,18].

GDL is also an electrical connection between the CL and the bipolar plate which collects the current generated at the CL and directs it to the external circuit. Hence, they should provide good electrical conductivity and minimize the electrons transportation losses. Thermal conductivity is another requirement for GDLs since they need to remove produced heat from the fuel cell. They should also be cheap, chemically and structurally stable through prolonged fuel cell operations.

The catalyst layer is the most important part of the fuel cell where reactions take place. The reactions are catalyzed by platinum (Pt) nanoparticles dispersed on an electron-conducting support material, typically carbon black [19]. Supporting Pt nanoparticles on porous carbon have resulted in a 10-100 fold increase in Pt surface area compared to the unsupported Pt used in the early PEMFC systems [20].

For electrocatalyst nanoparticles to take part in hydrogen oxidation reaction (HOR) and oxygen reduction reaction (ORR) reactions, the CL should establish contact with reactant gases and the electrolyte membrane. The highly porous carbon support is effective in transporting gaseous fuel from the flow field to the immersed catalyst nanoparticles. To achieve good proton transport from the electrolyte membrane to the catalyst, the CL is usually coated with a layer of perfluorosulfonic acid polymer, commercially known as Nafion® ionomer.

Fuel cell performance is strongly controlled by physical/chemical processes happening in the CL. Therefore, CL composition and structure plays a vital role in the operation of PEMFCs. The net electrochemical reaction rate occurring in the CL depends on how the three distinct species, electrons, ions and reactants, participating in reaction are transported to the active sites. For effective catalyst usage, Pt nanoparticles must be accessible to the dissolved gas molecules, the electron conducting material (carbon supports) and the proton conducting phase (ionomer phase) [21].

A schematic of cathode CL where ORR takes place is shown in Figure 1.3. Since ORR is much slower than the HOR, the cathodic CL structure play crucial role developing efficient PEMFC.

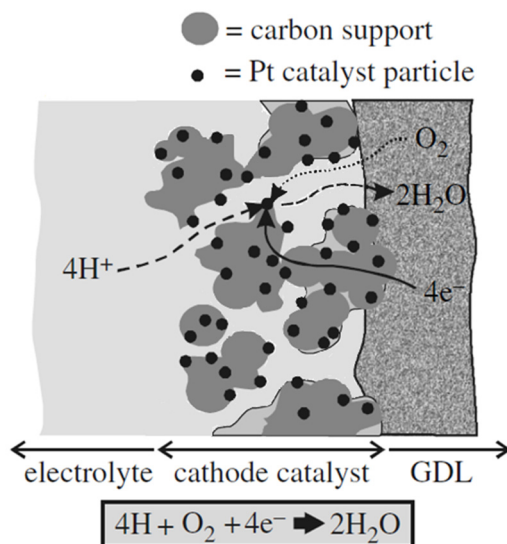


Figure 1.3 Schematic view of reaction pathway at PEMFC cathode (adopted from <http://rsta.royalsocietypublishing.org/content/364/1838/147>)

1.2.3 Polymer electrolyte membrane

The main function of electrolyte membrane in PEMFCs is to provide a pathway directing protons from the anode to the cathode. It also acts as a barrier separating gaseous fuel between the anode and cathode. The membrane allows only the ionic flow but resists the electronic flow in the cell. Nafion® developed by Dupont in the 1960's for NASA is the most widely used electrolyte membrane for PEMFCs. Figure 1.4 represents the molecular structure of Nafion®. This structure resembles Teflon and lends the ionomer its durability and resistance to chemical corrosion. Nafion® is essentially polytetrafluoroethylene (PTFE) which contains a fraction of pendant sulphonic acid groups. In presence of water, the hydrophilic HSO₃ group will absorb water and ionize to form hydronium ions. In existence of sufficient water, the hydronium ions can move through the membrane structure from anode side to cathode. The PTFE backbone is strongly hydrophobic and tends to repel water that not only accelerates water transport through the membrane but also avoid membrane from flooding.

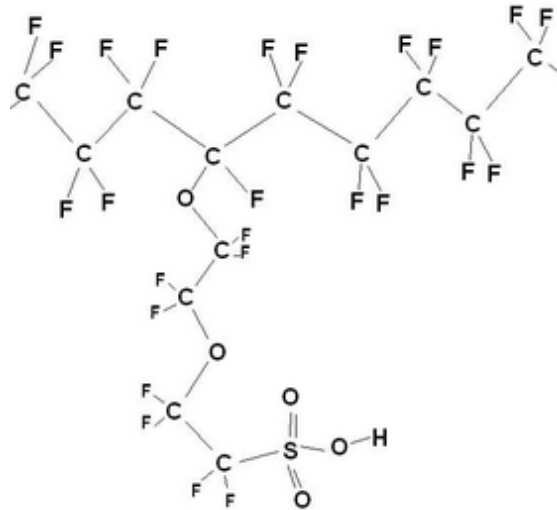


Figure 1.4 Chemical structure of Nafion (adopted from http://www.doitpoms.ac.uk/tlplib/fuel-cells/pem_membrane.php)

1.3 Thermodynamics of fuel cells

The first law of thermodynamics, the law of energy conservation, can be expressed as:

$$dU = dQ - dW \quad (1.4)$$

where dU is the change in internal energy of the system, dQ is the heat transferred to the system and dW is the work done by the system.

Considering fuel cell as the system, and the work to be consisting of both mechanical and electrical work, the latter can be defined as the work done by charge movement through an electrical potential difference:

$$dW = dW_{mech} + dW_{elec} = PdV + Eq \quad (1.5)$$

where E is the electrical potential difference, P is the pressure and V is the volume.

The total charge transfer can be expressed as:

$$q = nN_{Av}q_{el} \quad (1.6)$$

where n is the number of electrons transferred, N_{Av} is the Avogadro number and q_{el} is the charge of one electron. The product of Avogadro number and charge of an electron is known as Faraday constant; $F=96485$ coulombs mol^{-1} , thus dW_{elec} can be written as:

$$dW_{elec} = nFE \quad (1.7)$$

The equation (1.4) can now be written as:

$$dU = dQ - (PdV + nFE) \quad (1.8)$$

Equation (1.8) demonstrates the involvement of electrical potential when chemical energy (internal energy) transfers into electrical energy. To illustrate how energy can be transferred from one to another it is necessary to introduce some other important parameters such as Entropy and Gibbs free energy.

According to the second law of thermodynamics, defined through the following equation, entropy of an isolated system never decreases.

$$dS \geq 0 \quad (1.9)$$

In a reversible system, the change of entropy at constant pressure can be expressed as:

$$dS = \frac{dQ}{T} \quad (1.10)$$

where T is the system temperature. Equation (1.10) introduces entropy through employing the second law of thermodynamics.

The Gibbs free energy is defined as:

$$G = U - TS + PV \quad (1.11)$$

Taking the total differential and inserting equation (1.8) to this equation yields:

$$dG = -SdT + VdP - nFE \quad (1.12)$$

at constant temperature and pressure,

$$dG = -nFE = -dW_{elec} \quad (1.13)$$

or

$$E = \frac{-\Delta G_{T,P}}{nF} \quad (1.14)$$

Therefore, according to equation (1.13), for a fuel cell system at constant temperature and pressure, the maximum electric work is equal to the change of the Gibbs free energy of the electrochemical reaction. Based on equation (1.14), the fuel cell voltage can be expressed in terms of Gibbs free energy for the H₂-O₂ reaction (equation (1.3)) for liquid water production at constant temperature and pressure. At standard condition, $T = 25 \text{ }^\circ\text{C}$ and $P = 1 \text{ bar}$:

$$E = \frac{-\Delta G^o}{nF} = \frac{237.2}{2 * 96485} = 1.229 \text{ V} \quad (1.15)$$

The variation in cell voltage as a function of temperature at constant pressure can be expressed as:

$$\left(\frac{dE}{dT}\right)_P = \frac{\Delta S}{nF} \quad (1.16)$$

where ΔS is the entropy change for the fuel cell reaction (equation (1.3)). The entropy change of a given reaction can be set to the standard value [19]. Entropy change at 25 °C and 1 bar pressure (standard condition) is given by:

$$\begin{aligned}\Delta S^\circ &= S^\circ [H_2O]_{liq} - S^\circ [H_2]_g - \frac{1}{2} S^\circ [O_2]_g \\ &= 69.91 - 130.684 - \frac{1}{2} [205.138] = -163.343 \text{ J K}^{-1} \text{ mol}^{-1}\end{aligned}\quad (1.17)$$

Since the entropy change for the H₂/O₂ fuel cell reaction is negative, the reversible potential of the H₂/O₂ fuel cell decreases with an increase in temperature.

According to the equation (1.16),

$$\left(\frac{dE^\circ}{dT}\right)_P = \frac{-163.343}{2 * 96485} = -8.4647 * 10^{-4} \text{ V K}^{-1}\quad (1.18)$$

This means that the reversible voltage for the reaction will decrease with increasing temperature by about 0.846 mV K⁻¹. Although the reversible potential decreases with increasing temperature, the operating voltage indeed increases with an increase in operating temperature. This is due to higher reaction rate, higher mass transfer rate, and usually lower cell resistance arising from the higher ionic conductivity of the electrolyte that results in lower voltage losses in operating fuel cells. These can compensate the smaller loss of the reversible potential [16].

The variation in cell voltage as a function of pressure at constant temperature can be expressed as:

$$\left(\frac{dE}{dP}\right)_T = -\frac{\Delta V}{nF}\quad (1.19)$$

where $\Delta V = V_{H_2O(liq)} - V_{H_2} - \frac{1}{2} V_{O_2} \approx -V_{H_2} - \frac{1}{2} V_{O_2}$, assuming $P_{H_2} = P_{O_2}$:

$$\left(\frac{dE}{dP}\right)_T = \frac{1.5RT}{nFP}\quad (1.20)$$

Integrating equation (1.20) from standard pressure ($P^\circ=1.0$ bar) to an arbitrary pressure, P , at constant temperature yields:

$$E_T = E^\circ + \frac{1.5RT}{nF} \ln\left(\frac{P}{P^\circ}\right)\quad (1.21)$$

The effect of pressure, similar to temperature, on reversible cell voltage is minimal. Considering liquid water as the product of the PEM fuel cell, increasing the gases pressure

from 1 bar to 5 bar would increase the reversible cell potential by only 2.5%. However, under operating conditions the pressure effects can be significantly higher than those predicted by thermodynamics. The partial pressures of reactant gases, solubility, and mass transfer rates are higher at higher operating pressures [22].

In practice pure H₂ and O₂ are rarely used in fuel cells. H₂ as anode fuel is mostly mixed with other inert or active species such as water vapour, CO₂, CO, etc. At the cathode generally air is used as the oxidant which contains inert and active components. Even pure H₂ and O₂ are being humidified before entering the fuel cell to ensure that solid electrolyte membrane is kept hydrated. The water vapour affects the reversible cell voltage by decreasing the concentrations of both fuel and oxidant and increasing the mass transfer resistance to the catalytically active sites. Active species such as CO have a more significant effect on the reversible cell voltage causing poisoning of the noble metal catalyst. The Nernst equation indicates the variation of the voltage with concentration:

$$E = E^\circ - \frac{RT}{2F} \ln \frac{a_{H_2O}}{a_{H_2} a_{O_2}^{1/2}} \quad (1.22)$$

where a is the activity of the product and reactants. At the relatively low operating pressures of PEM fuel cells the gas activities can be replaced with their partial pressure. In addition, if the fuel cell is operated below 100 °C where the produced water is liquid, the activity of water can be assumed to be equal to one. Therefore, equation (1.22) can be rewritten as:

$$E = E^\circ + \frac{RT}{2F} \ln(P_{H_2} P_{O_2}^{1/2}) \quad (1.23)$$

Equation (1.23) confirms that increasing the pressure of the reactant gasses can slightly increase the reversible cell voltage.

1.3.1 Fuel cell efficiency

The efficiency of any energy conversion device is defined as the ratio between useful energy output and energy input. For a heat engine the thermal efficiency is defined as the ratio of the maximum amount of work that can be delivered by the engine to the thermal energy supplied to the engine. The efficiency limit for heat engines is known as Carnot limit:

$$\eta = \frac{W_{out}}{Q_{in}} = \frac{W_{out}}{\Delta H_{combust}} = 1 - \frac{T_{low}}{T_{high}} \quad (1.24)$$

where T_{low} is the temperature of the environment into which the engine exhausts its waste heat and T_{high} is the temperature at which the heat enters the engine.

Unlike heat engines, fuel cells work at constant temperature and both reactants and products can enter and exit the system at similar temperatures. Fuel cells don't share any characteristics with heat engines and therefore their efficiency is not limited by Carnot cycle. They are rather an electrochemical energy convertor and the maximum work obtained by them is the produced electrical energy which corresponds to Gibbs free energy of the reaction, and energy input is the enthalpy of hydrogen fuel:

$$\eta = \frac{\Delta G_{T,P}}{\Delta H} = \frac{nF\Delta E}{\Delta H} \quad (1.25)$$

According to equation (1.25), the maximum theoretical efficiency of H₂/O₂ fuel cell at standard condition (1 atm and 25 °C) is equal to $\frac{\Delta G^o}{\Delta H^o} = \frac{1.23}{1.48} = 0.83$. For an equivalent Carnot efficiency, the heat engine would have to run at $T_{high}=1480$ °C with $T_{low}=25$ °C.

For a practical fuel cell, losses have to be included when considering the real efficiency. The first one, voltage losses, is related to irreversible kinetic effects in the fuel cell. The voltage efficiency is the ratio of the real operating voltage (V) to the ideal reversible voltage (E).

$$\eta_V = \frac{V}{E} \quad (1.26)$$

The other one is fuel utilization losses, caused due to the fact that all the fuel fed to a fuel cell does not participate in the electrochemical reaction taking place at the anode. Some fuel will pass through the membrane and react with the oxygen on the other side or leaves the cell unreacted. This lowers the overall efficiency of the cell. The corresponding fuel utilization efficiency can be defined as the ratio of the fuel used versus the total fuel provided:

$$\eta_{fuel} = \frac{i/nF}{v_{fuel}} \quad (1.27)$$

where i is the current in the fuel cell and v_{fuel} is the rate at which fuel is supplied. Therefore, the overall energy conversion efficiency of the fuel cell is given by:

$$\eta = \frac{\Delta G_{T,P}}{\Delta H} * \eta_V * \eta_{fuel} \quad (1.28)$$

Although the maximum efficiency of a fuel cell depends on thermodynamics, the actual efficiency depends on electrode kinetics. Electrode kinetic is briefly discussed in the next section to present an overview of electrode kinetics and further elucidate the problem of efficiency as related to electrochemical conversion devices such as fuel cells.

1.4 Kinetics of fuel cells

In the previous section thermodynamics is used to demonstrate how chemical reaction can develop electrical potentials. In this section the electrical potentials developed based on reaction kinetics will be discussed.

When a chemical reaction occurs, it will develop electrical potential E and current i as discussed previously. According to Faraday's law:

$$i = \frac{dq}{dt} = nF \frac{dN}{dt} \quad (1.29)$$

$\frac{dN}{dt}$ is the rate of the electrochemical reaction as N is the number of moles of the species participating in the reaction. Introducing current density (j) which in fuel cell electrochemistry is more common than current equation (1.29) can be rewritten as:

$$j = \frac{nF}{A} \frac{dN}{dt} \quad (1.30)$$

This equation relates directly the current density to electrochemical reaction rate. The reaction rate can generally be written as:

$$v = kC_R \quad (1.31)$$

where v is the reaction rate, k is the reaction rate constant and C_R is the reactant concentration. Considering a general half-cell reaction as:



where Ox through a reduction reaction gains n electrons to form Red in the forward reaction, where as the backward reaction is an oxidation of Red which loses n electrons to produce Ox . Hence, for a net reaction the rate is given by:

$$v_{net} = k_f C_{Ox} - k_b C_{Red} \quad (1.33)$$

According to equation (1.30) for electrochemical reaction, this can be rewritten as:

$$j = \frac{nF}{A} (k_f C_{Ox} - k_b C_{Red}) \quad (1.34)$$

At equilibrium, the rate of forward reaction equals the rate of backward reaction, and thus there is no net current. The net current density at equilibrium is known as exchange current density, j_0 , and is considered as an important parameter to evaluate the fuel cell performance.

According to transition state theory, the rate constant for an electrochemical reaction can be described as:

$$k = \frac{k_B T}{h} \exp\left(\frac{-\Delta G}{RT}\right) \quad (1.35)$$

where k_B is Boltzmann's constant and h is Planck's constant. For electrochemical reaction, Gibbs free energy is consisting of both chemical and electrical terms. For the reduction reaction free energy is expressed as:

$$\Delta G = \Delta G_{chem} + n\alpha FE \quad (1.36)$$

And for the oxidation reaction it is defined as:

$$\Delta G = \Delta G_{chem} - n(1 - \alpha)FE \quad (1.37)$$

where α is the charge transfer coefficient. Combining equations (1.36) and (1.37) with (1.35), the rate constant for the reduction and oxidation reactions will be defined as:

$$k_f = \frac{k_B T}{h} \exp\left(\frac{-\Delta G_{chem,f}}{RT}\right) \exp\left(\frac{-n\alpha FE}{RT}\right) \quad (1.38)$$

$$k_b = \frac{k_B T}{h} \exp\left(\frac{-\Delta G_{\text{chem},b}}{RT}\right) \exp\left(\frac{n(1-\alpha)FE}{RT}\right) \quad (1.39)$$

or

$$k_f = k_{0,f} \exp\left(\frac{-n\alpha FE}{RT}\right) \quad (1.40)$$

$$k_b = k_{0,b} \exp\left(\frac{n(1-\alpha)FE}{RT}\right) \quad (1.41)$$

Substituting these equations into (1.34) provides the current density and potential relation as:

$$j = \frac{nF}{A} \left(k_{0,f} C_{\text{Ox}} \exp\left(\frac{-n\alpha FE}{RT}\right) - k_{0,b} C_{\text{Red}} \exp\left(\frac{n(1-\alpha)FE}{RT}\right) \right) \quad (1.42)$$

The above equation can describe the potential current ($V-I$) behavior of a fuel cell and is valid for both cathodic and anodic reactions. At equilibrium where the potential is E_r , net current is equal to zero and equation (1.42) can be written as:

$$j_0 = \frac{nF}{A} k_{0,f} C_{\text{Ox}} \exp\left(\frac{-n\alpha FE_r}{RT}\right) = \frac{nF}{A} k_{0,b} C_{\text{Red}} \exp\left(\frac{n(1-\alpha)FE_r}{RT}\right) \quad (1.43)$$

An expression that relates the overpotential to current density can be derived by substituting equation (1.43) into equation (1.42):

$$j = j_0 \left[\exp\left(\frac{-n\alpha F(E - E_r)}{RT}\right) - \exp\left(\frac{n(1-\alpha)F(E - E_r)}{RT}\right) \right] \quad (1.44)$$

This equation is called the ‘‘Butler-Volmer’’ equation and is considered as a principal equation for electrochemical systems. In most cases the Butler-Volmer equation is too complicated to deal with fuel cell reaction kinetics. Therefore, it typically is simplified into two useful approximate equations for two extreme conditions: (a) the overpotential is small or (b) the overpotential is large.

In case (a), where the overpotential is small, $\frac{nF(E-E_r)}{RT} \ll 1$, the Butler-Volmer equation can be expanded and simplified as [23]:

$$j = j_0 \left\{ \left[1 + (1 - \alpha) \frac{nF(E - E_r)}{RT} + \dots \right] - \left[1 - \frac{\alpha nF(E - E_r)}{RT} \right] + \dots \right\} \quad (1.45)$$

$$= \frac{j_0 nF(E - E_r)}{RT}$$

Equation (1.45) indicates that at low overpotentials ($\leq 0.015 V$), the current density is directly proportional to the overpotential. Based on this equation charge transfer resistance could be defined as:

$$R_{ct} = \frac{(E - E_r)}{j} = \frac{RT}{nFj_0} \quad (1.46)$$

R_{ct} refers to the effective resistance imposed at the electrode surface by the finite rate of the electron-transfer. The polarization resistance R_{ct} is the effective resistance imposed at the electrode surface by the finite rate of the electron-transfer process. If the overpotential is positive, an anodic (positive) current will be generated, and when the overpotential is negative, a cathodic (negative) current will be produced.

Another limiting situation, case (b), will arise at high overpotential ($> 0.1 V$). Under this condition, if the overpotential is positive, the first term in Butler-Volmer equation would be negligible and thus equation (1.44) can be rewritten as:

$$j = -j_0 \left[\exp \left(\frac{n(1 - \alpha)F(E - E_r)}{RT} \right) \right] \quad (1.47)$$

Similarly when the overpotential is negative, the second term of Butler-Volmer equation would be insignificant:

$$j = j_0 \left[\exp \left(\frac{-n\alpha F(E - E_r)}{RT} \right) \right] \quad (1.48)$$

This can be alternatively written as:

$$\eta = E - E_r = \frac{RT}{n\alpha F} \ln \left(\frac{j_0}{j} \right) \quad (1.49)$$

or

$$\eta = E - E_r = \frac{2.303RT}{n\alpha F} \log\left(\frac{j_0}{j}\right) \quad (1.50)$$

Defining two constants a and b as:

$$a = \frac{2.303RT}{n\alpha F} \log j_0 \quad (1.51)$$

$$b = -\frac{2.303RT}{n\alpha F} \quad (1.52)$$

Equation (1.48) can be simplified to:

$$\eta = a + b \log j \quad (1.53)$$

This is known as Tafel equation demonstrating that in a certain current density range, overpotential is a linear function of the logarithm of the current density. Tafel equation is generally used to describe the activation overpotential which represents an energy barrier required to be crossed in order to drive electrons to and from the electrode surface. Similarly equation (1.47) for the anodic positive overpotential can be written in Tafel form as:

$$\eta = a + b \log(-j) \quad (1.54)$$

where a and b are defined as:

$$a = -\frac{2.303RT}{(1-\alpha)nF} \log j_0 \quad (1.55)$$

$$b = \frac{2.303RT}{(1-\alpha)nF} \quad (1.56)$$

1.5 Polarization curve and voltage losses

In a practical PEM fuel cell, voltage is lower than ideal cell voltage. The open circuit voltage for PEM fuel cell working on H₂/O₂ at 25 °C and 1 atm with water as the by-product is 1.229 V. However, number of factors causes the real cell voltage to be less than this. The voltage losses can be classified into three main categories: 1) activation overpotential, 2) ohmic overpotential and 3) mass transfer overpotential. The performance of PEM fuel cells is

evaluated by polarization curve as shown in Figure 1.5. The three voltage losses are corresponding to three distinctive regions on this curve.

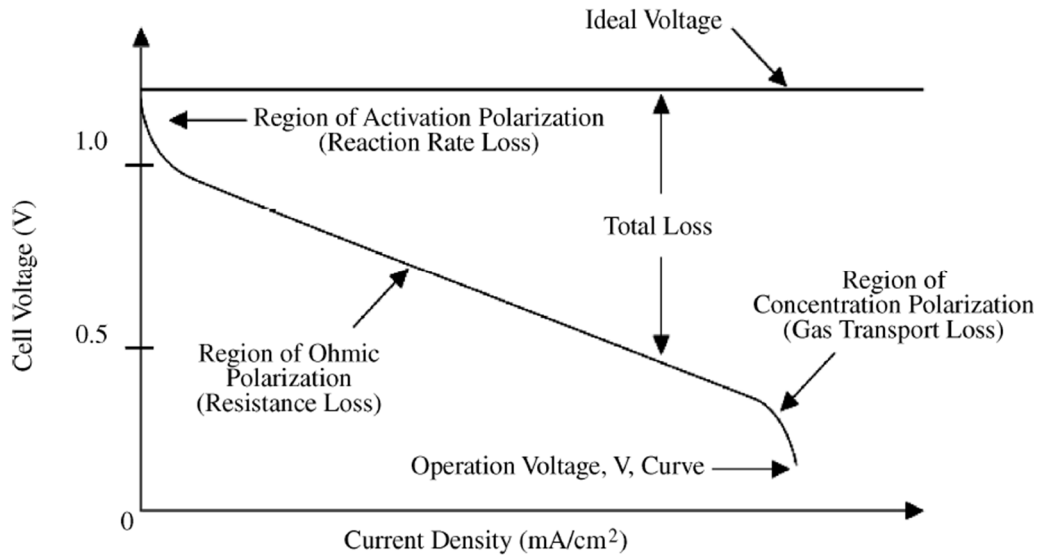


Figure 1.5 A typical polarization curve for a PEM fuel cell (adopted from http://www.altenergymag.com/content.php?issue_number=07.02.01&article=solar_polymer)

Activation overpotential occurs at low current densities (~ 1 to 100 mA cm^{-2}). It is caused by the sluggish kinetics of the electrochemical reactions taking place at the two electrode surfaces. As mentioned before, this is attributed to the rate of electron transfer to and from an electrode in an electrochemical reaction. A driving force is required to move the electrons through the external circuit. This is mostly provided by a portion of the voltage that is initially produced within the cell as it moves away from equilibrium and thus, this fraction of the voltage will not be available to do work. The difference between the open circuit voltage and the actual voltage is called the activation overpotential and described by following equation [19]:

$$\eta_{act} = -2.303 \left(\frac{RT}{n\alpha F} \right) \text{Log} \left(\frac{j}{j_0} \right) \quad (1.57)$$

which is just another form of Tafel equation. The first term is the Tafel slope and is a function of temperature and charge transfer coefficient (α). Charge transfer coefficient values range from 0 to 1 with a value of about 0.5 for the anode and 0.1 to 0.5 for the cathode of a H_2/O_2 PEM fuel cell. j_0 is called the exchange current density and indicates the reversibility of the electrochemical reaction; high j_0 values express a highly reversible electrode reaction with

low activation overpotential. According to equation (1.57), the activation overpotential can be reduced either by decreasing the Tafel slope, or increasing j_0 . In a PEM fuel cell while HOR (on Pt-based electrocatalyst) taking place at the anode, is relatively fast with j_0 values in the range of 1 mA cm^{-2} , the ORR at the cathode is slower with low j_0 values of 0.001 mA cm^{-2} [24,25]. This indicates that sluggish ORR at the cathode is responsible for several hundred millivolts losses of cell voltage (activation overpotential). Operating cell at higher temperature, employing more effective catalysts, increasing the reactant pressure, maximizing the electrode surface area and increasing the reactant concentration can reduce activation overpotential.

The second region on the polarization curve (Figure 1.5) demonstrates a linear decrease in voltage with increasing current density. This is due to ohmic resistance to the flow of electrons through the external circuit and protons through the ionomeric membrane. Electronic resistances mostly take place on the electrodes and bipolar plates, however, ionic resistance appears in the polymer membrane. Electronic resistance is almost negligible and the ohmic resistance is primarily caused by the polymer electrolyte membrane. The later is found to be a strong function of fuel cell temperature and membrane thickness. Temperature determines the membrane hydration level which in turn can affect the ionic resistance as water molecules are considered as the primary proton carriers in Nafion based membranes. The low membrane thickness can reduce the ionic resistance but this can lead to other types of problems such as fuel crossover and mechanical instability.

The potential losses due to ohmic resistance which is mostly pronounced at intermediate current densities ($100\text{-}500 \text{ mA cm}^{-2}$), is highly linear and can be expressed based on Ohm's law where voltage is the linear function of current:

$$V = IR \tag{1.58}$$

To express equation (1.58), in terms of current density, so that the ohmic losses can be compared to the other losses, area specific resistance, r ($\text{k}\Omega \text{ cm}^{-2}$), is defined and equation (1.58) is expressed in terms of this new quantity as:

$$\eta_{ohmic} = jr \tag{1.59}$$

Using appropriate materials for the fabrication of the electrodes, bipolar plates and other cell interconnect and incorporating a good design can reduce the ohmic overpotential.

Following the linear ohmic drop region at higher current densities ($> 500 \text{ mA cm}^{-2}$), concentration overpotential occurs. This is due to a decrease in concentration of reactants at the surface of the electrodes. At the anode a decrease in partial pressure of the hydrogen gas in the fuel mixture will reduce the cell potential. Using pure hydrogen as fuel, a pressure drop will still exist between the consumption side at the electrode surface and the supply container, the magnitude of which depends on the current being drawn from the cell and the design of the gas delivery system.

At the cathode side, a similar problem exists. Due to a decrease in the concentration of the oxidant, certain catalyst sites especially those situated within the interior of the electrode are devoid of fuel. In addition to oxidant consumption, its transport through the gas diffusion is affected at higher current densities, especially if air is used instead of pure oxygen. The presence of nitrogen in air forms a transport barrier across the gas diffusion layer as more and more current is drawn, leading to the sharp drop in voltage. The current at which such a voltage drop occurs is called the limiting current density. This value also strongly depends on the state of hydration in the cell, excessive water content in the cell accelerates the onset of limiting current density. Concentration polarization is commonly expressed using a simple equation as:

$$\eta_{conc} = -\frac{RT}{nF} \ln \left(1 - \frac{j}{j_{lim}} \right) \quad (1.60)$$

where j_{lim} is the limiting current density. This equation can only approximately determine the concentration losses. An empirical expression is often used to model the concentration losses:

$$\eta_{conc} = m e^{nj} \quad (1.61)$$

where m and n are fitted empirical constants related to mass transport limitation.

Combining the various overpotentials, the operating voltage of a fuel cell E at a given current density j can be written as:

$$E = E_0 - \eta_{act} - \eta_{ohmic} - \eta_{conc} \quad (1.62)$$

1.6 PEMFC issues and challenges

Energy requirements of the transportation sector contribute a significant proportion of the current global energy demands [26]. Generally, combusting petroleum-based fuels in an internal combustion engine (ICE) convert chemical energy into mechanical energy that is used to drive the vehicles. The fuel-to-work conversion efficiency for ICEs is low (30 to 35%) and more importantly, tailpipe emissions from an ICE cause urban pollution resulting from the unburnt hydrocarbons, soot, CO_x and NO_x. In addition, the carbon emissions contribute to the global warming effect. In 2012, the transportation sector stands for 33.7% greenhouse gases emission [26]. Therefore, the current world challenge is to respond to increasing transportation energy demand and, at the same time, to minimize vehicle exhaust emissions.

The automotive companies worldwide are following vigorous research and development programs to develop electrical power based vehicles, which indeed can minimize if not eliminate the urban pollution problem. Since 2009, more than 20 prototypes and demonstration fuel cell vehicles such as the GM HydroGen4, Honda FCX Clarity, and Mercedes-Benz F-Cell have been released. Toyota plans to produce 700 of Toyota Mirai fuel cell powered car for global sales during 2015. Finding a carbon-free source for hydrogen is an important technological issue that if it can be overcome the global warming effect will also be addressed.

The main focus for PEMFC research and development is to produce a commercially viable product. For automotive applications, since the PEMFC technology is considered as the replacement for the ICE technology, its cost must be reduced to the levels comparable to currently applied ICEs. The cost target, created by the U.S. Department of Energy (DOE) program for the development of automotive fuel cell system is 40 \$ per kW projected to high-volume production (500,000 systems per year) for the 80 kW net integrated transportation fuel cell power systems operating on direct hydrogen by 2020 [27]. The annual progress report of DOE shows that the catalyst layer makes up about 50% of the stack cost (Figure 1.6) [28]. Therefore, Pt content and cost contribution is the major barrier toward PEMFCs

commercialization and more reduction in Pt loading of the CL especially at the cathode side, is essential for large-scale automotive applications. The DOE has established 2020 technical target for reduction of the total Pt group metal (PGM) loading to 0.125 mg cm^{-2} [27].

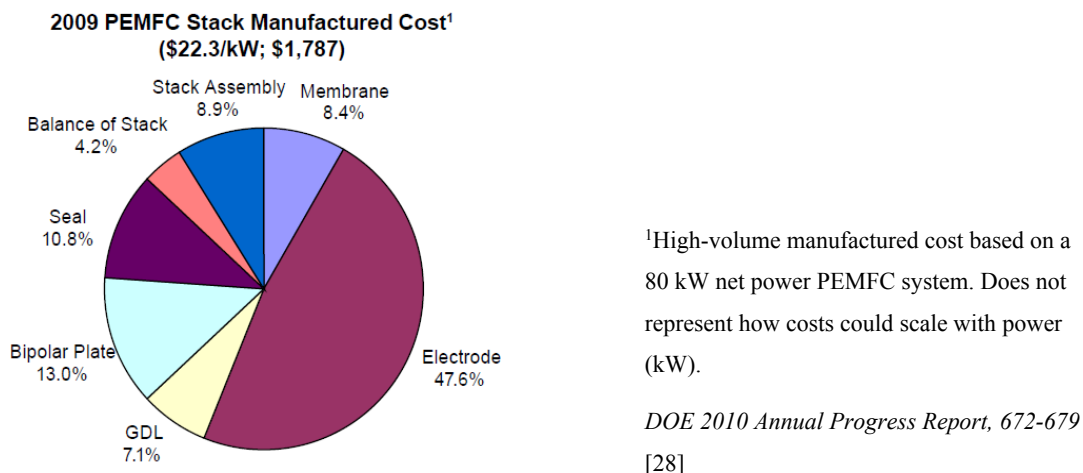


Figure 1.6 Cost analysis of a PEMFC stack

The reduction of Pt content while maintaining high enough electrochemical performance (conversion efficiencies $> 55\%$) is not a trivial task since the activation losses increase significantly with a decrease in catalyst (Pt) loading. While lowering the Pt-loading for anode electrode is straightforward¹ [29] due to the large activity of Pt toward the HOR [30], lowering of the cathode loading is limited by the poor activity of Pt for the ORR.

One approach toward reducing Pt loading of the cathode is to implement more active Pt-containing catalysts for ORR. One strategy for boosting the electrocatalytic activity of the Pt-based electrocatalysts is to alloy Pt in transition metal to develop a more effective Pt-M alloy catalyst. Platinum alloys in the form of core/shell particles are also attempted to reduce Pt-loading; they utilize a non-precious metal in the core and a thin platinum layer on the outer shell. Non-precious group metal (non-PGM) catalysts containing nitrogen-coordinated Fe or Co ions with high ORR activities comparable to the Pt-based catalysts has also been reported [31,32]. Non-PGM catalysts provide an alternative route to lower the PEMFC cost.

¹ For HOR the performance of Pt/C catalyst is only satisfactory when pure H_2 is applied. In the presence of CO there is strong adsorption of CO, which blocks the sites for the H adsorption causing a drastic decrease of the energy density, even for trace levels of CO.

Other methods to decrease the Pt loading of cathode electrode mainly are pursued by engineering catalyst layer structure. Nano-structured supports, such as carbon nanotubes (CNTs) are being used to increase the dispersion of the precious metal catalyst and enhance mass transport (of O₂ and H₂O) in the active layer. In chapter 2 the aspects regarding these strategies are discussed in more details.

Chapter 1 References:

- [1] W.R. Grove, On the Gas Voltaic Battery. Experiments Made with a View of Ascertaining the Rationale of Its Action and Its Application to Eudiometry, Philosophical Transactions of the Royal Society of London 133 (1843) 91-112.
- [2] G. Wand, Fuel Cells History Part 1, Jonson Matthew Plc. (2008). http://www.ogniwapaliwowe.info/Fuel_Cell_History_1.pdf
- [3] L. Mond, C. Langer, A New Form of Gas Battery, Proceedings of the Royal Society of London 46 (1889) 296-304.
- [4] K.R. Williams, Francis Thomas Bacon. 21 December 1904-24 May 1992, (1994).
- [5] J. Blomen, Fuel Cell Systems, Plenum Publishing Corporation, New York, NY, USA (1994).
- [6] X.-Z. Yuan, H. Wang, Fuel Cells, Handbook of Combustion, Wiley-VCH Verlag GmbH & Co. KGaA, (2010).
- [7] R.C. Makkus, A.H.H. Janssen, F.A. de Bruijn, R.K.A.M. Mallant, Stainless steel for cost-competitive bipolar plates in PEMFCs, Fuel Cells Bulletin 3 (2000) 5-9.
- [8] H. Tawfik, Y. Hung, D. Mahajan, Metal bipolar plates for PEM fuel cell--A review, Journal of Power Sources 163 (2007) 755-767.
- [9] Y. Wang, D.O. Northwood, Effects of O₂ and H₂ on the corrosion of SS316L metallic bipolar plate materials in simulated anode and cathode environments of PEM fuel cells, Electrochimica Acta 52 (2007) 6793-6798.
- [10] M. Kumagai, S.-T. Myung, S. Kuwata, R. Asaishi, H. Yashiro, Corrosion behavior of austenitic stainless steels as a function of pH for use as bipolar plates in polymer electrolyte membrane fuel cells, Electrochimica Acta 53 (2008) 4205-4212.
- [11] W.-L. Wang, S.-M. He, C.-H. Lan, Protective graphite coating on metallic bipolar plates for PEMFC applications, Electrochimica Acta 62 (2012) 30-35.
- [12] A. Kumar, M. Ricketts, S. Hirano, Ex situ evaluation of nanometer range gold coating on stainless steel substrate for automotive polymer electrolyte membrane fuel cell bipolar plate, Journal of Power Sources 195 (2010) 1401-1407.
- [13] C.-H. Lee, Y.-B. Lee, K.-M. Kim, M.-G. Jeong, D.-S. Lim, Electrically conductive polymer composite coating on aluminum for PEM fuel cells bipolar plate, Renewable Energy 54 (2013) 46-50.
- [14] O. Lavigne, C. Alemany-Dumont, B. Normand, S. Berthon-Fabry, R. Metkemeijer, Thin chromium nitride PVD coatings on stainless steel for conductive component as bipolar plates of PEM fuel cells: Ex-situ and in-situ performances evaluation, International Journal of Hydrogen Energy 37 (2012) 10789-10797.
- [15] L. Wang, J. Sun, B. Kang, S. Li, S. Ji, Z. Wen, X. Wang, Electrochemical behaviour and surface conductivity of niobium carbide-modified austenitic stainless steel bipolar plate, Journal of Power Sources 246 (2014) 775-782.
- [16] F. Barbir, PEM Fuel Cells: Theory and Practice, Elsevier Academic Press, Burlington, MA, USA (2005).
- [17] N. Yousfi-Steiner, P. Moçotéguy, D. Candusso, D. Hissel, A. Hernandez, A. Aslanides, A review on PEM voltage degradation associated with water management: Impacts, influent factors and characterization, Journal of Power Sources 183 (2008) 260-274.
- [18] U. Pasaogullari, C.-Y. Wang, Two-phase transport and the role of micro-porous layer in polymer electrolyte fuel cells, Electrochimica Acta 49 (2004) 4359-4369.

- [19] J. Larminie, A. Dicks, Fuel Cell Systems Explained, John Wiley & Sons Inc., West Sussex, England (2003).
- [20] P. Costamagna, S. Srinivasan, Quantum jumps in the PEMFC science and technology from the 1960s to the year 2000: Part I. Fundamental scientific aspects, Journal of Power Sources 102 (2001) 242-252.
- [21] W. Sun, B.A. Peppley, K. Karan, An improved two-dimensional agglomerate cathode model to study the influence of catalyst layer structural parameters, Electrochimica Acta 50 (2005) 3359-3374.
- [22] X. Li, Principles of Fuel Cells, Taylor & Francis Group, New York, NY, USA (2006).
- [23] P.W. Atkins, Physical Chemistry, W. H. Freeman and Company, New York, NY, USA (1978).
- [24] N.M. Markovic, Handbook of Fuel Cells–Fundamentals, Technology and Applications, W. Vielstich, A. Lamm, and H. A. Gasteiger, Editors, John Wiley & Sons Ltd., New York, NY, USA (2003).
- [25] A. Hamnett, Handbook of Fuel Cells–Fundamentals, Technology and Applications, W. Vielstich, A. Lamm, and H. A. Gasteiger, Editors, John Wiley & Sons Ltd., New York NY, USA (2003).
- [26] R. Schmidt, Information technology energy usage and our planet, Thermal and Thermomechanical Phenomena in Electronic Systems, 2008. IThERM 2008. 11th Intersociety Conference on, (2008) 1255-1275.
- [27] http://energy.gov/sites/prod/files/2014/12/f19/fcto_myRDD_fuel_cells.pdf.
- [28] DOE Annual Progress Report, (2010) 672-679.
- [29] H.A. Gasteiger, J.E. Panels, S.G. Yan, Dependence of PEM fuel cell performance on catalyst loading, Journal of Power Sources 127 (2004) 162-171.
- [30] N.M. Markovic, The hydrogen electrode reaction and the electrooxidation of CO and H₂/CO mixtures on well-characterized Pt and Pt-bimetallic surfaces, W. Vielstich, H. Gasteiger, A. Lamm Editors, Handbook of Fuel Cells–Fundamentals, Technology and Applications, Wiley, Chichester, UK, (2003).
- [31] M. Lefèvre, E. Proietti, F. Jaouen, J.-P. Dodelet, Iron-Based Catalysts with Improved Oxygen Reduction Activity in Polymer Electrolyte Fuel Cells, Science 324 (2009) 71-74.
- [32] E. Proietti, F. Jaouen, M. Lefèvre, N. Larouche, J. Tian, J. Herranz, J.-P. Dodelet, Iron-based cathode catalyst with enhanced power density in polymer electrolyte membrane fuel cells, Nat Commun 2 (2011) 416.

Chapter 2 PEM Fuel Cell Electrocatalysts

2.1 Platinum alloys

Pt-based alloy electrocatalysts for ORR were established by United Technologies Corporation (UTC) in 1980s, several Pt alloys (Pt-V, Pt-Co-Cr, Pt-Co, etc.) were applied as ORR electrocatalysts in PAFC with higher activity compared to Pt [1]. Subsequently, a large number of binary, ternary and quaternary electrocatalysts have been investigated. Mukerjee et al. [2-4] were among the first who exerted Pt-M alloy electrocatalysts for ORR in a PEMFC. Applying five binary alloys of Pt with first row transition metals (Cr, Mn, Fe, Co and Ni) activity enhancement was reported for all the alloy electrocatalysts. Comparison of ORR activity as iR corrected Tafel plots (Figure 2.1) at 95°C and 5 atm pressure in a PEMFC environment, showed lowering of the overpotential (20-30 mV) associated to specific activity (current density per unit electrochemical active area) enhancement (2-5 times) for all the alloy electrocatalysts. Pt-Cr explored as the most active binary alloy electrocatalyst.

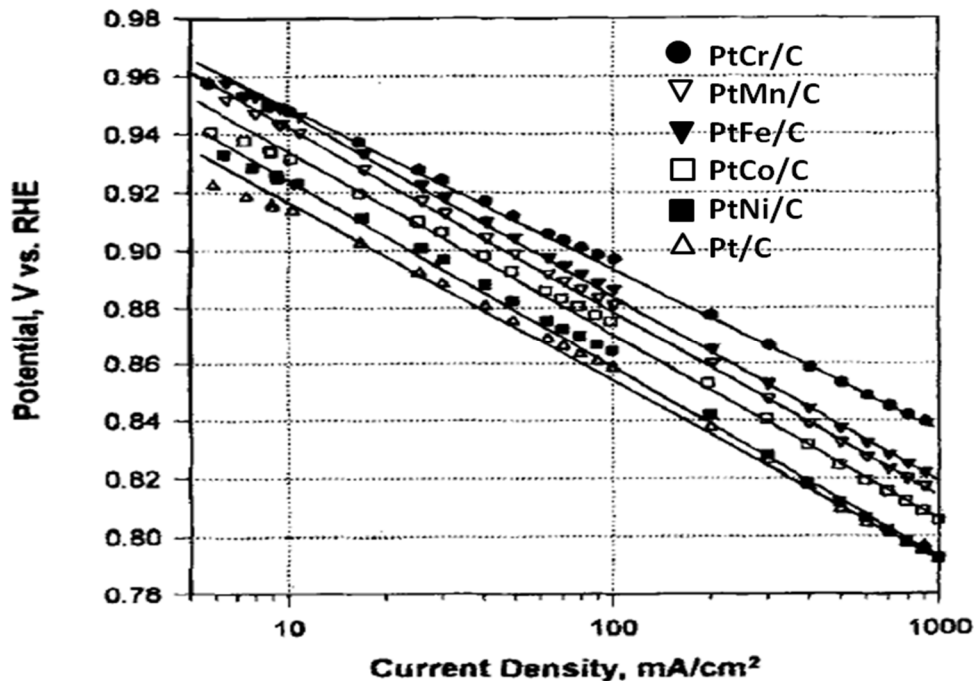


Figure 2.1 iR -corrected Tafel plots for ORR in PEMFCs at 95 °C and 5 atm pressure for Pt and Pt alloy electrocatalysts, Pt loading on electrodes 0.3 mg cm⁻² [3].

Later investigations have further confirmed the alloying strategy to be efficient in reducing Pt metal loading, as well as enhancing catalytic activity toward the ORR [5-8]. Toda et al. [5] studied the electrocatalytic activity of Pt alloys with Ni, Co, and Fe, prepared by the sputtering technique, toward the ORR in perchloric acid solution. Hydrodynamic voltammograms with rotated electrodes were applied to measure the electrocatalytic activity. Over the wide range of alloying compositions investigated, maximum activity was reported for 30, 40, and 50% content of Ni, Co, and Fe, respectively, by which 10, 15, and 20 times larger kinetic current densities were obtained compared to that of pure Pt.

Many arguments are made over the exact origin of the ORR activity enhancement caused by alloying Pt with another metal including shortening of the Pt-Pt inter-atomic distance (Structural Effect) [3,9,10]. Alloying Pt with transition metals of smaller atomic size is supposed to decrease the inter-atomic distance between the Pt atoms due to lattice contraction and provide favourable sites for adsorption of molecular oxygen. Min et al. [9] synthesized bimetallic alloys of Pt with Co, Cr, or Ni and employed EXAFS (extended X-ray absorption fine structure) analysis to determine the Pt-Pt neighbouring distances. They found nearly linear increase in specific activity with decreasing Pt-Pt bond distance of the catalysts. In addition, EXAFS studies indicated variations in electronic states upon alloying Pt with the transition metals.

Other theories correlated ORR activity improvement to an increased Pt d-band vacancy (Electronic Effect) [5,11-13]. Increased d-band vacancy is believed to strengthen Pt-O₂ bond and thus facilitates O-O bond cleavage. Toda et al. [5] proposed that the increased d-band vacancy in the Pt atoms leads to an increased 2π electron donation from O₂ to the surface Pt. This resulted in stronger Pt-O bond and a weaker O-O bond. The next step in the ORR is the initial electron transfer to form the superoxide intermediate ($O_{2,ads}^-$) where a single electron is back-donated from the Pt 5d orbital to the $2\pi^*$ anti-bonding O orbital. This step is considered as the rate determining step under most conditions and weakened 2π orbital that can accelerate this step, would increase the overall rate of the reaction. Stamenkovic et al. [11] studied the relationship between experimentally determined surface electronic structure (the d-band center) and the ORR activity of some Pt₃M (M = Ni, Co, Fe, Ti, V) surfaces. This relationship reveals “volcano-type” behaviour (Figure 2.2), which means that for the optimum catalytic activity there must be a balance between adsorption strength of reactive

intermediates and the ability to dissociate surface oxygen species. The adsorption and dissociation properties depend on the valence electronic structure of the metal, specifically, the density of states near the Fermi level [12]. A shifting of the metal d states upward relative to the Fermi level results in a strong metal-oxygen bond facilitating cleavage of O-O bond. On the other hand, if the d-band center is too close to the Fermi level, the strongly adsorbed intermediates limit the availability of free metal sites.

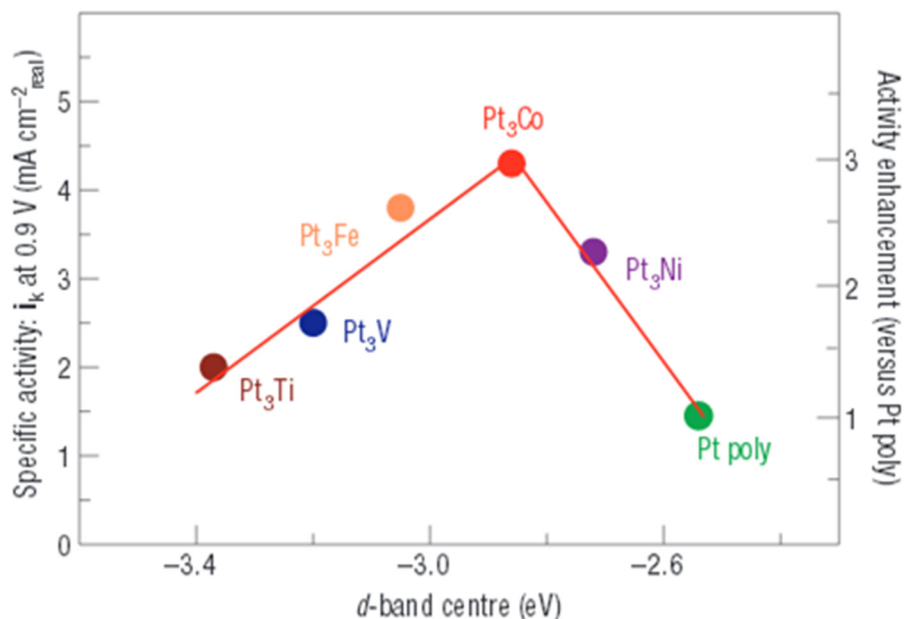


Figure 2.2 Relationships between the catalytic properties and electronic structure of Pt₃M alloys [11].

Nørskov et al. [13] investigated the ORR activity of a series of noble and non-noble metals as a function of the oxygen binding energy through density functional theory (DFT) calculations. This theoretical analysis also yielded a “volcano-type” relation (Figure 2.3) between the electrocatalyst activity toward cathode reaction and the oxygen adsorption energy. For the metals on the left side of the activity maximum with higher negative binding energy, stronger metal-oxygen binding energy exists. Therefore, on these catalysts (Fe, Ru, etc.) surface deactivation occurs due to strong oxygen binding. Weak metal-oxygen binding energy for the metals on the right arm of the plot (Ag and Au) illustrates inability of O₂ to bind on the surface to enable high ORR turnover rate. According to Figure 2.3, Pt and Pd are the best catalysts for ORR since they provide the “optimum” binding strength with adsorbed oxygen. Optimum interaction between the catalyst surface and the adsorbate can also be

elucidated through Sabatier principle [14]. If the interaction between the catalyst surface and the O₂ molecules is too strong, the catalyst surface gets blocked by strongly bonded O₂ species (OH or OOH) that are unable to dissociate. If the interaction is too weak, oxygen is unable to adsorb to any extent, resulting in an extremely high barrier to dissociation of O₂. Therefore, a better ORR electrocatalyst should bind O₂ more weakly than Pt, to increase the removal rate of adsorbed species.

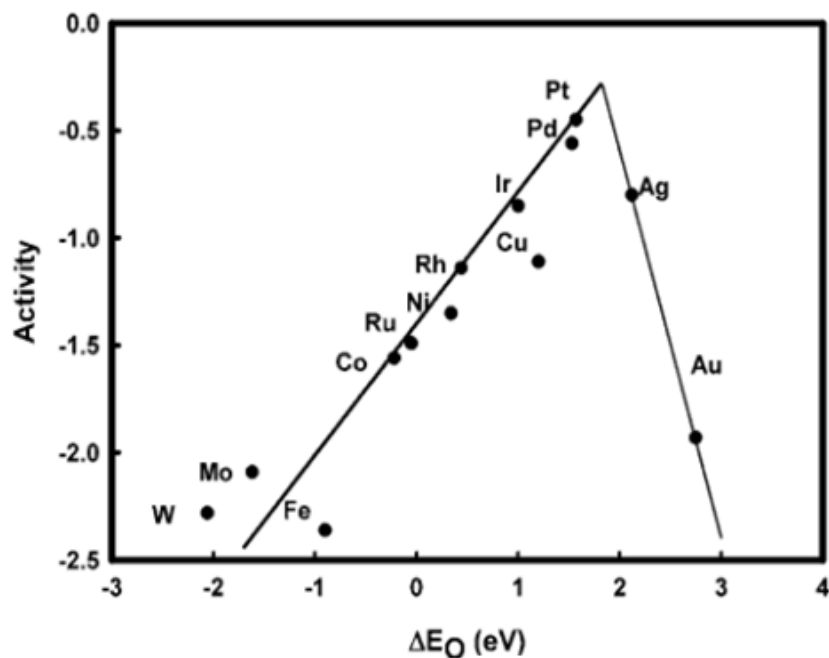


Figure 2.3 Volcano plot over the ORR activity as a function of atomic oxygen chemisorptions energy [13].

For ORR, the surface adsorbed oxygen species (OH or OOH) are supposed to act as intermediates, however, they are believed to also be poisoning species rather than intermediates (OH_{ads} Inhibition Effect). A maximum reaction rate is only attainable if oxygen binds to metal atom strongly enough to break the O-O bond, but loosely enough to desorb intermediates like OH⁻ after proton transfer. This gives rise to the classic “volcano-type” plot [15,16]. It was postulated that the alloy electrocatalysts show improvement in ORR by inhibiting OH⁻ adsorption. Mukerjee et al. [17-19] and Adzic et al. [20] observed a shift on the onset potential for Pt-OH formation depending on the alloying elements. This potential shift observed for OH⁻ formation is found responsible for activity enhancement of the Pt alloy electrocatalysts.

In practice, these effects are inseparable and a correlation of the surface structure, electronic arrangement and adsorption properties determine the activity and performance of Pt-based alloys. For instance the high activity of the Pt₃Ni (111) skin surface, 90 times more active than the current state-of-the-art Pt/C catalyst, was attributed to the synergy of the surface geometry, electronic structure, and surface adsorption [21]. Considering the surface structure in the near-surface region of Pt₃Ni (111), as shown in Figure 2.4 (A), the first atomic layer was completely made of Pt while the second layer was enriched in Ni (52% Ni as compared to 25% Ni in the bulk), and the third layer was again Pt-enriched (87%). A dramatic shift in the d-band center of Pt₃Ni (111) surface was also measured relative to a Pt (111) surface using corrected ultraviolet photoemission spectroscopy (UPS). The relations between the surface electronic properties and the potential-dependent surface coverage by adsorbing species (the adsorption isotherms in Figure 2.4 (C)) were found by comparing the experimentally determined position of the d-band centers to the fractional coverages of adsorbed hydrogen (H_{upd}) between $0.05 < E < 0.4$ V, where E is the applied potential, and hydroxyl species (OH_{ad}) above 0.6 V. As shown in the voltammograms of Figure 2.4 (B) a dramatic negative shift (~ 150 mV) in H_{upd} formation and a positive shift (~ 100 mV) in OH_{ad} formation occurred on the Pt₃Ni (111) skin relative to Pt (111). The fractional coverages by H_{upd} and OH_{ad} were dramatically reduced by 50% relative to Pt (111), which is in agreement with the large downshift (0.34 eV) of the d-band center position on the Pt-skin structure. The less adsorbed species (OH_{ad}) on Pt could reduce the inhibitory (site-blocking) effect on O₂ adsorption. Figure 2.4 (D) demonstrates the accelerated ORR kinetic on the Pt₃Ni (111) skin as compared with the results for Pt (111).

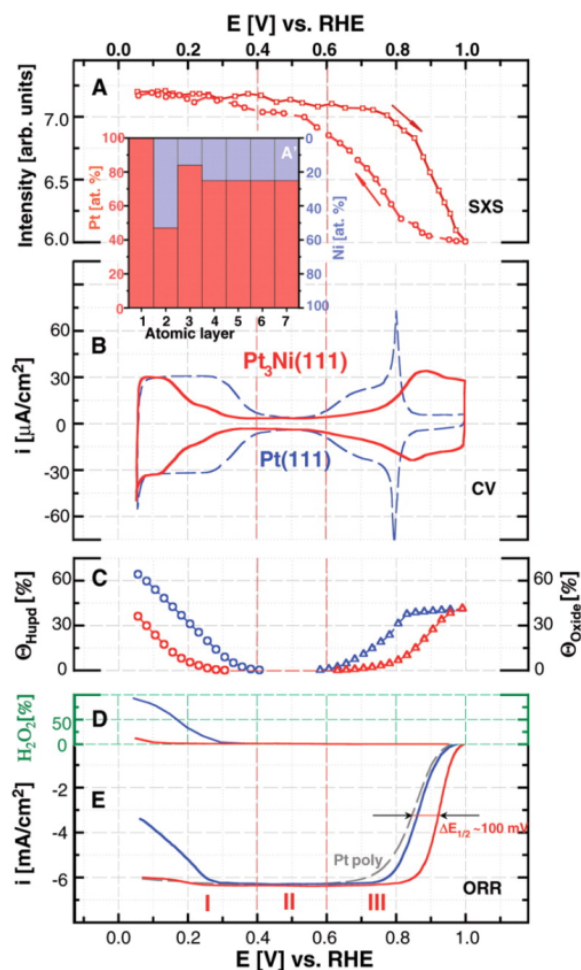


Figure 2.4 In situ characterization of the $\text{Pt}_3\text{Ni}(111)$ surface in HClO_4 (0.1 M) at 333 K [21].

2.1.1 Pt alloy nanoparticles: Effects of composition, structure, morphology and particle size on ORR electrocatalysis

Potential of Pt-based alloy electrocatalysts for ORR leads to different synthesis methods to produce nanoparticles with proper composition, ordering and morphology (the ratio of exposed facets), which indeed affect both activity and durability of the Pt-based alloy electrocatalysts. Colón-Mercado and Popov [22] studied the influence of the alloying metal nature on the catalytic performance of Pt alloy catalysts ($M = \text{Ni}, \text{V}, \text{Co}$ and Fe). The highest initial activity was found for the Pt-Fe catalyst while pure Pt catalyst demonstrated the lowest activity. The activity enhancement also revealed dependency on alloy composition. For Pt-Co alloy, higher activity was observed for the Pt:Co ratio of 3:1, while for the Pt-Ni alloy, the Pt:Ni ratio of 1:1 was found to be more active. Without considering the Pt:M ratio, most

Pt-M alloys presented better stability compared to Pt/C. The alloy composition effect on ORR activity was also studied for the Fe-Pt catalyst [23]. Monodispersed 3 nm $\text{Fe}_x\text{-Pt}_{1-x}$ ($x = 0.63, 0.58, 0.54, 0.42, 0.15,$ and 0) nanoparticles were synthesized and their composition-dependent ORR activities demonstrated that the $\text{Fe}_{0.42}\text{Pt}_{0.58}$ nanoparticles were more active than any other Fe-Pt nanoparticles. In a recent study, ORR catalytic activities of monodispersed 5 nm $\text{FePt}_3, \text{CoPt}_3,$ and NiPt_3 nanoparticles were investigated [24]. All the MPt_3 nanoparticles demonstrated higher ORR activity (2-3 times) than that of the conventional Pt/C catalyst. In addition, their catalytic performances showed a “volcano-type” dependence (Figure 2.5) on the type of M employed (similar to Figure 2.2). Among these three types of alloy, the CoPt_3 nanoparticles provided the highest specific and mass activity (expressed in terms of current per mass of Pt), which is consistent with what has been observed on extended surfaces [11].

Many alloys can form ordered structures during synthesis or during heat treatment at high temperatures. Xiong and Manthiram [25] synthesized several carbon-supported Pt-M alloys for oxygen reduction in PEMFCs. The Pt-M alloy catalysts were prepared by first precipitating the M^{n+} hydroxide ($\text{M} = \text{Fe}, \text{Co}, \text{Ni}$ or Cu) on commercially available Pt/C particles, and subsequently heat treating them at 900 °C in a flowing mixture of 90% Ar-10% H_2 . Upon heat treatment PtFe/C and PtCo/C , alloy catalysts with ordered structure were obtained. However, the PtNi and PtCu alloys demonstrated a disordered face-centered cubic (fcc) structure. The alloys with the ordered structures provided higher catalytic activity with lower polarization losses compared to Pt and the disordered Pt-M alloys. Optimal structural and electronic features such as optimum number of M atoms as Pt nearest neighbours, d-electron density in Pt atomic configuration on the surface and Pt-Pt distance were supposed to be responsible for catalytic activity enhancements. Kim et al. [26] prepared ordered FePt alloy nanoparticles through high temperature annealing of chemically disordered FePt nanoparticles at 750 °C under flowing mixture of 95% Ar-5% H_2 . Upon heat treatment, disordered FePt nanoparticles with face centered cubic (fcc) structure converted to a chemically ordered face centered tetragonal (fct) structure. To avoid aggregation of nanoparticles during the annealing process, fcc-FePt nanoparticles were coated with a layer of MgO that was completely removed by a dilute acid washing. (fct) FePt nanoparticles with a chemically ordered structure exhibited higher catalytic activity and durability toward ORR

in 0.5 M H₂SO₄ solution compared to (fcc) FePt nanoparticles and the commercial Pt/C. The results confirmed the importance of the ordered structure on the activity and durability of the Pt-based alloy nanoparticles.

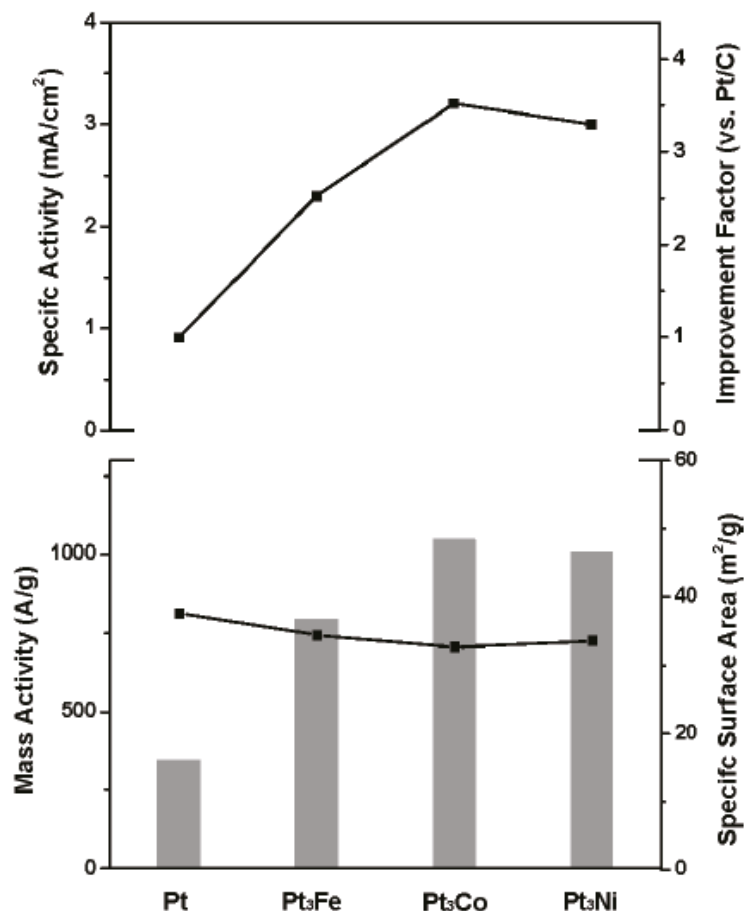


Figure 2.5 The dependence of specific activity (top), and mass activity (bottom, columns, left axis) and specific surface area (bottom, filled squares, right axis) on the types of alloys [24].

As discussed earlier, Pt₃Ni (111) extended surface revealed high activity toward ORR [21]. For Pt₃Ni nanocrystals, ORR activity was found to increase almost proportionally to the percentage of exposed (111) surfaces using cubes and other faceted crystals [27,28]. This demonstrated the significant role of the shape on ORR activity of these alloyed nanoparticles as it can determine the surface atomic arrangement and coordination. In other words, the shape of Pt alloys nanocrystal decides on which crystal facets are exposed at the surface. Thus, the well-defined octahedral and icosahedral nanocrystals of Pt₃Ni were synthesized and their catalytic activity was explored [29-31]. The ORR activity increased with the change of shapes from cube to octahedron, the specific area ORR activities at 0.9 V were found to

be $1.26 \text{ mA cm}_{Pt}^{-2}$ for the octahedral Pt₃Ni catalyst and $0.85 \text{ mA cm}_{Pt}^{-2}$ for the cubic Pt₃Ni catalyst [29]. Icosahedral nanocrystals of Pt₃Ni showed even further enhancement in ORR specific area activity ($1.83 \text{ mA cm}_{Pt}^{-2}$ at 0.9 V) compared to the octahedral nanocrystals [31]. In icosahedral nanocrystals, 20 tetrahedral subunits were bound by the (111) facets and formed 30 twin boundaries and a surface enclosed by the (111) facets [31]. The higher specific area activity of icosahedral Pt₃Ni catalysts (50% higher than that of the octahedral Pt₃Ni catalysts) was attributed to the strain-induced electronic effects [31]. The strains in the icosahedral geometry develop as the tetrahedral subunits stretch to convene at the twin boundaries. DFT calculations demonstrated large differences in both d-band center (0.36 eV) and hydroxyl adsorption energy (0.26 eV) for atoms on the (111) facet between Pt icosahedral and octahedral nanoparticles related to the surface strain [31].

Similar to pure Pt particles, Pt alloy particles show influence of particle size on ORR activity since the number and size of different facets changes as a function of the particle size. The effect of particle size of Pt/C on the ORR performances has abundantly been investigated [32-35] but fewer studies have been done with Pt-M (nano-alloys)/C [36-38]. Cyclic voltammograms for the Pt₃Co/C catalysts with particle size ranging from 3 to 9 nm showed that the H_{upd} peaks ($0.05 \text{ V} < E < 0.4 \text{ V}$ vs. RHE) shrink as the particle size increases as a result of the decrease in specific surface area [36]. Both the oxidation peak ($\sim 0.9 \text{ V}$) in the anodic scan and the reduction peak ($\sim 0.8 \text{ V}$) in the cathodic scan revealed a negative shift of $\sim 30 \text{ mV}$ from 9 to 3 nm Pt₃Co. This indicates that the smaller nanoparticles are oxidized at a lower potential due to the higher ratio of undercoordinated atoms (edge and corner sites) on the surface [39]. The results illustrated that the ORR specific activity of Pt₃Co increases with the particle size, and the maximum in mass activity can be achieved with nanoparticles of about 4.5 nm by balancing the specific surface area and specific activity [36].

2.1.2 Nanotextured Pt alloys: surface modification routes

In spite of enhanced ORR activity Pt alloy electrocatalysts have shown dissolution of the transition metals from the alloys in acidic environment of fuel cells. Base metals dissolution leads to instability of Pt alloy catalysts, compromising the advantages of Pt-M alloys. Therefore, bulk Pt alloy particles alternatively were replaced by so-called “core/shell”

structures. Applying core/shell materials, the entire Pt atoms are located only on the outer surface of the catalyst particle, where the catalytic process takes place and the non-precious metal atoms are used as the particle core. Complete encapsulation of the base metal by the noble Pt can protect the underlying metal from corrosion. In addition, the Pt dispersion would be very large regardless of the particle size because the Pt is located only in the near-surface region of the particle. Higher Pt dispersions result in lower Pt loadings. Furthermore, by supporting Pt (and Pt alloys) on other metal cores, the electronic properties of the Pt shell will be modified, resulting in further enhancements in ORR.

Initial works by Zhang et al. [40] showed that preparing Pt monolayers on both Pd (111) substrates and Pd/C nanoparticles enhanced ORR activity compare to pure Pd and Pt. The Pt mass-specific activity of the Pt/Pd/C electrode was 5-8 times higher than that of the Pt/C electrocatalyst. In terms of the noble metal (Pt + Pd) used, mass-specific activity enhancement of two was found compared to that of Pt/C. The improvement in ORR activity was attributed to the formation of Pd-OH species that, through repulsion effects, hindered the formation of Pt-OH until higher potentials. This was demonstrated in higher Tafel slopes (-95 mV/decade), representing no poisoning of the catalytic active sites by adsorbed OH species. The same group studied the ORR electrocatalytic activity of platinum monolayers supported on other substrates (Au, Rh, Ru, and Ir) in 0.1 M HClO₄ solution and employed DFT calculations to develop a rationale that can explain the experimentally measured results [41]. DFT calculations indicated “volcano-type” of dependency between ORR activity and calculated d-band centers of the platinum monolayer structures (relative to the Fermi level). The Pt monolayer supported on Pd (111) exhibited the maximum activity. The maximum activity was supposed to occur when the energies of O₂ dissociation and O hydrogenation were balanced. High energy of dissociation decreases the ORR activity because O-O bond breaking becomes difficult. Conversely, high energy of O hydrogenation lead to strong OH formation and block sites so that the activity will diminish. Zhang et al. [42] also investigated mixed Pt-M (M = Re, Ru, Os, Rh, Ir, Pd, Au) monolayers on Pd (111). The metals such as Re and Os which were found to facilitate the formation of M-OH (-O) species provided higher activity enhancements over Pt. Studying the effect of metal composition, designated Pt_{0.8}M_{0.2} demonstrated the best activity due to the balance between sufficient M to give enough surface M-OH groups to hinder Pt-OH formation and enough Pt to provide sites for

O₂ adsorption and turnover. In addition, they showed that these enhancements could be translated to carbon-supported Pd nanoparticles as core, with the Pt_{0.8}Re_{0.2}/Pd/C exhibiting 21 times greater ORR activity than that of the Pt/C catalyst based on Pt content. The same group also explored the long term stability of these catalysts since long-term durability of the Pt-containing shells for fuel cell application is a matter of concern. One long-term durability test reported the survival of Pt/Pd/C core/shell cathode for 2,900 h; however, considerable performance losses was observed (~140 mV) even under steady-state test condition without significant cycling [43].

An alternative approach based on core/shell structures has been reported by Koh and Strasser [44] applying electrochemical surface de-alloying, that is, selective electrochemical surface dissolution of non-noble (Cu) metal atoms from a homogeneous noble metal-poor alloy precursor. Rotating disk electrode measurements on these core-shell de-alloyed catalysts have shown 4-6 times enhancement in intrinsic reactivity over the state of the art Pt catalyst. In addition, they postulated that de-alloying could create favourable structural arrangements of Pt atom on the particle surface by forming more active crystallographic facets or more preferable Pt-Pt interatomic distances, both of which are beneficial for ORR. The same group also studied the activity of these electrocatalysts in a single PEMFC and reported up to 4 times of enhancement in terms of Pt mass activity and of more than 10 times in terms of specific activity compared to state-of-art Pt cathode catalyst [45]. In spite of providing significant activity improvement their durability in a fuel cell condition was found to be quite low [46,47]. This was mainly due to Cu leaching at the cathode side and its redeposition on the anode which ultimately led to anode deactivation. Later, they reported more active and surprisingly stable de-alloyed catalyst prepared from de-alloyed Ni-Pt core shell nanoparticles. The latest generation of this catalyst demonstrates up to 5 times activity enhancement (in terms of Pt mass activity) and high stability (less than 30 % loss in mass activity after 30,000 cycles) in both RDE and MEA tests [48-50].

2.2 Non-platinum electrocatalysts for ORR

2.2.1 Non-pyrolyzed/pyrolyzed transition-metal-containing macrocycles

N₄-Metallomacrocycles (Figure 2.6) are organometallic compounds consisting of a central metal atom (generally Fe or Co) bonded to four nitrogen atoms and surrounded by an organic

macrocyclic ligand (large molecules with a cyclic ring). The motivation to use N₄-metallomacrocycles originates from the fact that in living organisms such compounds (hemes) serve as co-enzymes for the majority of redox-catalyzing enzymes (cytochromes). Jasinski [51] first reported N₄-metallomacrocycle, namely cobalt phthalocyanine (CoPc) as ORR catalyst in alkaline media about 50 years ago.



Figure 2.6 Examples of N₄- metallomacrocycles used as catalysts for ORR

The nature of metal center, ligand, and to some extent substituents (functional groups attached to the ligand) were found to affect the activity of this type of electrocatalysts toward ORR [52]. Among several transition metal macrocycles investigated, Fe and Co metal centers provided the optimal electrocatalytic activities toward ORR, attributed to their distinct M(III)/(II) redox potential [53-55]. The ligand properties were also found to play a significant role in the ORR activity of these compounds [56,57]. This is related to the inductive and mesomeric effects of the ligands on modifying the electronic structure of the central metal atom. In this regard, the molecular and electronic structures of some transition metal macrocyclic complexes have been studied using DFT. Liao et al. [56] examined systematically the influence of some ligands (porphyrin (P), porphyrazine (Pz), and phthalocyanine (Pc)) on the electronic structure of a series of transition metal macrocyclic complexes (M = Fe, Co, Ni, Cu, and Zn). They found that replacing the CH-groups in the MP molecules by N atoms led to the stabilization of all valence molecular orbitals in the MPz molecules, while introducing the benzo rings into the MPz molecules to form the MPc molecules destabilized the occupied valence molecular orbitals [56]. Shi and Zhang [57] have used the DFT calculations to determine the adsorption structures of O₂ molecule on various MP and MPc complexes (M = Fe and Co). According to their calculations, ORR catalytic

activity was determined by the ionization potential and dioxygen-binding ability of the macrocyclic complexes. While in the case of P based complexes CoP provides higher ionization potentials and therefore better ORR activity, in the case of MPc systems, FePc demonstrates larger ionization potential and better ORR activity. This elucidated the effect of ligand on ORR activity of these materials. In addition, different substituent groups (electron donating or withdrawing substituents) were shown to change the activity and stability of transition metal macrocycle based electrocatalysts in acidic media by affecting the electron density of both the ring and the metal centre [58-62]. Baker et al. [62] investigated several substituted FePc structures (Figure 2.7) and proposed that by affecting the electron density of the active metal centers, substituent groups could determine turnover frequencies and activity of these macrocycles toward ORR. Substitution also found to play a significant role on stability. Of the four FePc species, FePcCl₁₆ (Figure 2.7c) demonstrated the highest stability in acidic ORR environment. Moreover, substituent groups were found to affect the exact mechanism of the ORR, with the overall electron transfer number varying between 1 and 3.

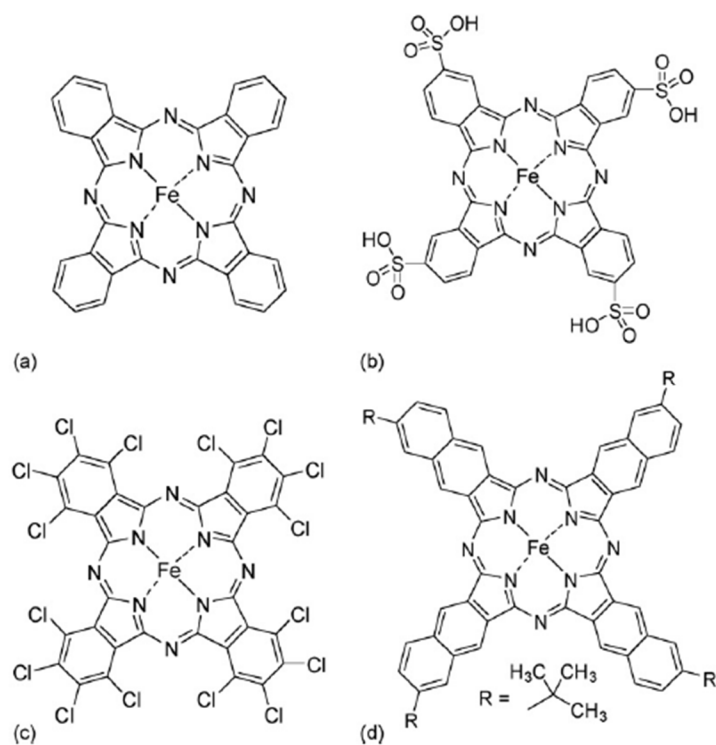


Figure 2.7 Molecular structure of (a) FePc and (b, c and d) various substituted FePc molecules [62].

While transition metal macrocycle based electrocatalysts showed significant activity toward ORR, the long-term stability of these catalysts in fuel cell acidic operating conditions was found to be poor [63,64]. Therefore, pyrolysis, heat treatment in an inert atmosphere (N_2 or Ar), was established to improve not only the ORR catalytic activity but also the long term stability of these materials. Considering the poor stability of non-pyrolyzed transition metal N_4 chelates, they have not been studied much recently.

Jahnke et al. [65] were the first, who found that heat treating the macrocycles in the presence of carbon support, pyrolysis, could produce more stable ORR catalyst. In the years afterward, investigations on pyrolyzed macrocycles mainly focused on optimizing synthesis conditions (i.e. temperature/duration of heat treatment, supporting material) to enhance the catalytic activity and stability. Wide range of pyrolysis temperature (400-1000 °C) was investigated over the years and the highest activity towards ORR was reported for pyrolysis temperatures between 500 and 800 °C in inert environments for macrocyclic compounds [66-68]. Faubert et al. [69] studied the effect of pyrolysis temperature on the activity and stability of Fe and Co tetraphenylporphyrins (FeTPP and CoTPP) adsorbed on carbon over the temperature range of 100–1000 °C. Higher catalytic activity was reported for those catalysts that were heat treated in the intermediate range (500–700 °C), however, higher pyrolysis temperatures (900 °C or above) led to the more stable catalysts [69]. The nature of the carbon support and its surface properties are also found to affect the overall activity and stability of the electrocatalysts. Gouerec et al. [70] found that oxygen containing surface groups are responsible for strong interactions between the metal centers and the carbon support that can protect the chelate structure from rapid destruction and sintering and thereby promote long term stability. The surface nitrogen content was also determined to play a significant role in improving ORR activity [71]. Meng et al. [71] reported chloroiron tetramethoxyphenylporphyrin (ClFeTMPP) adsorbed on a furnace grade carbon black and pyrolyzed at 950 °C in a NH_3 /Ar gas mixture with various NH_3 volume fractions (from 0% to 100%). A significant increase in ORR activity with as little as 1.3% NH_3 was observed. This enhancement was attributed to the concurrent increase in microporous surface area, N and Fe surface contents in these catalysts. However, considerable decrease in catalyst stability (compared to those pyrolyzed in pure Ar) was reported which was believed to be caused by a reduced degree of graphitization.

Many studies on pyrolyzed transition metal N₄-chelates have focused on the nature of the active sites, however, the real structure of these catalysts is yet to be revealed. All the theories put forward to this point will be discussed briefly here. First off, researchers from several different groups believed that the metal N₄ coordinated center remain intact after pyrolysis while the peripheral structure of the macrocyclic ligands react with the carbon support [66,72-74]. Activity enhancement of these catalysts was attributed to the binding of the active site to the carbon surface that can change electron density of the metal ion and hence improve the activity of the pyrolyzed macrocycles [66,72-74]. Others postulated the destruction of the M-N₄ environment of the macrocycles during pyrolysis. According to these studies although the M-N₄ structure can be maintained at low temperatures, but increasing the pyrolysis temperature they gradually disappear. Studying various Co and Fe macrocycle precursors via different characterization techniques, the presence of metal and metal oxide particles was reported after pyrolysis at high temperatures [75-77]. Exposed to air at room temperature the metal particles spontaneously oxidize to form metal oxides. In contact with the electrolyte solution, metal oxides undergo dissolution. It is thus possible that the dissolved metal ions could re-adsorb to nitrogen coordinated sites formed on the carbon surface upon pyrolysis to form new M-N_x/C structures which are believed to be the true catalytic site for oxygen reduction [78-80]. Other possible active sites could be either metal or metal oxide surface particles. Since TEM images showed that these metal particles become completely encased in layers of carbon [75,77] it is not clear how O₂ molecules could reach the surface of the metal particles. One explanation is that the underlying metal improves the catalytic activity of the carbon shell above. However this postulation cannot elucidate why the presence of nitrogen during the pyrolysis is required to achieve high catalytic activity, while these encased metal particles can also be formed in the absence of nitrogen.

Some other studies have doubted metal as a constituent of the real active site and considered metal-ion centers to only act as a catalyst toward formation of catalytically active sites during pyrolysis [67,81,82]. The very first report on this type of active sites demonstrated similar ORR activity with metallic and non-metallic precursors, except that there was an approximate shift of 350 °C in the required pyrolysis temperature [67]. In this type of electrocatalysts the N groups formed during pyrolysis on the carbon surface are considered as the ORR active sites [83,84]. Employing pyrolyzed FeP, Gojkovic et al. [84] reported the formation of

nitrogen groups during pyrolysis due to the reaction of the macrocycles with the support; the metal-ion is proposed to only serve as a catalyst for formation of the active sites.

While the pyrolyzed macrocycles showed improved stability and ORR activity in acidic media (compared to non-pyrolyzed macrocycles), the macrocycle precursors did not prove to be an economical solution. Therefore, investigations have shifted focus to the non-macrocylic materials.

2.2.2 Non-macrocylic heat treated catalysts (M/N/C type of catalysts)

Using precursors other than macrocycles to produce non-platinum-group metals (non-PGM) ORR electrocatalysts was first reported by Johansson and Larsson [85] in 1986, employing thermal activation of a Co polymer complex. Since this time, pyrolysis of a variety of simple sources of carbon, nitrogen and transition metals together has been used to produce ORR catalysts in acidic electrolytes. Even though pyrolysis of any mixture of nitrogen, metal, and carbon species can produce a sort of catalyst with some ORR activity, the choice of precursors, supports, and synthesis conditions plays a significant role in obtaining materials with high activity and long-term durability required for practical electrocatalysts [86,87]. Generally, there are two groups of non-macrocylic non-precious metal electrocatalysts: (1) catalysts derived from metal salts and gaseous nitrogen precursors, such as ammonia (NH₃) [88-96] or acetonitrile (CH₃CN) [97-99]; and (2) catalysts synthesized from inorganic metal salts and nitrogen-containing molecules such as cyanamide [100], ethylenediamine [101,102] nitroaniline [103], melamine [104], polyaniline [105,106] and etc. [107-109]. Using ammonia as a nitrogen precursor to produce ORR electrocatalysts, which belong to the first group, can have two major consequences. First, ammonia may etch and create porosity in the carbon support, and secondly, ammonia may create nitrogen bearing functionalities on the carbon surface [95,110-113]. Dodelet et al. [95,110-113] determined that micropores created during ammonia heat treatment via etching of the carbonaceous material, hosted a large number of Fe-N₄ sites that were believed to be catalytically active sites (Figure 2.8). They also found that NH₃ could react with the disordered carbon phase of the support more preferentially than the graphitic crystallites in the same carbon support [110,111]. This led to a more crystalline carbon support structure as disordered carbon is mainly gasified. Their latter investigation reveals that NH₃ as a very well recognized nitrogen precursor could dope

nitrogen functionalities on the surface of the carbon support [76,114] during high temperature pyrolysis. In some other studies where additional nitrogen containing precursors were also implemented as complementary nitrogen source during catalyst preparation no significant increase in total nitrogen content of the final catalyst was observed upon NH_3 heat treatment [115,116]. NH_3 always plays however a drastic role in increasing the porosity of the catalysts [116]. This confirms that the principal role of NH_3 is to form porosity during pyrolysis and this way bring the active sites buried in the material to the surface and make them more accessible to oxygen molecules and protons [116].

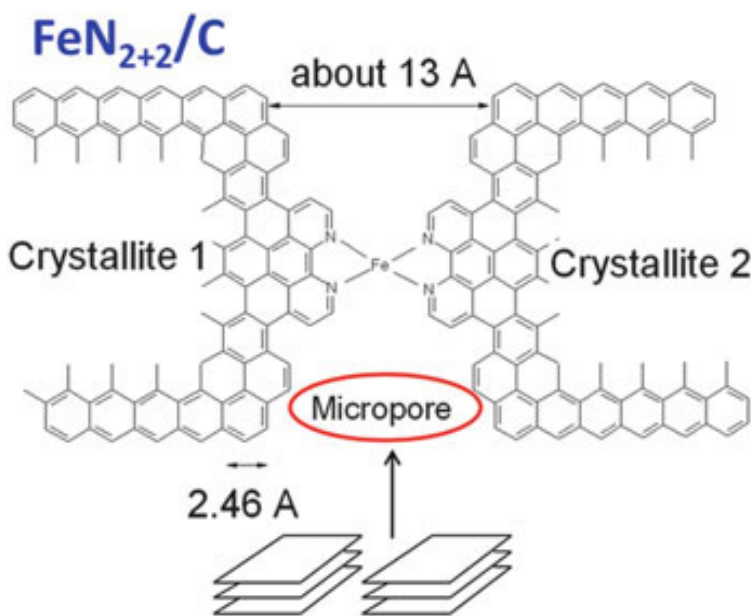


Figure 2.8 Schematic illustration of the micropore hosted active site structure present in ammonia-treated non-PGM electrocatalyst, consisting of Fe ion bridged between two adjacent nitrogen-doped graphitic crystallites [113].

The same group demonstrated that although pyrolysis in ammonia may result in highly active electrocatalysts, using even small quantity of ammonia during catalyst preparation led to major loss in stability [71, 95]. They postulated that micropores formed through ammonia pyrolysis are either prone to flooding during fuel cell operation or that undesirable chemical changes of active N bearing sites in the acidic medium lead to their poor stability [71]. Later, the same group [114] found that in this class of catalyst, some surface nitrogen species in proximity but not part of the active site structures cause the activity loss of catalyst during fuel cell operation. They claimed that the protonation of the aforementioned surface nitrogen species, followed by anion binding as represented schematically in Figure 2.9 led to

instability of these catalysts during PEM fuel cell operation. Although the former would not negatively affect ORR turnover frequencies of the active sites, once anion binding occurs, the ORR activity would be reduced significantly. More recently, they used Mössbauer spectroscopy to follow changes in the stability of these Fe/N/C catalysts while they were employed at the cathode of an MEA and tested in a fuel cell [117]. They found that potential excursions applied to the MEA led to oxidation of the carbon support that hosted catalytic sites. This is followed by leaching of active sites that causes activity decay and instability of fuel cell performance. Flooding would also occur at the cathode side due to an increased hydrophilicity of this carbon as a result of its oxidation.

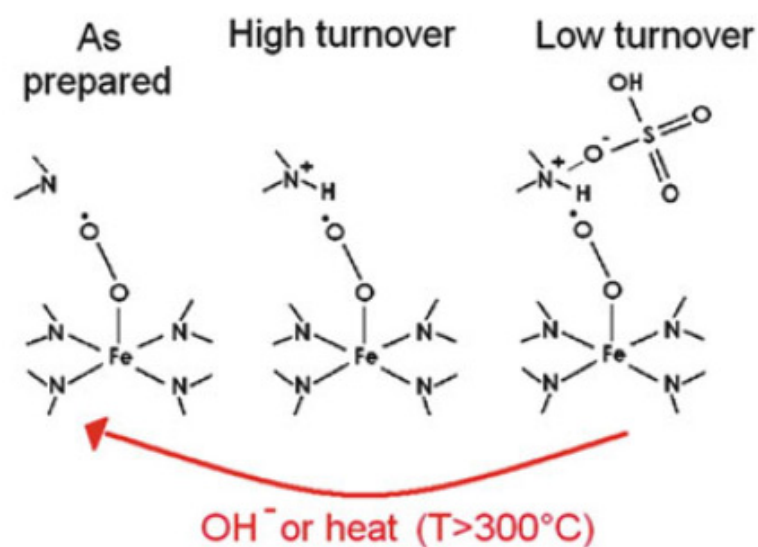


Figure 2.9 Schematic depicting (left) metal-centered active site structure in proximity to a surface nitrogen species, (center) protonation of the surface nitrogen species with the active site having a high turnover frequency, and (right) anion binding to protonated surface nitrogen species dramatically reducing active site turnover frequency [114]

Preparing electrocatalysts from the second group using N-containing material, polyaniline (PANI), an inexpensive and nontoxic aromatic polymer, was employed as a source of nitrogen [105, 106]. Structural similarities between PANI and the graphitic carbon support (Figure 2.10) was believed to cause better interaction between these two species and thus, facilitate the incorporation of nitrogen-containing active sites into the partially graphitized carbon matrix in the presence of Fe and/or Co and hence formation of the active sites on the carbon support during pyrolysis. Moreover, the high nitrogen content of PANI and its ordered structure lead to high active site density and uniform dispersion of active sites throughout the

entire catalyst surface area. The best reported PANI-based electrocatalyst demonstrated a half-wave potential only ca. 59 mV below a commercial Pt/C catalyst-coated electrode with Pt loading of $60 \mu\text{g cm}^{-2}$ [106]. Furthermore, the performance of these PANI-based catalysts was evaluated in a single PEM fuel cell and a maximum power density of 0.55 W cm^{-2} was obtained for the best reported electrocatalyst [106]. In addition, this PANI-based electrocatalyst is by far the most durable non-PGM M/N/C type of catalyst which demonstrated promising operational stability with negligible performance loss after 700 h of operation at a constant fuel cell voltage of 0.4 V [106]. This enhanced stability was attributed to the aromatic nature of PANI, which provides stronger interactions with the metal-ion centers. Moreover, the in-situ formation of graphene sheets throughout the PANI-derived catalysts was found responsible for the improved durability of catalysts.

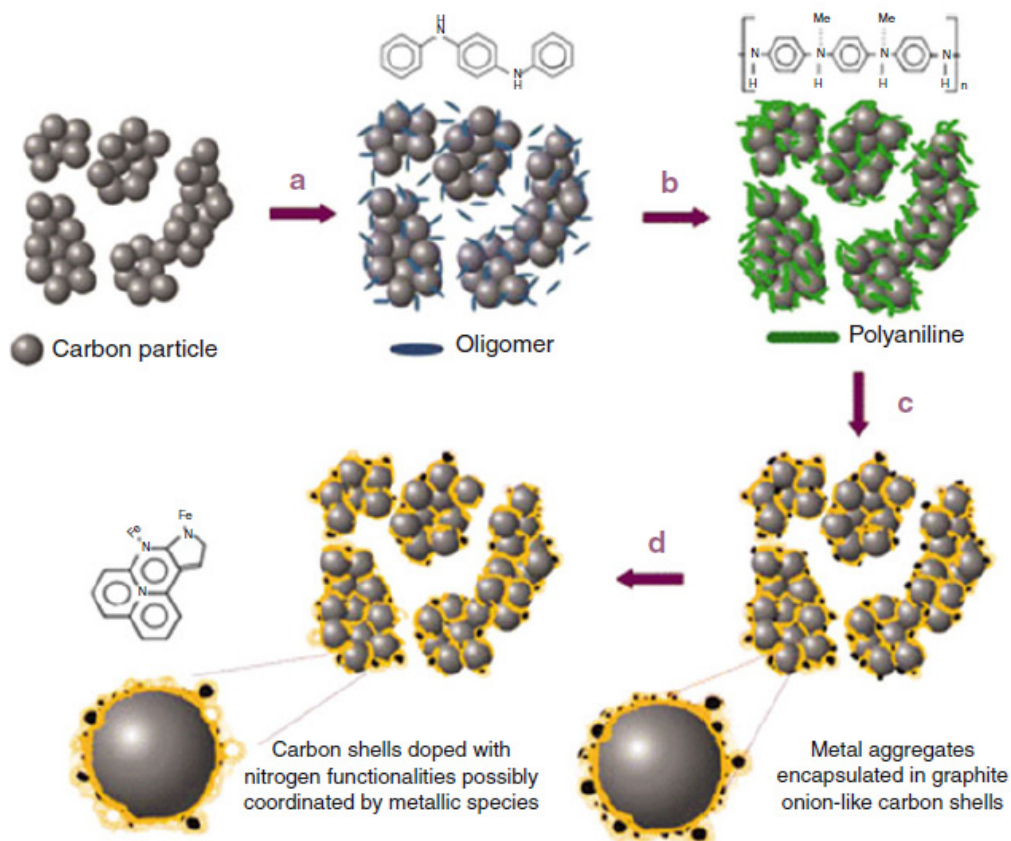


Figure 2.10 Schematic illustration of the fabrication of highly active PANI-based NPMCs. (a) Mixing carbon support particles with aniline monomer and transition metal precursors, (b) polymerization of aniline with ammonium persulfate, (c) heat treatment in nitrogen, and (d) acid leaching and second heat treatment [106].

The transition metal choice plays a significant role in the ORR activity and durability of the non-PGM electrocatalysts prepared from non-macrocyclic complexes. Although some other transition metals such as Ni [98,118,119] have been used along with Fe [82,87-92, 94,95, 97,98, 107, 113, 118] and Co [87,101,102, 107-109, 118,119], as metal precursor but those electrocatalysts made of Fe and Co have provided more promising results in terms of ORR activity [120]. It is worth mentioning that the nature of the active sites prepared from these two metals is believed to be different. While the active sites generated in the presence of Co exhibited an onset ORR potential similar to that observed in metal-free nitrogen-doped carbon catalysts with CN_x species (pyridinic, quaternary nitrogens) [102], Fe is found to directly participate in the ORR, most probably via the formation of a $Fe-N_x$ type of site. Generally $Fe-N_x$ sites showed higher ORR activity compared to the metal-free sites formed in Co-based catalysts [86,95,121]. According to ex situ EXAFS studies, the chemical environment of Fe and Co in Fe and Co based PANI-derived catalysts is quite different (Figure 2.11) [86]. While $Fe-(O/N)_x$ coordination structures were dominant in Fe-based catalysts which suggests that $Fe-N_x$ structures analogous to traditional macrocyclic ORR catalysts could exist in these catalysts only small fractions of $Co-(O/N)_x$ were present in Co based catalysts [86].

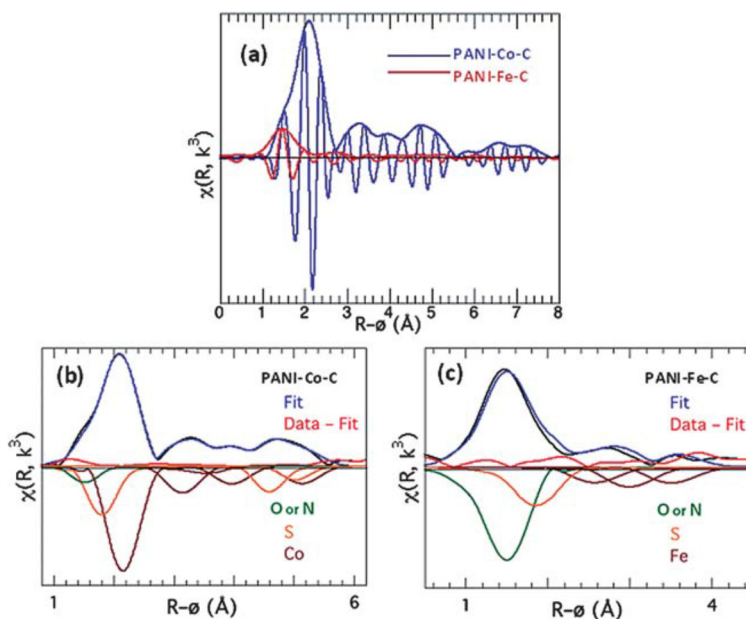


Figure 2.11 The radial distribution functions (RDFs) of (a) PANI-Fe-C and PANI-Co-C, (b) PANI-Co-C and (c) PANI-Fe-C catalysts [86].

No matter which category of nitrogen precursor has been used during preparation of non-macrocyclic catalysts, nitrogen doping into the (partially) graphitized carbon structure would occur during pyrolysis in the presence of the metal source. X-Ray photoelectron spectroscopy (XPS) studies demonstrated the existence of four different types of nitrogen species on the surface of these electrocatalysts: i) quaternary (graphitic)-nitrogen (~ 401 eV) which is integrated into the graphene layer and substitutes carbon atom within the graphene layer, ii) pyridinic-nitrogen (~ 398 eV) that refers to N atom bonded to two carbon atoms on the edge of a graphene layer contributing one p electron to the aromatic π system, iii) pyrrolic-nitrogen (~ 400 eV) which is incorporated into five-membered hetero-cyclic rings and contribute two p electrons to the π bonding and iv) pyridinic-nitrogen-oxide (~ 402 - 403 eV) that is bonded to two carbon atoms and one oxygen atom [88,92,98]. Representation of the various nitrogen functionalities is shown in Figure 2.12. Regardless of the applied nitrogen precursor, Fe-based catalysts displayed higher amounts of quaternary nitrogen compared to Co-based catalysts, indicating that Fe facilitates the nitrogen atoms doping at the interior rather than at the edges of the graphene layers [86]. The differences in the chemical and physical state of the active ORR sites are likely responsible for the lower ORR activity of the Co-based catalysts than Fe-based catalysts in acidic media. Currently, there is no clear correlation between the absolute content of quaternary or pyridinic nitrogen and the associated active-site density [86]. While some researchers believe that a higher content of pyridinic nitrogen leads to more active electrocatalysts [98,122,123], others attributed the electrocatalytic activity to the quaternary-N [93,124,125].

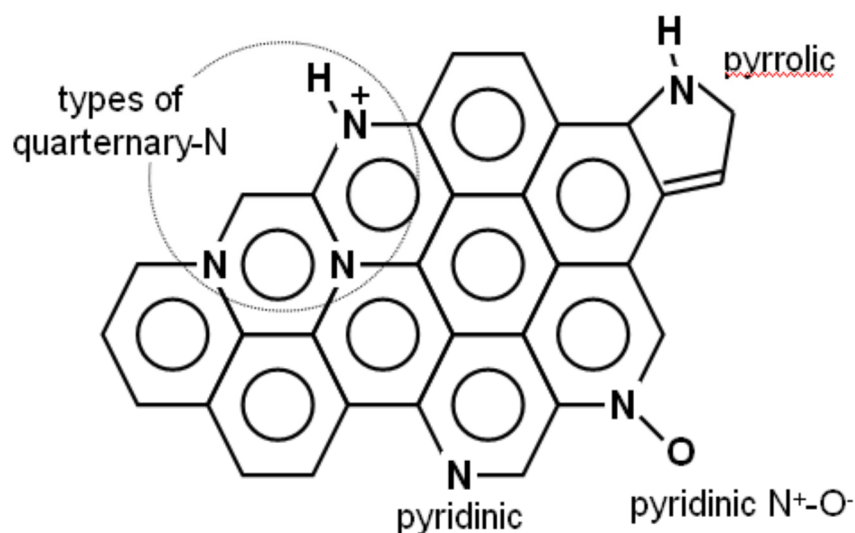


Figure 2.12 Depiction of the types of nitrogen species commonly present in pyrolyzed nitrogen-containing carbon.

Similar to what has been found with preparing non-PGM electrocatalysts employing M-N₄ macrocycles, in the case of non-macrocyclic electrocatalysts, the nature and surface properties of the carbon support present a significant impact on the ORR activity and stability of the catalysts. Jaouen et al [126] used 19 different carbon black supports to determine the effect of various carbon black characteristics on the activity of a Fe-based electrocatalyst. The nitrogen content was determined to be the most important factor of activity. With respect to this, several other studies have demonstrated that higher surface concentration of nitrogen can lead to an increase in the ORR activity [89,127,128]. Various carbon support materials including carbon black materials [97,113], oxidized [101] or activated carbons, [92] as well as carbon nanostructures like mesoporous carbon, carbon nanotubes (CNTs), carbon nanofibers (CNF) and graphene have been investigated in order to improve activity and durability of these types of electrocatalysts and they will be discussed in more details in Section 2.3 of this chapter.

Much debate has occurred in the literature on the nature of the active site and lots of studies tried to understand the active site nature for the ORR. Similar to heat treated macrocycles, controversy exist over the exact nature of the active sites and the role of Fe or Co metals in these M/N/C type of catalysts. During the last decade, the most significant support of the M (Fe)-centered active site has been provided by the Dodelet's research group. They proposed

the presence of two different catalytic sites with different catalytic behavior [122,129]. This was supported by Time-of-Flight Secondary Ion Mass Spectrometry (ToF-SIMS) measurements which confirmed the existence of two ion families. One ion family FeN_2C_y^+ , mainly FeN_2C_4^+ , comprised of two pyridinic nitrogen atoms (Figure 2.13a) and was considered as part of the catalytic site in these catalysts [122]. Other family consists of ions of the type FeN_xC_y^+ , containing one or three or four nitrogen atoms, with the most representative ion being FeN_4C_8^+ (Figure 2.13b). The later catalytic site was found to provide less catalytic activity compared to that of the former one. The full coordination of the former catalytic site unknown at that time was later [95,113] described as the combination of two FeN_2 active sites in near proximity to each other in carbon micropores to form a pseudo- FeN_4 site (labelled as FeN_{2+2} site), as illustrated in Figure 2.8.

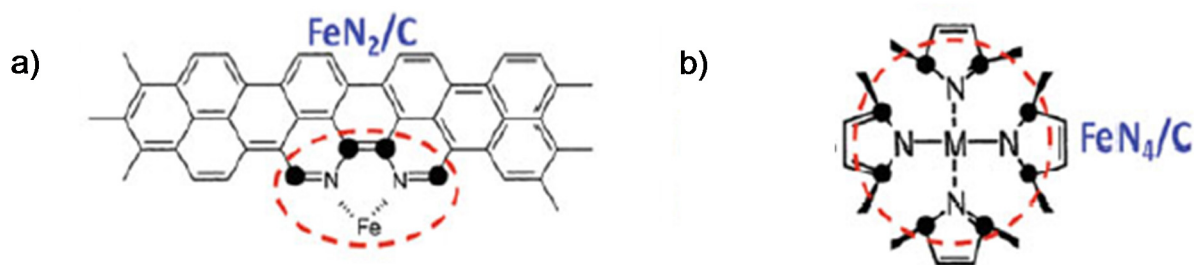


Figure 2.13 Initially proposed catalytically active FeN_2/C and FeN_4/C structures, a and b, respectively [113]

The same group used Mössbauer spectroscopy to obtain more information about all Fe-species present in their catalysts which were generally prepared via impregnating a non microporous carbon support with iron acetate and pyrolyzing this material under NH_3 at high temperature [130]. Four different Fe-species were detected at all iron concentrations (Figure 2.14): three broad doublets attributed to molecular FeN_4 -like sites with their ferrous ions in a low (D1), intermediate (D2) or high (D3) spin state and two narrow doublets assigned to a single Fe-species (D4 and D5) consisting of surface oxidized nitride nanoparticles (Fe_xN , with $x \leq 2.1$), as observed in high-resolution TEM images. A fifth Fe-species characterized by a broad singlet that appears in the spectrum only under conditions where Fe content reaches the values ≥ 0.27 wt%. This singlet was correlated to incomplete FeN_4 -like sites that irreversibly dissolve in contact with an acidic solution of H_2SO_4 at pH 1.

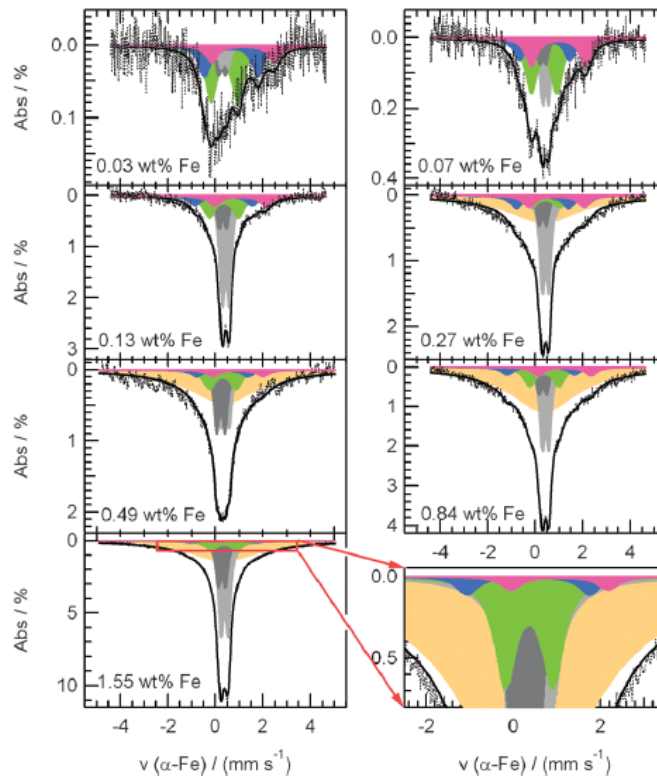


Figure 2.14 Deconvoluted Mössbauer spectra of the Fe/N/C-catalysts. The iron content of the original catalyst is given as an inset in each spectrum [130].

The possible structures of D1, D2 and D3 are demonstrated in Figure 2.15. These FeN₄-like moieties may settle either at the surface of the carbon to end up as the low turn-over frequency FeN₄/C sites (Figure 2.15a) assigned to Mössbauer doublet D1, or in micropores to end up as FeN₂₊₂/C or N-FeN₂₊₂/C sites (Figure 2.15b and c) assigned to Mössbauer doublets D2 and D3, respectively. Among all these Fe-species, only D1 and D3 exhibited ORR catalytic activity in the acid medium. This was related to 3d^{z²} orbital vacancy of Fe II ion in these two species (D1 with no electron and D3 with only one electron in 3d^{z²} orbital) which may interact with O₂ and hence provide ORR activity. Furthermore, the same group reported the presence of basic (pyridinic) nitrogen functionalities in the vicinity of N-FeN₂₊₂ active sites (with D3 featuring) which are protonable and thus can serve as an intermediate for fast transfer of proton to the Fe ion of the active site during ORR [114]. These composite sites (N-FeN₂₊₂...N_{prot}/C) demonstrated the highest ORR activity reported by far throughout the literature, with an estimated turn over frequency of 11.4 e⁻ per site per s at 0.8 V vs. RHE [130]. These highly active species were found to lose significantly their ORR activity upon

anion (SO_3^-) neutralization of the protonated NH^+ either in H_2SO_4 solution or a fuel cell which subsequently led to instability of these catalysts under operating conditions of a PEM fuel cell.

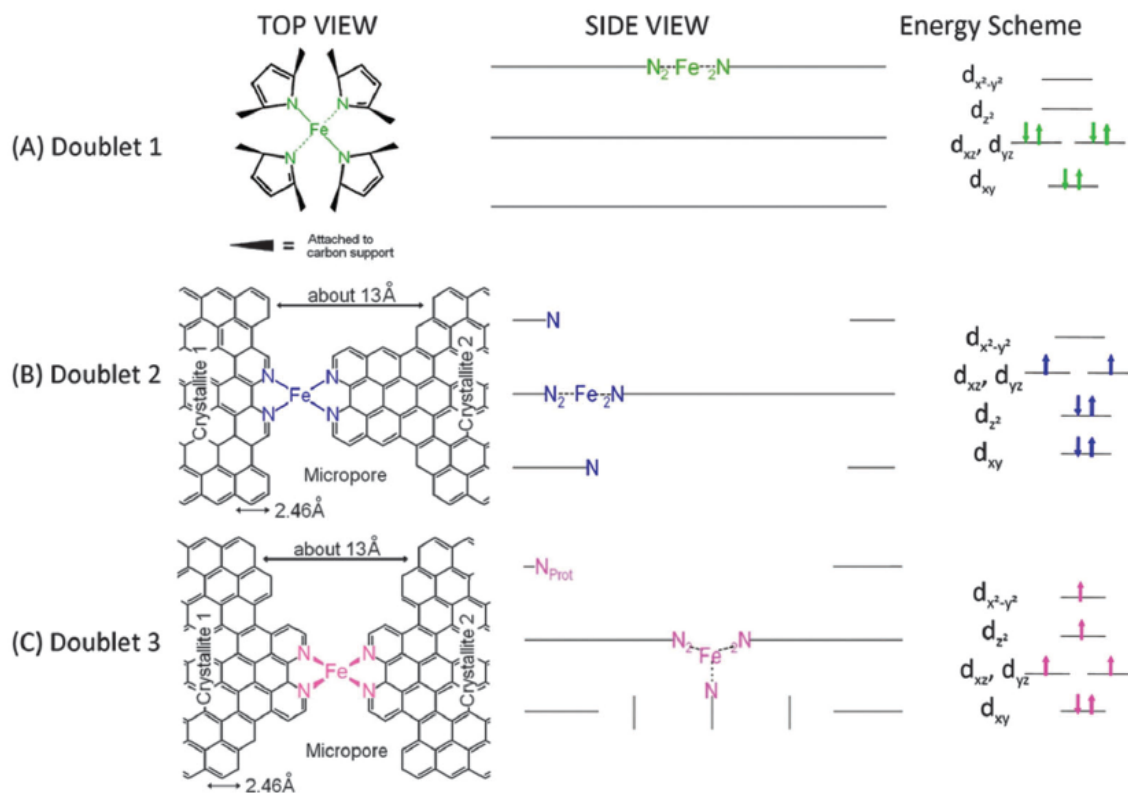


Figure 2.15 Side and top views of the proposed structures of: (A) the FeN_4/C catalytic site in heat-treated, macrocycle-based catalysts assigned to Mössbauer doublet D1, (B) the FeN_{2+2} -like micropore-hosted site found in the catalyst prepared with iron acetate and heat-treated in NH_3 assigned to doublet D2, and (C) the N-FeN_{2+2} -like composite site, where N-FeN_{2+2} is assigned to doublet D3. In all side views, graphene planes are drawn as lines. In (B), the distance between the two nitrogen atoms belonging to the graphene planes above and below the FeN_{2+2} -plane is similar to that in crystalline iron phthalocyanine, thus similarly influencing the lattice contribution to the quadrupole splitting. In (C), the iron (II) ion in N-FeN_{2+2} is coordinated by five pyridinic nitrogen atoms, one of them belonging to a plane located at the vertical below the N_4 -plane. This axial nitrogen coordination moves the iron (II) ion out of the N_4 -plane towards the fifth coordinating nitrogen atom. Doublet 3 may exist as $\text{N-FeN}_{2+2}/\text{C}$ or as a composite site $\text{N-FeN}_{2+2}\dots\text{N}_{\text{prot}}/\text{C}$, where N_{prot} is a protonable pyridinic nitrogen atom appearing at the edge of the upper plane in the side view of D3 [114]. N_{prot} is too far from N-FeN_{2+2} to have an influence on the Mössbauer spectrum of D3, but it is close enough to drastically improve the turn-over frequency of the composite site proposed in (C) [130].

Other researchers have a differing point of view regarding the active site nature and the possible role of the transition metals. Instead of being a part of the active site, they believe metal-ion center only serves as a catalyst to form N/C type of active sites during pyrolysis. Ozkan et al. [131,132] prepared N/C type of catalyst by pyrolyzing acetonitrile over a pure

alumina support (made with less than 1 ppm transition metals contamination), and supports containing 2 wt% Fe or Ni on alumina. These catalysts demonstrated significant ORR activity, after alumina support removal through HF leaching. While Fe-containing alumina provided catalysts with higher activity compared to transition metal-free alumina support, pyrolysis over Ni-containing alumina support led to less active ORR catalyst [131,132]. The most active sample prepared with Fe exhibited only 100 mV, greater overpotential than the commercial 20 wt% Pt/Vulcan Carbon catalyst. The same group also investigated other catalyst supports such as Vulcan carbon [98], silica and magnesia [133,134]. The ORR activity of all these catalysts was attributed to the pyridinic nitrogen functional groups located on the edge of graphitic edge planes. They postulated that a lone pair of electrons on the pyridinic nitrogen species can enhance the electron-donating characteristics of the neighboring carbon atoms which are the real ORR active sites. Therefore, the transition metal used during the preparation of these catalysts, plays only the role of catalyst to facilitate the formation of the active sites consisting of graphitic edge planes with pyridinic nitrogen groups [131-137]. They believed that transition metals do not participate in ORR, as significant ORR activity was observed with those catalysts developed on pure alumina support without employing transition metal precursor during catalyst preparation [131]. According to their explanation upon catalyst preparation, transition metal is either encased in the carbon structures or, if exposed, is leached away together with the oxide support during acid leaching step. Later, they suggested that Fe/N/C and N/C catalysts are indeed two different types of ORR catalysts, with probably different mechanisms for catalyzing the reaction [138]. This was based on several differences observed in activity and stability of Fe/N/C and N/C catalysts toward ORR. Although the former demonstrated higher initial activity, it was also found to degrade faster in both half-cell and fuel cell environments. On the other hand, the latter retained much of its initial activity. In addition, they studied the effect of acid washing on the ORR activity of these catalysts. While N/C type of catalysts gained remarkable activity enhancement upon acid-washing, the reverse was observed in the case of Fe/N/C catalysts. Moreover, X-ray absorption near-edge spectroscopy (XANES) and EXAFS results revealed significant differences in the effect of acid-washing on these two different types of catalysts. In the case of N/C, the oxidized Fe species exposed to air upon pyrolysis were leached out during the acid washing step which led to the presence of only

carbide-like or metallic Fe in the final electrocatalysts in which these species were encased within carbon. For Fe/N/C catalysts, although the acid-washing leached out some of the Fe from the catalyst structure, the remaining Fe in the catalyst demonstrated the same coordination environment, before and after acid washing. They applied H₂S as a probe molecule to examine the differences in the active sites of these materials [139,140]. In case of N/C catalysts the sulfur treatment was performed on the as-prepared catalysts in a variety of atmospheres (H₂S/N₂ or H₂/N₂) [139]. According to their results not only the ORR activity of these catalysts did not decrease upon sulfur treatment but instead they observed enhancement of the onset potential, 0.72 V vs. RHE after H₂S treatment compared to 0.64 V vs. RHE before the treatment [139]. Fe K-edge XANES analysis of these catalysts showed no change in the iron phase of the catalysts which were primarily composed of nanometer-sized metallic particles. For Fe/N/C type of catalyst not only they studied the effect of H₂S treatment on the as-prepared electrocatalysts (after Ar and NH₃ treatment) but also they ran in-situ poisoning experiments during RDE measurements [140]. In addition, they investigated the effect of poisoning on these catalysts before pyrolysis under Ar and NH₃ flow [140]. No matter at which step poisoning took place, they always observed negative effects on ORR activity. In the case of H₂S treatment before Ar and NH₃ treatment deactivation of the catalysts was attributed to a direct bonding of S to Fe along with loss of some of the nitrogen species. This was verified by different characterization techniques such as EXAFS and XPS. When H₂S treatment occurred before any pyrolysis step, sulfur found to interfere with the formation of catalytically active sites that finally led to less active catalysts. In this case, nitrogen could not be incorporated to the catalyst structure even after subsequent NH₃ heat treatment. The in situ H₂S poisoning during RDE measurements revealed a significant decrease in onset potential and the limiting current of these catalysts, which again confirmed the adverse effects of poisoning on electrocatalyst properties due to adsorption of the S on the Fe containing active sites.

Another most significant contribution in debate for ORR active site structure that also supports metal free active centers is provided by Popov and his colleagues. They [141] prepared metal free electrocatalysts by pyrolyzing the pre-treated (acid washed and oxidized) carbon support covered by different resins obtained through polymerization of formaldehyde with i) melamine, ii) urea, iii) thiourea or iv) selenourea. The ORR activity of these catalysts

in acidic media was correlated to the existence of pyridinic and quaternary nitrogen atoms in their structure. Later, they incorporated metal in their electrocatalyst by applying another method of preparation [142]. Silica and acrylonitrile were used as template and carbon source, respectively to produce porous carbon support that subsequently was impregnated with iron acetate solution and pyrolyzed under inert gas. The pyrolyzed sample was then acid leached to remove the metal species generated during pyrolysis. Finally, the catalysts were reactivated by performing another heat treatment step. Their best electrocatalyst contained considerable amount of transition metal (1.2 wt% Fe) and not the highest content of pyridinic and quaternary nitrogen, however, similar to their previous study [141], they considered pyridinic and quaternary nitrogen species responsible for ORR activity. According to their arguments Fe species embedded in carbon support could not take part in ORR but only could modify the electronic properties of the nitrogen-modified active sites and hence facilitate the ORR. They also provided a mechanism for ORR activity losses of their catalysts which was believed to take place via protonation of the pyridinic sites upon exposure to acid media to form catalytically inactive pyridinic-H⁺ sites [143,144].

In addition to these experimental studies, there have been some studies exploring the ORR active site of M/N/C catalysts using computational techniques. According to DFT calculations, while the formation of various nitrogen species alone in perfect carbon nanostructures such as graphene [145] and CNTs [146] is energetically unfavourable, the formation of M-N_x clusters (M = Fe and Co) embedded in graphene is still energetically more favourable [145]. This is why many researchers considered the embedded M-N_x clusters responsible for the ORR activity of M/N/C electrocatalysts [147-149]. Therefore, they investigated the progression of ORR on M-N_x clusters in perfect graphene using the first-principles DFT computational method [148,149]. For M = Ni, although the formation of graphitic Ni-N_x (x = 2, 4) and Ni-N₂ edge defect was energetically found favourable, interaction of the former species with O₂ and H₂O revealed to be very weak [148]. Hence, Ni-N₂ edge defects were considered as ORR active sites facilitating the O₂ and OOH⁻ chemisorptions and the decomposition of H₂O₂ via a 2 × 2 e⁻ single site mechanism in alkaline as well as in acidic medium. In the case of M = Co, the formation of graphitic Co-N₄ defect was energetically found more favourable than the formation of graphitic Co-N₂ defect [149]. In addition, graphitic Co-N₄ defects were found to be stable at all potentials (V

= 0–1.23 V) while, Co-N₂ defects revealed to lose their stability at high potentials. Although, O₂ was found capable of chemisorbing to both Co-N₄ and Co-N₂ defects the weak interaction between peroxide and Co-N₄ defect necessitated the presence of a second site for the reduction of peroxide to complete ORR no matter which pH the electrolyte possessed. In contrast, the much stronger interaction between peroxide and graphitic Co-N₂ defects supports a 2 × 2 e⁻ single site ORR pathway in both alkaline and acidic media. Later investigation of the same group, demonstrated that the formation of M-N₄ moieties near the graphitic pores is energetically favourable [150]. In the case of M = Fe or Co these M-N₄ moieties were found capable of chemisorbing O₂ to take part in ORR. Fe-N₄ and Co-N₄ moieties were found to promote the 4e⁻ ORR with a single active site configuration consisting of a central transition metal atom and four surrounding N atoms. Furthermore, they demonstrated that d-electron orbitals of the transition metal atom could act as an electronic descriptor to gauge the ORR activity of the M-N₄ structures. Another DFT calculation based study over the nature of the Fe/N/C type of catalysts was reported by Szakacs et al. [151]. Using DFT calculations they tried to verify the proposed FeN₂₊₂/C and N-FeN₂₊₂/C active site structures (Figure 2.16a and b) and correlate them to Mössbauer spectroscopy results reported by the same group [130]. The former structure consists of a Fe ion coordinated to four pyridinic nitrogen on the edges of opposed graphene planes located in a micropore of the carbon structure (Figure 2.16a, left), while the later structure contains a Fe ion coordinated to five pyridinic-type nitrogen atoms in which one of the pyridinic N is oriented along the normal to the graphitic plane (Figure 2.16a, right). FeN₄^{pyri}/C and N-FeN₄^{pyri}/C structures in which the Fe ion is embedded in an extended graphene sheet (Figure 2.16c) were also considered for the sake of comparison. In the case of FeN₂₊₂/C structure, two models were considered: i) the planar structure of FeN₂₊₂/C(A) (Figure 2.16a, left) and ii) the structure in which Fe is moved out of the plane as a *hill* (FeN₂₊₂/C(B)) and *valley* (FeN₂₊₂/C(B)[#]) sites (Figure 2.16b, left). These latter sites were found upon optimization of FeN₂₊₂/C structure. For N-FeN₂₊₂/C structure, the *valley* site (N-FeN₂₊₂/C(B)) related to the condition where pyridinic N was attached from the *valley* site and the adsorbates could be accommodated only on the *hill* site (Figure 2.16b, right). The *hill* sites (N-FeN₂₊₂/C(B)[#]) were attributed to the sites where the adsorbed species could attack only from the valley site. (Figure 2.16b, right). All the proposed structure were found to possess ORR catalytic activity

except for $\text{FeN}_{2+2}/\text{C}(\text{B})^\#$ and $\text{N-FeN}_{2+2}/\text{C}(\text{B})^\#$ on which the adsorbates attack from the valley site. They concluded that $\text{FeN}_{2+2}/\text{C}(\text{A})$ and/or $\text{N-FeN}_{2+2}/\text{C}(\text{A})$ structures could be associated with the doublets D2 ($S = 1$) and D3 ($S = 2$) earlier identified in their Mössbauer experiments [130]. In addition, these two structures were found to possess the lowest formation energy of all the considered structures.

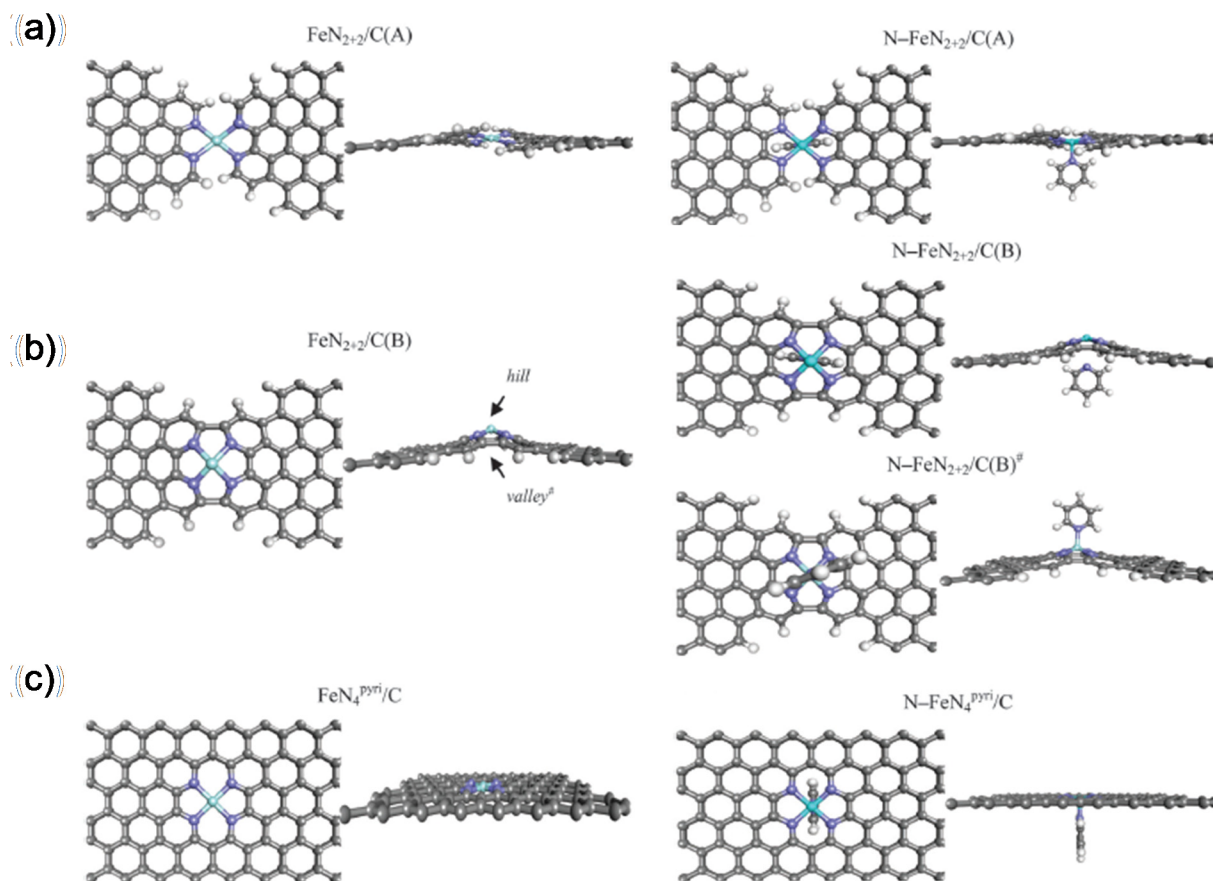


Figure 2.16 Optimized structures (top and side views) of (a and b) two $\text{FeN}_{2+2}/\text{C}$ -type structures without (left) and with axial pyridine group (right), and (c) a structure resulting from the FeN_4 moiety embedded in an extended graphene sheet without (left) and with axial pyridine group (right) [151].

At this point, the real nature of the active site in non-PGM electrocatalysts is still under question and this complicates the research for an active electrocatalyst. Today the structural model for the most active catalytic site is considered as what represented in Figure 2.15c with TOF value of 11.4 e^- per site per second at 0.8 V vs. RHE. This is nearly 50 % of what is reached with commercial Pt/C (based on RDE experiments at room temperature; under FC conditions, this value might even be larger) [152]. The main problem with this active site is its low stability due to neutralization of the protonated pyridinic nitrogen by sulfonate group

(SO₃⁻) of the proton conducting ionomer in the PEM fuel cell condition [130]. So, future works should focus on developing a stabilization mechanism for the N-FeN₂₊₂/C...NH⁺ type of active sites or looking for new electrocatalysts with higher density of and more stable active sites.

2.3 Support enhancement

The support of electrocatalyst plays significant roles in PEM fuel cell performance. As previously mentioned, today the commonly used electrocatalyst for PEMFCs is Pt supported on carbon black (Vulcan XC-72). Carbon support mainly provides the possibility to reduce the electrocatalyst loading by dispersing the Pt particles via reducing interparticle interactions and mitigating ripening effect. High surface area support materials can provide higher dispersion of the nanocatalyst particles and hence improve the catalyst utilization. The support material may also interact with Pt particles, which can affect the catalyst activity and enhance the fuel cell performance. In addition, carbon support can efficiently transfer electrons through the support toward the catalytic active sites, throughout the electrode, with minimal ohmic resistance. Besides, the corrosion resistance of the support material is important since it can determine the catalyst durability. There are some issues regarding the employment of carbon black as the electrocatalyst support: (i) numerous micropores in the carbon blacks structure can trap Pt nanoparticles. As a result, such electrocatalyst nanoparticles could neither establish an effective interaction with dissolved reactant gases nor the electrolyte solution. This will cause a reduction of Pt utilization since that fraction of Pt nanoparticles is not being utilized during the electrochemical reactions [153]; (ii) electrochemical surface oxidation of carbon black under PEM fuel cell operating conditions leads to decrease in hydrophobicity of the carbon support and hence affect the water transport in PEM fuel cells. Consequently this can cause instability and variability of PEM fuel cell performance [154]. As carbon black corrodes, Pt metal nanoparticles on carbon black will detach from the electrode and possibly aggregate to larger particles, resulting in Pt surface area loss, which subsequently lowers the performance of PEM fuel cells [155-157]. Therefore, many efforts have been made to search for new catalyst supports. Carbon based nanomaterials such as carbon nanotubes, carbon nanofibers, ordered mesoporous carbons, graphene as well as many other nanostructured materials show great potential for use as an

electrocatalyst support. The goal of using these supports is to enhance the durability and activity of the catalyst.

2.3.1 Carbon nanotubes

Carbon nanotubes (CNTs), first discovered by Iijima [158] in 1991, are one-dimensional, nanoscale materials with extraordinary mechanical, electronic and thermal properties that make this support materials suitable for use in many different applications. There are two types of CNTs: single-walled (SWNT) and multi-walled (MWNT). While SWNTs consist of perfect graphene sheets rolled into a seamless cylindrical tube, MWNTs can be considered as either concentric tubes or a single graphene sheet wrapped spirally around itself (Figure 2.17). MWNTs and SWNTs have similar properties, but the former show higher electrical conductivity whereas the latter provide larger surface areas. Both types of CNTs were extensively investigated as electrocatalyst support in PEMFCs.

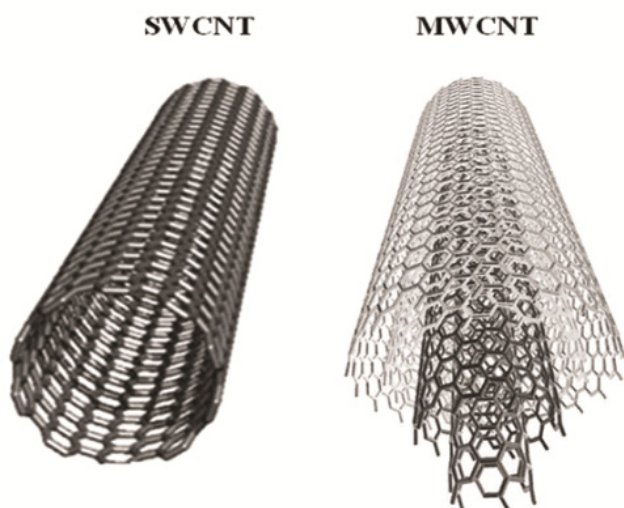


Figure 2.17 Structure of a single wall carbon nanotube (SWNT) and multi wall carbon nanotube (MWNT)

2.3.1.1 Carbon nanotubes as support for Pt-based catalysts

Several research papers reported that CNTs as support for Pt or Pt alloys catalysts provide higher ORR catalytic activities compared to commonly used Vulcan XC-72 carbon black support [159-163]. This was attributed to their distinctive structure and properties such as high surface area, good electronic conductivity and chemical stability [164,165]. Moreover, under operating conditions in a PEM fuel, CNT based catalysts demonstrated better durability

that could outlast the lifetime of conventional Vulcan XC-72 [166-170]. In spite of their great potential as a promising alternative catalyst support, producing well-dispersed Pt particles on CNT surfaces and further improving their activity and electrochemical stability remains an important challenge. This is mainly due to the inherent hydrophobic and inert nature of the surface of CNTs that hinder favorable interaction and dispersion of Pt particles [171,172]. Therefore, implanting surface functional groups on CNTs is compulsory toward effective Pt deposition. The most implemented method toward CNTs functionalization is covalent functionalization through acid oxidation process, where CNTs are treated with highly concentrated H₂SO₄, HNO₃ solution or a mixture of both under reflux at the temperature range of 90-140 °C [173-178]. This process introduces different surface-bound functional groups such as carboxyl (-COOH), hydroxyl (-OH) and carbonyl (>C=O) that are suitable for anchoring Pt metal ion for further nuclei formation and electrocatalyst deposition [175,179]. Furthermore, surface functional groups increase the hydrophilicity of the electrocatalysts and hence improve the diffusion of the reactants toward the active sites [180]. The harsh chemical condition during acid oxidation treatment has led to the formation of a large number of defects on CNTs surface that consequently diminishes their electrical conductivity and corrosion resistance [181]. Therefore, surface modification of CNTs under milder condition via electrochemical modification was attempted [182,183]. Wang et al. [183], demonstrated that using electrochemical modification technique much higher density and homogeneity of surface functional groups were introduced to CNTs compared to those prepared by conventional acid oxidation process without causing severe damage to the CNTs. Deposition of Pt particles onto the functionalized CNTs is another critical step toward preparation of optimal Pt/CNT catalyst, for which a wide variety of methods such as impregnation, colloidal deposition, ion-exchange, electrochemical and microwave heated polyol method have been reported. Both the functionalization process and Pt deposition methods could affect the Pt catalyst dispersion and hence the catalytic activity for fuel cell reactions [184].

Briefly, the impregnation method consists of homogeneous mixing of CNTs with the solution of the metal precursor through which metal ions adsorb to the surface of functionalized CNTs. Then metal ions pass a reduction step to produce metal nanoparticles. The reduction can be carried out using a liquid phase such as borohydride, formic acid or hydrazine as a

reductive agent, or by employing a reductive gas flow (i.e. hydrogen gas) under elevated temperature. Since the reduction step takes place after the impregnation stage, the size and distribution of Pt nanoparticles prepared by this method are mainly controlled by the structure of the CNTs. As one example, Matsumoto and co-workers [185] synthesized Pt nanoparticles supported on CNTs using the impregnation technique. Oxidized CNTs with surface defects were prepared by stirring CNTs in a mixture of HNO₃ (14 M, 50 ml) and H₂SO₄ (98%, 50 ml) for 12 h, followed by sonication in HNO₃ solution (14 M, 50 ml), and dissolution in 400 ml distilled water and filtration. To deposit Pt nanoparticles on the oxidized CNTs, they were stirred in distilled water followed by addition of 30 wt% K₂PtCl₄ solution in ethanol and refluxed at 373 K for 2 h. The Pt/CNT catalyst was found to contain ~12 wt% of Pt (based on elemental analysis). A commercial 29 wt% Pt-deposited on carbon black (Tanaka Kikinzoku Kogyo) was used as a control to compare the electrode's performance. They found that Pt/CNT electrode with Pt loading of 0.2 mg cm² provides 2-3 times higher voltages than Pt/CB (Pt loading ~ 0.5 mg cm²) per Pt atom below 600 mA cm² and reduces Pt utilization by 60% in PEMFCs. While this method provides simplicity in the execution, the catalysts prepared by this method present a broad size distribution for the Pt particle size with a large average particle size that leads to lower electrocatalytic activity [186].

To prepare Pt/CNTs catalyst using the colloidal method, the Pt metal colloid is prepared and subsequently adsorbed on the CNTs surface, or a Pt metal oxide colloid is formed and then, simultaneously reduced and adsorbed on the CNTs. Alternatively, it can be first adsorbed on the CNTs surface and afterward chemically reduced. Employing this colloidal method, protecting agents, such as ligands, surfactants or polymers were widely exploited to control the size of Pt nanoparticles [187]. For instance, using 3-(N,N-dimethyldodecylammonio) propanesulfonate (SB12) surfactant as a stabilizer, Li et al. [188,189] prepared Pt nanoparticles supported on functionalized CNTs by methanol reduction of H₂PtCl₆. Oxidative treatment of the CNTs was performed in a mixture of H₂SO₄ and HNO₃ solution to introduce the carboxyl groups on the surface of the CNTs. The oxygen-containing surface functionalities on the CNTs were found to provide a significant impact on the Pt dispersion via manipulating the anchoring and/or nucleating sites. Pt nanoparticles with an average size of 2.2 nm were well-dispersed on the external walls of the CNTs as shown in Figure 2.18 [188]. Although the colloidal method can lead to formation of Pt nanoparticles with narrow

size distribution, to ensure the accessibility of the catalyst sites along with effective electronic contact between the support and catalyst particle, the protecting agent needs to be removed prior to application in the PEM fuel cells. This causes further complication to this process as successive washing in an appropriate solvent or heat-treatment at elevated temperatures may need to be applied in order to get rid of these species. In addition, such post-treatment processes mainly diminish the catalytic performance due to the sintering effect that affects the distribution of Pt particles and leads to phase separation [190]. Therefore, the polyol process [191] is mainly employed as the preparation technique for Pt deposition on CNTs. In this process, ethylene glycol is employed as both reducing agent and solvent for the Pt precursor. During the reduction step the solution of ethylene glycol and Pt precursor is heated to 120–170 °C. This causes the decomposition of ethylene glycol which subsequently leads to formation of the reducing species (CH₃CHO). This species reduces the Pt ions to metallic Pt particles. More preferably, the microwave heating polyol method is applied to prepare Pt/CNT catalysts [192,193]. Fast heating by microwaves can increase the reduction rate of the Pt ions and hence accelerate the nucleation of Pt nanoparticles. Unlike the conventional conductive heating strategy, with heterogeneous temperature distribution, the homogeneous microwave heating reduces the temperature and concentration gradients in the reacting sample solution and thus provides a more uniform environment for nucleation and growth of Pt nanoparticles [192,193]. Zhang et al. [194], reported the preparation of Pt nanoparticles supported on H₂SO₄/HNO₃-treated CNTs by the microwave-assisted polyol process. Pt nanoparticles of 2.5-4 nm supported on such functionalized SWCNTs exhibited an enhanced electrochemically active catalytic surface area (ECSA) and PEM fuel cell performance compared to Pt nanoparticles supported on unfunctionalized CNTs or carbon black. The enhancement in catalytic performance was attributed to the better accessibility and dispersion of the Pt nanoparticles.

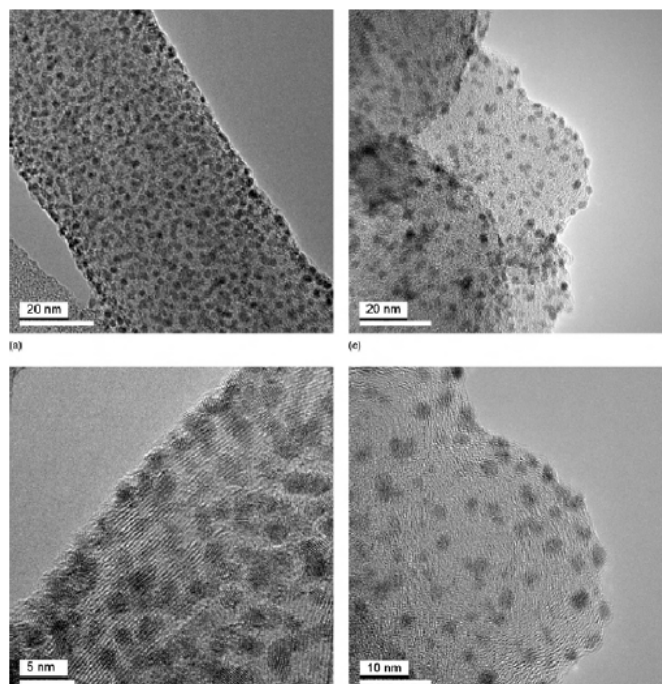


Figure 2.18 High-resolution TEM bright-field images of supported Pt catalysts prepared by SB12-stabilized method: (a) Pt/MWNTs-m, (b) Pt/MWNTs-m, (c) Pt/C, and (d) Pt/C [188].

The ion-exchange method is another efficient technique for deposition of highly dispersed Pt nanoparticles on CNT support without exploiting stabilizing or reducing agents [195]. The ion-exchange method is based on using a Pt cation complex which interacts with hydrogen ions of the acid functional groups on the surface of the CNTs and subsequently reduces to Pt nanoparticles under H_2 atmosphere. The dispersion and size of Pt particles is determined by this interaction [195]. Shao et al. [196] used this technique to prepare Pt/CNT catalyst by first introducing some carboxyl groups on their surface via electrochemical functionalization with H_2SO_4 in a three-electrode cell setup. Then the functionalized MWNT was immersed in the Pt precursor solution for 48 h so that the H^+ ions of the functional group on the CNT surface undergo an ion-exchange process with the Pt cation complex. The non-ion-exchanged Pt precursor solution was removed by dipping in ultrapure water. Finally, a heat-treatment under reductive H_2 gas was performed to convert the ion-exchanged Pt ions to Pt nanoparticles. The resulting Pt/CNT catalyst demonstrated higher ECSA, ORR activity and Pt utilization compared to the conventional electrode in a three-electrode cell. The enhanced Pt utilization and higher electrocatalytic activity were attributed to the specific structure of the ion-

exchanged electrode composed of highly dispersed Pt nanoparticles deposited on the electrochemically active sites.

The electrochemical method for preparation of Pt/CNTs, is indeed very similar to the impregnation method, except for electrochemical reduction of the adsorbed Pt ions rather than their chemical reduction. Such a technique that can lead to deposition of Pt nanoparticles by direct nucleation on CNTs can provide relatively superior contact between the support and the Pt surface compared to the colloidal based deposition methods [197]. To prepare Pt/CNTs via electrochemical process, functionalized CNTs are first mixed with an aqueous solution of a Pt precursor to produce a homogeneous solution. The reduction of Pt ions is then carried out by applying a pulse current, direct current or cyclic voltammetry, to deposit Pt nanoparticles on the surface of CNTs. Zhao et al. [198], used a three-step electrochemical process to fabricate Pt nanoparticles on MWCNTs. In the first step, potential cycling at 50 mV s^{-1} from 1.8 to -0.4 V was performed in 0.5 M K_2SO_4 solution to produce various functional groups on the CNTs. In the second step, PtCl_4^{2-} was oxidized to form a Pt(IV) complex using cyclic voltammetry from 0.3 to 1.3 V at 100 mV s^{-1} for 10 cycles in a pH 4 solution containing 2 M K_2PtCl_4 and 0.1 M K_2SO_4 . Finally, the Pt (IV) complex was transformed to Pt nanoparticles on the CNT surface by cycling the potential at 100 mV s^{-1} between 0.9 and -0.35 V in a 0.1 M H_2SO_4 solution until a steady state was reached. Increasing the number of cycling steps for the PtCl_4^{2-} to Pt (IV) conversion led to higher dispersion of the Pt nanoparticles on the MWCNTs, with a particle size of 2 nm achieved after 190 cycles, as well as enhanced electrocatalytic activity. The high dispersion of the Pt nanoparticles was believed to be attained due to the functionalization of the MWCNTs.

As mentioned before, CNTs as support for Pt nanoparticles provide higher durability for PEMFCs due to their resistance toward oxidation. Wang et al. [166] reported higher durability of MWCNTs compared to conventional Vulcan XC-72 carbon black. They compared electrochemical surface oxidation of these two types of supports by running potentiostatic treatments up to 168 h in 0.5 M H_2SO_4 solution purged by N_2 at 60 °C at a constant potential of 0.9 V to simulate the cathode environment in PEMFCs. The subsequent electrochemical characterization at different treatment time intervals, demonstrated that MWNTs were electrochemically more stable than Vulcan XC-72 with less surface oxide formation and 30% lower corrosion current under the investigated conditions. Due to higher

corrosion resistance, MWNTs exhibited lower loss of Pt surface area and ORR activity when applied as fuel cell catalyst support. Other groups have also reported on higher durability of CNT support than conventional carbon black due to their superior resistance to electrochemical oxidation [156, 167,168]. As mentioned before, CNTs are generally considered as rolled graphene sheets with a coaxial and with less dangling bonds and defects compared to carbon black [156]. Therefore, oxidative atoms/groups could not easily attack the closed structure of CNTs and this renders CNTs highly stable even in extremely oxidizing conditions. In addition, the delocalized π bond of CNTs is found to present more strength than that in carbon black due to their higher degree of graphitization. Pt is supposed to bond with carbon support through the interaction with π electrons of the graphene sheets in carbon support. Hence, stronger π bond (sp^2 -hybridized carbon), provides stronger interaction between Pt and CNTs that can contribute to the high stability of Pt/CNTs catalysts [167]. Moreover, doping CNTs with nitrogen was found not only to facilitate the ORR [199] but also to improve electrochemical stability for Pt/CNT catalyst [200, 201]. Chen et al. [200] demonstrated that using nitrogen doped carbon nanotubes (N-CNTs) as Pt support leads to significant enhancement of the Pt catalyst stability compared to pristine CNTs. They used ECSA to characterize a PEMFC catalyst. After 4000 cycles, Pt/N-CNTs with 1.5, 5.4 and 8.4 at% N content retained respectively 20.2%, 26.6% and 42.5%, of their initial ECSA while for Pt/CNTs only 11.2% of the initial ECSA was remained. The lower degree of ECSA degradation for N-CNTs was attributed to the lower extent of dissolution and agglomeration of the Pt nanoparticles. According to TEM images Pt/N-CNTs exhibited smaller Pt particle sizes compared with Pt/CNTs. Additionally, better stability was found for Pt/N-CNTs catalysts with higher nitrogen content. Later, the same group studied the fuel cell performance of these two catalyst supports [202]. They synthesized CNTs and N-CNTs under similar conditions for a comparison purpose. Upon nitrogen doping, the structure of CNTs considerably changed according to XPS, carbon K-edge near-edge X-ray absorption fine structure (NEXAFS) and Raman characterizations. Employing the ethylene glycol reduction method to deposit Pt nanoparticles on both supports, Pt/N-CNTs exhibited more uniform dispersion of Pt particles with smaller particle size. Pt/N-CNTs also demonstrated higher ORR catalytic activity, as indicated by a larger kinetic current, higher half-wave potential,

and higher four-electron transfer efficiency to H₂O. In addition, in a single cell PEM fuel cell Pt/N-CNTs, as a cathode catalyst, exhibited higher performances.

2.3.1.2 Carbon nanotubes as support for non-precious catalysts

Reddy et al. [203] employed MWNT as a support for Co-polypyrrole (PPY) compound and studied the ORR performance of the resulting electrocatalyst in a PEM fuel cell. The electrocatalyst was prepared by chemical polymerization of pyrrole monomer on the surface of MWCNT, followed by chemical reduction of the Co precursor in solution on PPY-MWCNT composite. PPY and Co nanoparticles were found to be uniformly dispersed over MWCNT and PPY-MWCNT composites, respectively. Although the effect of employing MWCNT as a support for cathode catalyst was not compared to commercially available carbon supported electrocatalyst, the overall performance of a PEM fuel cell working with Co-PPY/MWCNT at the cathode and Pt or Pt alloys (Pt-Ru) supported on MWCNT at the anode, demonstrated enhancement compared to reported results in a PEM fuel cell using Pt or Pt-Ru alloys supported on commercially available carbon at the anode side. Furthermore, a high stability over 50 hours of operation in a PEM fuel cell setup was achieved for the PPY-Co/MWCNT catalyst.

Lim et al. [204] reported synthesis of bimetal (FeCo) non-precious catalyst supported on MWCNTs. Poly(vinylpyrrolidone) polymers was wrapped around the CNT support to introduce 2-pyridone functional group on the surface that was exploited to facilitate the complexation of metal ions (Fe³⁺, Co²⁺). After annealing in 10% ammonia at 900 °C for 1 h a FeCo/MWCNT catalyst was obtained. The FeCo/MWCNT catalysts showed slightly better ORR performance and significantly better long-term stability compared to the commercially available platinum catalysts (20 wt%) supported on Black Pearl 2000. The higher ORR activity of FeCo/MWCNT was attributed to the excellent electrical conductivity of CNTs compared to Black Pearl 2000 carbon. This study demonstrated the potential of CNT based supports to improve the durability of non-PGM electrocatalysts. Wu et al. [205], prepared polyaniline (PANI)-Fe catalyst supported on MWCNT and other types of carbon black supports such as Vulcan XC-72, KJ-300J and BP-2000. The fuel cell polarization plots revealed nearly identical performance for all PANI-Fe catalysts in the high voltage region (e.g. at 0.8 V), but in the low voltage region (< 0.3 V) MWNT supports provided a noticeable

performance advantage over other carbon black supports related to their more open structure which causes better mass transfer of the relevant species in the fuel cell. Furthermore, the MWNT-supported catalyst demonstrated no performance degradation for more than 500 h at a cell voltage of 0.4 V. As can be seen in Figure 2.19, MWNT-supported catalyst represents a significant stability enhancement over the carbon-black-supported catalysts, as they showed varying degrees of performance losses.

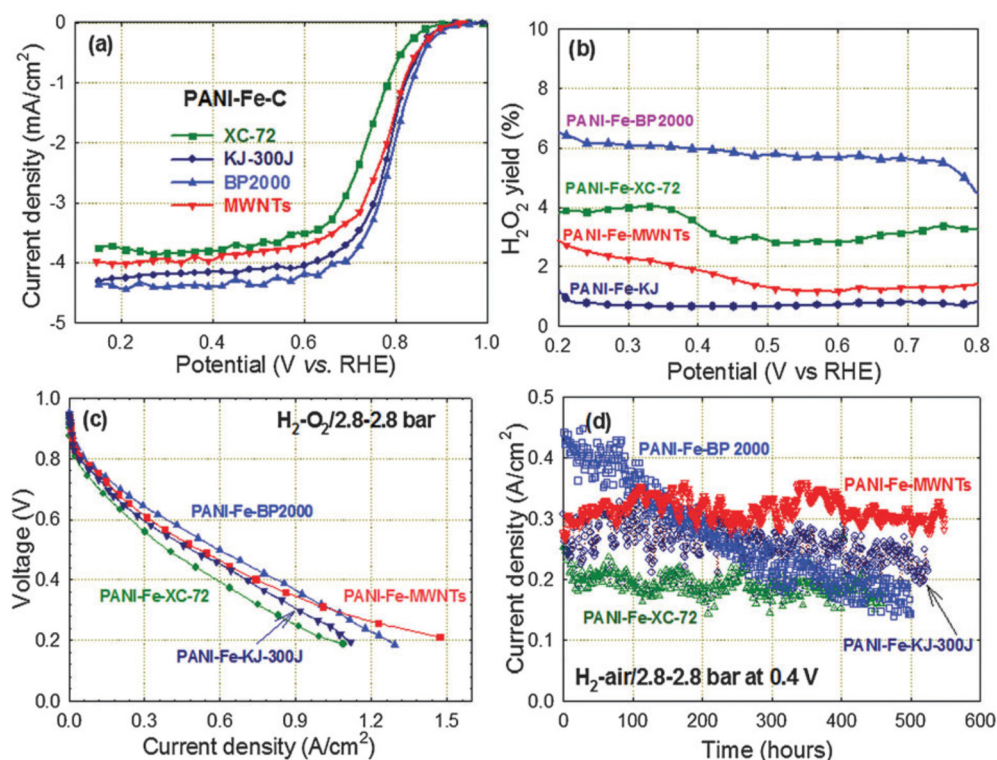


Figure 2.19 Catalytic performance of PANI–Fe catalysts supported on various carbon materials. (a) Steady-state RDE polarization plots, (b) hydrogen peroxide yield plots; (c) initial fuel cell polarization plots, and (d) fuel cell life test, cell temperature: 80 °C [205].

2.3.2 Ordered mesoporous carbon

Another type of catalyst support material with great potential for fuel cell application is mesoporous carbon as it can provide high surface area and high conductivity [206]. There are two types of mesoporous carbon materials according to their structures and morphologies: Ordered mesoporous carbon (OMC) and disordered mesoporous carbon (DOMC) [207]. The former is constructed of regular arrays of uniform three-dimensionally inter-connected mesopores while in the later case the mesopores are mainly isolated or irregularly interconnected. Therefore OMCs are mostly preferred over DOMCs as the electrocatalyst

support due to their higher specific surface area and electrical conductivity. OMC is synthesized by nanocasting ordered mesoporous silica (OMS) templates [208-211] or by directly templating triblock copolymer structure-directing species [212,213]. The mono-dispersed interconnected mesopores of OMCs can facilitate the diffusion of reactants and products during fuel cell operation and render these support materials the preferred properties in terms of mass transport [214,215].

2.3.2.1 OMC as support for Pt-based catalysts

OMC supported Pt and Pt alloy catalysts have been extensively investigated for PEM fuel cell application. Song et al. [208] reported synthesis of OMC (CMK-3), employing SBA-15 as a hard template. To investigate the effect of pore morphology on catalytic activity of Pt nanoparticles in PEM fuel cells, they also considered the disordered worm-like mesoporous carbon (WMC) prepared applying silica gel as the hard template. For both type of supports, the same amount of Pt (20 wt%) was loaded applying pulse-microwave assisted polyol process. Pt nanoparticles with similar size were uniformly dispersed on the pore surface of both supports. However, Pt/CMK-3 revealed superior ORR activity and higher ECSA which was attributed to the much easier mass transportation through such OMC support. The highly ordered structure of CMK-3 and very good 3D interconnection of the nanospacings of their hexagonally arrayed carbon nanorods led to a higher accessibility of Pt catalyst and hence higher Pt utilization.

Joo et al. [209] prepared two OMC samples employing phenanthrene and sucrose as carbon source. Although, the two OMC samples exhibited similar structures with large surface area and uniform mesopores, the OMC synthesized from phenanthrene showed higher electrical conductivity compared to the OMC derived from sucrose. The Pt nanoparticles were supported on both OMCs with very high dispersion as their particle size was found to be less than 3 nm despite relatively high metal loading of 60 wt%. Both OMC supported Pt catalysts exhibited much higher performance than the commercial catalyst in single DMFC. The better performance of Pt/OMCs was attributed to their high surface area and uniform mesopore networks. Moreover, the catalyst prepared from phenanthrene showed the best DMFC performance, related to the higher electrical conductivity compared to the one prepared from sucrose. This study demonstrated the importance of the graphitic character of OMCs on their

performances as a catalyst support for fuel cells. Suitable carbon supports for fuel cell catalysts have to combine a good electronic conductivity with a large and accessible surface area. However, OMC materials with good electronic conductivity are difficult to synthesize. Graphitization has been applied by Fuertes and Alvarez [210] to enhance the electrical conductivity of OMCs. The graphitized OMC was prepared by infiltration of the porosity of mesoporous silica with a solution containing the graphitizable carbon precursor (i.e. polyvinyl chloride, PVC) followed by the carbonization of the silica-PVC composite and finally silica removal. The graphitized carbons prepared via this method exhibited improved electrical conductivity (0.3 S cm^{-1}), which is two orders larger than that of a non-graphitizable carbon (prepared from furfuryl alcohol as carbon precursor). However, the graphitization strategies mainly result in remarkable reduction in the porosity and the specific surface area of the resultant carbon materials which consequently make metal nanoparticles deposition difficult. Another issue regarding OMC materials, is related to the small amount of functional groups on their surface for dispersion and anchoring of Pt particles. So, OMCs need to go through a functionalization process before metal deposition. The functionalization of OMCs still remains a challenge since their ordered structure could collapse during functionalization process. Calvillo et al. [211] modified the surface chemistry of the OMCs derived from SBA-15 by oxidation treatments in liquid phase using HNO_3 as the oxidative agent. Upon functionalization process Pt nanoparticles were deposited on the surface using incipient wetness impregnation technique. Although the morphological and textural properties of the carbon support were affected by the acid treatment, the highly ordered structure of the carbon support remained intact according to XRD and TEM analysis. Acid treatment was carried out both in concentrated and diluted HNO_3 solutions. In the former case larger (22.3-23.3 nm) Pt particles were formed on the CMK-3 carbon support while in the later case the Pt nanoparticles sized between 7-8 nm were observed. Increase in Pt particles size was attributed to the decrease in specific surface area and pore volume of the support along with considerable increase in surface functional groups (oxygen groups) which indicated the role of surface chemistry on the support properties. The Pt based electrocatalyst prepared from CMK-3 as a carbon support demonstrated better performance in terms of polarization and power density curves at the anode side in a home-made PEM single cell compared to commercially available electrode. The enhancement of the cell performance was attributed

to the ordered porous structure of the OMC support, which facilitated the efficient diffusion of hydrogen to the catalytic active sites.

Similar to CNTs, doping OMCs with nitrogen was found to enhance both activity and stability of Pt based electrocatalysts especially for ORR at the cathode side [214]. Lei et al. [215], reported the synthesis of nitrogen containing OMCs prepared by a liquid impregnation method, using aniline as carbon precursor and SBA-15 as hard template. The synthesis temperature (varied between 600–950 °C) was found responsible for structure parameters, such as pore size, specific surface area and the nitrogen concentration (atomic ratio of N/C). In addition, the nitrogen concentration was found critical to determine the size and dispersion of the Pt nanoparticles along with the CO tolerance of these electrocatalysts. Higher N/C ratio generally led to the Pt catalyst with smaller particle size and improved CO tolerance. The catalytic activity of these Pt/NOMCs for methanol oxidation was investigated through cyclic voltammetry and electrochemical impedance spectroscopy and demonstrated activities comparable to Pt/XC-72 along with high CO tolerance under identical conditions. Liu et al. [216] also reported synthesis of Pt/NOMC catalyst prepared through pyrolysis of carbon and Pt precursors using 3-[2-(2-aminoethylamino)ethylamino]propyl functionalized SBA-15 template. The functional group on silica was indeed used as the nitrogen source. With exception of one test, all samples demonstrated that increasing N content in the Pt-NOMC catalyst enhanced the dispersion of Pt nanoparticles and hence the ORR electrocatalytic activity of the catalyst compared to commercially available electrocatalyst (Pt/XC-72). The superior electrochemical performance of Pt-NOMC was attributed to the dispersion and unique nanostructure of Pt nanoparticles especially in the presence of pyridinic-N atoms in the mesoporous carbon supports. Moreover, Pt-NOMC catalyst demonstrated the optimal electrocatalytic activity, durability, and methanol tolerance stability during ORR in the presence of the methanol, surpassing that of a commercial catalyst. In DMFCs, methanol tolerance is an important parameter for ORR cathode catalysts in order to mitigate the deleterious effects of methanol crossover at the cathode.

2.3.2.2 OMC as support for non-precious catalysts

Liu et al. [142], used ordered mesoporous silica SBA-12 as the hard template and polyacrylonitrile (PAN) as the carbon and nitrogen precursor to prepare N-doped ordered

porous carbon upon pyrolysis at 900 °C under Ar flow. After etching the silica template with NaOH solution, different amounts of iron acetate were loaded onto the surface of the carbonaceous support, and it passed another pyrolysis step at temperature range of 700-1000 °C in an Ar atmosphere. They also considered several chemical and thermal post-treatments to modify the surface properties of the catalysts. The synthesized non-PGM catalysts were found to display a good activity for ORR, both in RDE measurements and fuel cell tests. The physical and electrochemical characterization results proposed pyridinic-N and quaternary-N to act as the catalytic active sites for the ORR. Employing OMCs as a support, Dombrovskis et al. [217] reported another type of non-Pt electrocatalyst in a single PEM fuel cell. KIT-6 as a hard silica template was impregnated with furfuryl amine saturated with transition metal salt (CoCl_2 or FeCl_3) and then underwent pyrolysis under inert gas flow at high temperature (800-1100 °C) followed by HF leaching to remove silica. Furfuryl amine was used as both carbon and nitrogen precursor. This way, chelated transition metal ions incorporated to nitrogen-containing OMCs were prepared and used as the ORR catalysts at the cathode side of a single fuel cell. Combination of EXAFS and high-resolution transmission electron microscopy (HRTEM) revealed that the transition metal ions were chelated to the nitrogen functionalized carbon and were not present in metallic, oxide, or carbide forms. The local structure of the transition metals was also found to be similar to the local chemical environment of the M (Fe/Co)-porphyrin structures. The Fe based electrocatalyst pyrolyzed at 1100 °C exhibited the highest electrochemical activity, up to one-third of a commercial Pt/C catalyst at 0.6 V.

Cheon et al. [218], reported an ordered mesoporous porphyrinic carbon catalyst (M-OMPC), which was synthesized through using ordered mesoporous silica as templates and Fe (or Co)- N_4 macrocycle molecules as the catalyst precursor. The mixture of template (SBA-15, KIT-6 and MSU-F) and transition metal containing macrocycle were ground and subsequently pyrolyzed at temperatures ranging between (600-1000 °C). The catalysts, especially FeCo-OMPC showed high ORR activity and stability comparable to the commercial Pt/C catalyst. This was attributed to the large number of porphyrinic active sites that were distributed in the high surface area silica template. Furthermore, direct conversion of porphyrin precursor inside the pores resulted in intact M-N active sites in final carbogenic structures as confirmed by EXAFS.

2.3.3 Graphene

Graphene is a single-atom thick layer of sp^2 -bonded carbon atoms densely arranged in a honeycomb crystal lattice to form a two-dimensional structure. Several highly desirable properties of graphene such as high specific surface area [219], excellent electrical [220] and thermal [221] conductivities, fast charge transport mobility [222], lead to exploring graphene and graphene based materials as promising catalyst support for PEM fuel cells. In addition, heteroatom-doped graphene has been found to show high electrocatalytic activity for ORR especially in alkaline solutions [223, 224]. Doping graphene with heteroatoms that possess different electron affinities than carbon can change its electrochemical properties [225].

Graphene based materials have been synthesized using different techniques such as arc-discharge approach [226, 227], chemical vapour deposition (CVD) on catalytically active metals [228, 229] and intercalation/exfoliation from graphite by mean of oxidation [230, 231]. To enhance long-range order and conductive connections between the individual graphene sheets novel synthetic approaches have been developed to produce 3D graphene foam with higher specific surface area and pore volume along with higher conductivity at extremely low density [232, 233].

Oxidized counterpart of graphene, graphene oxide (GO) has also been widely used as catalyst support in PEMFCs. Although, GO provides lower (two or three orders of magnitude) conductivity compared to graphene, it introduces some functional groups such as carboxyl and epoxides to its structure that can create defect sites which subsequently act as nucleation centers and anchoring sites for further growth of Pt nanoparticles. Examples of GO's application as catalyst support for PEMFCs are presented in the following section.

2.3.3.1 Graphene as support for Pt-based catalysts

Seger and Kamat [234] reported the deposition of Pt nanoparticles on GO sheets through NaBH_4 reduction of H_2PtCl_6 in a GO suspension. The performance of the Pt/GO electrocatalyst was then evaluated in a H_2/O_2 PEM fuel cell and delivered a maximum power of 161 mW cm^{-2} compared with 96 mW cm^{-2} for an unsupported Pt electrocatalyst. This revealed the role of GO as an effective support material toward developing an advanced PEMFC electrocatalyst. Using a modified polyol method, Ha et al. [235] deposited Pt

nanoparticles with diameter of ~ 2.9 nm on GO support. The metal precursor was first added to the GO colloidal suspension under stirring followed by drop wise addition of NaBH_4 dissolved in ethylene glycol under refluxing at 120°C . Electrochemical measurements demonstrated that this catalyst provides better catalytic performances compared to the commercially available Pt/C due to larger ECSA that can facilitate the diffusion of O_2 molecule to the Pt sites on the graphene surface.

To avoid the aggregation of Pt nanoparticles and enhance their uniform distribution, the surface treatment of graphene sheets via covalent or non-covalent functionalization was attempted [236-240]. Qie et al. [236] have used poly(diallyldimethylammoniumchloride) (PDDA) to functionalize the graphene support and subsequently deposit Pt nanoparticles with uniform size and high dispersion via NaBH_4 reduction process. PDDA is a widely used cationic polyelectrolyte that can be adsorbed on the surface of the graphene sheets via the π - π and electrostatic interactions [241]. TEM images (Figure 2.20) confirmed the formation of uniformly dispersed Pt nanoparticles with sizes of approximate 4.6 nm on graphene surface. They prepared Pt/graphene catalysts with different Pt loading between 30-78 wt% through varying the ratio of PDDA-graphene to Pt precursor. As can be seen in Figure 2.20 using this technique for all Pt loading densities, the same Pt particle size was maintained. The resultant Pt/graphene catalysts showed high ECSA and CO tolerance and hence excellent electrocatalytic activity toward the oxidation of methanol and the reduction of oxygen. Beside PDDA, poly(methacrylic acid sodium salt) [237], thiolated graphene [238], poly(sodium styrene sulfonate) [239] and perfluorosulfonic acid-functionalized graphene [240] have also been used to enhance the Pt dispersion on graphene surface and thus improve their electrocatalytic performances.

Furthermore, graphene based materials were used as the support for different Pt alloy catalysts. Guo et al. [242], reported facile preparation of PtFe nanoparticles on graphene surface (PtFe/Graphene). This catalyst demonstrated narrow particle size distribution with average diameter of ~ 7 nm. ORR measurement in 0.1 M HClO_4 solution demonstrated higher half wave potential ($0.557\text{ V vs. Ag/AgCl}$) for PtFe/Graphene compared to PtFe/C catalyst prepared from carbon black support ($0.532\text{ V vs. Ag/AgCl}$) or commercial Pt/C catalyst ($0.512\text{ V vs. Ag/AgCl}$) indicating better activity of the PtFe/Graphene catalyst toward ORR. In addition, this catalyst showed better stability under ORR operating conditions. Almost no

activity loss was observed upon accelerated durability testing (ADT), during which 10,000 potential sweeps were conducted between 0.4 and 0.8 V vs. Ag/AgCl in O₂ saturated 0.1 M HClO₄ solution. This study demonstrated that graphene is an effective support to improve the activity and durability of electrocatalysts. This was attributed to the strong interaction between graphene and FePt nanoparticles that makes the FePt surface more accessible for O₂ adsorption and activation. More recently, Xu et al. [243] have performed DFT calculations to unravel the high stability and activity of FePt/graphene for ORR from a theoretical perspective by exploring the geometric and electronic structure of several Fe_nPt_{13-n} (n = 0, 1, 2, and 3) nanoparticles deposited on graphene. They found that the alloying effect between Fe and Pt could improve the stability and catalytic performance of these nanoparticles. In addition, the monovacancy site in the graphene was found to play a crucial role in anchoring these bimetallic nanoparticles by providing strong metal-substrate interaction that can yield the high stability. Moreover, such strong interfacial interaction and the alloying effect led to the change in the averaged d-band center of these nanoparticles that could affect the O₂ adsorption on these composites. The calculated adsorption energy of O₂ on these composites revealed a good accordance with the measured shift of the average d-band center. This weakened O₂ could provide a balance in the O₂ binding strength that allows an optimal turnover for superior ORR catalytic performance.

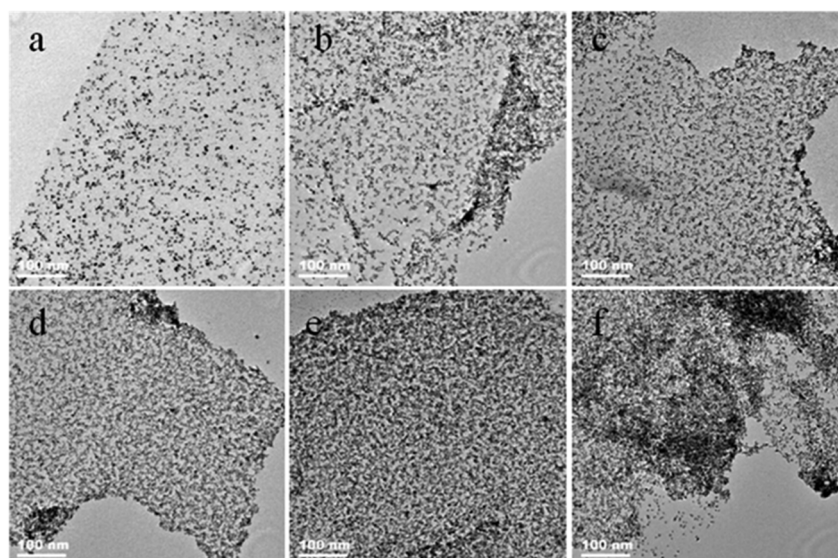


Figure 2.20 TEM images of the Pt/graphene-PDDA nanocomposites synthesized at different mass ratios of PDDA-GO to H₂PtCl₆: (a) 1:1, (b) 1:1.5, (c) 1:2.5, (d) 1:3.5, (e) 1:6.0, and (f) 1:8.5 [236].

2.3.3.2 Graphene as support for non-precious catalysts

The potential offered by graphene to enhance the activity and durability of Pt-based catalysts raised even more interest to employ them toward developing more effective non-PGM electrocatalysts. Hence, monolayer or multilayer of graphene or its oxide have been widely used as support for Fe/N/C catalysts. Using an instantaneous one-pot synthesis to modify graphene sheets with iron and nitrogen over a very short pyrolysis period (45 s), Kamiya et al. [244] prepared non-noble graphene based electrocatalysts (Fe-N/graphene) that exhibited much enhanced catalytic activity for ORR compared to the N-graphene and Fe-graphene in 0.5 M H₂SO₄. TEM images and XRD analysis demonstrated the absence of Fe particles and Fe carbides in the electrocatalyst precursor. Based on XPS results, they considered the atomic iron coordinated with N, (Fe-N/graphene hybrid) as the active catalytic site for ORR. In another study, Tsai et al. [245] reported an iron nitrogen catalyst (Fe-N_x) supported on N-doped graphene, that was prepared through chemical impregnation of Fe and nitrogen precursors in the presence of NH₃ under thermal treatment process. This catalyst showed superb performance toward ORR compared to the FeN_x, and FeN_x/C (supported on carbon black) with the highest stability and almost 4e⁻ transfer reaction. The better performance and higher activity of the Fe-N_x/N-doped graphene was attributed to both graphitic N and the Fe-N_x active sites. He et al. [246] reported a non-PGM and graphene based electrocatalyst that revealed even better ORR performance than a Pt/C catalyst. They employed a simple and scalable resin-based synthesis methodology to prepare N-self-doped graphene that subsequently served as the precursor for Fe-based catalyst. The N-doped graphene itself demonstrated an outstanding ORR activity in alkaline solution [247], however, to enhance the performance especially in acidic media it was enwrapped with Fe nanoparticles to produce (Fe-N-graphene). The electrochemical characterization showed that Fe-N-graphene catalyst could provide a performance superior to Pt/C catalyst in terms of ORR catalytic activity, stability and fuel (methanol and CO) tolerance.

2.4 Conclusion

In the previous sections different approaches toward enhancing electrocatalyst performance of PEMFCs were discussed. Pt-based alloys of different composition, size and shape were surveyed to enhance the inherent activity of the catalyst toward ORR. In addition, Pt-based

alloys reduce the required amount of the noble metal which is important from the cost point of view. However, applying Pt or Pt alloy-based material and even transition metal-N-C required employing a preparation method which can provide high dispersion of metal sites on the support and prevent sintering of the particles. In addition the stability and durability of these catalysts and electrodes are important to insure the requirements for commercial application. As has been mentioned different support materials and structures are also used to assist dispersion of metal for the sake of improving catalyst utilization. It was also tried to apply support material which can improve the long-term stability of the fuel cell performance. However to meet the cost targets required for commercialization, many ingenious improvements are still remaining to be done. In this study we aim at applying Metal Organic Framework (MOF) materials as a new class of precursor for preparing ORR catalysts. Different from previous approaches, using MOFs has the following advantages: MOFs have clearly-defined three-dimensional crystalline structures. Metal species are distributed evenly through the crystalline MOF structure. The organic linkers can be carbonized via pyrolysis while maintaining the porous framework, leading to catalysts with high surface area and uniformly distributed active sites. Carbonization will provide conductive media through which the electrons can be transferred. This is an important requirement for an electrocatalyst. Therefore, there will be no need for a carbon support. Furthermore, the initial entities such as Pt or $M-N_4$ $M-N_2$ ($M = Fe, Co, etc.$) can be grafted into MOFs structure with high density which is an appealing characteristic, especially in the case of transition metal catalysts, to achieve high active site density through regularly arranged structure. An important barrier to transition metal application is the low catalytic activity. To compensate this more transition metal active sites must be introduced in the catalyst layer which causes a thicker electrode and mass transfer limitations. In addition, the MOF surface area and pore size are tunable by the choice of organic linker length. In the next chapter a review of literature regarding MOFs characteristics and catalytic applications in PEM fuel cells will be provided.

Chapter 2 References:

- [1] D. Thompsett, Pt alloys as oxygen reduction catalysts, in W. Vielstich, H.A. Gasteiger and A. Lamm, Editors, Handbook of fuel cells—fundamentals, technology and applications, John Wiley & Sons, New York, USA (2003).
- [2] S. Mukerjee, S. Srinivasan, Enhanced electrocatalysis of oxygen reduction on platinum alloys in proton exchange membrane fuel cells, *Journal of Electroanalytical Chemistry* 357 (1993) 201-224.
- [3] S. Mukerjee, S. Srinivasan, M.P. Soriaga, J. McBreen, Role of Structural and Electronic Properties of Pt and Pt Alloys on Electrocatalysis of Oxygen Reduction: An In Situ XANES and EXAFS Investigation, *Journal of The Electrochemical Society* 142 (1995) 1409-1422.
- [4] S. Mukerjee, S. Srinivasan, O₂ reduction and structure-related parameters for supported catalysts, in W. Vielstich, H.A. Gasteiger, A. Lamm, Editors. Handbook of fuel cells—fundamentals, technology and applications, John Wiley & Sons, New York, NY, USA (2003).
- [5] T. Toda, H. Igarashi, H. Uchida, M. Watanabe, Enhancement of the Electroreduction of Oxygen on Pt Alloys with Fe, Ni, and Co, *Journal of The Electrochemical Society* 146 (1999) 3750-3756.
- [6] J. Shim, D.-Y. Yoo, J.-S. Lee, Characteristics for electrocatalytic properties and hydrogen–oxygen adsorption of platinum ternary alloy catalysts in polymer electrolyte fuel cell, *Electrochimica Acta* 45 (2000) 1943-1951.
- [7] L. Xiong, A.M. Kannan, A. Manthiram, Pt–M (M=Fe, Co, Ni and Cu) electrocatalysts synthesized by an aqueous route for proton exchange membrane fuel cells, *Electrochemistry Communications* 4 (2002) 898-903.
- [8] E. Antolini, R.R. Passos, E.A. Ticianelli, Electrocatalysis of oxygen reduction on a carbon supported platinum–vanadium alloy in polymer electrolyte fuel cells, *Electrochimica Acta* 48 (2002) 263-270.
- [9] M.-k. Min, J. Cho, K. Cho, H. Kim, Particle size and alloying effects of Pt-based alloy catalysts for fuel cell applications, *Electrochimica Acta* 45 (2000) 4211-4217.
- [10] L. Xiong, A. Manthiram, Influence of atomic ordering on the electrocatalytic activity of Pt-Co alloys in alkaline electrolyte and proton exchange membrane fuel cells, *Journal of Materials Chemistry* 14 (2004) 1454-1460.
- [11] V.R. Stamenkovic, B.S. Mun, M. Arenz, K.J.J. Mayrhofer, C.A. Lucas, G. Wang, P.N. Ross, N.M. Markovic, Trends in electrocatalysis on extended and nanoscale Pt-bimetallic alloy surfaces, *Nat Mater* 6 (2007) 241-247.
- [12] I. Chorkendorff, J.W. Niemantsverdriet, Concepts of Modern Catalysis and Kinetics, WILEY-VCH Verlag GmbH & Co. KGaA, Weinheim, Germany (2003).
- [13] J.K. Nørskov, J. Rossmeisl, A. Logadottir, L. Lindqvist, J.R. Kitchin, T. Bligaard, H. Jónsson, Origin of the Overpotential for Oxygen Reduction at a Fuel-Cell Cathode, *The Journal of Physical Chemistry B* 108 (2004) 17886-17892.
- [14] P. Sabatier, Hydrogenation and dehydrogenation of catalyst. *Ber. Deutschen Chem. Gesellschaft* 44 (1911) 1984-2001.
- [15] V. Stamenković, T.J. Schmidt, P.N. Ross, N.M. Marković, Surface Composition Effects in Electrocatalysis: Kinetics of Oxygen Reduction on Well-Defined Pt₃Ni and Pt₃Co Alloy Surfaces, *The Journal of Physical Chemistry B* 106 (2002) 11970-11979.
- [16] V. Stamenkovic, B.S. Mun, K.J.J. Mayrhofer, P.N. Ross, N.M. Markovic, J. Rossmeisl, J. Greeley, J.K. Nørskov, Changing the Activity of Electrocatalysts for Oxygen Reduction by Tuning the Surface Electronic Structure, *Angewandte Chemie International Edition* 45 (2006) 2897-2901.
- [17] V.S. Murthi, R.C. Urian, S. Mukerjee, Oxygen Reduction Kinetics in Low and Medium Temperature Acid Environment: Correlation of Water Activation and Surface Properties in Supported Pt and Pt Alloy Electrocatalysts, *The Journal of Physical Chemistry B* 108 (2004) 11011-11023.

- [18] M. Teliska, V.S. Murthi, S. Mukerjee, D.E. Ramaker, Correlation of Water Activation, Surface Properties, and Oxygen Reduction Reactivity of Supported Pt–M/C Bimetallic Electrocatalysts Using XAS, *Journal of The Electrochemical Society* 152 (2005) A2159-A2169.
- [19] J. Roques, A.B. Anderson, V.S. Murthi, S. Mukerjee, Potential Shift for OH(ads) Formation on the Pt Skin on Pt₃Co (111) Electrodes in Acid: Theory and Experiment, *Journal of The Electrochemical Society* 152 (2005) E193-E199.
- [20] Y. Xu, M. Shao, M. Mavrikakis, R. R. Adzic, Recent developments in the Electrocatalysis of the O₂ Reduction Reaction, in M. T. M. Koper, Editor, *Fuel Cell Catalysis. A Surface Science Approach*, John Wiley & Sons, Hoboken, NJ, USA (2009).
- [21] V.R. Stamenkovic, B. Fowler, B.S. Mun, G. Wang, P.N. Ross, C.A. Lucas, N.M. Marković, Improved Oxygen Reduction Activity on Pt₃Ni(111) via Increased Surface Site Availability, *Science* 315 (2007) 493-497.
- [22] H.R. Colón-Mercado, B.N. Popov, Stability of platinum based alloy cathode catalysts in PEM fuel cells, *Journal of Power Sources* 155 (2006) 253-263.
- [23] W. Chen, J. Kim, S. Sun, S. Chen, Electrocatalytic Reduction of Oxygen by FePt Alloy Nanoparticles, *The Journal of Physical Chemistry C* 112 (2008) 3891-3898.
- [24] C. Wang, M. Chi, D. Li, D. van der Vliet, G. Wang, Q. Lin, J. F. Mitchell, K.L. More, N.M. Markovic, V.R. Stamenkovic, Synthesis of Homogeneous Pt-Bimetallic Nanoparticles as Highly Efficient Electrocatalysts, *ACS Catalysis* 1 (2011) 1355-1359.
- [25] L. Xiong, A. Manthiram, Effect of Atomic Ordering on the Catalytic Activity of Carbon Supported PtM (M = Fe, Co, Ni, and Cu) Alloys for Oxygen Reduction in PEMFCs, *Journal of The Electrochemical Society* 152 (2005) A697-A703.
- [26] J. Kim, Y. Lee, S. Sun, Structurally Ordered FePt Nanoparticles and Their Enhanced Catalysis for Oxygen Reduction Reaction, *Journal of the American Chemical Society* 132 (2010) 4996-4997.
- [27] J. Wu, J. Zhang, Z. Peng, S. Yang, F.T. Wagner, H. Yang, Truncated Octahedral Pt₃Ni Oxygen Reduction Reaction Electrocatalysts, *Journal of the American Chemical Society* 132 (2010) 4984-4985.
- [28] J. Wu, H. Yang, Synthesis and electrocatalytic oxygen reduction properties of truncated octahedral Pt₃Ni nanoparticles, *Nano Research* 4 (2011) 72-82.
- [29] J. Zhang, H. Yang, J. Fang, S. Zou, Synthesis and Oxygen Reduction Activity of Shape-Controlled Pt₃Ni Nanopolyhedra, *Nano Letters* 10 (2010) 638-644.
- [30] J. Wu, A. Gross, H. Yang, Shape and Composition-Controlled Platinum Alloy Nanocrystals Using Carbon Monoxide as Reducing Agent, *Nano Letters* 11 (2011) 798-802.
- [31] J. Wu, L. Qi, H. You, A. Gross, J. Li, H. Yang, Icosahedral Platinum Alloy Nanocrystals with Enhanced Electrocatalytic Activities, *Journal of the American Chemical Society* 134 (2012) 11880-11883.
- [32] F. Maillard, S. Pronkin, E. R. Savinova, "Size effects in electrocatalysis of fuel cells reactions on supported metal nanoparticles", In *Fuel Cell Catalysis, A Surface Science Approach*, M. T. M. Koper, Editor, John Wiley & Sons, Hoboken, NJ, USA (2009).
- [33] F. Maillard, S. Pronkin, E. R. Savinova, "Influence of size on the electrocatalytic activities of supported metal nanoparticles in fuel cells related reactions", In *Handbook of Fuel Cells Vol. 5 "Advances in Electrocatalysis, Materials, Diagnostics and Durability"*, in W. Vielstich, H.A. Gasteiger, H. Yokokawa, Editors, John Wiley & Sons, Inc., New York, NY, USA (2009).
- [34] K.J.J. Mayrhofer, B.B. Bliznac, M. Arenz, V.R. Stamenkovic, P.N. Ross, N.M. Markovic, The Impact of Geometric and Surface Electronic Properties of Pt-Catalysts on the Particle Size Effect in Electrocatalysis, *The Journal of Physical Chemistry B* 109 (2005) 14433-14440.
- [35] J. Greeley, J. Rossmeisl, A. Hellmann, J. Nørskov, Theoretical trends in particle size effects for the oxygen reduction reaction, *Zeitschrift für Physikalische Chemie* 221 (2007) 1209-1220.

- [36] C. Wang, D. van der Vliet, K.-C. Chang, H. You, D. Strmcnik, J.A. Schlueter, N.M. Markovic, V.R. Stamenkovic, Monodisperse Pt₃Co Nanoparticles as a Catalyst for the Oxygen Reduction Reaction: Size-Dependent Activity, *The Journal of Physical Chemistry C* 113 (2009) 19365-19368.
- [37] C. Wang, G. Wang, D. van der Vliet, K.-C. Chang, N.M. Markovic, V.R. Stamenkovic, Monodisperse Pt₃Co nanoparticles as electrocatalyst: the effects of particle size and pretreatment on electrocatalytic reduction of oxygen, *Physical Chemistry Chemical Physics* 12 (2010) 6933-6939.
- [38] J.X. Wang, H. Inada, L. Wu, Y. Zhu, Y. Choi, P. Liu, W.-P. Zhou, R.R. Adzic, Oxygen Reduction on Well-Defined Core–Shell Nanocatalysts: Particle Size, Facet, and Pt Shell Thickness Effects, *Journal of the American Chemical Society* 131 (2009) 17298-17302.
- [39] K. Kinoshita, Particle Size Effects for Oxygen Reduction on Highly Dispersed Platinum in Acid Electrolytes, *Journal of The Electrochemical Society* 137 (1990) 845-848.
- [40] J. Zhang, Y. Mo, M.B. Vukmirovic, R. Klie, K. Sasaki, R.R. Adzic, Platinum Monolayer Electrocatalysts for O₂ Reduction: Pt Monolayer on Pd(111) and on Carbon-Supported Pd Nanoparticles, *The Journal of Physical Chemistry B* 108 (2004) 10955-10964.
- [41] J. Zhang, M.B. Vukmirovic, Y. Xu, M. Mavrikakis, R.R. Adzic, Controlling the Catalytic Activity of Platinum-Monolayer Electrocatalysts for Oxygen Reduction with Different Substrates, *Angewandte Chemie International Edition* 44 (2005) 2132-2135.
- [42] J. Zhang, M.B. Vukmirovic, K. Sasaki, A.U. Nilekar, M. Mavrikakis, R.R. Adzic, Mixed-Metal Pt Monolayer Electrocatalysts for Enhanced Oxygen Reduction Kinetics, *Journal of the American Chemical Society* 127 (2005) 12480-12481.
- [43] M.B. Vukmirovic, J. Zhang, K. Sasaki, A.U. Nilekar, F. Uribe, M. Mavrikakis, R.R. Adzic, Platinum monolayer electrocatalysts for oxygen reduction, *Electrochimica Acta* 52 (2007) 2257-2263.
- [44] S. Koh, P. Strasser, Electrocatalysis on Bimetallic Surfaces: Modifying Catalytic Reactivity for Oxygen Reduction by Voltammetric Surface Dealloying, *Journal of the American Chemical Society* 129 (2007) 12624-12625.
- [45] P. Mani, R. Srivastava, P. Strasser, Dealloyed Pt–Cu Core–Shell Nanoparticle Electrocatalysts for Use in PEM Fuel Cell Cathodes, *The Journal of Physical Chemistry C* 112 (2008) 2770-2778.
- [46] K.C. Neyerlin, R. Srivastava, C. Yu, P. Strasser, Electrochemical activity and stability of dealloyed Pt–Cu and Pt–Cu–Co electrocatalysts for the oxygen reduction reaction (ORR), *Journal of Power Sources* 186 (2009) 261-267.
- [47] F. Hasché, M. Oezaslan, P. Strasser, Activity, Stability, and Degradation Mechanisms of Dealloyed PtCu₃ and PtCo₃ Nanoparticle Fuel Cell Catalysts, *ChemCatChem* 3 (2011) 1805-1813.
- [48] L. Gan, M. Heggen, S. Rudi, P. Strasser, Core–Shell Compositional Fine Structures of Dealloyed Pt_xNi_{1-x} Nanoparticles and Their Impact on Oxygen Reduction Catalysis, *Nano Letters* 12 (2012) 5423-5430.
- [49] L. Gan, M. Heggen, R. O'Malley, B. Theobald, P. Strasser, Understanding and Controlling Nanoporosity Formation for Improving the Stability of Bimetallic Fuel Cell Catalysts, *Nano Letters* 13 (2013) 1131-1138.
- [50] A. Kongkanand, F.T. Wagner, High-activity dealloyed catalysts. 2013 DOE Hydrogen Program Annual Merit Review (2013) FC-087,
http://www.hydrogen.energy.gov/pdfs/review13/fc087_kongkanand_2013_o.pdf.
- [51] R. Jasinski, A New Fuel Cell Cathode Catalyst, *Nature* 201 (1964) 1212-1213.
- [52] J.H. Zagal, Macrocycles, in *Handbook of Fuel Cells—Fundamentals, Technology and Applications*, in W. Vielstich, H. Gasteiger, and A. Lamm, Editors, John Wiley & Sons Ltd., New York, NY, USA (2003).
- [53] M. Savy, P. Andro, C. Bernard, G. Magner, Study On Oxygen Reduction On Monomeric and Polymeric Phthalocyanines. 1. Basic Principles, Selection of Central Ion, *Electrochimica Acta* 18 (1973) 191-197.
- [54] P. Vasudevan, Santosh, N. Mann, S. Tyagi, Transition metal complexes of porphyrins and phthalocyanines as electrocatalysts for dioxygen reduction, *Transition Metal Chemistry* 15 (1990) 81-90.

- [55] J.H. Zagal, Metallophthalocyanines as catalysts in electrochemical reactions, *Coordination Chemistry Reviews* 119 (1992) 89-136.
- [56] M.-S. Liao, S. Scheiner, Comparative study of metal-porphyrins, -porphyrazines, and -phthalocyanines, *Journal of Computational Chemistry* 23 (2002) 1391-1403.
- [57] Z. Shi, J. Zhang, Density Functional Theory Study of Transitional Metal Macrocyclic Complexes' Dioxygen-Binding Abilities and Their Catalytic Activities toward Oxygen Reduction Reaction, *The Journal of Physical Chemistry C* 111 (2007) 7084-7090.
- [58] A. Bettelheim, D. Ozer, R. Harth, R.W. Murray, Electrochemistry of various substituted aminophenyl iron porphyrins: Part I. Redox properties of dissolved, adsorbed and electropolymerized species, *Journal of Electroanalytical Chemistry and Interfacial Electrochemistry* 266 (1989) 93-108.
- [59] D. Ozer, R. Harth, U. Mor, A. Bettelheim, Electrochemistry of various substituted aminophenyl iron porphyrins: Part II. catalytic reduction of dioxygen by electropolymerized films, *Journal of Electroanalytical Chemistry and Interfacial Electrochemistry* 266 (1989) 109-123.
- [60] E. Song, C. Shi, F.C. Anson, Comparison of the Behavior of Several Cobalt Porphyrins as Electrocatalysts for the Reduction of O₂ at Graphite Electrodes, *Langmuir* 14 (1998) 4315-4321.
- [61] M. Yuasa, R. Nishihara, C. Shi, F.C. Anson, A comparison of several meso-tetraalkyl cobalt porphyrins as catalysts for the electroreduction of dioxygen, *Polymers for Advanced Technologies* 12 (2001) 266-270.
- [62] R. Baker, D.P. Wilkinson, J. Zhang, Electrocatalytic activity and stability of substituted iron phthalocyanines towards oxygen reduction evaluated at different temperatures, *Electrochimica Acta* 53 (2008) 6906-6919.
- [63] C. Kretzschmar, K. Wiesner, Study of the operation of tungsten carbide anode and iron phthalocyanine cathodes in fuel cells with a sulphuric acid electrolyte, *Elektrokhimiya* 14 (1978) 1330-1334.
- [64] A. Biloul, P. Gouérec, M. Savy, G. Scarbeck, S. Besse, J. Riga, Oxygen electrocatalysis under fuel cell conditions: behaviour of cobalt porphyrins and tetraazaannulene analogues, *Journal of Applied Electrochemistry* 26 (1996) 1139-1146.
- [65] H. Jahnke, M. Schönborn, G. Zimmermann, Organic dyestuffs as catalysts for fuel cells, in: F.P. Schäfer, H. Gerischer, F. Willig, H. Meier, H. Jahnke, M. Schönborn, G. Zimmermann (Eds.), *Physical and Chemical Applications of Dyestuffs*, Springer Berlin Heidelberg, 1976, pp. 133-181.
- [66] J.A.R. van Veen, J.F. van Baar, K.J. Kroese, Effect of heat treatment on the performance of carbon-supported transition-metal chelates in the electrochemical reduction of oxygen, *Journal of the Chemical Society, Faraday Transactions 1: Physical Chemistry in Condensed Phases* 77 (1981) 2827-2843.
- [67] K. Wiesener, N₄-chelates as electrocatalyst for cathodic oxygen reduction, *Electrochimica Acta* 31 (1986) 1073-1078.
- [68] K. Wiesener, D. Ohms, V. Neumann, R. Franke, N₄ macrocycles as electrocatalysts for the cathodic reduction of oxygen, *Materials Chemistry and Physics* 22 (1989) 457-475.
- [69] G. Faubert, G. Lalande, R. Côté, D. Guay, J.P. Dodelet, L.T. Weng, P. Bertrand, G. Dénès, Heat-treated iron and cobalt tetraphenylporphyrins adsorbed on carbon black: Physical characterization and catalytic properties of these materials for the reduction of oxygen in polymer electrolyte fuel cells, *Electrochimica Acta* 41 (1996) 1689-1701.
- [70] P. Gouérec, M. Savy, J. Riga, Oxygen reduction in acidic media catalyzed by pyrolyzed cobalt macrocycles dispersed on an active carbon: The importance of the content of oxygen surface groups on the evolution of the chelate structure during the heat treatment, *Electrochimica Acta* 43 (1998) 743-753.
- [71] H. Meng, N. Larouche, M. Lefèvre, F. Jaouen, B. Stansfield, J.-P. Dodelet, Iron porphyrin-based cathode catalysts for polymer electrolyte membrane fuel cells: Effect of NH₃ and Ar mixtures as pyrolysis gases on catalytic activity and stability, *Electrochimica Acta* 55 (2010) 6450-6461.
- [72] J.A.R. van Veen, H.A. Colijn, J.F. van Baar, On the effect of a heat treatment on the structure of carbon-supported metalloporphyrins and phthalocyanines, *Electrochimica Acta* 33 (1988) 801-804.

- [73] A. Widelöv, R. Larsson, ESCA and electrochemical studies on pyrolysed iron and cobalt tetraphenylporphyrins, *Electrochimica Acta* 37 (1992) 187-197.
- [74] A. Widelöv, Pyrolysis of iron and cobalt porphyrins sublimated onto the surface of carbon black as a method to prepare catalysts for O₂ reduction, *Electrochimica Acta* 38 (1993) 2493-2502.
- [75] M.C.M. Alves, J.P. Dodelet, D. Guay, M. Ladouceur, G. Tourillon, Origin of the electrocatalytic properties for oxygen reduction of some heat-treated polyacrylonitrile and phthalocyanine cobalt compounds adsorbed on carbon black as probed by electrochemistry and x-ray absorption spectroscopy, *The Journal of Physical Chemistry* 96 (1992) 10898-10905.
- [76] G. Lalande, R. Côté, D. Guay, J.P. Dodelet, L.T. Weng, P. Bertrand, Is nitrogen important in the formulation of Fe-based catalysts for oxygen reduction in solid polymer fuel cells?, *Electrochimica Acta* 42 (1997) 1379-1388.
- [77] S.L. Gojkovic, S. Gupta, R.F. Savinell, Heat-Treated Iron(III) Tetramethoxyphenyl Porphyrin Supported on High-Area Carbon as an Electrocatalyst for Oxygen Reduction, *Journal of The Electrochemical Society* 145 (1998) 3493-3499.
- [78] E. Yeager, Electrocatalysts for O₂ reduction, *Electrochimica Acta* 29 (1984) 1527-1537.
- [79] D. Scherson, A.A. Tanaka, S.L. Gupta, D. Tryk, C. Fierro, R. Holze, E.B. Yeager, R.P. Lattimer, Transition metal macrocycles supported on high area carbon: Pyrolysis—mass spectrometry studies, *Electrochimica Acta* 31 (1986) 1247-1258.
- [80] A. Tanaka, S.L. Gupta, D. Tryk, C. Fierro, E.B. Yeager, D.A. Scherson, Electrochemical and spectroscopic aspects of heat-treated transition metal macrocycles as electrocatalysts for oxygen reduction, in D. Scherson, D. Tryk, M. Daroux, X. Xing, Editors, Proceedings of the symposium “on structural effects in electrocatalysis and oxygen electrochemistry”, The Electrochemical Society, Pennington, NJ, USA (1992).
- [81] G. Gruenig, K. Wiesener, S. Gamburzev, I. Iliev, A. Kaisheva, Investigations of catalysts from the pyrolyzates of cobalt-containing and metal-free dibenzotetraazaannulenes on active carbon for oxygen electrodes in an acid medium, *Journal of Electroanalytical Chemistry and Interfacial Electrochemistry* 159 (1983) 155-162.
- [82] R. Franke, D. Ohms, K. Wiesener, Investigation of the influence of thermal treatment on the properties of carbon materials modified by N₄-chelates for the reduction of oxygen in acidic media, *Journal of Electroanalytical Chemistry and Interfacial Electrochemistry* 260 (1989) 63-73.
- [83] P. Gouérec, A. Biloul, O. Contamin, G. Scarbeck, M. Savy, J. Riga, L.T. Weng, P. Bertrand, Oxygen reduction in acid media catalyzed by heat treated cobalt tetraazaannulene supported on an active charcoal: correlations between the performances after longevity tests and the active site configuration as seen by XPS and ToF-SIMS, *Journal of Electroanalytical Chemistry* 422 (1997) 61-75.
- [84] S.L. Gojkovic, S. Gupta, R.F. Savinell, Heat-treated iron(III) tetramethoxyphenyl porphyrin chloride supported on high-area carbon as an electrocatalyst for oxygen reduction: Part II. Kinetics of oxygen reduction, *Journal of Electroanalytical Chemistry* 462 (1999) 63-72.
- [85] L.Y. Johansson, R. Larsson, Electrochemical reduction of oxygen in sulphuric acid catalyzed by porphyrin-like complexes, *Journal of Molecular Catalysis* 38 (1986) 61-70.
- [86] G. Wu, C.M. Johnston, N.H. Mack, K. Artyushkova, M. Ferrandon, M. Nelson, J.S. Lezama-Pacheco, S.D. Conradson, K.L. More, D.J. Myers, P. Zelenay, Synthesis-structure-performance correlation for polyaniline-Me-C non-precious metal cathode catalysts for oxygen reduction in fuel cells, *Journal of Materials Chemistry* 21 (2011) 11392-11405.
- [87] F. Jaouen, J. Herranz, M. Lefèvre, J.-P. Dodelet, U.I. Kramm, I. Herrmann, P. Bogdanoff, J. Maruyama, T. Nagaoka, A. Garsuch, J.R. Dahn, T. Olson, S. Pylypenko, P. Atanassov, E.A. Ustinov, Cross-Laboratory Experimental Study of Non-Noble-Metal Electrocatalysts for the Oxygen Reduction Reaction, *ACS Applied Materials & Interfaces* 1 (2009) 1623-1639.

- [88] H. Wang, R. Côté, G. Faubert, D. Guay, J.P. Dodelet, Effect of the Pre-Treatment of Carbon Black Supports on the Activity of Fe-Based Electrocatalysts for the Reduction of Oxygen, *The Journal of Physical Chemistry B* 103 (1999) 2042-2049.
- [89] D. Villers, X. Jacques-Bédard, J.-P. Dodelet, Fe-Based Catalysts for Oxygen Reduction in PEM Fuel Cells: Pretreatment of the Carbon Support, *Journal of The Electrochemical Society* 151 (2004) A1507-A1515.
- [90] F. Jaouen, M. Lefèvre, J.-P. Dodelet, M. Cai, Heat-Treated Fe/N/C Catalysts for O₂ Electroreduction: Are Active Sites Hosted in Micropores?, *The Journal of Physical Chemistry B* 110 (2006) 5553-5558.
- [91] G.C.-K. Liu, J.R. Dahn, Fe-N-C oxygen reduction catalysts supported on vertically aligned carbon nanotubes, *Applied Catalysis A: General* 347 (2008) 43-49.
- [92] S. Barazzouk, M. Lefèvre, J.-P. Dodelet, Oxygen Reduction in PEM Fuel Cells: Fe-Based Electrocatalysts Made with High Surface Area Activated Carbon Supports, *Journal of The Electrochemical Society* 156 (2009) B1466-B1474.
- [93] H. Niwa, K. Horiba, Y. Harada, M. Oshima, T. Ikeda, K. Terakura, J.-i. Ozaki, S. Miyata, X-ray absorption analysis of nitrogen contribution to oxygen reduction reaction in carbon alloy cathode catalysts for polymer electrolyte fuel cells, *Journal of Power Sources* 187 (2009) 93-97.
- [94] F. Jaouen, J.-P. Dodelet, O₂ Reduction Mechanism on Non-Noble Metal Catalysts for PEM Fuel Cells. Part I: Experimental Rates of O₂ Electroreduction, H₂O₂ Electroreduction, and H₂O₂ Disproportionation, *The Journal of Physical Chemistry C* 113 (2009) 15422-15432.
- [95] M. Lefèvre, E. Proietti, F. Jaouen, J.-P. Dodelet, Iron-Based Catalysts with Improved Oxygen Reduction Activity in Polymer Electrolyte Fuel Cells, *Science* 324 (2009) 71-74.
- [96] X. Wang, J.S. Lee, Q. Zhu, J. Liu, Y. Wang, S. Dai, Ammonia-Treated Ordered Mesoporous Carbons as Catalytic Materials for Oxygen Reduction Reaction, *Chemistry of Materials* 22 (2010) 2178-2180.
- [97] J. Fournier, G. Lalande, R. Côté, D. Guay, J.P. Dodelet, Activation of Various Fe-Based Precursors on Carbon Black and Graphite Supports to Obtain Catalysts for the Reduction of Oxygen in Fuel Cells, *Journal of The Electrochemical Society* 144 (1997) 218-226.
- [98] P.H. Matter, L. Zhang, U.S. Ozkan, The role of nanostructure in nitrogen-containing carbon catalysts for the oxygen reduction reaction, *Journal of Catalysis* 239 (2006) 83-96.
- [99] K. Prehn, A. Warburg, T. Schilling, M. Bron, K. Schulte, Towards nitrogen-containing CNTs for fuel cell electrodes, *Composites Science and Technology* 69 (2009) 1570-1579.
- [100] H.T. Chung, C.M. Johnston, K. Artyushkova, M. Ferrandon, D.J. Myers, P. Zelenay, Cyanamide-derived non-precious metal catalyst for oxygen reduction, *Electrochemistry Communications* 12 (2010) 1792-1795.
- [101] N.P. Subramanian, S.P. Kumaraguru, H. Colon-Mercado, H. Kim, B.N. Popov, T. Black, D.A. Chen, Studies on Co-based catalysts supported on modified carbon substrates for PEMFC cathodes, *Journal of Power Sources* 157 (2006) 56-63.
- [102] V. Nallathambi, J.-W. Lee, S.P. Kumaraguru, G. Wu, B.N. Popov, Development of high performance carbon composite catalyst for oxygen reduction reaction in PEM Proton Exchange Membrane fuel cells, *Journal of Power Sources* 183 (2008) 34-42.
- [103] T.E. Wood, Z. Tan, A.K. Schmoekkel, D. O'Neill, R. Atanasoski, Non-precious metal oxygen reduction catalyst for PEM fuel cells based on nitroaniline precursor, *Journal of Power Sources* 178 (2008) 510-516.
- [104] V. Nallathambi, N. Leonard, R. Kothandaraman, S.C. Barton, Nitrogen Precursor Effects in Iron-Nitrogen-Carbon Oxygen Reduction Catalysts, *Electrochemical and Solid-State Letters* 14 (2011) B55-B58.
- [105] G. Wu, Z. Chen, K. Artyushkova, F.H. Garzon, P. Zelenay, Polyaniline-derived Non-Precious Catalyst for the Polymer Electrolyte Fuel Cell Cathode, *ECS Transactions* 16 (2008) 159-170.
- [106] G. Wu, K.L. More, C.M. Johnston, P. Zelenay, High-Performance Electrocatalysts for Oxygen Reduction Derived from Polyaniline, Iron, and Cobalt, *Science* 332 (2011) 443-447.

- [107] P. Wang, Z. Ma, Z. Zhao, L. Jia, Oxygen reduction on the electrocatalysts based on pyrolyzed non-noble metal/poly-o-phenylenediamine/carbon black composites: New insight into the active sites, *Journal of Electroanalytical Chemistry* 611 (2007) 87-95.
- [108] R. Kobayashi, J.-i. Ozaki, Novel N-Doped Carbon Cathode Catalyst for Polymer Electrolyte Membrane Fuel Cells Formed on Carbon Black, *Chemistry Letters* 38 (2009) 396-397.
- [109] W. Martínez Millán, T. Toledano Thompson, L.G. Arriaga, M.A. Smit, Characterization of composite materials of electroconductive polymer and cobalt as electrocatalysts for the oxygen reduction reaction, *International Journal of Hydrogen Energy* 34 (2009) 694-702.
- [110] F. Jaouen, J.-P. Dodelet, Non-Noble Electrocatalysts for O₂ Reduction: How Does Heat Treatment Affect Their Activity and Structure? Part I. Model for Carbon Black Gasification by NH₃: Parametric Calibration and Electrochemical Validation, *The Journal of Physical Chemistry C* 111 (2007) 5963-5970.
- [111] F. Jaouen, A.M. Serventi, M. Lefèvre, J.-P. Dodelet, P. Bertrand, Non-Noble Electrocatalysts for O₂ Reduction: How Does Heat Treatment Affect Their Activity and Structure? Part II. Structural Changes Observed by Electron Microscopy, Raman, and Mass Spectroscopy, *The Journal of Physical Chemistry C* 111 (2007) 5971-5976.
- [112] M. Lefèvre, J.-P. Dodelet, Fe-based electrocatalysts made with microporous pristine carbon black supports for the reduction of oxygen in PEM fuel cells, *Electrochimica Acta* 53 (2008) 8269-8276.
- [113] F. Charreureur, F. Jaouen, S. Ruggeri, J.-P. Dodelet, Fe/N/C non-precious catalysts for PEM fuel cells: Influence of the structural parameters of pristine commercial carbon blacks on their activity for oxygen reduction, *Electrochimica Acta* 53 (2008) 2925-2938.
- [114] J. Herranz, F.d.r. Jaouen, M. Lefèvre, U.I. Kramm, E. Proietti, J.-P. Dodelet, P. Bogdanoff, S. Fiechter, I. Abs-Wurmbach, P. Bertrand, T.M. Arruda, S. Mukerjee, Unveiling N-Protonation and Anion-Binding Effects on Fe/N/C Catalysts for O₂ Reduction in Proton-Exchange-Membrane Fuel Cells, *The Journal of Physical Chemistry C* 115 (2011) 16087-16097.
- [115] U.I. Kramm, I. Herrmann-Geppert, P. Bogdanoff, S. Fiechter, Effect of an Ammonia Treatment on Structure, Composition, and Oxygen Reduction Reaction Activity of Fe–N–C Catalysts, *The Journal of Physical Chemistry C* 115 (2011) 23417-23427.
- [116] U.I. Kramm, M. Lefèvre, N. Larouche, D. Schmeisser, J.-P. Dodelet, Correlations between Mass Activity and Physicochemical Properties of Fe/N/C Catalysts for the ORR in PEM Fuel Cell via ⁵⁷Fe Mössbauer Spectroscopy and Other Techniques, *Journal of the American Chemical Society* 136 (2013) 978-985.
- [117] U.I. Kramm, M. Lefèvre, P. Bogdanoff, D. Schmeißer, J.-P. Dodelet, Analyzing Structural Changes of Fe–N–C Cathode Catalysts in PEM Fuel Cell by Mössbauer Spectroscopy of Complete Membrane Electrode Assemblies, *The Journal of Physical Chemistry Letters* 5 (2014) 3750-3756.
- [118] K. Sawai, N. Suzuki Heat-Treated Transition Metal Hexacyanomethylates as Electrocatalysts for Oxygen Reduction Insensitive to Methanol, *Journal of The Electrochemical Society* 151 (2004) A682-A688.
- [119] R. Yang, K. Stevens, J.R. Dahn, Investigation of Activity of Sputtered Transition-Metal (TM)–C–N (TM = V, Cr, Mn, Co, Ni) Catalysts for Oxygen Reduction Reaction, *Journal of The Electrochemical Society* 155 (2008) B79-B91.
- [120] C.W.B. Bezerra, L. Zhang, K. Lee, H. Liu, A.L.B. Marques, E.P. Marques, H. Wang, J. Zhang, A review of Fe–N/C and Co–N/C catalysts for the oxygen reduction reaction, *Electrochimica Acta* 53 (2008) 4937-4951.
- [121] M. Ferrandon, A.J. Kropf, D.J. Myers, K. Artyushkova, U. Kramm, P. Bogdanoff, G. Wu, C.M. Johnston, P. Zelenay, Multitechnique Characterization of a Polyaniline–Iron–Carbon Oxygen Reduction Catalyst, *The Journal of Physical Chemistry C* 116 (2012) 16001-16013.
- [122] M. Lefèvre, J.P. Dodelet, P. Bertrand, Molecular Oxygen Reduction in PEM Fuel Cells: Evidence for the Simultaneous Presence of Two Active Sites in Fe-Based Catalysts, *The Journal of Physical Chemistry B* 106 (2002) 8705-8713.

- [123] N.P. Subramanian, X. Li, V. Nallathambi, S.P. Kumaraguru, H. Colon-Mercado, G. Wu, J.-W. Lee, B.N. Popov, Nitrogen-modified carbon-based catalysts for oxygen reduction reaction in polymer electrolyte membrane fuel cells, *Journal of Power Sources* 188 (2009) 38-44.
- [124] R. Liu, D. Wu, X. Feng, K. Müllen, Nitrogen-Doped Ordered Mesoporous Graphitic Arrays with High Electrocatalytic Activity for Oxygen Reduction, *Angewandte Chemie International Edition* 49 (2010) 2565-2569.
- [125] S.M. Lyth, Y. Nabae, N.M. Islam, S. Kuroki, M. Kakimoto, S. Miyata, Electrochemical Oxygen Reduction Activity of Carbon Nitride Supported on Carbon Black, *Journal of The Electrochemical Society* 158 (2011) B194-B201.
- [126] F. Jaouen, S. Marcotte, J.-P. Dodelet, G. Lindbergh, Oxygen Reduction Catalysts for Polymer Electrolyte Fuel Cells from the Pyrolysis of Iron Acetate Adsorbed on Various Carbon Supports, *The Journal of Physical Chemistry B* 107 (2003) 1376-1386.
- [127] J.-i. Ozaki, S.-i. Tanifuji, A. Furuichi, K. Yabutsuka, Enhancement of oxygen reduction activity of nanoshell carbons by introducing nitrogen atoms from metal phthalocyanines, *Electrochimica Acta* 55 (2010) 1864-1871.
- [128] F. Jaouen, F. Charretier, J.P. Dodelet, Fe-Based Catalysts for Oxygen Reduction in PEMFCs: Importance of the Disordered Phase of the Carbon Support, *Journal of The Electrochemical Society* 153 (2006) A689-A698.
- [129] M. Lefèvre, J.P. Dodelet, P. Bertrand, O₂ Reduction in PEM Fuel Cells: Activity and Active Site Structural Information for Catalysts Obtained by the Pyrolysis at High Temperature of Fe Precursors, *The Journal of Physical Chemistry B* 104 (2000) 11238-11247.
- [130] U.I. Kramm, J. Herranz, N. Larouche, T.M. Arruda, M. Lefevre, F. Jaouen, P. Bogdanoff, S. Fiechter, I. Abs-Wurmbach, S. Mukerjee, J.-P. Dodelet, Structure of the catalytic sites in Fe/N/C-catalysts for O₂-reduction in PEM fuel cells, *Physical Chemistry Chemical Physics* 14 (2012) 11673-11688.
- [131] P. Matter, U. Ozkan, Non-metal Catalysts for Dioxygen Reduction in an Acidic Electrolyte, *Catalysis Letters* 109 (2006) 115-123.
- [132] P.H. Matter, E. Wang, M. Arias, E.J. Biddinger, U.S. Ozkan, Oxygen Reduction Reaction Catalysts Prepared from Acetonitrile Pyrolysis over Alumina-Supported Metal Particles, *The Journal of Physical Chemistry B* 110 (2006) 18374-18384.
- [133] P.H. Matter, E. Wang, U.S. Ozkan, Preparation of nanostructured nitrogen-containing carbon catalysts for the oxygen reduction reaction from SiO₂- and MgO-supported metal particles, *Journal of Catalysis* 243 (2006) 395-403.
- [134] P.H. Matter, E. Wang, M. Arias, E.J. Biddinger, U.S. Ozkan, Oxygen reduction reaction activity and surface properties of nanostructured nitrogen-containing carbon, *Journal of Molecular Catalysis A: Chemical* 264 (2007) 73-81.
- [135] P.H. Matter, E. Wang, J.-M.M. Millet, U.S. Ozkan, Characterization of the Iron Phase in CN_x-Based Oxygen Reduction Reaction Catalysts, *The Journal of Physical Chemistry C* 111 (2007) 1444-1450.
- [136] E. Biddinger, D. von Deak, U. Ozkan, Nitrogen-Containing Carbon Nanostructures as Oxygen-Reduction Catalysts, *Topics in Catalysis* 52 (2009) 1566-1574.
- [137] D. Singh, I.I. Soykal, J. Tian, D. von Deak, J. King, J.T. Miller, U.S. Ozkan, In situ characterization of the growth of CN_x carbon nano-structures as oxygen reduction reaction catalysts, *Journal of Catalysis* 304 (2013) 100-111.
- [138] D. Singh, J. Tian, K. Mamtani, J. King, J.T. Miller, U.S. Ozkan, A comparison of N-containing carbon nanostructures (CN_x) and N-coordinated iron-carbon catalysts (FeNC) for the oxygen reduction reaction in acidic media, *Journal of Catalysis* 317 (2014) 30-43.
- [139] D. von Deak, D. Singh, E.J. Biddinger, J.C. King, B. Bayram, J.T. Miller, U.S. Ozkan, Investigation of sulfur poisoning of CN_x oxygen reduction catalysts for PEM fuel cells, *Journal of Catalysis* 285 (2012) 145-151.

- [140] D. Singh, K. Mamtani, C.R. Bruening, J.T. Miller, U.S. Ozkan, Use of H₂S to Probe the Active Sites in FeNC Catalysts for the Oxygen Reduction Reaction (ORR) in Acidic Media, *ACS Catalysis* 4 (2014) 3454-3462.
- [141] V. Nallathambi, X. Li, J.W. Lee, B.N. Popov, Development of nitrogen-modified carbon-based catalysts for oxygen reduction in PEM fuel cells, *ECS Transactions* 16 (2008) 405-417.
- [142] G. Liu, X. Li, P. Ganesan, B.N. Popov, Development of non-precious metal oxygen-reduction catalysts for PEM fuel cells based on N-doped ordered porous carbon, *Applied Catalysis B: Environmental* 93 (2009) 156-165.
- [143] G. Liu, X. Li, P. Ganesan, B.N. Popov, Studies of oxygen reduction reaction active sites and stability of nitrogen-modified carbon composite catalysts for PEM fuel cells, *Electrochimica Acta* 55 (2010) 2853-2858.
- [144] G. Liu, X. Li, J.-W. Lee, B.N. Popov, A review of the development of nitrogen-modified carbon-based catalysts for oxygen reduction at USC, *Catalysis Science & Technology* 1 (2011) 207-217.
- [145] S. Kattel, P. Atanassov, B. Kiefer, Stability, Electronic and Magnetic Properties of In-Plane Defects in Graphene: A First-Principles Study, *The Journal of Physical Chemistry C* 116 (2012) 8161-8166.
- [146] Y. Shang, J.-x. Zhao, H. Wu, Q.-h. Cai, X.-g. Wang, X.-z. Wang, Chemical functionalization of pyridine-like and porphyrin-like nitrogen-doped carbon (CN_x) nanotubes with transition metal (TM) atoms: a theoretical study, *Theoretical Chemistry Accounts* 127 (2010) 727-733.
- [147] A. Titov, P. Zapol, P. Král, D.-J. Liu, H. Iddir, K. Baishya, L.A. Curtiss, Catalytic Fe-xN Sites in Carbon Nanotubes, *The Journal of Physical Chemistry C* 113 (2009) 21629-21634.
- [148] S. Kattel, P. Atanassov, B. Kiefer, Density Functional Theory Study of Ni-N_x/C Electrocatalyst for Oxygen Reduction in Alkaline and Acidic Media, *The Journal of Physical Chemistry C* 116 (2012) 17378-17383.
- [149] S. Kattel, P. Atanassov, B. Kiefer, Catalytic activity of Co-N_x/C electrocatalysts for oxygen reduction reaction: a density functional theory study, *Physical Chemistry Chemical Physics* 15 (2013) 148-153.
- [150] S. Kattel, G. Wang, A density functional theory study of oxygen reduction reaction on Me-N₄ (Me = Fe, Co, or Ni) clusters between graphitic pores, *Journal of Materials Chemistry A* 1 (2013) 10790-10797.
- [151] C.E. Szakacs, M. Lefevre, U.I. Kramm, J.-P. Dodelet, F. Vidal, A density functional theory study of catalytic sites for oxygen reduction in Fe/N/C catalysts used in H₂/O₂ fuel cells, *Physical Chemistry Chemical Physics* 16 (2014) 13654-13661.
- [152] U.I. Kramm, Fuel Cells, Non-Precious Metal Catalysts for Oxygen Reduction Reaction, *Encyclopedia of Applied Electrochemistry* (2014) 909-918.
- [153] W. Zhu, D. Ku, J.P. Zheng, Z. Liang, B. Wang, C. Zhang, S. Walsh, G. Au, E.J. Plichta, Buckypaper-based catalytic electrodes for improving platinum utilization and PEMFC's performance, *Electrochimica Acta* 55 (2010) 2555-2560.
- [154] K.H. Kangasniemi, D.A. Condit, T.D. Jarvi, Characterization of Vulcan Electrochemically Oxidized under Simulated PEM Fuel Cell Conditions, *Journal of The Electrochemical Society* 151 (2004) E125-E132.
- [155] S.D. Knights, K.M. Colbow, J. St-Pierre, D.P. Wilkinson, Aging mechanisms and lifetime of PEFC and DMFC, *Journal of Power Sources* 127 (2004) 127-134.
- [156] Y. Shao, G. Yin, J. Zhang, Y. Gao, Comparative investigation of the resistance to electrochemical oxidation of carbon black and carbon nanotubes in aqueous sulfuric acid solution, *Electrochimica Acta* 51 (2006) 5853-5857.
- [157] X. Yu, S. Ye, Recent advances in activity and durability enhancement of Pt/C catalytic cathode in PEMFC: Part II: Degradation mechanism and durability enhancement of carbon supported platinum catalyst, *Journal of Power Sources* 172 (2007) 145-154.
- [158] S. Iijima, Helical microtubules of graphitic carbon, *Nature* 354 (1991) 56-58.

- [159] T. Yoshitake, Y. Shimakawa, S. Kuroshima, H. Kimura, T. Ichihashi, Y. Kubo, D. Kasuya, K. Takahashi, F. Kokai, M. Yudasaka, S. Iijima, Preparation of fine platinum catalyst supported on single-wall carbon nanohorns for fuel cell application, *Physica B: Condensed Matter* 323 (2002) 124-126.
- [160] J. Cao, C. Du, S.C. Wang, P. Mercier, X. Zhang, H. Yang, D.L. Akins, The production of a high loading of almost monodispersed Pt nanoparticles on single-walled carbon nanotubes for methanol oxidation, *Electrochemistry Communications* 9 (2007) 735-740.
- [161] J. Narayanamoorthy, S. Durairaj, Y. Song, Y. Xu, J. Choi, Tenfold catalytic activity enhancement of Pt/C by doping with single walled carbon nanotube for methanol oxidation, *Applied Physics Letters* 90 (2007) 063112-(1-3).
- [162] J. Wang, G. Yin, Y. Shao, Z. Wang, Y. Gao, Platinum Deposition on Multiwalled Carbon Nanotubes by Ion-Exchange Method as Electrocatalysts for Oxygen Reduction, *Journal of The Electrochemical Society* 154 (2007) B687-B693.
- [163] A. Kongkanand, S. Kuwabata, G. Girishkumar, P. Kamat, Single-Wall Carbon Nanotubes Supported Platinum Nanoparticles with Improved Electrocatalytic Activity for Oxygen Reduction Reaction, *Langmuir* 22 (2006) 2392-2396.
- [164] P.J. Britto, K.S.V. Santhanam, A. Rubio, J.A. Alonso, P.M. Ajayan, Improved Charge Transfer at Carbon Nanotube Electrodes, *Advanced Materials* 11 (1999) 154-157.
- [165] R.S. Oosthuizen, V.O. Nyamori, Carbon Nanotubes as Supports for Palladium and Bimetallic Catalysts for Use in Hydrogenation Reactions, *Platinum Metals Review* 55 (2011) 154-169.
- [166] X. Wang, W. Li, Z. Chen, M. Waje, Y. Yan, Durability investigation of carbon nanotube as catalyst support for proton exchange membrane fuel cell, *Journal of Power Sources* 158 (2006) 154-159.
- [167] Y. Shao, G. Yin, Y. Gao, P. Shi, Durability Study of Pt/C and Pt/CNTs Catalysts under Simulated PEM Fuel Cell Conditions, *Journal of The Electrochemical Society* 153 (2006) A1093-A1097.
- [168] L. Li, Y. Xing, Electrochemical Durability of Carbon Nanotubes in Noncatalyzed and Catalyzed Oxidations, *Journal of The Electrochemical Society* 153 (2006) A1823-A1828.
- [169] Y. Shao, G. Yin, Y. Gao, Understanding and approaches for the durability issues of Pt-based catalysts for PEM fuel cell, *Journal of Power Sources* 171 (2007) 558-566.
- [170] S.M. Andersen, M. Borghei, P. Lund, Y.-R. Elina, A. Pasanen, E. Kauppinen, V. Ruiz, P. Kauranen, E.M. Skou, Durability of carbon nanofiber (CNF) & carbon nanotube (CNT) as catalyst support for Proton Exchange Membrane Fuel Cells, *Solid State Ionics* 231 (2013) 94-101.
- [171] X. Sun, R. Li, D. Villers, J.P. Dodelet, S. Désilets, Composite electrodes made of Pt nanoparticles deposited on carbon nanotubes grown on fuel cell backings, *Chemical Physics Letters* 379 (2003) 99-104.
- [172] T. Zhou, H. Wang, J. Key, S. Ji, V. Linkov, R. Wang, Highly dispersed ultrafine Pt nanoparticles on hydrophilic N-doped carbon tubes for improved methanol oxidation, *RSC Advances* 3 (2013) 16949-16953.
- [173] T.W. Ebbesen, H. Hiura, M.E. Bisher, M.M.J. Treacy, J.L. Shreeve-Keyer, R.C. Haushalter, Decoration of carbon nanotubes, *Advanced Materials* 8 (1996) 155-157.
- [174] Z. Liu, X. Lin, J.Y. Lee, W. Zhang, M. Han, L.M. Gan, Preparation and Characterization of Platinum-Based Electrocatalysts on Multiwalled Carbon Nanotubes for Proton Exchange Membrane Fuel Cells, *Langmuir* 18 (2002) 4054-4060.
- [175] Y. Xing, Synthesis and Electrochemical Characterization of Uniformly-Dispersed High Loading Pt Nanoparticles on Sonochemically-Treated Carbon Nanotubes, *The Journal of Physical Chemistry B* 108 (2004) 19255-19259.
- [176] J. Prabhuram, T.S. Zhao, Z.K. Tang, R. Chen, Z.X. Liang, Multiwalled Carbon Nanotube Supported PtRu for the Anode of Direct Methanol Fuel Cells, *The Journal of Physical Chemistry B* 110 (2006) 5245-5252.
- [177] Z.D. Wei, C. Yan, Y. Tan, L. Li, C.X. Sun, Z.G. Shao, P.K. Shen, H.W. Dong, Spontaneous Reduction of Pt(IV) onto the Sidewalls of Functionalized Multiwalled Carbon Nanotubes as Catalysts for Oxygen Reduction Reaction in PEMFCs, *The Journal of Physical Chemistry C* 112 (2008) 2671-2677.

- [178] P. Hernández-Fernández, M. Montiel, P. Ocón, J.L.G. de la Fuente, S. García-Rodríguez, S. Rojas, J.L.G. Fierro, Functionalization of multi-walled carbon nanotubes and application as supports for electrocatalysts in proton-exchange membrane fuel cell, *Applied Catalysis B: Environmental* 99 (2010) 343-352.
- [179] N. Rajalakshmi, H. Ryu, M.M. Shaijumon, S. Ramaprabhu, Performance of polymer electrolyte membrane fuel cells with carbon nanotubes as oxygen reduction catalyst support material, *Journal of Power Sources* 140 (2005) 250-257.
- [180] S. Dong Jin, P. Tae-Jin, I. Son-Ki, Effect of surface oxygen groups of carbon supports on the characteristics of Pd/C catalysts, *Carbon* 31 (1993) 427-435.
- [181] J. Zhang, H. Zou, Q. Qing, Y. Yang, Q. Li, Z. Liu, X. Guo, Z. Du, Effect of Chemical Oxidation on the Structure of Single-Walled Carbon Nanotubes, *The Journal of Physical Chemistry B* 107 (2003) 3712-3718.
- [182] D.-J. Guo, H.-L. Li, High dispersion and electrocatalytic properties of Pt nanoparticles on SWNT bundles, *Journal of Electroanalytical Chemistry* 573 (2004) 197-202.
- [183] S. Wang, S.P. Jiang, X. Wang, Polyelectrolyte functionalized carbon nanotubes as a support for noble metal electrocatalysts and their activity for methanol oxidation, *Nanotechnology* 19 (2008) 265601.
- [184] J. Zhongqing, Z.-J. Jiang, Carbon Nanotubes Supported Metal Nanoparticles for the Applications in Proton Exchange Membrane Fuel Cells (PEMFCs), *Carbon Nanotubes—Growth and Applications*, M. Naraghi, Editor, (2011). Available from:
<http://www.intechopen.com/books/carbon-nanotubes-growth-and-applications/carbon-nanotubes-supported-metal-nanoparticles-for-the-applications-in-proton-exchange-membrane-fuel>
- [185] T. Matsumoto, T. Komatsu, K. Arai, T. Yamazaki, M. Kijima, H. Shimizu, Y. Takasawa, J. Nakamura, Reduction of Pt usage in fuel cell electrocatalysts with carbon nanotube electrodes, *Chemical Communications* (2004) 840-841.
- [186] H. Liu, J. Zhang, *Electrocatalysis of Direct Methanol Fuel Cells*, WILEY-VCH Verlag GmbH & Co. KGaA, Weinheim, Germany (2009).
- [187] P.-L. Kuo, C.-C. Chen, M.-W. Jao, Effects of Polymer Micelles of Alkylated Polyethylenimines on Generation of Gold Nanoparticles, *The Journal of Physical Chemistry B* 109 (2005) 9445-9450.
- [188] X. Li, S. Ge, C. Hui, I.-M. Hsing, Well-dispersed multiwalled carbon nanotubes supported platinum nanocatalysts for oxygen reduction, *Electrochemical and Solid-State Letters* 7 (2004) A286-A289.
- [189] X. Li, I.M. Hsing, The effect of the Pt deposition method and the support on Pt dispersion on carbon nanotubes, *Electrochimica Acta* 51 (2006) 5250-5258.
- [190]] M.A. Islam, M.A. Bhuiya, M.S. Islam, A Review on Chemical Synthesis Process of Platinum Nanoparticles, *Asia Pacific Journal of Energy and Environment* 1 (2014) 107-120.
- [191] F. Fievet, J.P. Lagier, B. Blin, B. Beaudoin, M. Figlarz, Homogeneous and heterogeneous nucleations in the polyol process for the preparation of micron and submicron size metal particles, *Solid State Ionics* 32–33, Part 1 (1989) 198-205.
- [192] W. Chen, J. Zhao, J.Y. Lee, Z. Liu, Microwave heated polyol synthesis of carbon nanotubes supported Pt nanoparticles for methanol electrooxidation, *Materials Chemistry and Physics* 91 (2005) 124-129.
- [193] Z. Liu, L.M. Gan, L. Hong, W. Chen, J.Y. Lee, Carbon-supported Pt nanoparticles as catalysts for proton exchange membrane fuel cells, *Journal of Power Sources* 139 (2005) 73-78.
- [194] W. Zhang, J. Chen, G.F. Swiegers, Z.-F. Ma, G.G. Wallace, Microwave-assisted synthesis of Pt/CNT nanocomposite electrocatalysts for PEM fuel cells, *Nanoscale* 2 (2010) 282-286.
- [195] J. Wang, G. Yin, Y. Shao, Z. Wang, Y. Gao, Platinum Deposition on Multiwalled Carbon Nanotubes by Ion-Exchange Method as Electrocatalysts for Oxygen Reduction, *Journal of The Electrochemical Society* 154 (2007) B687-B693.
- [196] Y. Shao, G. Yin, J. Wang, Y. Gao, P. Shi, Multi-walled carbon nanotubes based Pt electrodes prepared with in situ ion exchange method for oxygen reduction, *Journal of Power Sources* 161 (2006) 47-53.

- [197] R. Sharma, K.K. Kar, Particle size and crystallographic orientation controlled electrodeposition of platinum nanoparticles on carbon nanotubes, *Electrochimica Acta* 156 (2015) 199-206.
- [198] Z. Yue, F. Louzhen, Z. Haizheng, L. Yongfang, Electrodeposition and electrocatalytic properties of platinum nanoparticles on multi-walled carbon nanotubes: effect of the deposition conditions, *Microchimica Acta* 158 (2007) 327-334.
- [199] K. Gong, F. Du, Z. Xia, M. Durstock, L. Dai, Nitrogen-Doped Carbon Nanotube Arrays with High Electrocatalytic Activity for Oxygen Reduction, *Science* 323 (2009) 760-764.
- [200] Y. Chen, J. Wang, H. Liu, R. Li, X. Sun, S. Ye, S. Knights, Enhanced stability of Pt electrocatalysts by nitrogen doping in CNTs for PEM fuel cells, *Electrochemistry Communications* 11 (2009) 2071-2076.
- [201] M.S. Saha, R. Li, X. Sun, S. Ye, 3-D composite electrodes for high performance PEM fuel cells composed of Pt supported on nitrogen-doped carbon nanotubes grown on carbon paper, *Electrochemistry Communications* 11 (2009) 438-441.
- [202] Y. Chen, J. Wang, H. Liu, M.N. Banis, R. Li, X. Sun, T.-K. Sham, S. Ye, S. Knights, Nitrogen Doping Effects on Carbon Nanotubes and the Origin of the Enhanced Electrocatalytic Activity of Supported Pt for Proton-Exchange Membrane Fuel Cells, *The Journal of Physical Chemistry C* 115 (2011) 3769-3776.
- [203] A.L. Mohana Reddy, N. Rajalakshmi, S. Ramaprabhu, Cobalt-polypyrrole-multiwalled carbon nanotube catalysts for hydrogen and alcohol fuel cells, *Carbon* 46 (2008) 2-11.
- [204] S.H. Lim, Z. Li, C.K. Poh, L. Lai, J. Lin, Highly active non-precious metal catalyst based on poly(vinylpyrrolidone)-wrapped carbon nanotubes complexed with iron-cobalt metal ions for oxygen reduction reaction, *Journal of Power Sources* 214 (2012) 15-20.
- [205] G. Wu, K.L. More, P. Xu, H.-L. Wang, M. Ferrandon, A.J. Kropf, D.J. Myers, S. Ma, C.M. Johnston, P. Zelenay, A carbon-nanotube-supported graphene-rich non-precious metal oxygen reduction catalyst with enhanced performance durability, *Chemical Communications* 49 (2013) 3291-3293.
- [206] S. Sharma, B.G. Pollet, Support materials for PEMFC and DMFC electrocatalysts—A review, *Journal of Power Sources* 208 (2012) 96-119.
- [207] J. Lee, J. Kim, T. Hyeon, Recent Progress in the Synthesis of Porous Carbon Materials, *Advanced Materials* 18 (2006) 2073-2094.
- [208] S. Song, Y. Liang, Z. Li, Y. Wang, R. Fu, D. Wu, P. Tsiakaras, Effect of pore morphology of mesoporous carbons on the electrocatalytic activity of Pt nanoparticles for fuel cell reactions, *Applied Catalysis B: Environmental* 98 (2010) 132-137.
- [209] S.H. Joo, C. Pak, D.J. You, S.-A. Lee, H.I. Lee, J.M. Kim, H. Chang, D. Seung, Ordered mesoporous carbons (OMC) as supports of electrocatalysts for direct methanol fuel cells (DMFC): Effect of carbon precursors of OMC on DMFC performances, *Electrochimica Acta* 52 (2006) 1618-1626.
- [210] A.B. Fuertes, S. Alvarez, Graphitic mesoporous carbons synthesised through mesostructured silica templates, *Carbon* 42 (2004) 3049-3055.
- [211] L. Calvillo, M. Gangeri, S. Perathoner, G. Centi, R. Moliner, M.J. Lázaro, Synthesis and performance of platinum supported on ordered mesoporous carbons as catalyst for PEM fuel cells: Effect of the surface chemistry of the support, *International Journal of Hydrogen Energy* 36 (2011) 9805-9814.
- [212] A. Hayashi, H. Notsu, K.i. Kimijima, J. Miyamoto, I. Yagi, Preparation of Pt/mesoporous carbon (MC) electrode catalyst and its reactivity toward oxygen reduction, *Electrochimica Acta* 53 (2008) 6117-6125.
- [213] M. Momčilović, M. Stojmenović, N. Gavrilov, I. Pašti, S. Mentus, B. Babić, Complex electrochemical investigation of ordered mesoporous carbon synthesized by soft-templating method: charge storage and electrocatalytic or Pt-electrocatalyst supporting behavior, *Electrochimica Acta* 125 (2014) 606-614.
- [214] Y. Zhou, K. Neyerlin, T.S. Olson, S. Pylypenko, J. Bult, H.N. Dinh, T. Gennett, Z. Shao, R. O'Hayre, Enhancement of Pt and Pt-alloy fuel cell catalyst activity and durability via nitrogen-modified carbon supports, *Energy & Environmental Science* 3 (2010) 1437-1446.

- [215] Z. Lei, L. An, L. Dang, M. Zhao, J. Shi, S. Bai, Y. Cao, Highly dispersed platinum supported on nitrogen-containing ordered mesoporous carbon for methanol electrochemical oxidation, *Microporous and Mesoporous Materials* 119 (2009) 30-38.
- [216] S.-H. Liu, M.-T. Wu, Y.-H. Lai, C.-C. Chiang, N. Yu, S.-B. Liu, Fabrication and electrocatalytic performance of highly stable and active platinum nanoparticles supported on nitrogen-doped ordered mesoporous carbons for oxygen reduction reaction, *Journal of Materials Chemistry* 21 (2011) 12489-12496.
- [217] J.K. Dombrowskis, H.Y. Jeong, K. Fossum, O. Terasaki, A.E.C. Palmqvist, Transition Metal Ion-Chelating Ordered Mesoporous Carbons as Noble Metal-Free Fuel Cell Catalysts, *Chemistry of Materials* 25 (2013) 856-861.
- [218] J.Y. Cheon, T. Kim, Y. Choi, H.Y. Jeong, M.G. Kim, Y.J. Sa, J. Kim, Z. Lee, T.-H. Yang, K. Kwon, O. Terasaki, G.-G. Park, R.R. Adzic, S.H. Joo, Ordered mesoporous porphyrinic carbons with very high electrocatalytic activity for the oxygen reduction reaction, *Sci. Rep.* 3 (2013).
- [219] S. Stankovich, D.A. Dikin, G.H.B. Dommett, K.M. Kohlhaas, E.J. Zimney, E.A. Stach, R.D. Piner, S.T. Nguyen, R.S. Ruoff, Graphene-based composite materials, *Nature* 442 (2006) 282-286.
- [220] Y. Zhu, S. Murali, M.D. Stoller, K.J. Ganesh, W. Cai, P.J. Ferreira, A. Pirkle, R.M. Wallace, K.A. Cychoz, M. Thommes, D. Su, E.A. Stach, R.S. Ruoff, Carbon-Based Supercapacitors Produced by Activation of Graphene, *Science* 332 (2011) 1537-1541.
- [221] A.A. Balandin, S. Ghosh, W. Bao, I. Calizo, D. Teweldebrhan, F. Miao, C.N. Lau, Superior Thermal Conductivity of Single-Layer Graphene, *Nano Letters* 8 (2008) 902-907.
- [222] M. Orlita, C. Faugeras, P. Plochocka, P. Neugebauer, G. Martinez, D.K. Maude, A.L. Barra, M. Sprinkle, C. Berger, W.A. de Heer, M. Potemski, Approaching the Dirac Point in High-Mobility Multilayer Epitaxial Graphene, *Physical Review Letters* 101 (2008) 267601.
- [223] L. Qu, Y. Liu, J.-B. Baek, L. Dai, Nitrogen-Doped Graphene as Efficient Metal-Free Electrocatalyst for Oxygen Reduction in Fuel Cells, *ACS Nano* 4 (2010) 1321-1326.
- [224] K. Parvez, S. Yang, Y. Hernandez, A. Winter, A. Turchanin, X. Feng, K. Müllen, Nitrogen-Doped Graphene and Its Iron-Based Composite As Efficient Electrocatalysts for Oxygen Reduction Reaction, *ACS Nano* 6 (2012) 9541-9550.
- [225] H. Wang, T. Maiyalagan, X. Wang, Review on Recent Progress in Nitrogen-Doped Graphene: Synthesis, Characterization, and Its Potential Applications, *ACS Catalysis* 2 (2012) 781-794.
- [226] K.S. Subrahmanyam, L.S. Panchakarla, A. Govindaraj, C.N.R. Rao, Simple Method of Preparing Graphene Flakes by an Arc-Discharge Method, *The Journal of Physical Chemistry C* 113 (2009) 4257-4259.
- [227] L.S. Panchakarla, K.S. Subrahmanyam, S.K. Saha, A. Govindaraj, H.R. Krishnamurthy, U.V. Waghmare, C.N.R. Rao, Synthesis, Structure, and Properties of Boron- and Nitrogen-Doped Graphene, *Advanced Materials* 21 (2009) 4726-4730.
- [228] D. Wei, Y. Liu, Y. Wang, H. Zhang, L. Huang, G. Yu, Synthesis of N-Doped Graphene by Chemical Vapor Deposition and Its Electrical Properties, *Nano Letters* 9 (2009) 1752-1758.
- [229] A. Reina, X. Jia, J. Ho, D. Nezich, H. Son, V. Bulovic, M.S. Dresselhaus, J. Kong, Large Area, Few-Layer Graphene Films on Arbitrary Substrates by Chemical Vapor Deposition, *Nano Letters* 9 (2009) 30-35.
- [230] L.M. Viculis, J.J. Mack, O.M. Mayer, H.T. Hahn, R.B. Kaner, Intercalation and exfoliation routes to graphite nanoplatelets, *Journal of Materials Chemistry* 15 (2005) 974-978.
- [231] Y. Si, E.T. Samulski, Exfoliated Graphene Separated by Platinum Nanoparticles, *Chemistry of Materials* 20 (2008) 6792-6797.
- [232] X. Cao, Y. Shi, W. Shi, G. Lu, X. Huang, Q. Yan, Q. Zhang, H. Zhang, Preparation of Novel 3D Graphene Networks for Supercapacitor Applications, *Small* 7 (2011) 3163-3168.
- [233] X. Cao, Z. Zeng, W. Shi, P. Yep, Q. Yan, H. Zhang, Three-Dimensional Graphene Network Composites for Detection of Hydrogen Peroxide, *Small* 9 (2013) 1703-1707.

- [234] B. Seger, P.V. Kamat, Electrocatalytically Active Graphene-Platinum Nanocomposites. Role of 2-D Carbon Support in PEM Fuel Cells, *The Journal of Physical Chemistry C* 113 (2009) 7990-7995.
- [235] H.-W. Ha, I.Y. Kim, S.-J. Hwang, R.S. Ruoff, One-Pot Synthesis of Platinum Nanoparticles Embedded on Reduced Graphene Oxide for Oxygen Reduction in Methanol Fuel Cells, *Electrochemical and Solid-State Letters* 14 (2011) B70-B73.
- [236] J.-D. Qiu, G.-C. Wang, R.-P. Liang, X.-H. Xia, H.-W. Yu, Controllable Deposition of Platinum Nanoparticles on Graphene As an Electrocatalyst for Direct Methanol Fuel Cells, *The Journal of Physical Chemistry C* 115 (2011) 15639-15645.
- [237] S. Guo, D. Wen, Y. Zhai, S. Dong, E. Wang, Platinum Nanoparticle Ensemble-on-Graphene Hybrid Nanosheet: One-Pot, Rapid Synthesis, and Used as New Electrode Material for Electrochemical Sensing, *ACS Nano* 4 (2010) 3959-3968.
- [238] M.S. Ahmed, D. Kim, H.S. Han, H. Jeong, S. Jeon, Covalent Hybridization of Thiolated Graphene Sheet and Platinum Nanoparticles for Electrocatalytic Oxygen Reduction Reaction, *Journal of Nanoscience and Nanotechnology* 12 (2012) 8349-8355.
- [239] S. Mayavan, H.-S. Jang, M.-J. Lee, S.H. Choi, S.-M. Choi, Enhancing the catalytic activity of Pt nanoparticles using poly sodium styrene sulfonate stabilized graphene supports for methanol oxidation, *Journal of Materials Chemistry A* 1 (2013) 3489-3494.
- [240] K.-W. Nam, J. Song, K.-H. Oh, M.-J. Choo, H. Park, J.-K. Park, J. Choi, Perfluorosulfonic acid-functionalized Pt/graphene as a high-performance oxygen reduction reaction catalyst for proton exchange membrane fuel cells, *Journal of Solid State Electrochemistry* 17 (2013) 767-774.
- [241] D.-Q. Yang, J.-F. Rochette, E. Sacher, Spectroscopic Evidence for π - π Interaction between Poly(diallyl dimethylammonium) Chloride and Multiwalled Carbon Nanotubes, *The Journal of Physical Chemistry B* 109 (2005) 4481-4484.
- [242] S. Guo, S. Sun, FePt Nanoparticles Assembled on Graphene as Enhanced Catalyst for Oxygen Reduction Reaction, *Journal of the American Chemical Society* 134 (2012) 2492-2495.
- [243] D. Xu, Y. Tian, J. Zhao, X. Wang, High stability and reactivity of defective graphene-supported Fe_nPt_{13-n} (n = 1, 2, and 3) nanoparticles for oxygen reduction reaction: a theoretical study, *Journal of Nanoparticle Research* 17 (2015) 1-12.
- [244] K. Kamiya, K. Hashimoto, S. Nakanishi, Instantaneous one-pot synthesis of Fe-N-modified graphene as an efficient electrocatalyst for the oxygen reduction reaction in acidic solutions, *Chemical Communications* 48 (2012) 10213-10215.
- [245] C.-W. Tsai, M.-H. Tu, C.-J. Chen, T.-F. Hung, R.-S. Liu, W.-R. Liu, M.-Y. Lo, Y.-M. Peng, L. Zhang, J. Zhang, D.-S. Shy, X.-K. Xing, Nitrogen-doped graphene nanosheet-supported non-precious iron nitride nanoparticles as an efficient electrocatalyst for oxygen reduction, *RSC Advances* 1 (2011) 1349-1357.
- [246] C. He, J.J. Zhang, P.K. Shen, Nitrogen-self-doped graphene-based non-precious metal catalyst with superior performance to Pt/C catalyst toward oxygen reduction reaction, *Journal of Materials Chemistry A* 2 (2014) 3231-3236.
- [247] C. He, Z. Li, M. Cai, M. Cai, J.-Q. Wang, Z. Tian, X. Zhang, P.K. Shen, A strategy for mass production of self-assembled nitrogen-doped graphene as catalytic materials, *Journal of Materials Chemistry A* 1 (2013) 1401-1406.

Chapter 3 Metal Organic Frameworks

3.1 Introduction

Metal-organic frameworks (MOFs) as the name suggests, are frameworks comprised of metal ions or metal ion clusters linked together by bifunctional organic ligands via metal-ligand interactions. They possess highly crystalline, porous structures of varying dimensionality. The intrinsic lability of the metal-ligand interactions along with their reversibility results in such highly crystalline structures being prepared under mild conditions. In addition, these strong metal-ligand interactions enable the formation of permanent pores throughout their structure. The porosity of MOF materials will be discussed in more details later in this chapter. Moreover, MOF materials provide the possibility to somewhat predict the geometry of their coordination by judicious choice of metal center and bridging organic ligand that can further tune the size, the shape and the functionality of the pores. Early works in the field of MOF materials mainly focused on developing strategies for the successful design and synthesis of 2D and 3D framework structures. Two major approaches were considered, namely, a node-and-spacer approach, outlined by Robson [1], and the building block approach popularized by Yaghi and co-workers [2].

3.1.1 Node and Spacer Approach

This approach was originally described by Wells [3] for the characterization of inorganic compounds in terms of their topology. “Node and spacer” approach was exploited in the field of MOF materials by considering single metal ions with fixed coordination geometry, as node, and organic ligands as spacer. The metal ion nodes were linked to organic spacers via a typical coordination bond where the rigid bridging ligands also offer fixed shapes and linkage geometries [1]. According to this approach, the preference of single metal center node for a specific geometry along with its coordination environment affects the resulting MOF structure. For instance, using a linear bifunctional 4,4'-bipyridine spacer, the Ni²⁺ [4] metal ion with octahedral coordination mode resulted in 2D (4,4) square grid MOF, [Ni(4,4'-bipyridine)₂(NO₃)₂]_n (Figure 3.1a), while in the case of Cu²⁺ [5] with tetrahedral coordination mode a 3D diamondoid [Cu(4,4'-bipy)₂](PF₆) MOF structure was attained (Figure 3.1b).

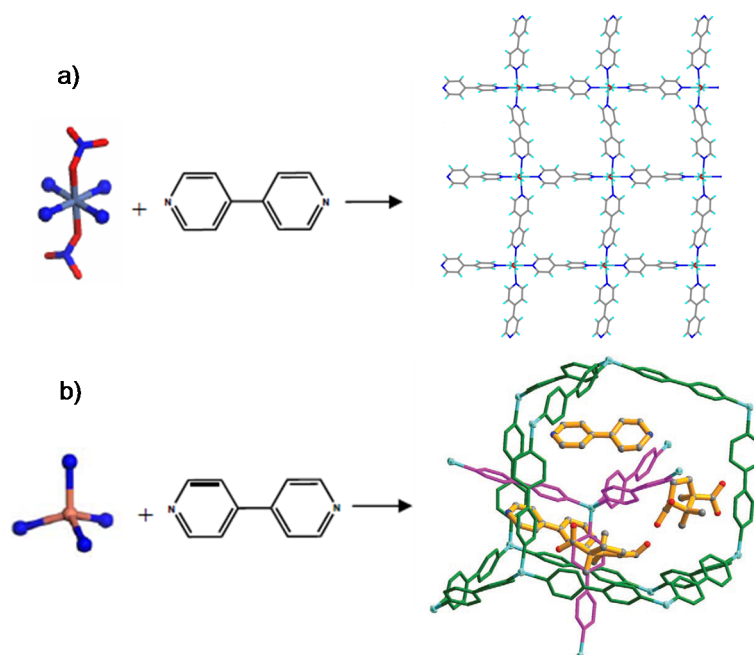


Figure 3.1 Formation of square grid (4,4) network by square planar metal nodes and 4,4'-bipyridine [4]
(b) Formation of diamondoid network by tetrahedral nodes and 4,4'-bipyridine [5]

Although this approach could enable controllable design and synthesis of MOF materials at least to a certain extent, under practical (solvothermal) synthesis conditions, control over various probable metal ion coordination geometries and coordination linkages is not always possible [6]. Moreover, solvent molecules present during MOF synthesis process were found to affect MOF structure through contributing towards their crystal growth, structural assemblies and dynamic transformations [7]. Reticular synthesis, a conceptual approach based on the use of secondary building units (SBUs) is therefore developed to address the limitations of this approach.

3.1.2 Building Block Approach

This method uses common structural motifs called SBUs as nodes for construction of ordered networks via employing polytopic linkers [8]. SBUs, a concept used in zeolites to describe the subunits, are molecular complexes and cluster entities in which metal coordination environment and ligand coordination mode could be used to expand these fragments into ordered structures. The geometry of a SBU is defined by those atoms representing points of extension to other SBUs [8]. Rigid SBUs with a variety of geometries have been identified and used in MOFs. Examples of three commonly occurring SBUs, including metal

carboxylate paddle wheel ($M_2(OOC^-)_4$) [9,10], octahedral zinc-carboxylate, ($Zn_4O(OOC^-)_6$) [11,12] and oxo-centered trinuclear iron clusters ($Fe_3O(COO^-)_6$) [13,14] are illustrated in Figure 3.2.

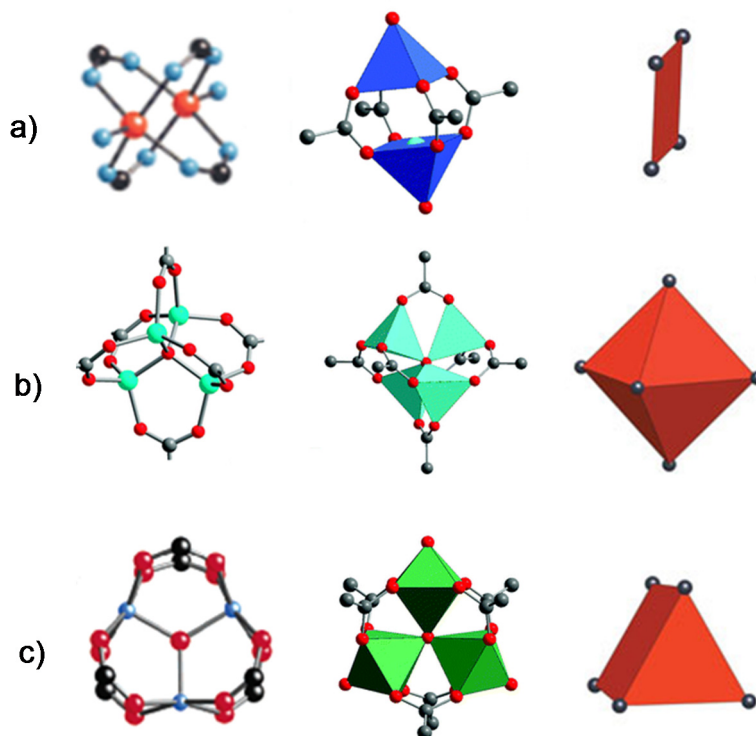


Figure 3.2 Three common MOF SBUs (a) Metal carboxylate paddle-wheel $M_2(OOC^-)_4$ ($M= Cu^{2+}, Zn^{2+}, Ni^{2+}, Fe^{2+}$ and Co^{2+}) [9,10]; (b) Octahedral zinc carboxylate $Zn_4O(OOC^-)_6$ [11,12]; (c) Trigonal prismatic building units $Fe_3O(COO^-)_6$ [13,14].

The inorganic SBUs are generally not introduced directly, but formed in situ under specific reaction conditions and their linkage to predesigned ligands with fixed linking geometries leads to the formation of MOF structures with a targeted topology [8].

Using SBUs concept, Yaghi and coworkers [11,15] have developed a family of microporous MOF materials based on the zinc acetate ($Zn_4O(CO_2)_6$) SBU. These MOFs possess a simple cubic framework, in which the vertices of the cube are composed of octahedral $Zn_4O(CO_2)_6$ SBUs, each linked by an aromatic or polyaromatic spacer (Figure 3.3). The first and most well known member of this family is MOF-5, where the spacer is benzene [15]. By simply altering the aromatic spacer a series of so-called isorecticular frameworks (IRMOFs) were created, where both the size and surface functionality of the pores could be controlled [11,16,17] (Figure 3.3).

The SBUs approach proposed by Yaghi and colleagues can be considered as an evolutionary version of the “node and spacer” approach where single metal ions were replaced by SBUs. Implementation of this approach, at least in concept, provides the possibility to design and synthesize MOF materials with predetermined structural topologies and pore properties [18]. Therefore, SBUs introduced several important features such as predictability and designability along with larger porosity into the field of MOF materials.

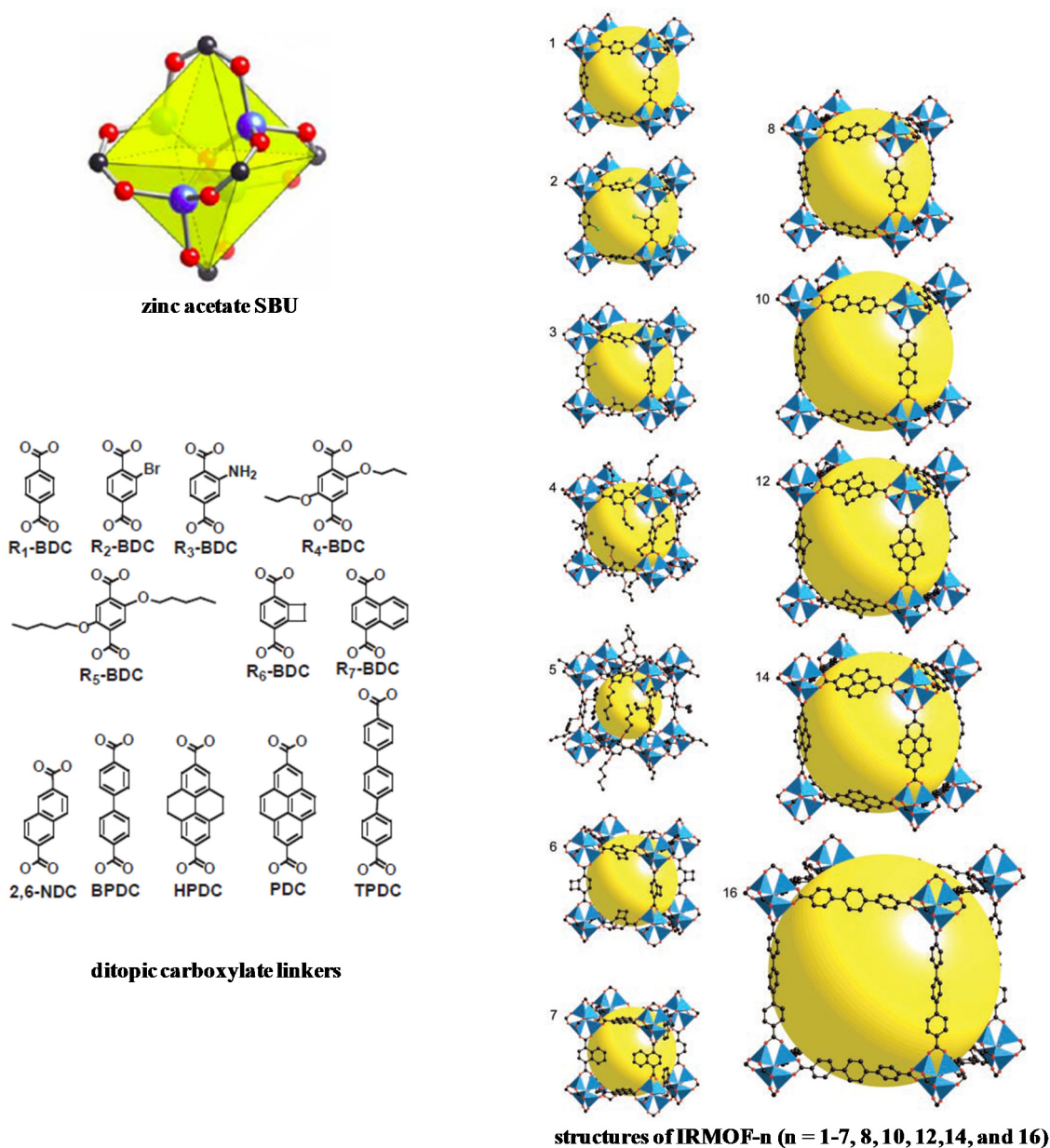


Figure 3.3 Structure of the zinc acetate SBU and its use in the construction of representative IRMOFs [11].

3.2 Porosity

As mentioned before, MOFs structure comprises long organic linkers that can introduce some void space throughout the structure and hence render them the potential to become permanently porous. Compared with two conventional porous materials namely zeolite and active carbon-based materials, MOFs possess higher porosity and surface area along with pore regularity and designability. The porosity in these structures could be achieved through removing solvent molecules, guest ligands or counter anions occupying the pores. Kitagawa et al. [19] classified MOF materials into three categories: 1st, 2nd, and 3rd generation. In the 1st generation MOFs, the pores could not be retained after guest molecules removal due to the framework collapse. The 2nd generation MOFs preserve their framework structure upon solvent exchange and evacuation and hence possess permanent porosity. The 3rd generation MOFs exhibit flexible and dynamic framework structure, which respond to external stimuli, such as light and guest molecules. Furthermore, framework topology of MOF materials can limit their porosity as some longer ligands were found to produce dense crystals via the interpenetration of networks instead of constructing large pores. Interpenetration in MOFs may be described as the periodic entanglement of two or more independent, unconnected frameworks [20]. Interpenetration of MOF structures can fill the large voids created by the longer linkers.

A unique set of characteristics, such as high surface area, various pore sizes and geometry, and diverse surface composition and properties leads to extensive investigations toward the potential industrial use of MOFs. Gas storage and gas separation are widely investigated in MOFs [21-23]. Moreover, MOFs have been introduced as ideal candidates for a better control of drug delivery [24,25]. Some other applications include sensor field [26] or magnetism [27]. Furthermore, MOFs have been applied as highly active and/or selective catalysts in a large number of reactions [28-30]. In the coming sections of this chapter application of MOFs as electrocatalyst for ORR will be discussed in more details.

3.3 Electrocatalyst derived from non-pyrolyzed MOFs (preserved MOF structure)

Mao et al. [31] were first to report on utilization of a MOF material as electrocatalyst for ORR. They synthesized a mixed-ligand copper based MOF (Cu-bipy-btc) structure in which 2,2'-bipyridine (bipy) was used as a secondary ligand along with main ligand, benzene-1,3,5-tricarboxylatebipy (btc), to stabilize the MOF structure in aqueous medium. As can be seen from Figure 3.4a, in Cu-bipy-btc, each Cu atom is coordinated with two carboxyl groups from two different btc ligands, one O atom from water, and two chelated N atoms from bipy. In a phosphate buffer (pH 6.0) the Cu-bipy-btc demonstrated electrocatalytic activity with one pair of well-defined redox wave at a potential of ca. -0.15 V vs. Ag/AgCl (Figure 3.4b, dotted curve), assigned to the redox process of $\text{Cu}^{2+}/\text{Cu}^{+}$ in the MOF structure. Moreover, introducing O_2 into the buffer solution revealed a clear increase in the reduction peak current along with diminution in the reversed oxidation peak current (Figure 3.4b, solid curve). As can be observed from Figure 3.4c, Cu-bipy-btc MOF revealed a large positive shift of ca. 0.40 V vs. Ag/AgCl for the ORR compared to bare glassy carbon electrode. The number of electrons involved in the Cu-bipy-btc-catalyzed ORR was evaluated using rotating ring-disk electrode (RRDE) voltammetry. The calculated value of 3.8 obtained for this electrocatalyst was indeed very close to the theoretical value of 4, which demonstrated the effectiveness of Cu-bipy-btc electrocatalyst for ORR.

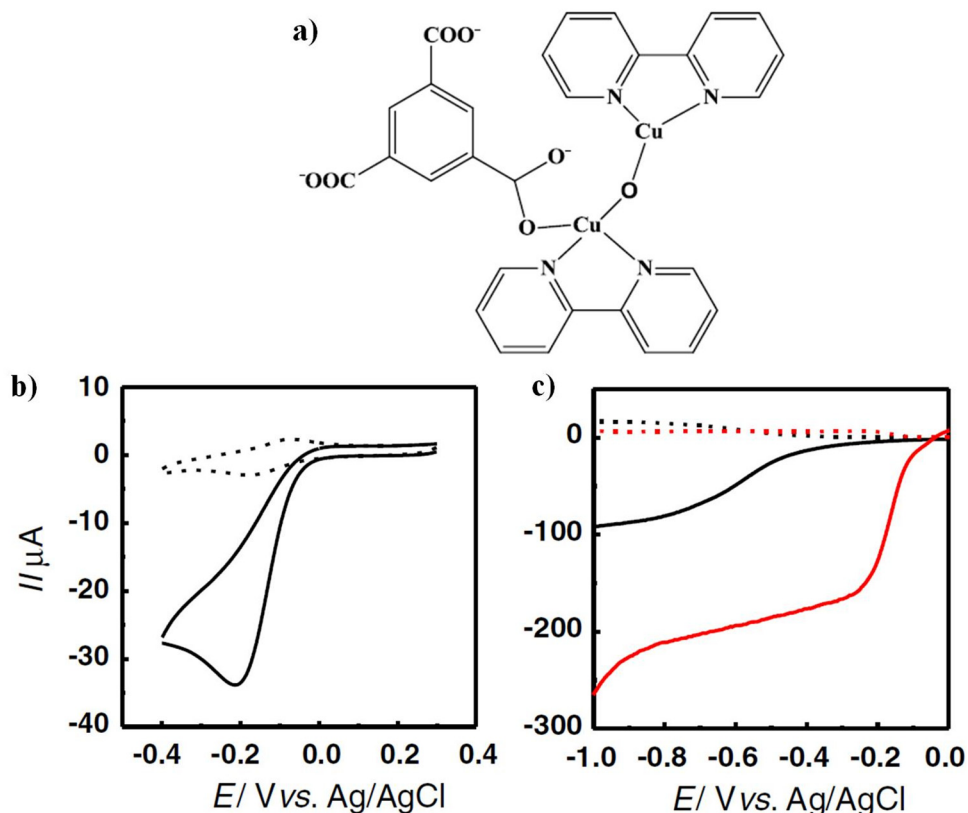


Figure 3.4 (a) Coordination geometry of Cu atoms in Cu-bipy-btc, (b) Typical CVs obtained at the Cu-bipy-btc modified GC electrodes in 0.1 M phosphate buffer (pH 6) saturated with N₂ (dotted curve) or O₂ (solid curve). Scan rate, 20 mV s⁻¹, (c) Typical RRDE voltammograms obtained with bare (black curves) and Cu-bipy-btc-modified (red curves) GC electrodes as disk electrodes (solid curves) and platinum ring electrode (dotted curves) in 0.1 M phosphate buffer (pH 6) under air-saturated O₂. Electrode rotation rate: 400 rpm, Scan rate: 10 mV s⁻¹ [31].

Using a similar approach, Jiang et al. [32] employed a highly porous copper containing MOF with nanocage structure as a non-PGM electrocatalyst for ORR. As can be seen in Figure 3.5a, the di-copper paddle-wheel SBUs are connected via methyl functionalized dicarboxylate ligands and forms a network of closely arranged nanoscale polyhedron cages. These nanocages possess large enough windows ($d \sim 0.6$ nm) to let the gas molecules pass through. Their previous investigations demonstrated that activation of the as-synthesized MOF via solvent-exchange method followed by an evacuation step could remove the solvent molecules from these nanocages and render this MOF a high gas storage capacity. The high O₂ adsorption capacity along with contiguity of O₂ molecules with open metal sites that could facilitate the ORR raised their interest to investigate the electrochemical properties of this MOF structure. In a phosphate buffer (pH 6.0) solution, both the as-synthesized and activated MOF samples (NPC-4) displayed electrochemical activity with a pair of redox waves,

ascribed to $\text{Cu}^{2+}/\text{Cu}^+$ (Figure 3.5b). However, in the presence of O_2 in the buffer solution, only the activated MOF samples revealed electrocatalytic activity toward ORR (Figure 3.5c). In comparison with Cu-bipy-btc, the NPC-4 catalyst demonstrated a positive shift of ca. 0.1 V vs. Ag/AgCl in the occurrence potential of ORR. In spite of providing ORR activity, detachment of the activated NPC-4 from the electrode surface led to a low-effective electron-transfer pathway during electrochemical scanning in aqueous solution and hence limited its application. Therefore, reduced graphene oxide (RGO) was immobilized onto a glassy carbon electrode surface as a binder and electron transfer mediator under MOF active layer. The RGO was believed to provide more contact points for MOF to adhere to the electrode due to presence of dense exposed edges in RGO along with large specific surface area. In addition, the high electronic conductivity of RGO could enhance the electron transport between MOF layer and electrode. The MOF layer on RGO immobilized glassy carbon electrode demonstrated catalytic ORR activity via a 2-4 electrons reduction pathway depending on the overpotential.

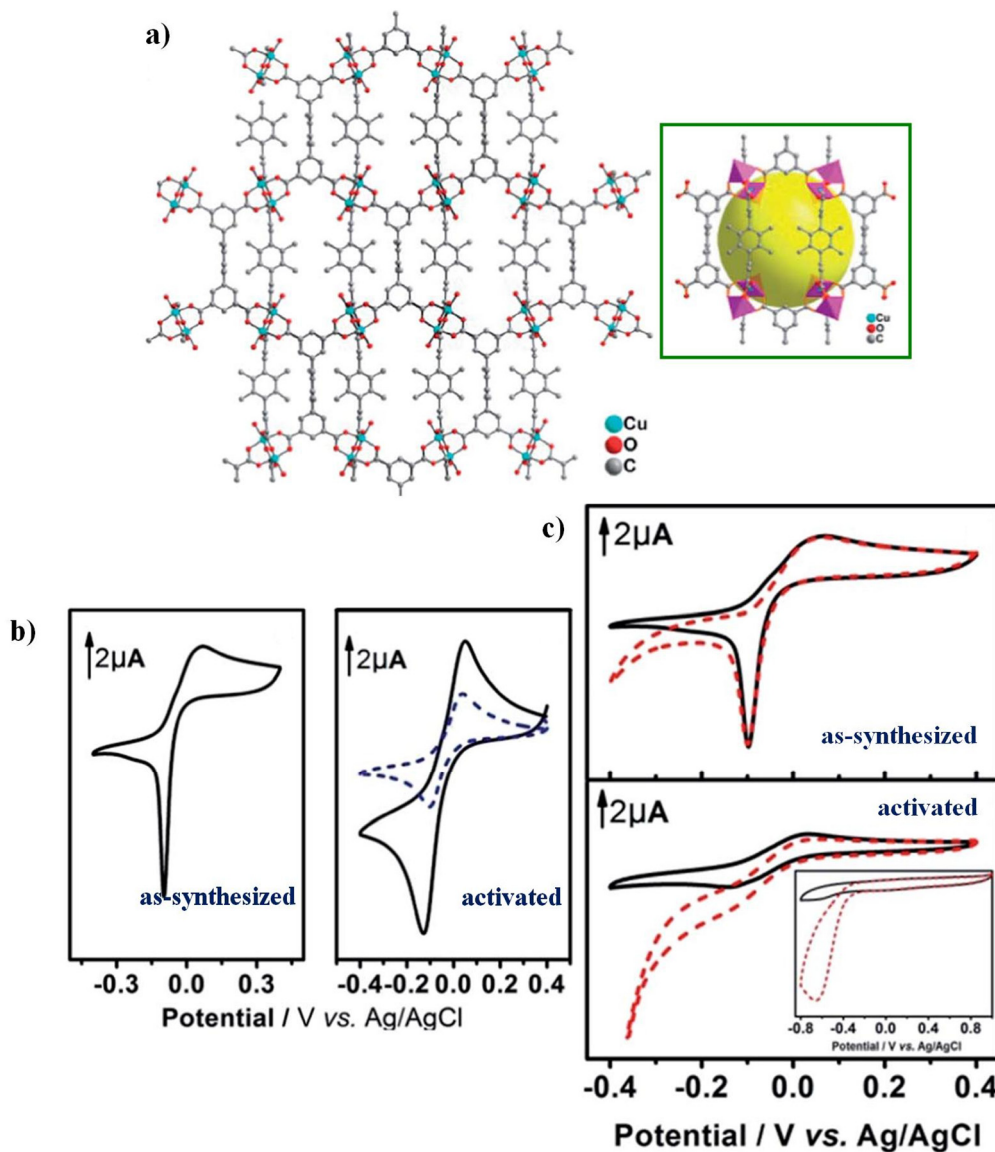


Figure 3.5 (a) Crystal structure of NPC-4, (b) CVs of as-prepared NPC-4 and activated NPC-4 modified onto the GCE in 0.1 mol L⁻¹ phosphate buffer (pH 6.0) solution. Dash line represents CV of activated NPC-4 after tens of CV cycles. Scan rate: 20 mV s⁻¹, (c) CVs of as-prepared NPC-4 (a) and activated NPC-4 (b) modified onto the GCE in 0.1 mol L⁻¹ phosphate buffer (pH 6.0) solution saturated with N_2 (solid curves) and O_2 (dot curves). The inset represents the CVs obtained at bare GCE. Scan rate: 20 mV s⁻¹ [32].

Another strategy to implement MOF as ORR electrocatalyst was reported by Jahan et al. [33] through developing a composite made from the assembly of GO and another type of mixed-linker copper containing MOF material (Cu-bdc-*ted*). Figure 3.6a and b exhibit the structure of this Cu-based MOF and the corresponding SBU composed of $Cu_2(COO)_4(ted)_2$ paddle-wheel, respectively. Each paddle-wheel SBU is linked by 1,4-benzenedicarboxylic acid (*bdc*) within the layer to form a 2D net, which is further connected by triethylene-diamine (*ted*)

molecules to produce the 3D MOF. To synthesize this GO/MOF composite, various concentrations of GO (2-8 wt%) were introduced to the reaction medium during hydrothermal synthesis of MOF. Although crystalline MOF structure could be retained in the presence of GO, they caused phase transformation in the MOF structure due to the twisting of the bdc ligand from covalent bonding with functional groups (hydroxyl and epoxy) present on GO plane. This was more pronounced at higher GO contents, at GO content of 20 wt% the GO/MOF composite was found to lose its crystallinity and become completely amorphous. Cyclic voltammetry in 0.5 M H₂SO₄ solution, revealed electrochemical activity for GO/MOF composite (GO = 2-8 wt%). In contrast to GO, which displayed no distinctive redox peak, two redox peaks was resolved in pure Cu-MOF and GO/MOF composite (GO = 2 wt%), ascribed to the redox reactions of the Cu²⁺ containing center (Figure 3.6c). As can be seen in this figure, increasing the GO content to 8 wt%, increased the anodic and cathodic current significantly so that only one peak appeared in the scanned potential range. This was attributed to the GO's impact on fastening the electron transfer process. As can be seen from Figure 3.6d, GO/MOF composite (GO 8 wt%) provides the highest onset potential (0.29 V vs. RHE) and oxygen reduction current density (-5.3 mA cm^{-2}) along with more positive shifted reduction potential compared to the rest of the composites. This again, confirms the role of incorporated GO in enhancing the electrocatalytic performance of Cu-MOF. RRDE measurements showed that while for GO/MOF composite (GO 8 wt%) the electron transfer number was close to 4 in the case of pure Cu-MOF, the number of transferred electron was between 2 to 4 over the same potential range. The unique porous scaffold structure of this composite along with improved charge transport and synergistic interactions of the GO and MOF, was found responsible for the enhanced electrocatalytic properties and stability of GO/MOF composite compared to pure MOF or GO alone. GO/MOF composite (GO 8 wt%) was further investigated in a PEM fuel cell and delivered a power density that was 76% that of the commercial Pt catalyst (Figure 3.7).

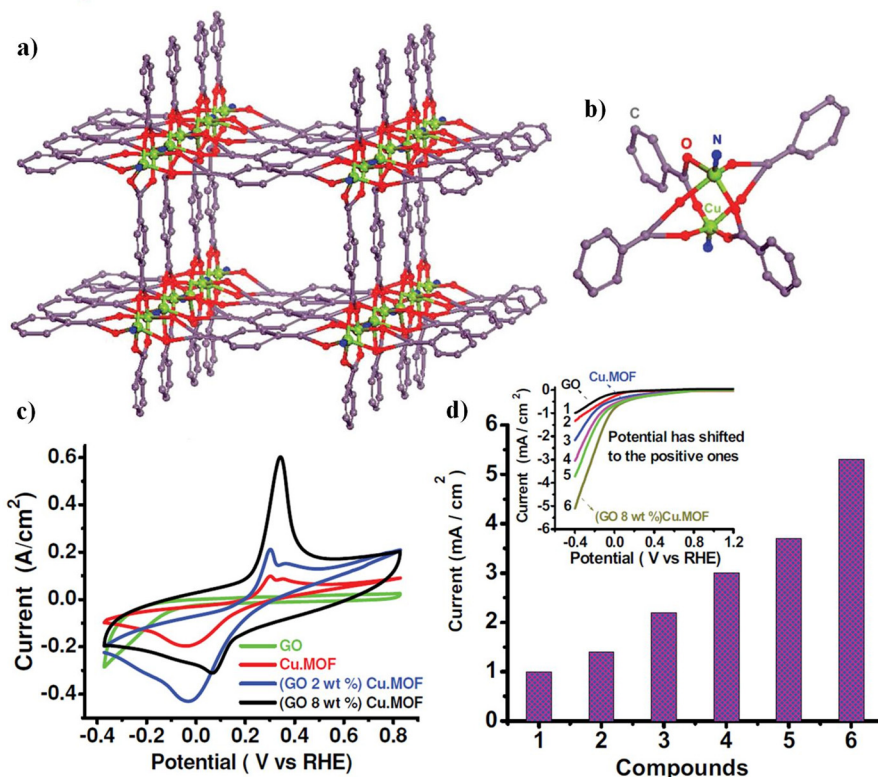


Figure 3.6 (a) Schematic of the chemical structures of Cu-MOF, (b) the paddle-wheel SBUs of pure Cu-MOF, (c) Cyclic voltammograms of catalysts drop casted on GC electrode; GO, Cu-MOF, (GO 2 wt%) Cu-MOF, and (GO 8 wt%) Cu-MOF in 0.5 M H₂SO₄; scan rate: 50 mV s⁻¹, (d) Comparing ORR current density of: 1) GO, 2) (graphene 2 wt%) Cu-MOF, 3) Cu-MOF, 4) (GO 4 wt%) Cu-MOF, 5) (GO 6 wt%) Cu-MOF, and 6) (GO 8 wt%) Cu-MOF. The inset shows the corresponding ORR RDE voltammograms at a rotation rate of 3500 rpm; scan rate: 2 mV s⁻¹ [33].

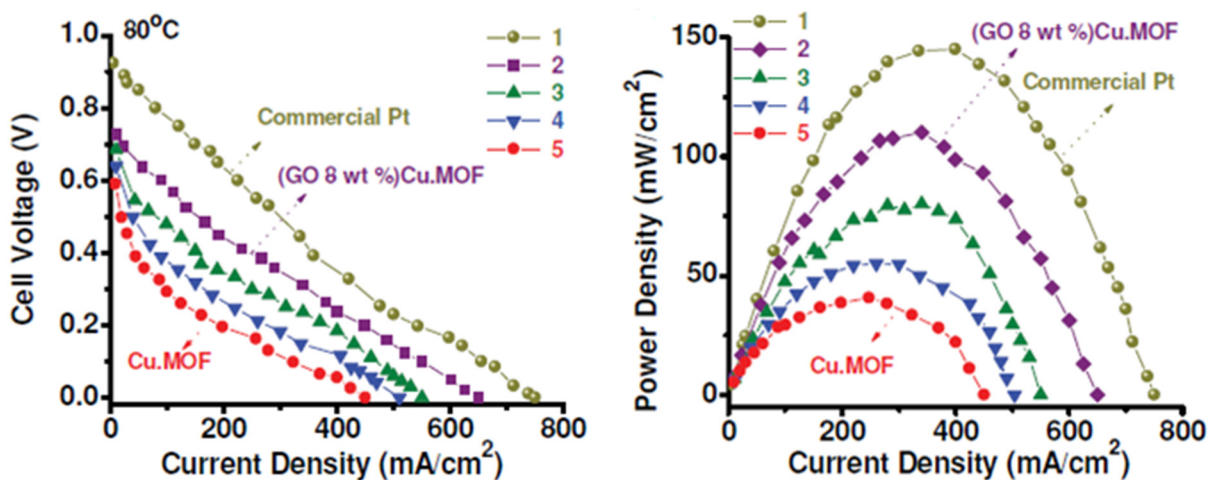


Figure 3.7 PEMFC study of the (GO X wt%) Cu-MOF composite compared with Pt/C for the H₂/O₂ fuel cell MEAs operating at 80 °C with different cathodes catalysts: 1) 20 wt.% Pt/C, 2) (GO 8 wt%) Cu-MOF, 3) (GO 6 wt%) Cu-MOF, 4) (GO 4 wt%) Cu-MOF, and 5) Cu-MOF [33].

Using a similar concept, the same group prepared a composite MOF structure as ORR electrocatalyst [34]. This composite MOF $(\text{G-dye-FeP})_n$, comprised of pyridine-functionalized graphene (G-dye), RGO sheets functionalized with donor- π - acceptor dye terminating with pyridinium moieties, and an iron porphyrin (FeP), 5,10,15,20-tetrakis(4-carboxyl)-iron-porphyrin (Figure 3.8a). Indeed, they used RGO sheets functionalized on either side of the basal plane with pyridine ligands as struts (building blocks) to link metalloporphyrin nodes to form the MOF structure. They performed a systematic characterization of the structural and electrochemical properties of these composites as a function of the weight percentage of the G-dye added to the FeP framework. The results showed that the addition of G-dye affect the crystallization of FeP and increased the porosity and electrochemical charge transfer rate of FeP in the MOF. The $(\text{G-dye-FeP})_n$ composite MOF revealed electrocatalytic activity in alkaline solution reflected by a well-defined cathodic peak which appeared during cyclic voltammetry in the O_2 -saturated electrolyte. In addition, the reduction potential for ORR is shifted increasingly to more positive values when G-dye content increased in the MOF composite (Figure 3.8b). The larger bond polarity due to nitrogen ligands in the G-dye, the catalytic activity of FeP and the framework porosity performed synergistically to afford a near 4 electron ORR pathway in $(\text{G-dye-FeP})_n$. The composite also exhibited higher selectivity for ORR and a significantly reduced methanol crossover effects compared to Pt catalyst which demonstrates its potential to be applied in alkaline DMFCs.

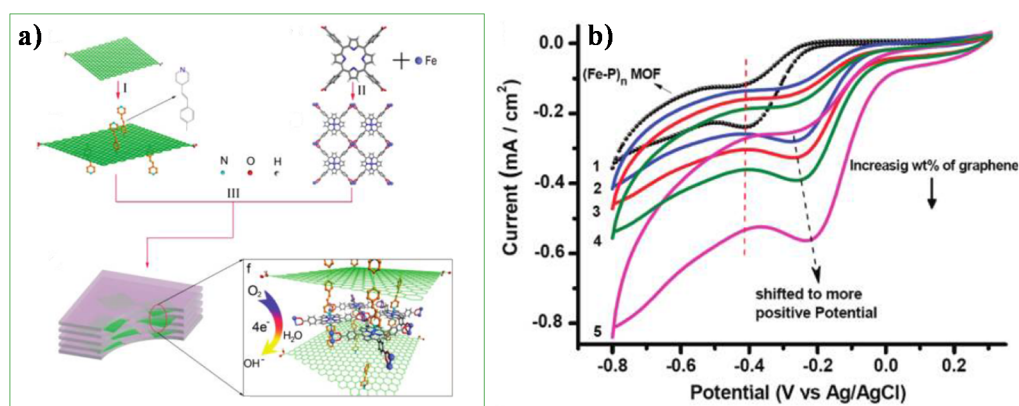


Figure 3.8 (a) Synthetic routes to make Graphene-Porphyrin MOF, (b) Cyclic voltammograms of oxygen reduction on the (1) $(\text{Fe-P})_n$ MOF, (2) $(\text{G-dye 5 wt \% -FeP})_n$ MOF, (3) $(\text{G-dye 10 wt \% -FeP})_n$ MOF, (4) $(\text{G-dye 25 wt \% -FeP})_n$ MOF, (5) $(\text{G-dye 50 wt \% -FeP})_n$ MOF electrodes obtained in O_2 -saturated 0.1 M KOH, scan rate: 50 mV s^{-1} [34].

Although these examples confirm the capability of non-pyrolyzed MOF to be used as electrocatalyst toward ORR, some limitations including the low electronic conductivity of the MOF materials raised interest for another different approach in which MOF undergoes a heat-treatment process through which the organic moieties of the MOF are carbonized to form porous and partially graphitized carbon.

While some researchers employed MOF as a self-sacrificing template to prepare metal free electrocatalysts others developed metal-based electrocatalysts from MOF materials. The former type of electrocatalysts was mainly tested in alkaline environment as they are considered as possible alternative catalysts in alkaline DMFCs. The later electrocatalysts are mainly investigated as a replacement to conventional Pt/C electrocatalysts in PEM fuel cell. These two approaches are discussed thoroughly in the following sections.

3.4 Metal free electrocatalyst derived from pyrolyzed MOFs

While some covalent-organic framework (COF) materials have been used to fabricate metal free ORR electrocatalysts [35,36], here we only discuss those catalysts that were derived from MOF precursor. In the structure of COF materials which indeed is very similar to MOF materials, again SBUs are linked into a periodic framework, however, in the case of COFs all the SBU components are organic.

Zhang et al. [37] used a very-well known zeolite-type nanoscale MOF, namely ZIF-8, as both the precursor and template to prepare N-doped graphitic porous carbon nanopolyhedras (NGPCs) as ORR electrocatalyst upon pyrolysis at temperature range of 700-1000 °C. The resultant product was thoroughly washed in 3 M H₂SO₄ solution to remove residual Zn species. As can be seen in Figure 3.9a, in ZIF-8 structure, zinc ions are solely coordinated by the N atoms from four imidazolate groups to produce a network structure which resembles zeolite topology (SOD). The reason for choosing ZIF-8 was related to their being free of oxygen and highly enriched in nitrogen (molar ratio: N/C = 1/2) structure in which nitrogen atoms are directly incorporated into the aromatic ring, and thus facilitated the incorporation of abundant nitrogen-containing active sites into the carbon matrix. In addition, the resultant NGPCs catalyst was found to retain not only the polyhedral morphology of the parent ZIF-8 but also to preserve the structural integrity and monodispersity of the MOF structure upon

pyrolysis. The presence of short-range ordered pores along with the retention of parent MOF morphology, verified the perfect selection of ZIF-8 as template (Figure 3.9b). Furthermore, the NGPC samples revealed high surface area and hierarchical porosity as well as high N content and electrical conductivity provided from sp^2 -hybridized carbon resulting from methyl imidazole ligand, which due to its aromatic nature is believed to promote graphitization of the carbon skeletons. Cyclic voltammetry in O_2 -saturated 0.1 M KOH solution confirmed the ORR activity of NGPCs as they showed a steep rise in the oxygen reduction current with a well-defined cathodic peak (Figure 3.9c). By increasing the pyrolysis temperature, the peak potentials of various NGPCs positively shifted toward higher voltages. Their most promising electrocatalyst (NGPC-1000-10) was obtained upon 10 h of carbonization at 1000 °C and demonstrated the highest positively shifted onset potential (less than 40 mV negatively shifted compared to Pt/C) and current density (4.3 mA cm^{-2}) comparable to Pt/C (4.5 mA cm^{-2}) at $-0.60 \text{ V vs. Ag/AgCl}$. The same catalyst also found to accelerate the ORR via an efficient 4 electron process coupled with superior methanol tolerance and cycling stability in alkaline solution. Their controlled experimental approach to study the impact of structural character of the NGPCs on their ORR performance, revealed that the synergistic contributions of excellent reactant transport due to high hierarchical pore structures, high electron transfer rate due to high degree of graphitization, and abundant catalytic sites provided by high N heteroatom loading, led to the optimum catalytic performance for the NGPC-1000-10.

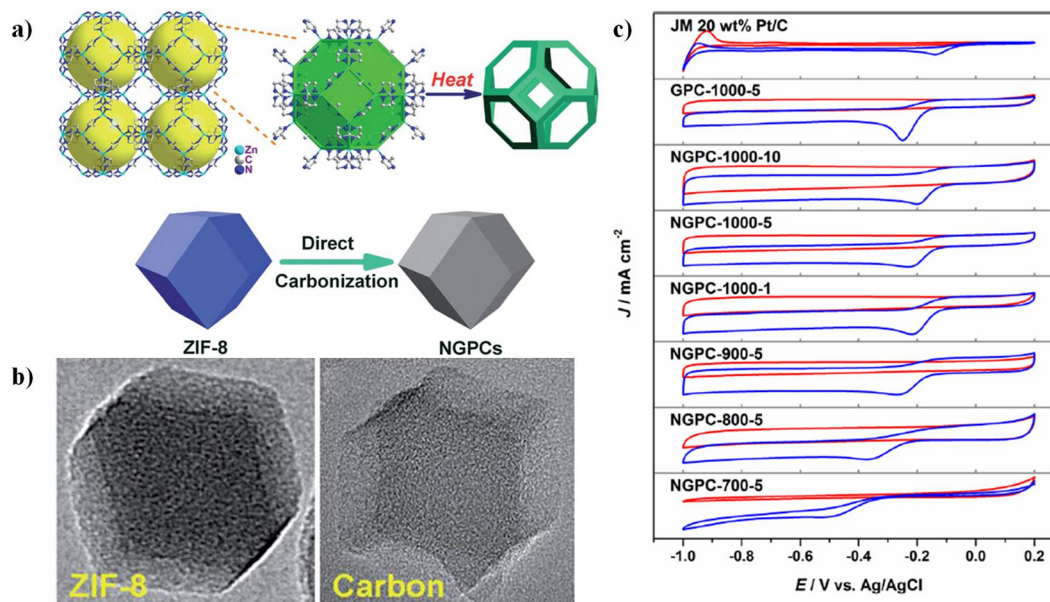


Figure 3.9 (a) Schematic illustration of the NMOFs-driven template synthesis of highly graphitized nitrogen-doped porous carbon nanopolyhedra, (b) TEM images of typical ZIF-8 and NGPC polyhedron nanoparticle, (c) CV curves of different NGPC samples, GPC-1000-5 and commercial 20 wt.% Pt/C sample (red line, N₂; blue line, O₂) in 0.1 M KOH solution (scan rate: 10 mV s⁻¹) [37].

While the results obtained by Zhang et al. [37] clearly showed the potential of solely ZIF-8 derived electrocatalyst as an efficient metal-free ORR catalyst, in another study, Aijaz et al. [38] used ZIF-8 along with furfuryl alcohol and NH₄OH as the secondary carbon and nitrogen sources, respectively to prepare a metal-free ORR electrocatalyst. Furfuryl alcohol and NH₄OH were first introduced into the pores of activated ZIF-8 via stirring their mixture for 12 h at room temperature. After filtration and ethanol washing, a series of heat-treatment processes were performed to polymerize the furfuryl alcohol and pyrolyze the composite at a temperature range of 600-1000°C, finally acid washing with HF was performed to remove Zn metal and other Zn-containing species. They investigated the surface area, mesoporosity and N content of these electrocatalysts along with their ORR activity in a 0.1 M KOH solution. Those samples prepared at higher pyrolysis temperature of 900 and 1000 °C (NC900 and NC1000), showed moderate N contents, high surface areas and large numbers of mesopores favouring the 4 electron reduction pathway. The electrocatalyst prepared at 800 °C (NC800) demonstrated a high N content, a moderate surface area, and a large number of micropores favouring the 2 electron reduction process. These results exhibited that pyrolysis temperature could significantly affect the properties of the resultant electrocatalyst including their graphitization degree, porosity, and nitrogen content and hence could control the

catalyst performance and dominating electrochemical reaction pathway. Their most promising electrocatalyst, CN900, showed onset potential of 0.83 V vs. RHE compared to 0.95 vs. RHE obtained for commercial 10 wt% Pt/C.

Zhong et al. [39] reported a 2D sandwich-like ZIF-8 derived graphene-based nitrogen-doped porous carbon sheets (GNPCSs) prepared by in situ growing of ZIF-8 on GO. Employing this approach, the synergistic effect between ZIF-8 derived N-doped porous carbon and GO-derived graphene, could be exploited to provide a consecutive conductive network, which is crucial for ORR electrocatalysts in terms of N-doped active sites and electron/mass transport. Achieving such a consecutive conductive network entails homogenous and complete coating of ZIF-8 on GO to ensure their close contact. Therefore, the surface of GO was enriched with the amide carbonyl groups of poly(vinyl pyrrolidone) (PVP) to facilitate the uniform nucleation of ZIF-8. Indeed, these functional groups act as coordination sites for ZIF-8 nucleation. To prepare the electrocatalyst precursor, this ZIF-8/GO composite underwent a pyrolysis under Ar atmosphere at 650-950 °C, followed by HCl (2 M) acid washing to remove the excess Zn or other impurities. The most promising GNPCS electrocatalyst was attained at a pyrolysis temperature of 800 °C, showing onset potential of 0.957 V vs. RHE, comparable to commercial 20%wt Pt/Vulcan XC-72R catalyst in 0.1 M KOH solution. Furthermore, GNPCSs-800 exhibited a number of transferred electron of 3.98, close to the theoretical value of Pt/C, indicating a near 4 electron ORR pathway. This catalyst also demonstrated an excellent tolerance to methanol crossover and superior durability compared to commercial Pt/Vulcan XC-72R. These properties were attributed to a synergistic effect between N-doped porous carbon and graphene with regard to structure and composition. Furthermore, the performance of GNPCSs-800 was evaluated in ADMFC and higher open-circuit voltage (0.71 V) and maximum power density (33.8 mW cm⁻²) were obtained compared with commercial Pt/Vulcan XC-72R (0.65 V and 22.5 mW cm⁻²).

In another work, Zhang et al. [40] used another type of zeolitic MOF precursor, called ZIF-7 as electrocatalyst precursor along with glucose as an additional carbon source. Similar to ZIF-8, ZIF-7 possesses a SOD topology formed from Zn cations bridged by a different imidazole based ligand, namely benzimidazole. In a similar manner as the one used in [38] to introduce the complementary C and N sources into porous ZIF-8 structure, ZIF-7 was soaked in glucose aqueous solution and stirred for 1 h to be impregnated with complementary

carbon source. This was followed by filtration and ethanol washing. The ZIF-7/glucose composite was then passed two step carbonization processes to form Carbon-L electrocatalyst. Another method was also used to prepare the Carbon-S electrocatalyst via solid phase mixing of MOF and carbon precursor. In this study, glucose was found to significantly affect the morphology of porous carbon via promoting the formation of graphitized carbon. While both Carbon-L and Carbon-S showed sheet-like or graphene-like structure, containing the clear-cut carbon nanosheets, the carbonaceous sample derived solely from ZIF-7 revealed a flower-like structure. In addition, glucose was found to play a key role in complete removal of residual Zn metal and zinc compound impurities hence, further acid leaching process was not required to form a metal-free electrocatalyst. This is unlike the previous reports [37-39] in which acid washing was employed to remove the residual Zn-containing species. As can be noticed all these metal free electrocatalysts [37-40] are derived from a Zn-based MOF and that is related to the boiling temperature of Zn ~ 908 °C, which is close to the pyrolysis temperature and thus can lead to evaporation of Zn metal. Cyclic voltammetry in O₂-saturated 0.1 M KOH solution, revealed electrocatalytic activity with a well-defined oxygen reduction peak for both Carbon-L and Carbon-S samples. The most promising electrocatalyst, Carbon-L, demonstrated onset potential of 0.861 V vs. RHE and limiting current of -4.592 mA cm⁻² compared to corresponding values of 0.925 V vs. RHE and -4.868 mA cm⁻² obtained for commercial 20% Pt/C. Besides providing high electrocatalytic activity, Carbon-L exhibited better stability and increased tolerance to the methanol crossover effects superior to the 20% Pt/C catalyst. Employing glucose as secondary carbon source was also found to affect the ORR activity of the MOF derived electrocatalyst as the sample prepared in the absence of glucose showed a lower onset potential of 0.743 V vs. RHE and limiting current of -2.505 mA cm⁻² far from the values obtained for Carbon-L and Carbon-S. Indeed, the increase of mesoporosity owing to the introduction of glucose in ZIF-7 resulted in enhanced electrical conductivity and hence the electron transportation in the corresponding electrode.

In addition to N-doped carbonaceous samples, dual (N and S-doped) [41] or triple (N, S and P-doped) [42] porous carbons prepared from MOF precursor have been attempted as materials to produce metal-free ORR electrocatalyst. To prepare N and S-doped carbon, Li et al. [41], used MOF-5 as template and urea and dimethyl sulfoxide, respectively, as N and

S sources and introduced them into cavities of MOF via soaking MOF-5 in methanol solution of these precursors. This sample was then pyrolyzed at 900 °C and washed with diluted HCl solution to remove the metal containing species. The co-doped electrocatalysts denoted as NS(A:B)-C-MOF-5, where A:B represents the atomic N:S ratio. Cyclic voltammetry in O₂-saturated 0.1 M KOH solution, revealed electrocatalytic activity with a well-defined oxygen reduction peak for all the samples. The peak potential for these samples was however slightly negative compared with the commercial 20 wt% Pt/C catalyst. The most promising electrocatalyst, NS(3:1)-C-MOF 5 showed onset potential very close to the commercial electrocatalyst reflecting its high ORR activity. The higher electrocatalytic activity of this co-doped sample compared to solely N or S-doped samples prepared in a similar manner only in the absence of corresponding precursor, was attributed to the synergetic effect of N and S atoms. The larger electronegativity of N (3.04) with respect to C atoms (2.55), creates a positive charge densities on the adjacent C atoms. While the electronegativity of S (2.58) is similar to that of carbon, the simultaneous incorporation of these species into porous carbon materials, change the spin and charge densities and results in an increase in the number of active C atoms and the very favourable adsorption of O₂. Furthermore, the NS(3:1)-C-MOF-5 electrocatalyst exhibited long-term stability and excellent resistance to the methanol crossover, superior to those obtained for commercial Pt/C.

MOF-5 was also used as a template for dicyandiamid, triarylphosphine and dimethyl sulfoxide as N, P and S sources to prepare a ternary-doped porous carbon as a metal-free electrocatalyst for ORR [42]. The doping process was carried out by soaking the dried MOF-5 in a methanol solution of all heteroatoms precursors followed by carbonization at 900 °C under inert gas. The resultant material was washed with diluted HCl solution to produce NPS-C-MOF-5 catalyst. NPS-C-MOF-5 exhibited high electrocatalytic activity for ORR as reflected by its high onset potential (−0.007 V vs. Ag/AgCl), very close to the commercial Pt/C catalyst (0.03 V vs. Ag/AgCl). The number of electrons involved in ORR by NPS-C-MOF-5 catalyst was almost four, suggesting a favourable 4 electron pathway for the ORR. The kinetic limiting current density of NPS-C-MOF-5 catalyst at −0.6 V vs. Ag/AgCl was up to ~−11.6 mA cm^{−2}, which was 1.2 times higher than that of the commercial Pt/C catalyst (−9.7 mA cm^{−2} at −0.6 V vs. Ag/AgCl). Furthermore, the NPS-C-MOF-5 demonstrated outstanding methanol tolerance and excellent long-term stability superior to those of the

commercial Pt/C catalyst. The electrocatalytic performance of this ternary-doped carbon sample was compared with other carbon materials containing no, one or two of these heteroatoms in their structure (Figure 3.10). As can be seen in this figure, NPS-C-MOF-5 provides the best ORR electrocatalytic performance among all these samples attributed to the synergistic effect resulting from N, P and S ternary-doping.

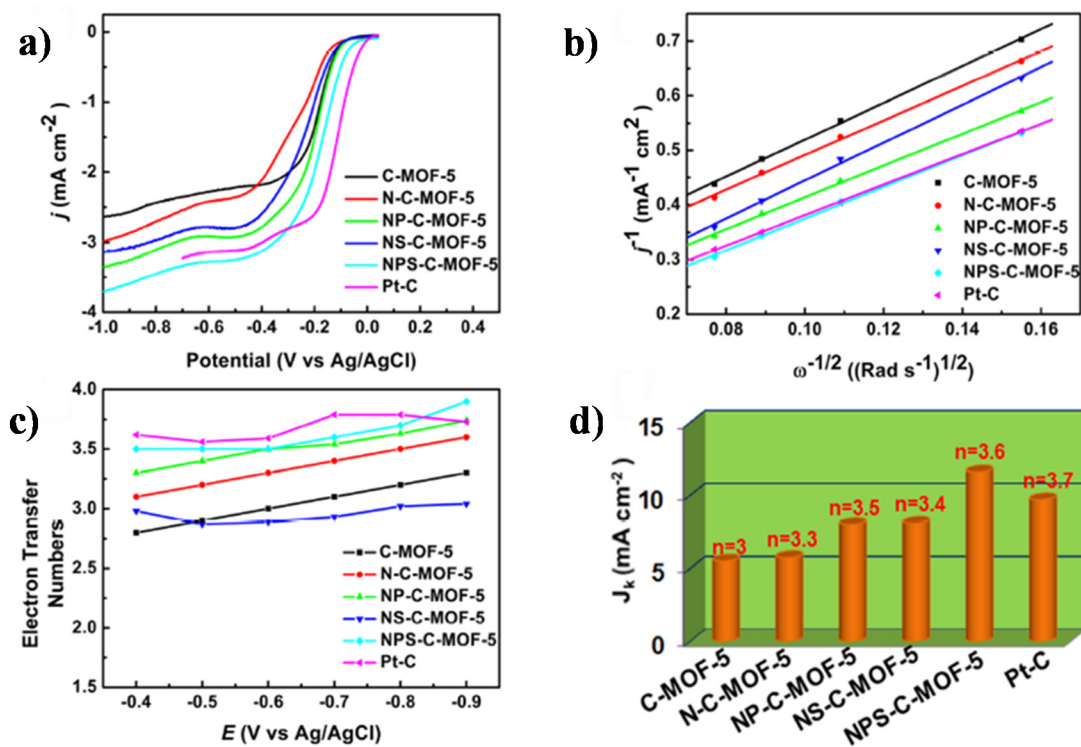


Figure 3.10 (a) LSVs of different samples at a rotation rate of 1600 rpm; (b) K-L plots of different samples at 20.6 V; (c) Electron-transfer numbers of different samples from 20.4 to 20.9 V; (d) Kinetic limiting current densities of different samples and the corresponding electron-transfer numbers at 20.6 V [42].

Besides MOF-5, two other MOF structures, namely MOF-177 and UMCM-1 were used as templates to prepare ternary-doped porous carbon electrocatalysts (Figure 3.11). The order of onset and peak potentials of these three porous carbons was found to be C-MOF-5 > C-UMCM-1 > C-MOF-177. This revealed that different structures and compositions of MOF materials could affect the ORR electrocatalytic activities of the resulting electrocatalysts.

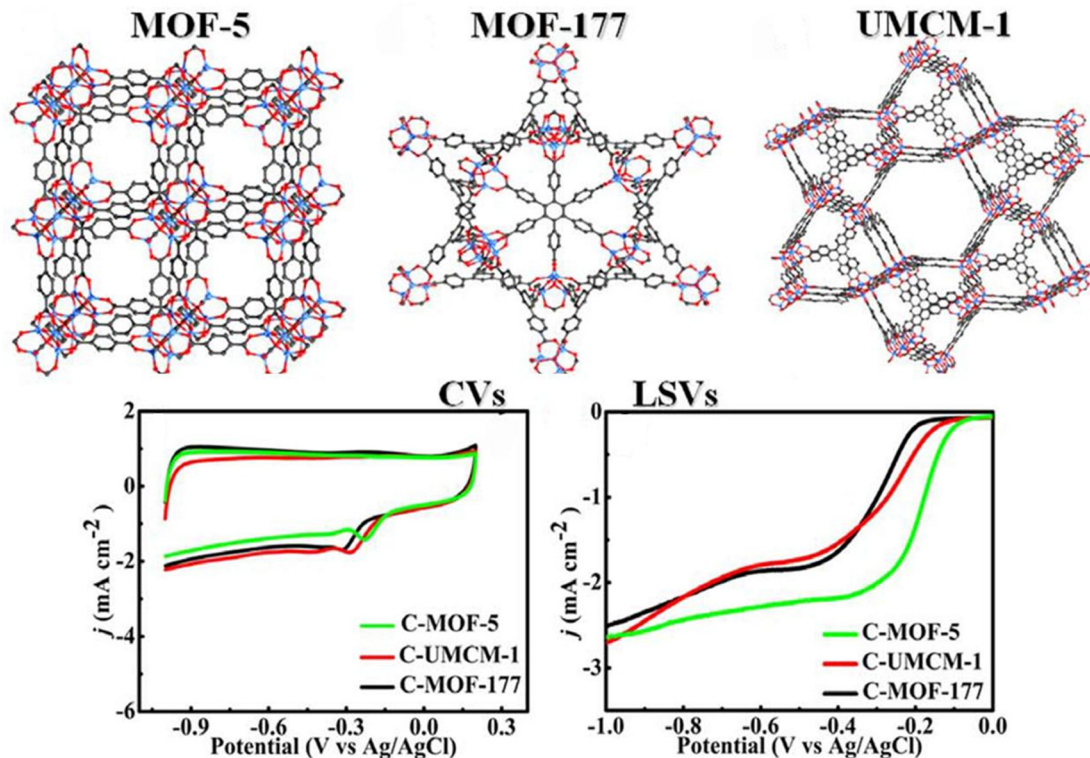


Figure 3.11 Structures, CVs and LSVs of different samples in O₂ saturated 0.1 M KOH solution [42].

In addition, they investigated the influence of carbonization temperature on ORR. Three pyrolysis temperature of 700, 900 and 1000 °C were attempted and the catalyst obtained at 900 °C provided the best ORR activity. During pyrolysis under different conditions heteroatoms were doped into the carbon materials and this caused changes in the pore structure of these samples. Therefore, different pyrolysis conditions led to the doped samples with different active sites and different percentages of mesopores that may cause the difference in ORR activities.

3.5 Metal containing electrocatalyst derived from pyrolyzed MOFs

The first report on preparation of ORR electrocatalyst using MOF materials as precursor was provided by Ma et al. [43]. They used a cobalt-based zeolitic framework (CoIm) in which, each cobalt atom was coordinated by four nitrogen atoms from the imidazolate ligand (Fig. 3.12a) to produce ORR electrocatalyst upon pyrolysis. As can be seen in this figure, CoIm contained, Co-N₄ moieties within its structure analogous to the active centers observed in macrocyclic precursors previously reported to provide ORR activity (as discussed in chapter

2). A single crystal of CoIm supposed to possess 3.6×10^{21} Co-N₄ sites per cm³. Such a high active site density distributed evenly throughout the MOF precursor could be exploited to produce highly active non-PGM electrocatalyst after pyrolysis. A range of pyrolysis temperatures between 500-900 °C was tried and the most promising electrocatalyst was obtained at a pyrolysis temperature of 750 °C. This catalyst demonstrated high ORR catalytic activity with an onset potential of 0.83 V vs. RHE in an acidic medium (Figure 3.12b). The number of transported electrons per O₂ molecule was found to be between 3.2–3.5 electrons which demonstrated a dominant favourable 4 electron pathway. The results revealed catalytic performances comparable to those obtained for state-of-the-art Co-based non-PGM catalysts.

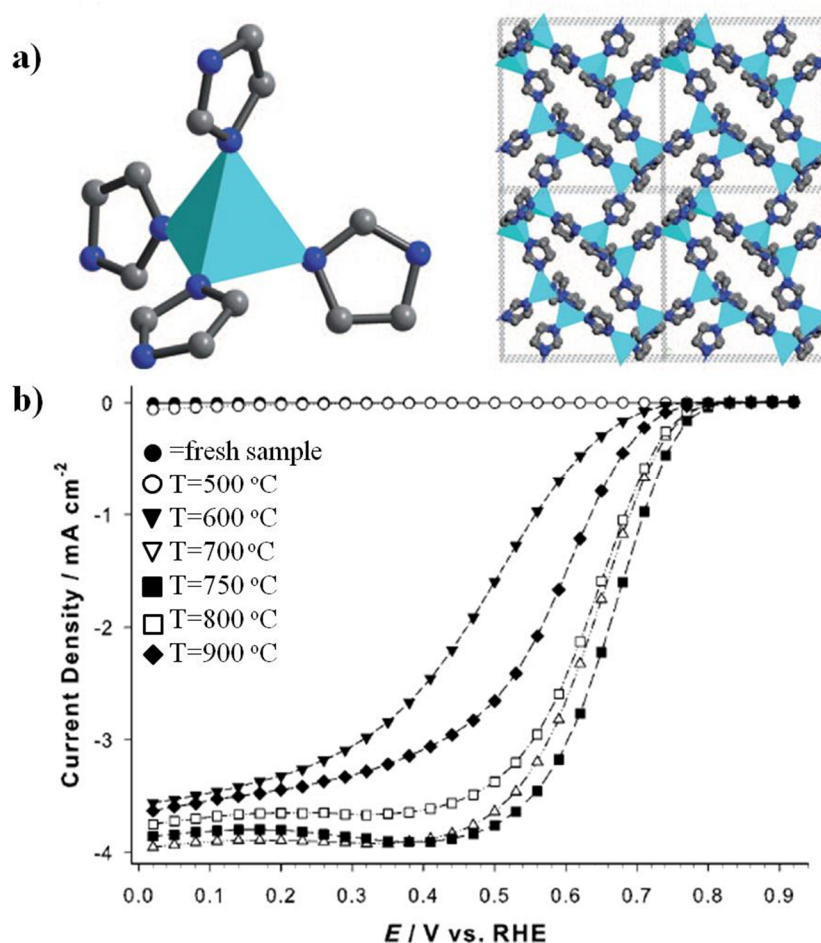


Figure 3.12 (a) Coordination geometry in CoIm framework, (b) ORR polarization curves for CoIm samples pyrolyzed at different temperatures [43].

Later, the same group tried to replace Co with Fe in the MIm MOF structure as Fe-based non-PGM electrocatalysts were reported to exhibit higher ORR catalytic activity with typically 0.1 V higher onset potentials [43]. Therefore, they developed a FeIm MOF structure via solvent-free synthesis reaction of ferrocene with imidazole ligand [44]. Similar to the structure observed for CoIm, FeIm exhibited a MOF structure in which Fe²⁺ ions were coordinated to four N atoms from different imidazolate groups to form a continuous 3D framework (Figure 3.13a). Two step heat-treatment in the temperature range of 700-900 °C was performed to produce the final electrocatalyst precursor first under inert gas and then under NH₃ (FeIm700-FeIm900). Between these two steps acid washing with 1 M H₂SO₄ was conducted to remove the metallic Fe crystallites formed during pyrolysis. While FeIm800 revealed the highest onset potential (0.859 V vs. RHE) and mass activity, FeIm700 showed a preferred 4 electron mechanism ($n = 3.70-3.81$). To enhance the performance of these catalysts, they used ZIF-8 along with FeIm MOF and performed ball-milling to mix these two precursors effectively and conducted pyrolysis at 1050 °C under inert gas and 950 °C under NH₃ (FeIm/ZIF-8) to produce the electrocatalyst precursor. This approach was similar to the protocol used in Dodelet's group to develop non-PGM electrocatalyst and will be explained in more details in the following paragraphs. FeIm/ZIF-8 showed the best ORR catalytic performance with a high onset potential of 0.915 V vs. RHE (Figure 3.13b). While CoIm-based electrocatalysts were not tried in a PEM fuel cell setup, the most promising FeIm-based electrocatalyst, FeIm/ZIF-8, was used in a cathodic catalyst layer of a single cell operated with H₂ and air and showed an onset potential of 0.977 V and volumetric activity of 12 A cm³ at 0.8 V (Figure 3.13c). The better catalytic performance of FeIm/ZIF-8 was attributed to its higher N content and surface area. In addition, they postulated that lower Fe contents in the MOF structure could provide better performances and hence, in their later study [45] tried to synthesize a bimetal ZIF, containing Fe as the minor part and Zn as the major part. They postulated that while Fe contributes in the formation of catalytic sites, the Zn centers produce the pore structures and suppress the graphitization.

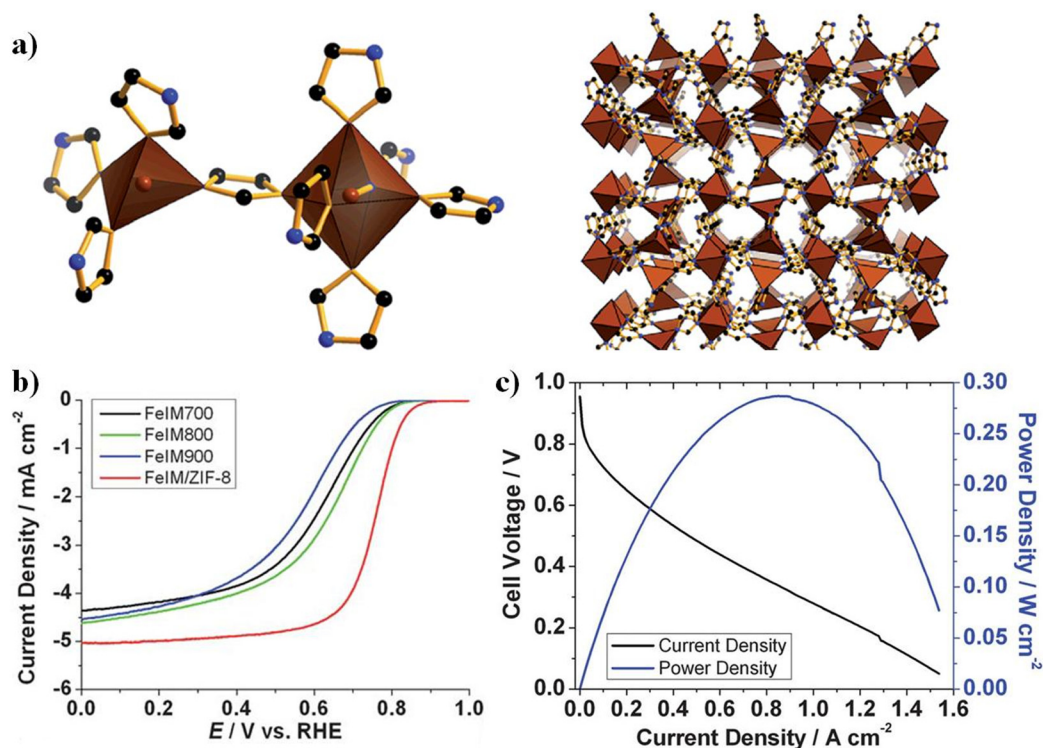


Figure 3.13 (a) Coordination geometry in FeIm framework, (b) ORR polarization curve measured by RRDE, (c) Polarization and power density curves of the single cell using FeIm/ZIF-8 as the cathode catalyst (Nafion® 211 membrane) operated with H₂-air at the cell temperature of 80 °C and the active area of the 5 cm² [44].

Developing the bimetal MOF precursor, they reported a facile one-pot and solid-state synthesis of ZIF structure via heat-treatment of nanopowder ZnO with different imidazolate containing ligands such as 2-methylimidazole (HmIm), imidazole (HIm), 2-ethylimidazole (HeIm) and 4-azabenzimidazole (H4abIm), to prepare four different ZIF structures as presented in Figure 3.14a [45]. To introduce the Fe centers to these MOF materials 5 wt% of tris-1,10-phenanthroline iron(II) perchlorate (TPI, Figure 3.14a) was added during the solid-state synthesis of ZIFs. Although by employing this method, Fe could not act as a node in the framework structure, it would not disturb the formation of ZIFs. They found TPI to either be dispersed on the external surface of ZIF crystals in the cases of non-porous Zn(Im)₂, Zn(eIm)₂ and Zn(4abIm)₂, or be incorporated into ZIF cavities in the case of porous Zn(mIm)₂. To prepare the final electrocatalyst precursor (Zn(ligand)₂TPIP), the synthesized Zn(ligand)₂TPI precursors were then pyrolyzed at 1050 °C under Ar, followed by an acid-washing step and a second heat-treatment at 950 °C under NH₃. Except Zn(mIm)₂, these ZIF based MOFs were found to be non-porous, however, upon pyrolysis, all four samples showed

hybrid micro/meso-porous structures, with considerably high BET specific surface area ranging from 443 to 1277 m² g⁻¹ (Table 3.1). Hence, they demonstrated that the porosity of MOF precursors is not a prerequisite to obtain porous electrocatalyst samples. Among the four electrocatalysts, Zn(Im)₂TPIP revealed a different structure containing iron carbide along with the amorphous structure. This was related to the higher content of C-Fe in its structure. The same sample also revealed the highest degree of graphitization, lowest nitrogen content and surface area and lowest ORR electrocatalytic activity. ORR catalytic activities of these samples were studied using the RRDE method. As can be seen in Table 3.1 and Figure 3.14b, Zn(eIm)₂TPIP exhibited the highest mass activity and onset potential (0.914 V vs. RHE) among all the samples. Considering the results presented in Table 3.1, they found an interesting trend in which the size of the alkyl side-chain substitution of the imidazole was found to affect the catalytic performance. Increasing the size by replacing H in Im with methyl group in mIm and replacing the latter one by ethyl group in the eIm enhanced the catalytic performance, however, further size increment in the case of 4abIm, reduced the catalytic activity. Although they could not elucidate the reason for higher activity of Zn(eIm)₂TPIP as it didn't provide the highest nitrogen content or surface area whereas these two parameters are generally postulated to determine the catalytic activity of non-PGM electrocatalysts, they suggested some structural factors associated with the initial ligand composition along with pyrrolic to pyridinic nitrogen ratio to affect the catalytic activity of these ZIF derived materials. In a single PEM fuel cell the most promising catalyst, Zn(eIm)₂TPIP as the cathode catalyst, revealed an onset potential of 0.929 V and current density of 88.1 A cm³ at 0.8 V. At higher current densities, where mass transfer resistance plays a determining role on fuel cell performance, the Zn(mIm)₂TPIP catalyst that provided the highest surface area and porosity (Table 3.1) outperformed the Zn(eIm)₂TPIP catalyst (Figure 3.14c). Therefore, the former one provides the highest maximum power density (P_{max}) of 620 mW cm⁻² at the cell potential of 0.43 V, whereas Zn(eIm)₂TPIP reached the P_{max} of 500 mW cm⁻² at the same cell potential (Table 3.1).

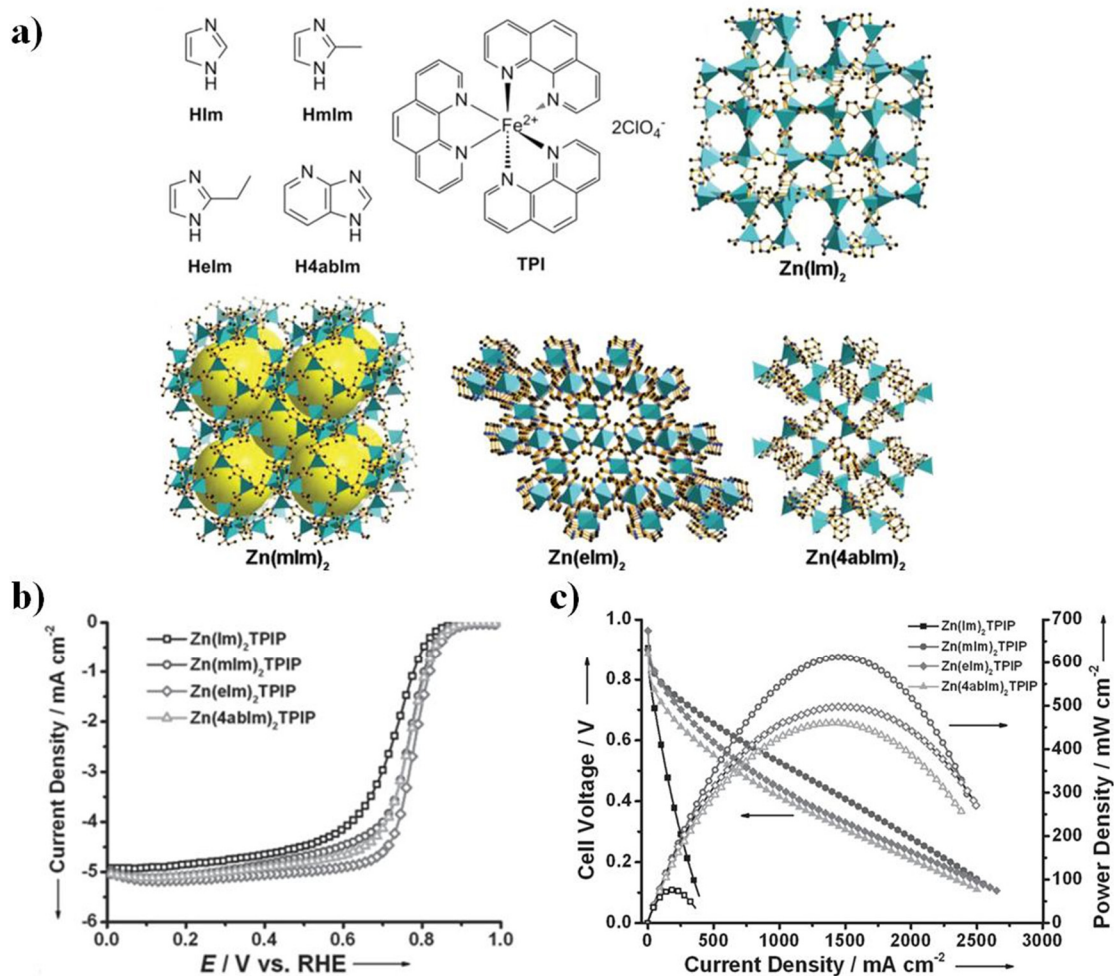


Figure 3.14 (a) Chemical structures of ligands and iron additive along with crystal structure of different ZIFs, (b) ORR polarization curve measured by RRDE, (c) The current-voltage polarizations (solid symbols) and power densities (hollow symbols) from single cell tests, membrane = Nafion 211, cathode catalyst loading = 2.2 mg cm^{-2} , anode catalyst = Pt/C @ $0.25 \text{ mg}_{\text{Pt}} \text{ cm}^{-2}$, cell area = 5 cm^2 , $T = 80 \text{ }^\circ\text{C}$, $P_{\text{O}_2} = P_{\text{H}_2} = 1.5 \text{ bar}$, flow-rates @ 400 ml min^{-1} [45].

Table 3.1 Specific surface area (SSA), onset potential (E_0), half-wave potential ($E_{1/2}$), volumetric current density (I_v), and peak power density (P_{max}) of electrocatalysts [45].

Electrocatalysts	SSA	E_0	$E_{1/2}$	I_v	P_{max}
	$m^2 g^{-1}$	V vs. RHE	V vs. RHE	$A cm^{-3} @ 0.8 V$	$mW cm^{-2}$
Zn(Im)₂TPIP	443	0.881	0.73	5.9	80
Zn(mIm)₂TPIP	1277	0.902	0.76	67.0	620
Zn(eIm)₂TPIP	920	0.914	0.78	88.1	500
Zn(4abIm)₂TPIP	976	0.904	0.76	39.4	460

A breakthrough in developing non-PGM electrocatalyst not only for the ones prepared from MOF precursor but among all the non-PGM electrocatalyst reported in the literature was reported by Proietti et al. [46]. They used ZIF-8 as an alternative to conventional carbon supports along with the nitrogen (1,10-phenanthroline) and Fe metal (ferrous acetate) sources to prepare a non-PGM electrocatalyst. Pyrolysis under Ar in the temperature range of 400-1050 °C with a fixed duration of 1 h, followed by an optional NH₃ heat-treatment at 950 °C were conducted and the electrocatalyst precursors containing Fe-N_x catalytic active sites in their microporous structure were obtained. Along with different Ar pyrolysis temperatures and NH₃ heat-treatment durations, different phenanthroline and ferrous acetate contents were attempted in research for optimum electrocatalyst precursor. The performance of the best performing catalyst, contained 1 wt% nominal Fe content with N-source to ZIF-8 mass ratio of 20 to 80 pyrolyzed under Ar at 1050 °C and heat-treated with NH₃ at 950 °C for 15 min, was tested in a PEM fuel cell. This catalyst yielded a current density and a power density of 1.2-1.3 A cm⁻² and 0.75 W cm⁻², respectively at 0.6 V (Figure 3.15). The volumetric activity provided by this catalyst was 230 A cm³ at 0.8 V_{iR-free}, which is among the highest achieved by non-PGM catalysts. Based on scanning and TEM images, they attributed such a high ORR catalytic activity to the interconnected alveolar carbon nanostructure attained in Fe/Phen/Z8-derived catalysts which could improve the mass-transport properties in the cathodes.

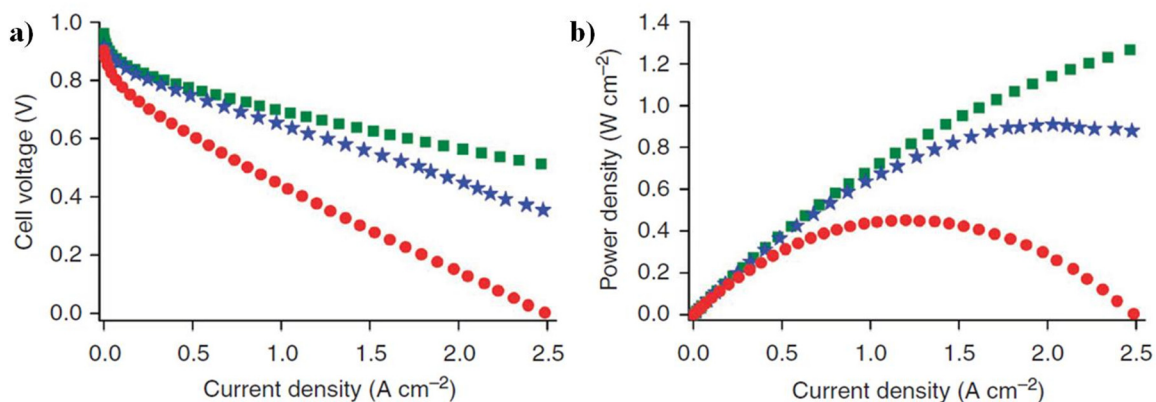


Figure 3.15 (a) Polarization and (b) power density curves for MEAs comprising a cathode made with the most active Fe/Phen/Z8-derived catalyst (blue stars), previously reported most active iron-based catalyst [47] in a similar manner using carbon black as catalyst support (red circles) and a state-of-the-art Pt-based cathode with a loading of 0.3 mg_{Pt} cm⁻² (green squares) For the two MEAs made with iron-based cathodes, the catalyst loading was 3.9 mg cm⁻². For all MEAs, NRE 211 membranes were used [46].

Using the same electrocatalyst preparation approach, ball-milling of ZIF-8 based support with metal and N sources, the same group replaced 1,10-phenanthroline (phen) ligand with 2,4,6-tris(2-pyridyl)-s-triazine (TPTZ) to investigate the effect of the coordination chemistry of this Fe^{II}/ligand/ZIF-8 based catalyst precursors [48]. This study demonstrated the importance of synthesis and preparation conditions, in which competition between two different ligands (ligand used as N source and 2-MeIm ligand of ZIF-8) to interact with two present metal entities (Fe as metal source for active site formation and Zn from the ZIF-8 support) led to cationic metal exchange (displacement of Zn²⁺ ions in ZIF-8 structure by Fe²⁺ ions) that subsequently could affect the ORR catalytic activity of these catalysts. According to their results, the localization of Fe²⁺ on the surface of ZIF-8 particles is favourable for a better performance of these catalysts compared to the situation where Fe²⁺ ions diffuse to the interior of the porous structure. This was related to higher accessibility of O₂ molecules and protons to the Fe-N_x catalytic active sites formed during the pyrolysis process which eventually could enhance the ORR. Later, Morozan et al. [49] investigated the effect of furfuryl alcohol as an additional carbon source and pore-forming agent on the performance of Fe/phen/ZIF-8 electrocatalysts. In addition, they explored the effects of several synthesis parameters such as pyrolysis temperature, heating rate and microporous host nature on the electrochemical performance of these electrocatalysts. Two main strategies were applied to prepare Fe/phen/ZIF-8 electrocatalysts (Figure 3.16): 1) formation of porous N-doped carbon

through pyrolysis of the furfuryl alcohol-impregnated ZIF-8, followed by encapsulation of iron acetate and phenanthroline through wet impregnation and low-energy ball-milling, and pyrolysis in Ar to produce the electrocatalyst precursor; 2) impregnation of ZIF-8 with furfuryl alcohol iron acetate and phenanthroline, respectively, followed by low-energy ball-milling and pyrolysis under Ar. The final pyrolysis step in NH_3 was also conducted for both synthesis approaches. Approach (1) was found to be more effective toward implementation of additional carbon source throughout preparation of Fe/phen/ZIF-8 based electrocatalysts. The catalysts prepared via implementation of approach (1) provided higher electrocatalytic performances compared with approach (2). The later one basically revealed similar performances with or without furfuryl alcohol. Moreover, their investigation illustrated that the high microporosity combined with sufficient mesopores in the range of 2-4 nm provides a higher power performance in PEMFC. Large mesopores (> 4 nm) did not yield any better mass-transport properties. According to spectroscopic analysis results while approach (1) produced a large fraction of Fe- N_4 type moieties in the electrocatalyst precursor, approach (2) mainly caused the formation of crystalline Fe phases instead of Fe- N_4 type species. Furthermore, they noticed that although the one-step pyrolysis under Ar is capable of formation of an active electrocatalyst, the second-step pyrolysis under NH_3 clearly improved the fuel cell performance of these catalysts. This was attributed to the enhancement of surface area and active site density due to the formation of micropores and small mesopores in the samples upon NH_3 pyrolysis that could bring the pre-existing active sites to the surface.

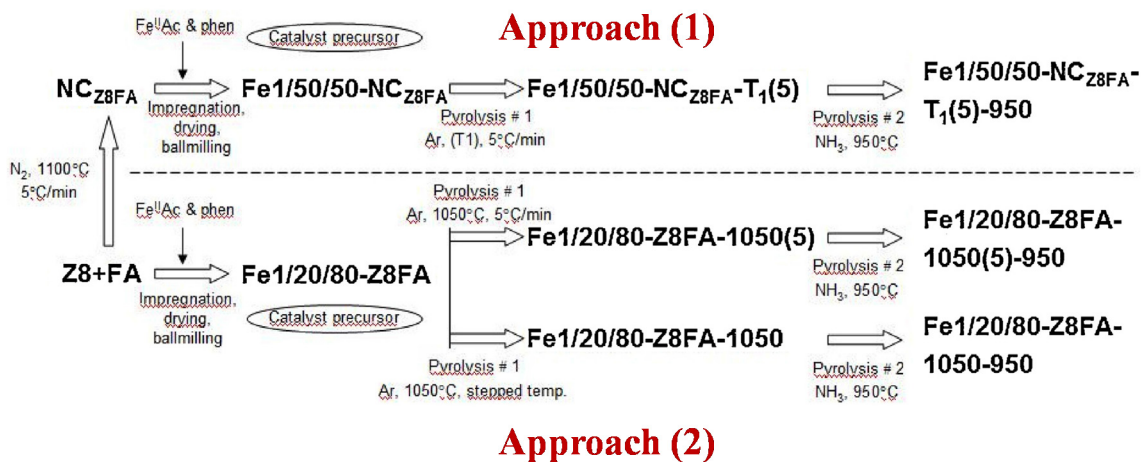


Figure 3.16 Flowchart of the synthesis approaches and steps [49].

There are some other reports on using MOFs as precursors for developing non-PGM electrocatalyst for ORR. For instance, Su et al. [50] reported the nitrogen-doped carbon nanotubes (NCNTs) prepared via direct pyrolysis of bimetal (Zn/Fe) ZIF material. They used dicyandiamide (DCDA) as complementary nitrogen source and found that this precursor favours the formation of NCNTs at relatively low temperature (700 °C). This was related to an inducing effect of DCDA for graphitic structure. Furthermore, the in situ generated Fe and Fe₃C species act as catalysts during the pyrolysis process and facilitate the formation of NCNTs. These NCNTs containing iron species along with high amounts of graphitic N revealed ORR activity higher than those obtained with commercial 20%wt Pt/C catalyst in 0.1 M KOH solution. Palaniselvam et al. [51], used other members of the ZIF family, namely, ZIF-70, ZIF-68 and ZIF-69 as a template along with ferrous acetate and phenanthroline as Fe and N sources, respectively, to prepare metal containing non-PGM electrocatalyst for ORR upon pyrolysis at 900 °C under Ar. Among the obtained materials, FeNC-70 derived from ZIF-70 exhibited the highest ORR activity with an onset potential of 0.80 V vs. NHE through a pathway that involves 3.3-3.8 electron in 0.5 M HClO₄ solution. Electrochemical analysis and structural characterizations predicted that the active sites for ORR are most likely the in situ generated N-FeN₂₊₂/C moieties.

Xia et al. [52] attempted to enhance the ORR catalytic activity of their ZIF-67 derived electrocatalyst by reducing their size and synthesizing a nanoscale MOF material. Their idea to use nanoscale MOF materials instead of bulk materials was expected to expose more catalytic surface and improve the mass and electron transfer efficiency. Through precise control over the growth of ZIF-67 nuclei by simply altering the solvent and reaction temperature, they synthesized uniform ZIF-67 precursors of various crystalline sizes ranging from 300 nm to several micrometers (Figure 3.17). Upon pyrolysis in a temperature range of 600-900 °C, the most promising electrocatalyst, which was derived from the smallest ZIF-67 MOF at pyrolysis temperature of 750 °C, revealed the highest ORR activity in 0.1 M HClO₄ solution with an onset potential of 0.86 V vs. RHE. Furthermore, the electron transfer numbers attained with different samples provided a direct evidence of the size effect on catalyst performance. While catalysts derived from 300 nm MOF led to the electron transfer number of 3.7, the 800 nm and 1.7 μm ZIF-67 demonstrated the electron transfer number of 3.5 and 3.2, respectively. The kinetic current density also exhibited a significantly higher

value in the case of smaller parent MOF compared with larger samples, proposing that the higher surface-to-volume ratio could result in better catalytic performance.

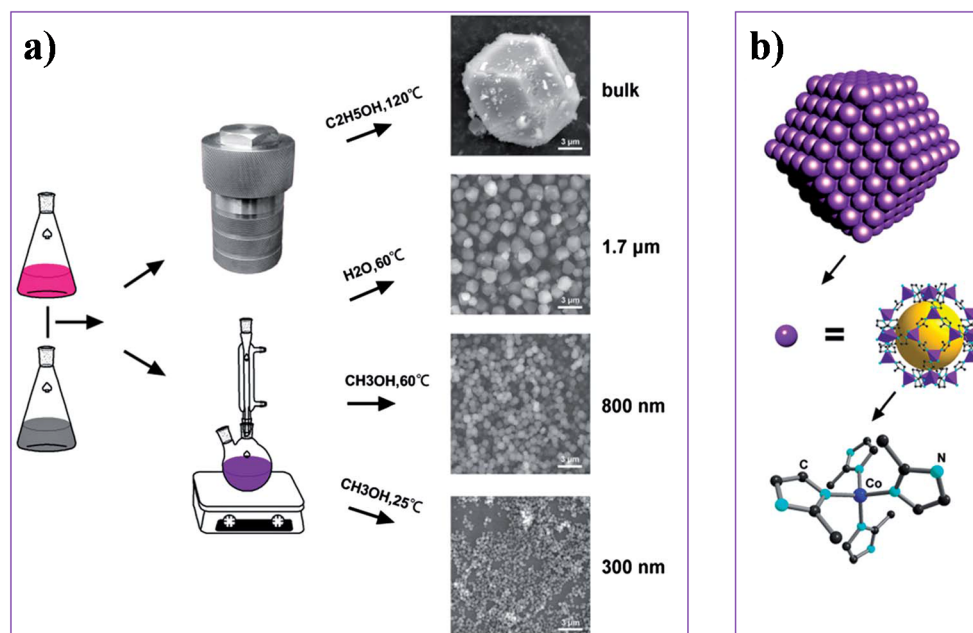


Figure 3.17 Schematic representation of synthesizing ZIF-67 with various sizes, (b) Structure information of the ZIF-67 crystal [52].

Following a similar concept, Zhao et al [53] developed a nanoscale MOF from MIL-88B-NH₃. This nanoscale MOF precursor was expected to resist the drastic structural and/or morphological damage of MOF structure caused by high temperature pyrolysis and to provide larger surface-to-volume ratio that would be beneficial for ORR. MIL-88B-NH₃[Fe₃O(H₂N-BDC)₃, H₂N-BDC = 2-aminoterephthalic acid], is an Fe-based MOF material with N, O-containing organic ligands (Figure 3.18a). Upon pyrolysis, this MOF material formed spindle-like nanoparticles with uniform diameters of ~ 50 nm and lengths of ~ 140 nm comprised of Fe containing species such as metallic Fe and Fe carbide (CNFs). They compared the structure of this nanoscale MOF with the micro scale particles and found that in the case of nanoscale material, both shape and size of the parent MOF remained intact after the pyrolysis process (Figure 3.19a and b), however, in the case of larger particles the microstructures was completely collapsed accompanied with appearance of many small particles on their surfaces (Figure 3.19c and d). In addition, the electrocatalyst nanoparticles provide higher surface area and porosity compared to the one derived from the microscale MIL-88B-NH₃. These findings confirmed the important role of the nanoscale materials in

preventing the destruction of the morphology, size, and porous structure of the parent MOF during pyrolysis.

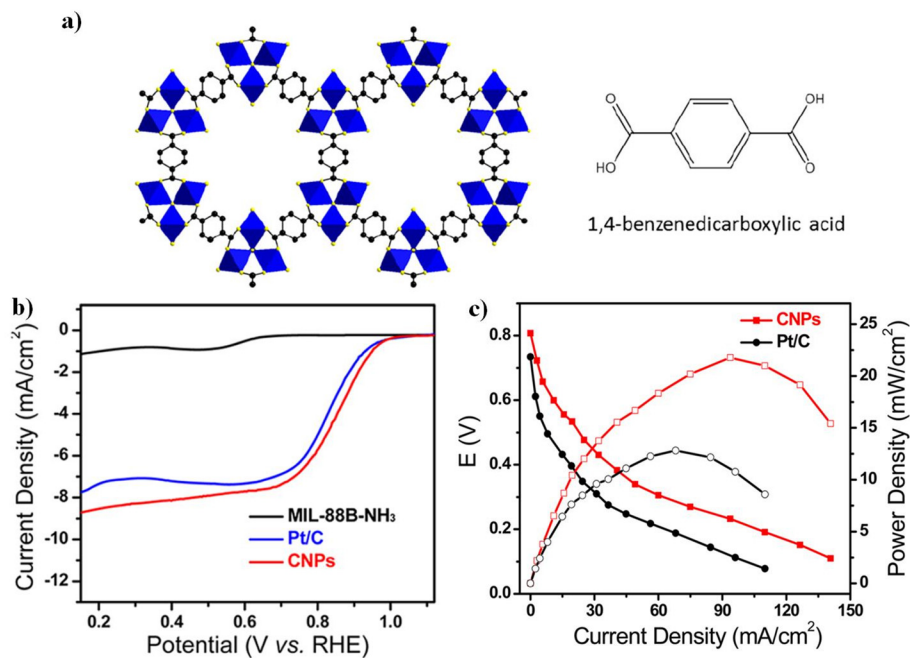


Figure 3.18 (a) Coordination geometry in MIL-88B-NH₃, (b) LSV curves of MIL-88B-NH₃ nanoparticles, CNPs, and Pt/C at a rotation rate of 1600 rpm, (c) ADMFC single-cell performance constructed with CNPs and Pt/C catalysts at 60 °C under the same condition [53].

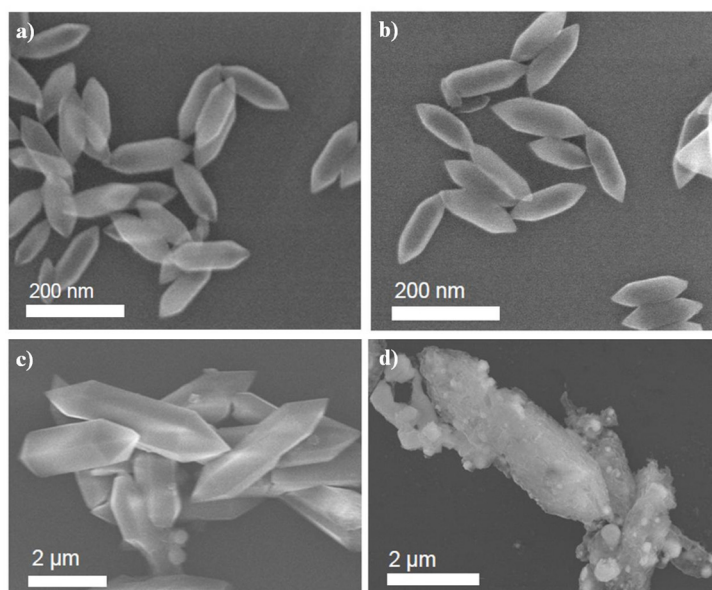


Figure 3.19 (a) SEM image of MIL-88B-NH₃ nanoparticles, (b) SEM image of pyrolyzed MIL-88B-NH₃ nanoparticles, (c) SEM image of MIL-88B-NH₃ microparticles, (d) SEM image of pyrolyzed MIL-88B-NH₃ microparticles [53].

These nanoscale non-PGM electrocatalysts demonstrated electrocatalytic activity toward ORR in 0.1 M KOH solution superior to the commercial Pt/C catalysts (Figure 3.18b). The onset potential of 1.03 V vs. RHE more positive than that of Pt/C (1.01 V vs. RHE) was obtained for these nanoparticles. Furthermore, they provided diffusion-limited current density of 8.31 mA cm⁻² at 0.30 V vs. RHE, much larger than that of commercial Pt/C (7.08 mA cm⁻² at 0.30 V vs. RHE). According to the RRDE measurement results, the number of transported electrons was about 3.98 close to the favourable 4 electron pathway. These electrocatalysts were further tested in an ADMFC setup. Under identical conditions, these electrocatalysts at the cathode side yielded an open circuit voltage of 0.81 V, higher than 0.74 V for the Pt/C cathode, indicating better methanol tolerance of these nanoscales MOF derived electrocatalysts (Figure 3.18c). Furthermore, these electrodes provided a superior ADMFC performance compared to the commercial Pt/C in terms of both peak power density and current density. They reached a peak power density of 22.7 mW cm⁻² and a peak current density of 93.9 mA cm⁻² at the cathode compared with 13.5 mW cm⁻² and 68.1 mA cm⁻² obtained with the Pt/C cathode (Figure 3.18c).

The above discussed literature reveals the great potential of MOFs as precursor for developing effective ORR electrocatalysts. As can be noticed this concept is a very newly released one and it only goes to back to 2011 when the first report on ORR electrocatalyst derived from Co containing ZIF was provided [43]. The current dissertation was defined a year before this time and together with other research groups around the world we were trying to exploit the great inherent potential of MOFs in practice to address existent issues toward PEMFC commercialization. In the coming chapters the outcomes from this research work is presented in terms of four scientific publications.

Chapter 3 References:

- [1] R. Robson, A net-based approach to coordination polymers, *Journal of the Chemical Society, Dalton Transactions* (2000) 3735-3744.
- [2] O.M. Yaghi, M. O'Keeffe, N.W. Ockwig, H.K. Chae, M. Eddaoudi, J. Kim, Reticular synthesis and the design of new materials, *Nature* 423 (2003) 705-714.
- [3] A.F. Wells, Further studies of three-dimensional nets, American Crystallographic Association, 1979.
- [4] K. Biradha, A. Mondal, B. Moulton, M.J. Zaworotko, Coexisting covalent and non-covalent planar networks in the crystal structures of $[M(\text{bipy})_2(\text{NO}_3)_2 \text{ arene}]_n$ ($M = \text{Ni}, 1; \text{Co}, 2$; arene = chlorobenzene, o-dichlorobenzene, benzene, nitrobenzene, toluene or anisole), *Journal of the Chemical Society, Dalton Transactions* (2000) 3837-3844.
- [5] J. Zhang, R. Liu, P. Feng, X. Bu, Organic Cation and Chiral Anion Templated 3D Homochiral Open-Framework Materials with Unusual Square-Planar $M_4(\text{OH})$ Units, *Angewandte Chemie International Edition* 46 (2007) 8388-8391.
- [6] J.-R. Li, J. Sculley, H.-C. Zhou, Metal–Organic Frameworks for Separations, *Chemical Reviews* 112 (2012) 869-932.
- [7] C.-P. Li, M. Du, Role of solvents in coordination supramolecular systems, *Chemical Communications* 47 (2011) 5958-5972.
- [8] M. Eddaoudi, D.B. Moler, H. Li, B. Chen, T.M. Reineke, M. O'Keeffe, O.M. Yaghi, Modular Chemistry: Secondary Building Units as a Basis for the Design of Highly Porous and Robust Metal–Organic Carboxylate Frameworks, *Accounts of Chemical Research* 34 (2001) 319-330.
- [9] H. Abourahma, G.J. Bodwell, J. Lu, B. Moulton, I.R. Pottier, R.B. Walsh, M.J. Zaworotko, Coordination Polymers from Calixarene-Like $[\text{Cu}_2(\text{Dicarboxylate})_2]_4$ Building Blocks: Structural Diversity via Atropisomerism, *Crystal Growth & Design* 3 (2003) 513-519.
- [10] M. Eddaoudi, J. Kim, M. O'Keeffe, O.M. Yaghi, $\text{Cu}_2[\text{o-Br-C}_6\text{H}_3(\text{CO}_2)_2]_2(\text{H}_2\text{O})_2 \cdot (\text{DMF})_8(\text{H}_2\text{O})_2$: A Framework Deliberately Designed To Have the NbO Structure Type, *Journal of the American Chemical Society* 124 (2002) 376-377.
- [11] M. Eddaoudi, J. Kim, N. Rosi, D. Vodak, J. Wachter, M. O'Keeffe, O.M. Yaghi, Systematic Design of Pore Size and Functionality in Isoreticular MOFs and Their Application in Methane Storage, *Science* 295 (2002) 469-472.
- [12] H.K. Chae, D.Y. Siberio-Perez, J. Kim, Y. Go, M. Eddaoudi, A.J. Matzger, M. O'Keeffe, O.M. Yaghi, A route to high surface area, porosity and inclusion of large molecules in crystals, *Nature* 427 (2004) 523-527.
- [13] A.C. Sudik, A.P. Côté, O.M. Yaghi, Metal-Organic Frameworks Based on Trigonal Prismatic Building Blocks and the New “acs” Topology, *Inorganic Chemistry* 44 (2005) 2998-3000.
- [14] A.C. Sudik, A.R. Millward, N.W. Ockwig, A.P. Côté, J. Kim, O.M. Yaghi, Design, Synthesis, Structure, and Gas (N_2 , Ar, CO_2 , CH_4 , and H_2) Sorption Properties of Porous Metal-Organic Tetrahedral and Heterocuboidal Polyhedra, *Journal of the American Chemical Society* 127 (2005) 7110-7118.
- [15] H. Li, M. Eddaoudi, M. O'Keeffe, O.M. Yaghi, Design and synthesis of an exceptionally stable and highly porous metal-organic framework, *Nature* 402 (1999) 276-279.
- [16] J.L.C. Rowsell, O.M. Yaghi, Metal-organic frameworks: a new class of porous materials, *Microporous and Mesoporous Materials* 73 (2004) 3-14.
- [17] J.L.C. Rowsell, A.R. Millward, K.S. Park, O.M. Yaghi, Hydrogen Sorption in Functionalized Metal–Organic Frameworks, *Journal of the American Chemical Society* 126 (2004) 5666-5667.
- [18] M. O'Keeffe, Design of MOFs and intellectual content in reticular chemistry: a personal view, *Chemical Society Reviews* 38 (2009) 1215-1217.

- [19] S. Kitagawa, R. Kitaura, S.-i. Noro, Functional Porous Coordination Polymers, *Angewandte Chemie International Edition* 43 (2004) 2334-2375.
- [20] N.L. Rosi, M. Eddaoudi, J. Kim, M. O'Keeffe, O.M. Yaghi, Infinite Secondary Building Units and Forbidden Catenation in Metal-Organic Frameworks, *Angewandte Chemie International Edition* 41 (2002) 284-287.
- [21] S. Ma, H.-C. Zhou, Gas storage in porous metal-organic frameworks for clean energy applications, *Chemical Communications* 46 (2010) 44-53.
- [22] Y. He, W. Zhou, G. Qian, B. Chen, Methane storage in metal-organic frameworks, *Chemical Society Reviews* 43 (2014) 5657-5678.
- [23] J.-R. Li, R.J. Kuppler, H.-C. Zhou, Selective gas adsorption and separation in metal-organic frameworks, *Chemical Society Reviews* 38 (2009) 1477-1504.
- [24] P. Horcajada, T. Chalati, C. Serre, B. Gillet, C. Sebrie, T. Baati, J.F. Eubank, D. Heurtaux, P. Clayette, C. Kreuz, J.-S. Chang, Y.K. Hwang, V. Marsaud, P.-N. Bories, L. Cynober, S. Gil, G. Ferey, P. Couvreur, R. Gref, Porous metal-organic-framework nanoscale carriers as a potential platform for drug delivery and imaging, *Nat Mater* 9 (2010) 172-178.
- [25] J. Della Rocca, D. Liu, W. Lin, Nanoscale Metal–Organic Frameworks for Biomedical Imaging and Drug Delivery, *Accounts of Chemical Research* 44 (2011) 957-968.
- [26] M.D. Allendorf, C.A. Bauer, R.K. Bhakta, R.J.T. Houk, Luminescent metal-organic frameworks, *Chemical Society Reviews* 38 (2009) 1330-1352.
- [27] M. Kurmoo, Magnetic metal-organic frameworks, *Chemical Society Reviews* 38 (2009) 1353-1379.
- [28] A. Corma, H. García, F.X. Llabrés i Xamena, Engineering Metal Organic Frameworks for Heterogeneous Catalysis, *Chemical Reviews* 110 (2010) 4606-4655.
- [29] A. Dhakshinamoorthy, H. Garcia, Metal-organic frameworks as solid catalysts for the synthesis of nitrogen-containing heterocycles, *Chemical Society Reviews* 43 (2014) 5750-5765.
- [30] J. Gascon, A. Corma, F. Kapteijn, F.X. Llabrés i Xamena, Metal Organic Framework Catalysis: Quo vadis?, *ACS Catalysis* 4 (2014) 361-378.
- [31] J. Mao, L. Yang, P. Yu, X. Wei, L. Mao, Electrocatalytic four-electron reduction of oxygen with Copper (II)-based metal-organic frameworks, *Electrochemistry Communications* 19 (2012) 29-31.
- [32] M. Jiang, L. Li, D. Zhu, H. Zhang, X. Zhao, Oxygen reduction in the nanocage of metal-organic frameworks with an electron transfer mediator, *Journal of Materials Chemistry A* 2 (2014) 5323-5329.
- [33] M. Jahan, Z. Liu, K.P. Loh, A Graphene Oxide and Copper-Centered Metal Organic Framework Composite as a Tri-Functional Catalyst for HER, OER, and ORR, *Advanced Functional Materials* 23 (2013) 5363-5372.
- [34] M. Jahan, Q. Bao, K.P. Loh, Electrocatalytically Active Graphene–Porphyrin MOF Composite for Oxygen Reduction Reaction, *Journal of the American Chemical Society* 134 (2012) 6707-6713.
- [35] P. Pachfule, V.M. Dhavale, S. Kandambeth, S. Kurungot, R. Banerjee, Porous-Organic-Framework-Templated Nitrogen-Rich Porous Carbon as a More Proficient Electrocatalyst than Pt/C for the Electrochemical Reduction of Oxygen, *Chemistry – A European Journal* 19 (2013) 974-980.
- [36] Z. Xiang, D. Cao, L. Huang, J. Shui, M. Wang, L. Dai, Nitrogen-Doped Holey Graphitic Carbon from 2D Covalent Organic Polymers for Oxygen Reduction, *Advanced Materials* 26 (2014) 3315-3320.
- [37] L. Zhang, Z. Su, F. Jiang, L. Yang, J. Qian, Y. Zhou, W. Li, M. Hong, Highly graphitized nitrogen-doped porous carbon nanopolyhedra derived from ZIF-8 nanocrystals as efficient electrocatalysts for oxygen reduction reactions, *Nanoscale* 6 (2014) 6590-6602.
- [38] A. Aijaz, N. Fujiwara, Q. Xu, From Metal–Organic Framework to Nitrogen-Decorated Nanoporous Carbons: High CO₂ Uptake and Efficient Catalytic Oxygen Reduction, *Journal of the American Chemical Society* 136 (2014) 6790-6793.

- [39] H.-x. Zhong, J. Wang, Y.-w. Zhang, W.-l. Xu, W. Xing, D. Xu, Y.-f. Zhang, X.-b. Zhang, ZIF-8 Derived Graphene-Based Nitrogen-Doped Porous Carbon Sheets as Highly Efficient and Durable Oxygen Reduction Electrocatalysts, *Angewandte Chemie International Edition* 53 (2014) 14235-14239.
- [40] P. Zhang, F. Sun, Z. Xiang, Z. Shen, J. Yun, D. Cao, ZIF-derived in situ nitrogen-doped porous carbons as efficient metal-free electrocatalysts for oxygen reduction reaction, *Energy & Environmental Science* 7 (2014) 442-450.
- [41] J. Li, Y. Chen, Y. Tang, S. Li, H. Dong, K. Li, M. Han, Y.-Q. Lan, J. Bao, Z. Dai, Metal-organic framework templated nitrogen and sulfur co-doped porous carbons as highly efficient metal-free electrocatalysts for oxygen reduction reactions, *Journal of Materials Chemistry A* 2 (2014) 6316-6319.
- [42] J.-S. Li, S.-L. Li, Y.-J. Tang, K. Li, L. Zhou, N. Kong, Y.-Q. Lan, J.-C. Bao, Z.-H. Dai, Heteroatoms ternary-doped porous carbons derived from MOFs as metal-free electrocatalysts for oxygen reduction reaction, *Sci. Rep.* 4 (2014).
- [43] S. Ma, G.A. Goenaga, A.V. Call, D.-J. Liu, Cobalt Imidazolate Framework as Precursor for Oxygen Reduction Reaction Electrocatalysts, *Chemistry – A European Journal* 17 (2011) 2063-2067.
- [44] D. Zhao, J.-L. Shui, C. Chen, X. Chen, B.M. Repragle, D. Wang, D.-J. Liu, Iron imidazolate framework as precursor for electrocatalysts in polymer electrolyte membrane fuel cells, *Chemical Science* 3 (2012) 3200-3205.
- [45] D. Zhao, J.L. Shui, L.R. Grabstanowicz, C. Chen, S.M. Commet, T. Xu, J. Lu, D.J. Liu, Highly Efficient Non-Precious Metal Electrocatalysts Prepared from One-Pot Synthesized Zeolitic Imidazolate Frameworks, *Advanced Materials* 26 (2014) 1093-1097.
- [46] E. Proietti, F. Jaouen, M. Lefèvre, N. Larouche, J. Tian, J. Herranz, J.-P. Dodelet, Iron-based cathode catalyst with enhanced power density in polymer electrolyte membrane fuel cells, *Nat Commun* 2 (2011) 416.
- [47] M. Lefèvre, E. Proietti, F. Jaouen, J.-P. Dodelet, Iron-Based Catalysts with Improved Oxygen Reduction Activity in Polymer Electrolyte Fuel Cells, *Science* 324 (2009) 71-74.
- [48] J. Tian, A. Morozan, M.T. Sougrati, M. Lefèvre, R. Chenitz, J.-P. Dodelet, D. Jones, F. Jaouen, Optimized Synthesis of Fe/N/C Cathode Catalysts for PEM Fuel Cells: A Matter of Iron–Ligand Coordination Strength, *Angewandte Chemie* 125 (2013) 7005-7008.
- [49] A. Morozan, M.T. Sougrati, V. Goellner, D. Jones, L. Stievano, F. Jaouen, Effect of Furfuryl Alcohol on Metal Organic Framework-based Fe/N/C Electrocatalysts for Polymer Electrolyte Membrane Fuel Cells, *Electrochimica Acta* 119 (2014) 192-205.
- [50] P. Su, H. Xiao, J. Zhao, Y. Yao, Z. Shao, C. Li, Q. Yang, Nitrogen-doped carbon nanotubes derived from Zn-Fe-ZIF nanospheres and their application as efficient oxygen reduction electrocatalysts with in situ generated iron species, *Chemical Science* 4 (2013) 2941-2946.
- [51] T. Palaniselvam, B.P. Biswal, R. Banerjee, S. Kurungot, Zeolitic Imidazolate Framework (ZIF)-Derived, Hollow-Core, Nitrogen-Doped Carbon Nanostructures for Oxygen-Reduction Reactions in PEFCs, *Chemistry – A European Journal* 19 (2013) 9335-9342.
- [52] W. Xia, J. Zhu, W. Guo, L. An, D. Xia, R. Zou, Well-defined carbon polyhedrons prepared from nano metal-organic frameworks for oxygen reduction, *Journal of Materials Chemistry A* 2 (2014) 11606-11613.
- [53] S. Zhao, H. Yin, L. Du, L. He, K. Zhao, L. Chang, G. Yin, H. Zhao, S. Liu, Z. Tang, Carbonized Nanoscale Metal–Organic Frameworks as High Performance Electrocatalyst for Oxygen Reduction Reaction, *ACS Nano* 8 (2014) 12660-12668.

Chapter 4 Electrocatalyst synthesized from metal organic frameworks

Foroughzham Afsahi, Hoang Vinh-Thang, Serguei Mikhailenko, Serge Kaliaguine*

Department of Chemical Engineering, Laval University, Québec (Québec), Canada, G1V 0A6

Published in Journal of Power Sources (239) 2013 415-423

Résumé

Des nanoparticules de Pt qui constituent l'électrocatalyseur habituel pour les piles à combustible à membrane échangeuse de protons (PEMFC) ont été préparées pour la première fois à partir de réseaux organiques métalliques (MOF). Un MOF contenant du Pt a été synthétisé et ensuite soumis à une carbonisation par pyrolyse sous atmosphère de gaz non réactif. Lors de la pyrolyse, des nanoparticules de Pt incorporées dans un milieu de carbone conducteur ont été produites. Les matériaux MOFs tels que synthétisés et les électrocatalyseurs préparés ont été caractérisés par DRX, physisorption d'azote, TEM et XPS. La dispersion du Pt dans les électrocatalyseurs obtenus a été déterminée par chimisorption d'hydrogène. Leur conductivité a été mesurée par spectroscopie d'impédance. Les ensembles membrane-électrodes (MEAs) fabriquées avec ces électrocatalyseurs ont été testés à la fois comme anode et comme cathode dans un pile à combustible H₂/air à un seul élément. Comme anode, l'électrocatalyseur le plus prometteur (C3) a démontré une tension en circuit ouvert de 970 mV et une densité de puissance de $0,58 \text{ W mg}_{Pt}^{-1}$ comparable à la densité de puissance d'électrodes commerciales ($0,64 \text{ W mg}_{Pt}^{-1}$) à 0,6 V dans un test à une seule cellule. A la cathode, une densité de puissance de $0,38 \text{ W mg}_{Pt}^{-1}$ à 0,6 V a été atteinte. Cela confirme le potentiel prometteur de cette approche simple comme technique pour préparer des électrocatalyseurs efficaces de piles à combustible.

Abstract

Pt nanoparticles as the common electrocatalyst for proton exchange membrane fuel cells (PEMFCs) were prepared for the first time from metal organic frameworks (MOFs). Pt containing MOF was synthesized and subsequently subjected to pyrolytic carbonization under non-reactive gas atmosphere. Upon pyrolysis, Pt nanoparticles embedded in electronically conductive carbon media were produced. The as-synthesized MOF materials and the prepared electrocatalysts were characterized by XRD, N₂ physisorption, TEM and XPS. The Pt dispersion of obtained electrocatalysts was determined by hydrogen chemisorption. Their conductivity was measured by impedance spectroscopy. The membrane electrode assemblies (MEAs) made of these electrocatalysts were tested as both anode and cathode in a H₂/air single cell fuel cell. As the anode, the most promising electrocatalyst (C₃) demonstrated an open circuit voltage of 970 mV and power density of $0.58 \text{ W mg}_{Pt}^{-1}$ comparable to the commercial electrode power density ($0.64 \text{ W mg}_{Pt}^{-1}$) at 0.6 V in a single cell test. At the cathode, a power density of $0.38 \text{ W mg}_{Pt}^{-1}$ at 0.6 V was achieved. This confirms the promising potential of this simple approach to be used as a technique to prepare efficient fuel cell electrocatalysts.

4.1 Introduction

Proton exchange membrane fuel cells (PEMFCs) operated on hydrogen fuel and air (or oxygen), are considered as promising electrical power sources. Unlike internal combustion engines, PEMFCs provide high energy conversion efficiency at relatively low operating temperatures with zero or low greenhouse gas emissions [1,2]. In spite of these advantages, the high cost of PEMFCs mostly related to platinum (Pt)-based electrocatalysts strongly impedes their large-scale commercialization [3,4].

Extensive efforts toward developing effective non-platinum group metal (non-PGM) catalysts during past decades have failed to provide both high activity comparable to Pt and long-term stability under practical fuel cell operating conditions. Therefore, Pt or Pt alloys are remaining as the only realistic choice at least until some phenomenal innovation happens in the development of these materials [5-7]. In this context, it is vital to develop appropriate strategies to reduce Pt content and maximize Pt utilization in the electrodes.

Pt nanoparticles ranging from 2 to 3 nm in size supported on carbon black (CB) with high specific surface area represent the most widely used catalyst material for PEMFC. Apart from the particle size, a significant role in catalytic activity of metal nanoparticles is played by the particle shape [8] and the structural features of a catalyst support [9].

In order to minimize the Pt loading and maximize its utilization, while reaching high catalytic activity, numerous synthetic approaches have been attempted. Most of these techniques involve first the formation of a conductive and porous carbon support followed by deposition of Pt onto the support. Pt deposition is most commonly performed by wet chemical method (impregnation with a soluble salt followed by reduction) [10]. Other methods such as atomic layer deposition [11], vacuum deposition [12], etc., have been used less frequently. All these methods have some limitations regarding effective Pt dispersion and therefore do not allow maximum catalyst utilization to be achieved. They mainly bring about the metal particles, distributed in a stochastic manner on the surface of carbon support with sizes higher or at best equal to 2 nm. The broad size distribution of the catalyst particles along with randomness of their spatial scattering are the main obstacles toward developing efficient catalysts with a regular structure and controlled properties.

In the present study, a Pt-based metal organic framework (MOF) is synthesized and applied as a novel precursor for preparing PEMFC electrocatalyst. The synthesized material is subsequently pyrolyzed to form a carbon based support and provide electronic conductivity. MOF materials as the name suggests, are frameworks comprised of metal ions or metal ion clusters linked together by bifunctional organic ligands [13,14]. These highly crystalline structures possess a set of unique characteristics, such as high specific surface area, various pore sizes and geometry, and diverse surface composition, which leads to extensive investigations toward many important applications such as gas storage [15-17], gas separation [18-22], drug delivery [23-25], and catalysis [26-28]. Furthermore, MOF materials have been used as a template and/or carbon source to synthesize nanoporous carbon (NPC) materials with high specific surface area [29-31].

The application of MOFs as electrocatalyst in fuel cell is a quite novel approach. Zeolitic imidazolate frameworks (ZIFs) as a subclass of MOFs have been investigated as precursors for non-PGM electrocatalysts [32-34]. Co [32] and Fe [34] imidazolate frameworks, in which each metal atom is coordinated with four nitrogen atoms of imidazolate ligands to form Co (or Fe) N_4 moieties regularly dispersed in the framework, are used as ORR catalyst precursors. However, the catalytic performances of these materials in PEMFCs are not reported. In another approach [33], ZIF-8 (Zn(II) zeolitic imidazolate framework), with a high nitrogen content and high microporous surface area, is used as the host for Fe and N precursors for preparing PEMFCs catalysts. The highest volumetric activity of 230 A cm⁻³ at 0.8 V_{iR-free}, reported to date is measured for non-PGM-based ORR catalysts in PEMFCs. In this work, we report for the first time a Pt-based MOF material as a precursor to prepare PEMFC electrocatalysts. MOFs have clearly-defined three-dimensional crystalline structures in which metal species are distributed evenly through the crystal. Using Pt containing MOFs as a precursor is expected to provide the high and uniform dispersion of active sites required for an ideal performance of PEMFC electrocatalyst. In addition, the organic linkers can be carbonized via pyrolysis, while maintaining the porous framework, leading to catalysts with high surface area and uniformly distributed active sites. Carbonization will also provide electron conductive media. Therefore, there will be no need for a preformed carbon support which is an essential part of traditional FC electrocatalysts.

4.2 Experimental

4.2.1 Synthesis of Pt-based MOF

Pt-based MOF-253 materials as the electrocatalyst precursor were synthesized in two steps according to the reported procedure [35]. To synthesize MOF-253 (first step), 0.625 mmol (151 mg) of $\text{AlCl}_3 \cdot 6\text{H}_2\text{O}$ was dissolved in DMF (10 mL), followed by the addition of 0.625 mmol (153 mg) of 2,2'-bipyridine-5,5'-dicarboxylic acid (bpydc) (Figure 4.1a). The obtained mixture was then placed in a Teflon-capped vial and heated at 120 °C for 24 h. The resulting white microcrystalline powder was then filtered and washed with DMF. To obtain fully desolvated framework, this powder was subsequently washed with methanol via soxhlet extraction for 24 h, then collected by filtration and finally dried at 180 °C under dynamic vacuum for 12 h. In order to introduce Pt atoms (second step), 1.75 mmol (500 mg) of the desolvated MOF-253 was mixed with 1.11 mmol (386 mg) of $\text{PtCl}_2(\text{CH}_3\text{CN})_2$ and acetonitrile (15 mL) (Figure 4.1b). This mixture was then heated at 85 °C in a Teflon-capped vial for 72 h. The resulting solid was collected by filtration and immersed in acetonitrile (15 mL). The total immersion time was three days and the solvent was replaced with fresh acetonitrile after each 24 h. Finally, the product (hereafter referred to as Pt-MOF) was collected by filtration and dried at 150 °C for 12 h under vacuum.

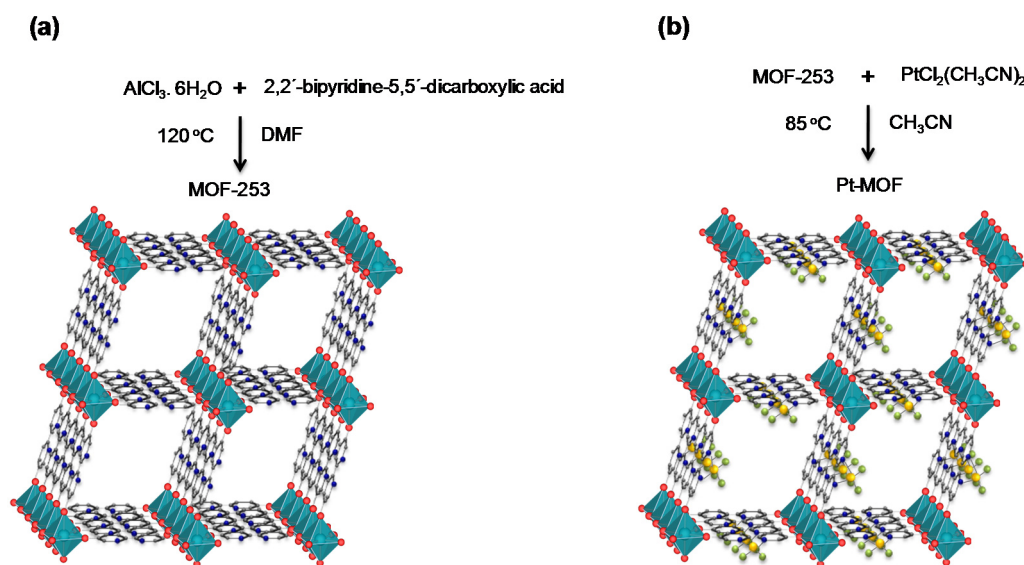


Figure 4.1 Synthesis and structure of Pt-MOF. Al atoms (cyan octahedra), yellow, green, red, blue, and gray spheres stand for Pt, Cl, O, N, and C atoms, respectively; H atoms are omitted for simplicity.

4.2.2 Pyrolytic transformation of the Pt-based MOF into electrocatalysts

To prepare the PEMFC electrocatalysts, the Pt-MOF materials were heat treated at temperatures ranging between 700 to 1050 °C. A quartz tube (6 mm diameter) containing 150 mg of the sample was weighed and placed inside a furnace. The tube was sealed airtight and then purged with argon for 1 h prior to the treatment. The materials were typically heated at the ramp rate of 1 °C min⁻¹ for 4 h under flow of argon at a rate of 20 mL min⁻¹. The yield after the heat treatment was normally about 50 wt%. A set of four batches of electrocatalyst were prepared, which were designated as C₁-C₄ for samples pyrolyzed at 700, 800, 950 and 1050 °C, respectively.

4.2.3 Characterization of the synthesized Pt-MOF and electrocatalysts

The phase identification and crystallinity of the synthesized Pt-MOF and the prepared electrocatalysts were determined by X-ray diffraction (XRD) using a SIEMENS D5000 diffractometer with Cu K α radiation ($\lambda = 0.15406$ nm). Phase recognition was obtained by comparison to Joint Committee on Powder Diffraction Standards (JCPDS) files. The specific surface areas of the Pt-MOF and C₁-C₄ electrocatalysts were established by Brunauer-Emmett-Teller (BET) analysis of the nitrogen adsorption-desorption isotherms recorded at -196 °C using a Quantachrome instrument. All the samples were degassed by heating at 150 °C under vacuum prior to measuring the surface area. The BET specific surface areas (S_{BET}) were calculated from the isotherm analysis in the relative pressure range, where a linear BET plot with positive C constant was obtained. The total pore volumes were calculated at $P/P_0 = 0.95$. The transmission electron microscopy (TEM) images were obtained using a Jeol JEM 1230 operated at 120kV. X-ray photoelectron spectroscopy (XPS) was performed on a Kratos Axis Ultra spectrometer using a monochromatic Al K α source operating at 300 W. The survey and high-resolution spectra were acquired at pass energies of 160 eV and 20/40 eV, respectively. The electrical conductivity of the electrocatalysts (σ) was measured at room temperature by impedance spectroscopy over the frequency range of 1-1,000,000 Hz with a voltage of 0.1 V using an SI 1260 impedance/gain-phase analyser from Solartron (Farnborough, Hampshire, UK). The pyrolyzed sample (~ 50 mg) was compressed in a hollow glass cylinder (with an inner diameter of 6 mm) between two metal plungers at thrust

pressure of 1.04 MPa. The electrical connections to the impedance analyzer are at the end of each of those pistons. The very small sample thickness l (cm) was measured with a calliper as a difference between plunger distance in empty and filled cell. The electrical conductivity was calculated using equation (4.1):

$$\sigma = \frac{l}{R.A} \quad (4.1)$$

where R is the resistance (Ω) and A is the area of the plunger surface (cm^2). The dispersion of platinum on electrocatalyst samples was measured by hydrogen chemisorption using a RXM-100 multicatalyst testing and characterization system (Advanced Scientific Design Inc.). The first H_2 adsorption isotherm was measured at room temperature, followed by outgassing for 1 h prior to a second H_2 adsorption isotherm determination under the same conditions. The Pt content of the electrocatalysts was measured using atomic absorption spectroscopy. The analysis was carried out using a Perkin-Elmer 1100B atomic absorption spectrometer. The carbon component was first removed by dry-ashing the catalysts in air at $900\text{ }^\circ\text{C}$. The ash residue was then digested in aqua regia and the resultant solution was filtered and diluted with de-ionized water to the appropriate concentration.

4.2.4 Performance tests of membrane-electrode assemblies (MEAs)

The catalyst ink was prepared by ultrasonic blending of the electrocatalysts with Nafion[®] solution (5 wt%, Sigma-Aldrich) in isopropyl alcohol for 2 h. To create the anode or cathode, this ink was then applied to the commercial gas diffusion layer (GDL, BASF) by successive brushing until the Pt loading of $\sim 0.5\text{ mg cm}^{-2}$ was reached. The Nafion[®] content in the dry electrocatalyst was maintained at ca. 20 wt%. A commercially available gas-diffusion electrode (GDE, BASF, $0.5\text{ mg}_{\text{Pt}}\text{ cm}^{-2}$) was used at the other side without any further processing. The cathode and anode were applied to a Nafion[®]NRE-212 membrane to fabricate the membrane electrode assembly (MEA). The geometric active area of the MEA was 2 cm^2 . Fuel cell testing was carried out in a single cell. Hydrogen and air, humidified at $80\text{ }^\circ\text{C}$, were supplied to the anode and cathode at flow rates of 120 and 250 mL min^{-1} , respectively. Both electrodes were maintained at the same backpressure of 30 psig.

Polarization experiments were conducted using a test station (Fideris™ Hydrogen Test Kit™) at cell temperature of 80 °C.

4.3 Results and discussion

4.3.1 Characteristic properties

In MOF-253, one-dimensional chains of hydroxide-bridged, octahedrally coordinated Al^{3+} cations are linked via bpydc²⁻ ligands to give a three-dimensional framework with rhombic channels (Figure 4.2) [35]. According to the previous observations upon insertion within the framework, the Pt atom is expected to fit the usual square planar geometry, with two Cl^- ions and two N atoms from bpydc [35].

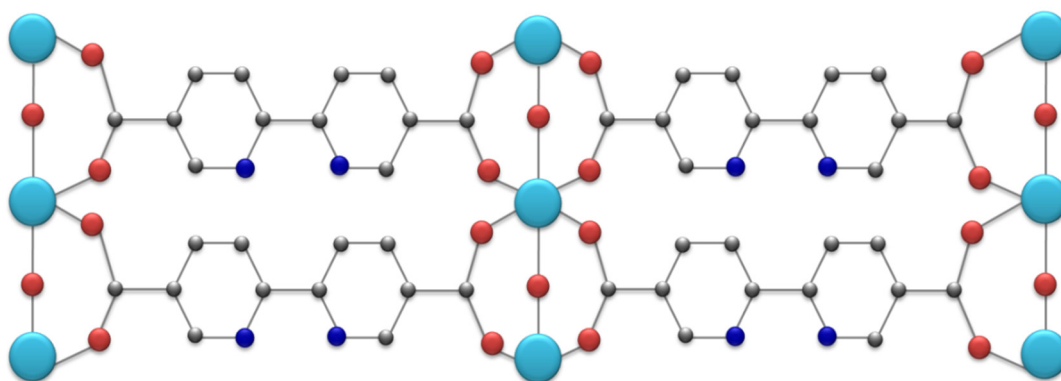


Figure 4.2 (001) view of MOF-253 crystal

As shown in Figure 4.3a, XRD pattern of Pt-MOF exhibits similar diffraction peaks to that of the synthesized MOF-253 (and the previously reported Pd-MOF [35]), confirming that the MOF-253 structure is retained. To produce the PEMFC electrocatalysts, the Pt-MOF was pyrolyzed under flow of Ar atmosphere to form Pt nanoparticles. It was also expected that during pyrolysis the organic part of the synthesized Pt-MOFs would be carbonized to produce carbon, which provides the required electronic conductivity. In order to study the effect of pyrolysis temperature, the Pt-MOF was pyrolyzed at 700, 800, 950, and 1050 °C. The evidence for the formation of Pt nanoparticles was clearly verified by XRD analysis. Figure 4.3b shows the XRD patterns of the four carbonized Pt-MOF samples (C₁-C₄). In all cases, the diffraction peaks observed at around $2\theta = 40^\circ$, 46° , 68° , and 81° were attributed to Pt (111), (200), (220), and (311) crystalline planes, respectively, representing typical crystalline Pt face-centered cubic (fcc) structure. It can also be seen from Figure 4.3b that Al although

present in high content is not XRD visible. In addition, the XRD patterns did not show any trace of Pt oxide phases.

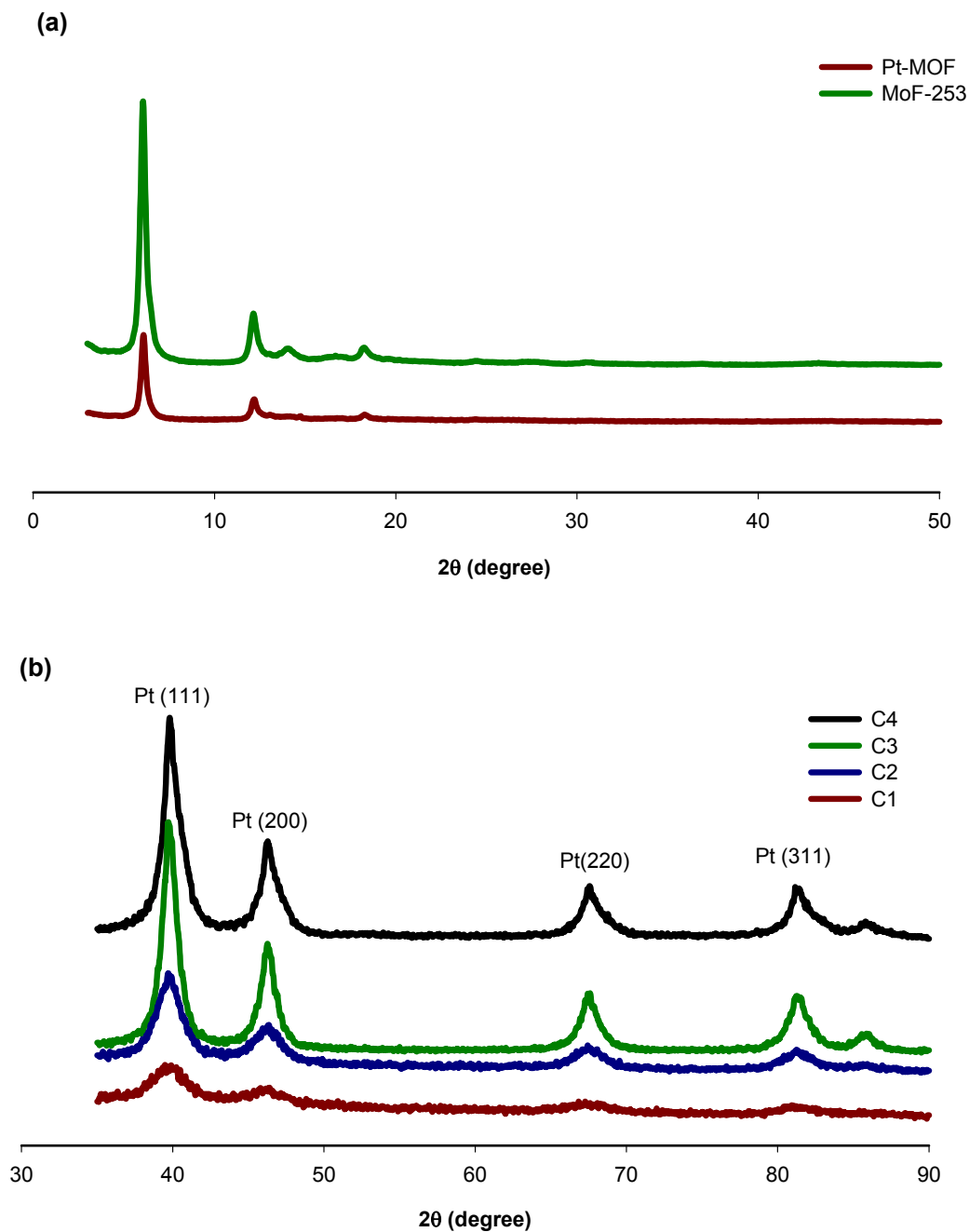


Figure 4.3 XRD patterns of (a) MOF-253 and Pt-MOF (b) carbonized C₁-C₄ samples

For these samples, the diffraction peaks are indeed broad, confirming the formation of small Pt crystal domains. The average Pt crystal domain sizes were calculated from the Pt (220)

reflection using Scherrer equation. Table 4.1 shows that the Pt crystal domain sizes in the carbonized samples were between 7 and 10 nm. With increasing carbonization temperature, the Pt crystal domain sizes first decreased and then increased. This most probably reflects the competition of two simultaneous processes occurring during the pyrolytic transformation of the Pt-MOF: 1) the formation of germinal Pt nanoparticles, 2) the coalescence of these nanoparticles to form larger Pt particles. As can be seen from Table 4.1, the minimum Pt crystal domain size was found for the sample carbonized at 800 °C (C₂), confirming the initial nanoparticle formation. At higher temperatures the coalescence of Pt crystal domains prevailed over formation of the initial Pt nanoparticles giving rise to bigger average crystal domain size.

Table 4.1 Average Pt particle size of the carbonized C₁-C₄ samples

Electrocatalyst	Platinum average particle size (nm)
C ₁	7.8
C ₂	7.4
C ₃	7.7
C ₄	9.2

Nitrogen adsorption-desorption isotherms of the MOF-253 and Pt-MOF (see Figure 4.4a) reveal a type I adsorption isotherm characteristic of a microporous solid. Table 4.2 shows reduced BET specific surface area and pore volume of the Pt-MOF compared to those of the MOF-253. The shape of isotherms of the carbonized Pt-MOF indicates the existence of both micropores and mesopores (see Figure 4.4b). The steep increase at low relative pressure demonstrates the presence of micropores. The type IV isotherm with a capillary condensation step and a hysteresis loop near relative pressure (P/P_0) of ~ 0.5 in the desorption branch indicates the presence of mesopores. The pore size distributions were determined by using NLDFT method considering sorption of N₂ at -196 °C in slit/cylindrical carbon pores. The kernel of equilibrium NLDFT isotherms (desorption branch) was applied for pore width determination. As can be seen from the inset of Figure 4.4b, the majority of pores are located in the mesopore region. This mesopore size corresponded to that of nanoporous carbon formed by carbonization of Pt-MOF. The presence of micropores (~ 10 Å equal to that of Pt-MOF) is reminiscent of the MOF structure. All samples display similar pore size distribution

with a peak centered at ca. 5.0 nm, except for sample C₂ which shows an additional mode centered at 7.5 nm. As can be seen in Table 4.2, the specific surface areas and pore volumes did not vary too much with calcination temperature indicating evidently a minor restructuration of the carbon support above 700 °C. However, the platinum phase was affected by calcination more strongly, according to the following results.

Table 4.2 BET specific surface areas and pore volumes of the MOF materials and carbonized C₁-C₄ samples

	S _{BET}	V _{pore}
	m ² gr ⁻¹	cm ³ gr ⁻¹
MOF-253	1155	0.51
Pt-MOF	540	0.27
C ₁	165	0.23
C ₂	160	0.22
C ₃	165	0.26
C ₄	185	0.25

TEM images (Figure 4.5) of the carbonized Pt-MOFs reveal that all C₁-C₄ samples were amorphous carbon with a “foam-like” porous texture with embedded dark spherically shaped Pt nanoparticles. Figure 4.5 shows that the size distribution of Pt particles is temperature dependent. The calculated average particle diameters are 3.5, 5.0, 6.2 and 7.2 for C₁, C₂, C₃ and C₄, respectively. TEM analysis of the electrocatalysts shows agreement with rough XRD evaluation of Pt crystal domain sizes (Table 4.1).

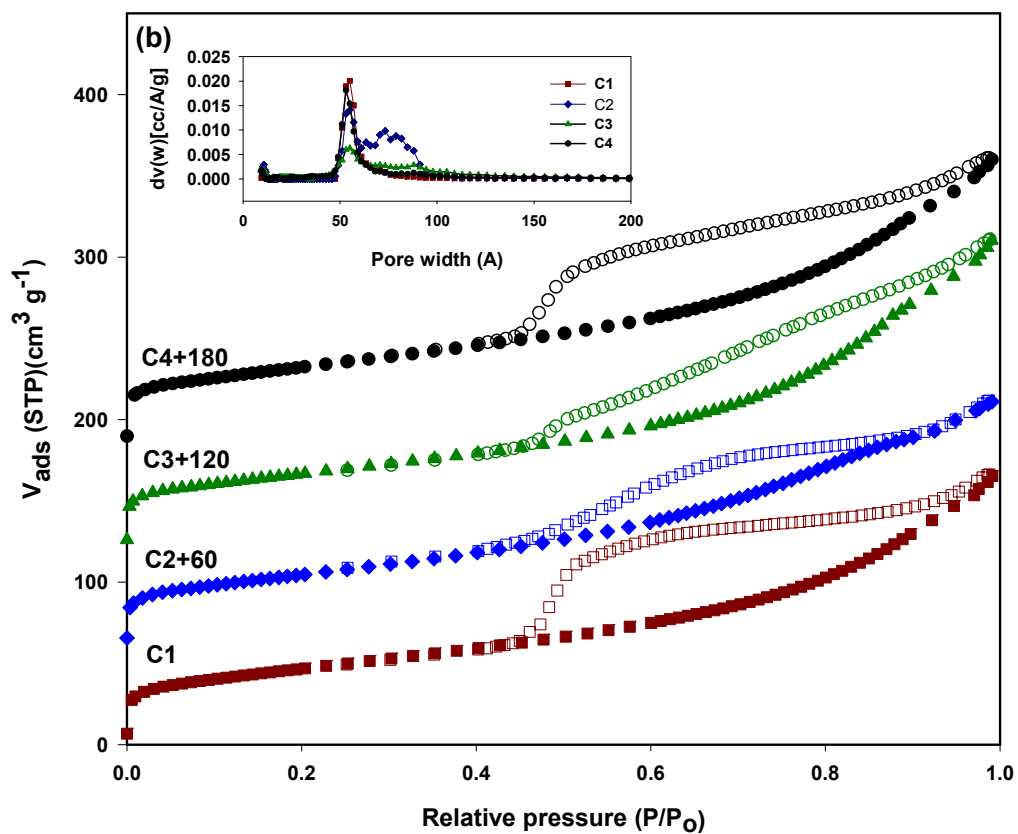
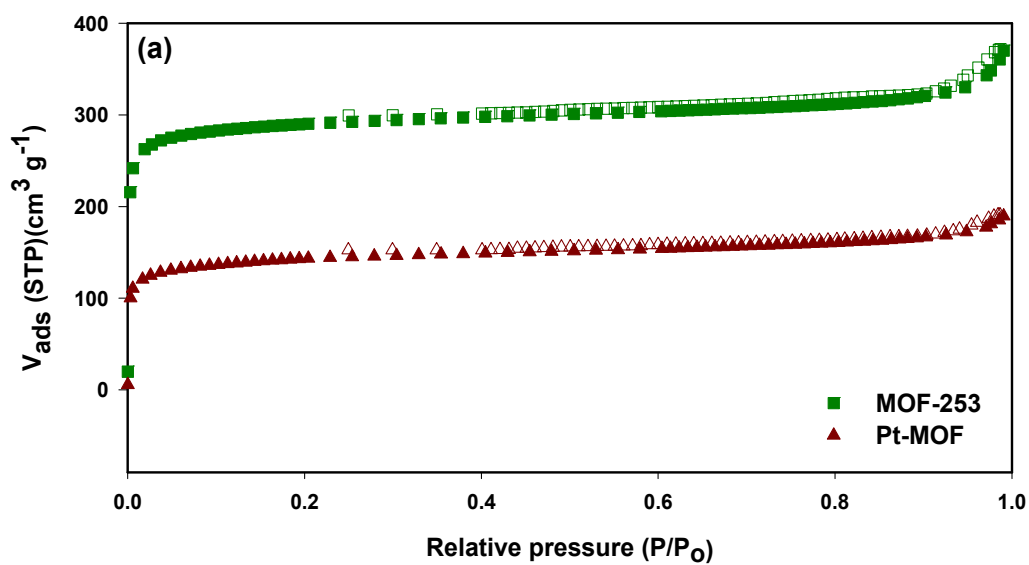


Figure 4.4 N₂ adsorption-desorption isotherms of (a) MOF-253 and Pt-MOF (b) carbonized C₁-C₄ samples (closed: adsorption; open: desorption)

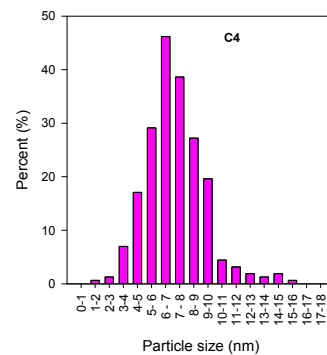
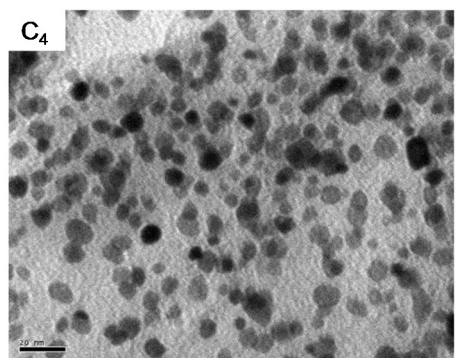
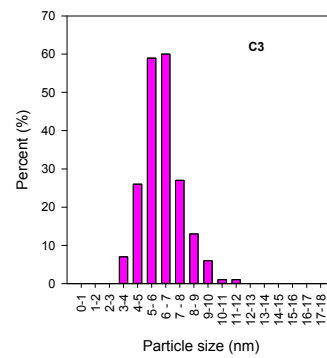
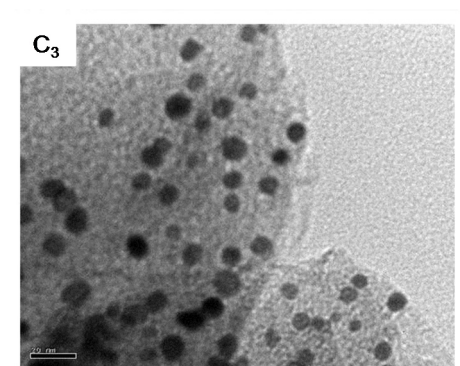
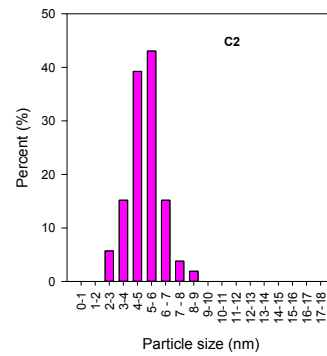
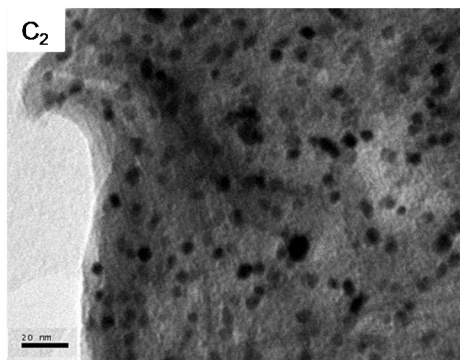
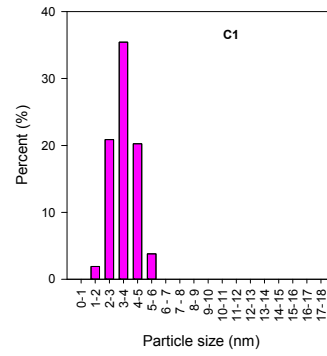
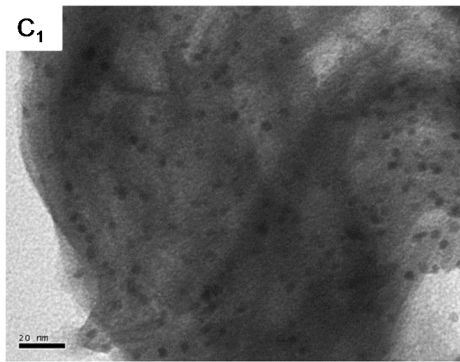


Figure 4.5 TEM images and their corresponding histograms of particle size distribution of C1-C4 (the length of the bar in each photograph is 20nm)

X-Ray photoelectron spectroscopy (XPS) was used to characterize the nature of platinum and carbon species of the prepared electrocatalysts, as exemplified by the results obtained from the C₁ and C₄ samples (carbonized respectively at the minimal and maximal temperatures in this study). The Pt 4*f* XPS spectrum of C₁ (Figure 4.6a) could be deconvoluted into two pairs of doublets with weak peaks centered at binding energies of 71.2 and 74.6 eV, respectively. These two peaks are attributed to Pt 4*f*_{7/2} and Pt 4*f*_{5/2} excitations of metallic platinum, whereas the other intense peaks at 72.3 and 75.6 eV are due to oxidized platinum. In contrast for C₄, the Pt XPS spectrum (Figure 4.6b) demonstrates only one pair of doublet with intense peaks centered at binding energies of 71.4 and 74.7 eV, respectively. These results indicate that a substantial amount of Pt was reduced to metallic Pt(0) during pyrolysis at higher temperatures. The C 1s XPS spectrum of the C₁ and C₄ samples (Figures 4.6c and 4.6d, respectively) consist of a peak at ca. 284.6 eV, which could be attributed to the sp² graphitic carbon species. For C₄, this peak has a full-width at half-maximum (FWHM) linewidth of 0.92 eV, close to that of the graphitized carbon black (0.82 eV) [36-38], revealing a well-ordered packing of graphene layers. However, in the case of C₁, this peak is broader with (FWHM) linewidth of 1.52 eV, suggesting the presence of less ordered graphene layers compared to the graphitized carbon black. In addition, N 1s XPS experiments showed the presence of pyridinic and pyrrolic N in these samples (Figures 4.6e and 4.6f).

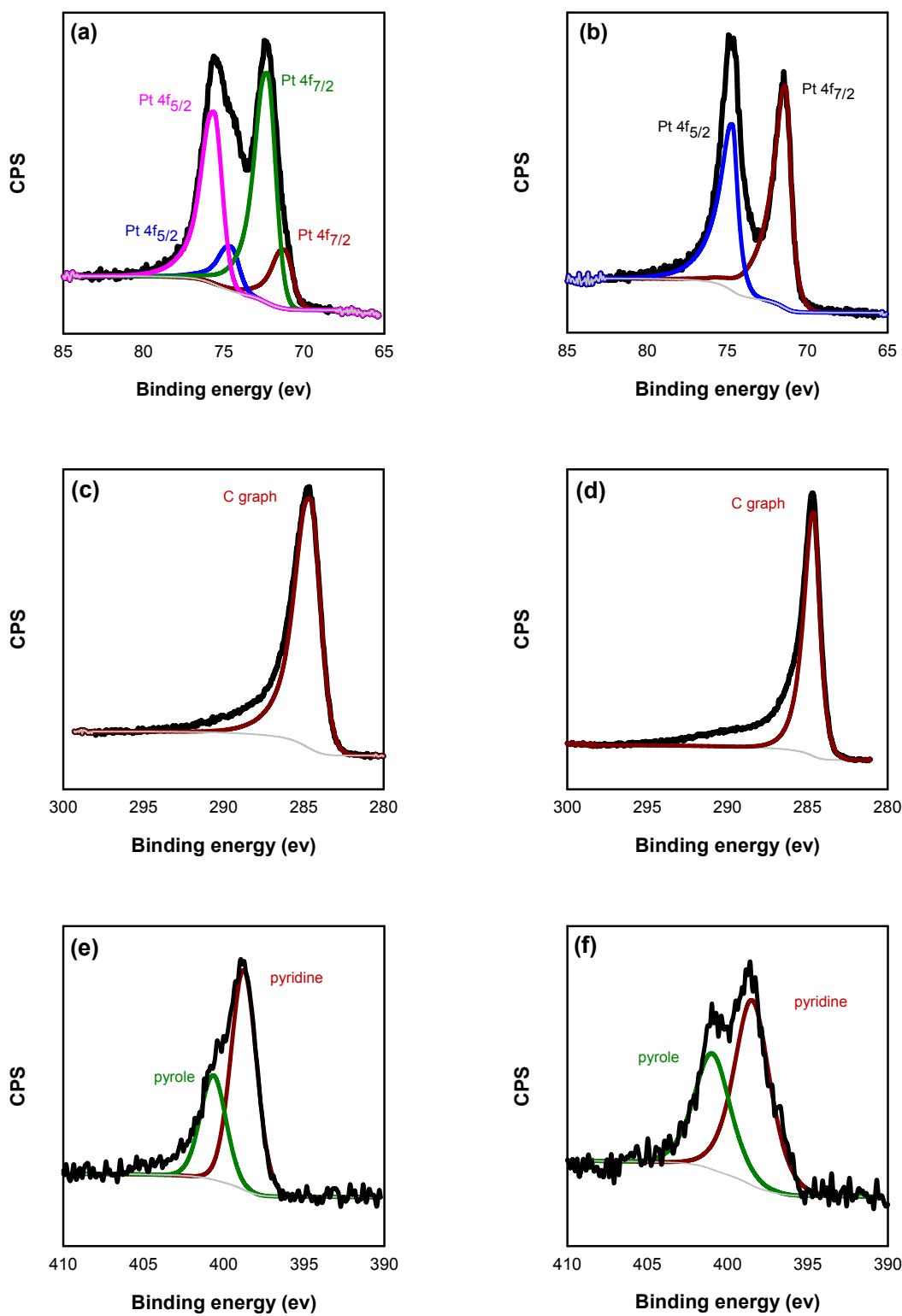


Figure 4.6 Pt 4f XPS spectra of (a) C₁ and (b) C₄, C 1s XPS spectra of (c) C₁ and (d) C₄, and N 1s XPS spectra of (e) C₁ and (f) C₄

The results of complex impedance spectroscopy experiments carried out at room temperature are shown in Figure 4.7. A plateau on $\text{Re}(Z)$ versus frequency plot is observed at frequencies below 10-100 kHz for all four samples. The absence of electrode effects and diffusion phenomena at low frequencies definitely evidences existence of an electronic component in the conductivity of all four samples. It can be seen that the resistance of the electrocatalysts decreased with calcination temperature from 320 Ω to 1.8 Ω with corresponding rise of conductivity from 0.0024 S cm^{-1} to 0.4 S cm^{-1} .

As can be seen in Figure 4.7a, the less conductive samples C_1 and C_2 demonstrates resistance decrease at higher frequencies (> 100 kHz), which most probably can be attributed to the existence of an ionic conductance in these samples along with electronic component. In the same frequency range (> 100 kHz), the resistance values are raised above the plateaux for samples C_3 and C_4 (Figure 4.7b), which can be ascribed to inductive distortions of the impedance response, accompanied by positive values of $\text{Im}(Z)$ (Nyquist plot is not shown). It must be noted that these two samples show purely electronic conductance.

The origin of electronic conductivity in the pyrolyzed MOFs is obviously related to the graphitized carbon and partially to metallic Pt as follows from the results of XPS analysis. The conductivity of C_4 sample was found to be 0.4 S cm^{-1} , which is only one order of the magnitude lower than that of Vulcan XC-72 (4 S cm^{-1}) [39].

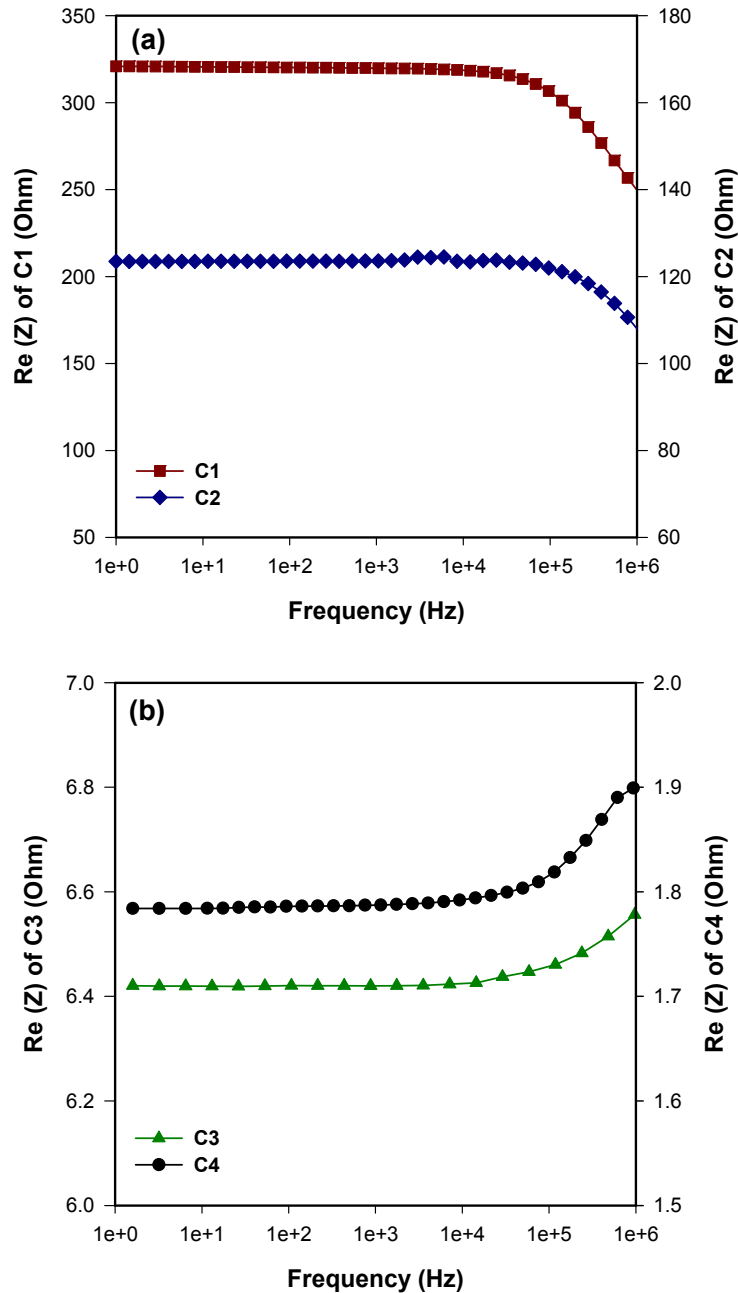


Figure 4.7 Re (Z) vs. frequency for (a) C₁ and C₂ (b) C₃ and C₄ samples

In Table 4.3, the values of Pt dispersion obtained from the hydrogen chemisorption isotherms are summarized. The C₁ and C₂ electrocatalysts carbonized at relatively lower temperatures exhibit slightly better dispersion compared to C₃ and C₄ samples. The average size of the Pt particles (d) can be obtained from the dispersion (N_S/N_T) resorting to the equation developed by van der Klink [40]:

$$N_T = 2\pi/3 (d/a)^3 \quad (4.2)$$

$$N_T = (10/3)l^3 - 5l^2 + (11/3)l - 1 \quad (4.3)$$

$$N_S = 10l^2 - 20l + 12 \quad (4.4)$$

where N_T is the total number of atoms, N_S is the number of surface atoms, l is the number of atomic layers, and a is the lattice parameter, which is equal to 0.392 nm for Pt. It can be observed in Table 4.3 that, the Pt dispersion values of all electrocatalysts correlate with the Pt particle sizes determined by XRD.

Table 4.3 Pt dispersion and average particle size of carbonized C₁-C₄ samples determined by H₂ chemisorption

	Dispersion	Pt average particle size (d)
	%	nm
C ₁	24	5.3
C ₂	29	4.2
C ₃	22	5.8
C ₄	20	6.1

4.3.2 Single cell polarization test

Since only samples C₃ and C₄ showed a pure electronic conductivity of a few S cm⁻¹, these two samples were tested in a fuel cell. The primary investigation showed that the presence of Al in these electrocatalysts reduce their catalytic performance in the fuel cell, therefore, these samples were base-leached in 5 wt% NaOH solution at 70 °C for 6 h to remove inactive Al species from the electrocatalysts, and then thoroughly washed in de-ionized water until neutral pH. XRD patterns and TEM images showed no changes in Pt particle size upon this leaching step. Single-cell performance of the MEAs made with C₃ and C₄ electrocatalysts as the anode and a commercial electrode (BASF, 0.5 mg_{Pt} cm⁻²) as the cathode is shown in Figure 4.8. For comparison, the single-cell performance of the MEA made with commercial electrode for both anode and cathode is also included. The Pt loading was maintained at 0.5 mg cm⁻² on each electrode. The anode fabricated from C₃ electrocatalyst showed an open circuit voltage (OCV) of ~ 970 mV almost equal to the OCV of commercial electrode (~ 960

mV). However, in the case of anode made of C₄ electrocatalyst the OCV was somewhat smaller (~ 950 mV). Figure 4.8 demonstrates that the anode prepared using C₃ electrocatalyst shows very similar power and polarization curves to the commercial electrode, especially in the kinetic range (low-current density). At a fixed cell voltage of 0.6 V, the current density of this electrode is 482 mA cm⁻², which is comparable to the commercial electrode (537 mA cm⁻²). However, for the anode fabricated from C₄ electrocatalyst, the current density is 427 mA cm⁻², which is 20% smaller than that of the commercial electrode. The corresponding power densities normalized on the basis of Pt loading were 0.58 W mg_{Pt}⁻¹ (C₃ based anode), 0.51 W mg_{Pt}⁻¹ (C₄ based anode) and 0.64 W mg_{Pt}⁻¹ (commercial electrode) at 0.6 V. Unlike the anode side, the performance of the cathode electrode (Figure 4.9) prepared from C₃ deviates from the commercial electrode. This deviation is again more pronounced in the case of cathode fabricated from C₄. At a fixed cell voltage of 0.6 V, the current density of the cathode prepared from C₃ and C₄ electrocatalysts were found to be 317 and 234 mA cm⁻², respectively, which is 40 and 56 % smaller than that of the commercial electrode (537 mA cm⁻²). The corresponding power densities normalized on the basis of Pt loading were 0.38 W mg_{Pt}⁻¹ (C₃ based cathode), 0.28 W mg_{Pt}⁻¹ (C₄ based cathode) and 0.64 W mg_{Pt}⁻¹ (commercial electrode) at 0.6 V.

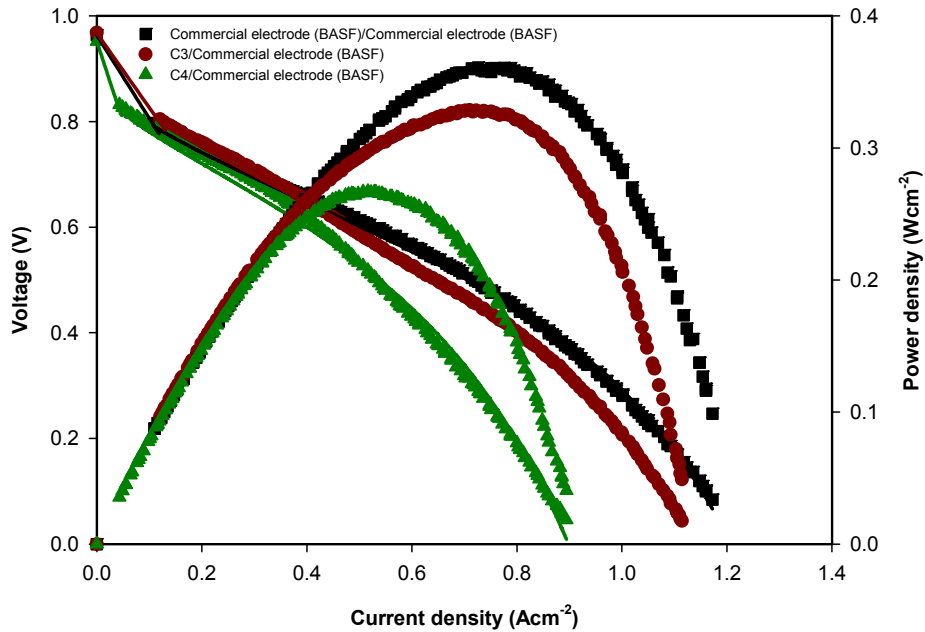


Figure 4.8 Polarization and power curves of PEMFCs with anode: commercial (BASF) electrode, C₃ and C₄ based electrode, cathode: commercial (BASF) electrode. Polymer electrolyte membrane: Nafion®NRE-212. Pt loading on both the cathode and the anode: 0.5 mg cm^{-2} , Test conditions: cell temperature at $80\text{ }^{\circ}\text{C}$, H₂ and air flow rate of $120\text{ and }250\text{ ml min}^{-1}$, respectively, and 100% humidified gases at 30 psig. (solid lines are based on equation (4.5)).

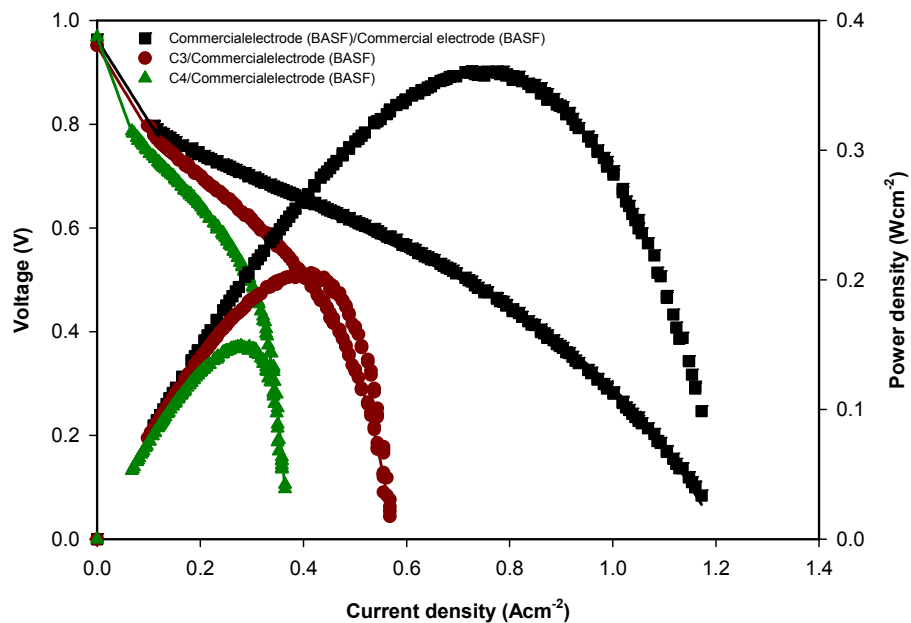


Figure 4.9 Polarization and power curves of PEMFCs with anode: commercial (BASF) electrode, cathode: commercial (BASF) electrode, C₃ and C₄ based electrode. Polymer electrolyte membrane: Nafion®NRE-212. Pt loading on both the cathode and the anode: 0.5 mg cm^{-2} , Test conditions: cell temperature at $80\text{ }^{\circ}\text{C}$, H₂ and air flow rate of $120\text{ and }250\text{ ml min}^{-1}$, respectively, and 100% humidified gases at 30 psig. (solid lines are based on equation (4.5)).

In order to obtain more detailed information about the electrode kinetic parameters for the oxygen reduction on these electrodes, the experimental polarization data were fitted to the following empirical equations [41]:

$$E = E^0 - b \log i - Ri - m \exp^{ni} \quad (4.5)$$

$$E^0 = E_r + b \log i^0 \quad (4.6)$$

where E (V) and i (A) are experimentally measured cell voltage and current, E_r (V) is the reversible cell voltage, i^0 (A) and b (V dec⁻¹) are the exchange current and the Tafel slope for oxygen reduction, respectively. R (Ω cm²) represents the total DC resistance, which is a summation of resistances in the polymer membrane and other electrode components accountable for the linear part of the variation of potential with current. In particular, the two parameters m (V) and n (cm² A⁻¹) mean mass transport phenomena in PEMFC. The electrical cell potential linearly depends on parameter m, while it correlates with parameter n exponentially. Knowing m and n, mass transfer overpotential in the high current density region of the I-V curve, where the cell potential decreases exponentially because of mass transport limitation, can be estimated. The experimental data were fitted to Equations (4.5) and (4.6) using Matlab[®]'s curve fitting tool. The fitting method used was non-linear least square and the algorithm used was trust-region approach. The kinetic parameters of these electrocatalysts are summarized in Table 4.4. The two electrocatalysts have similar b values of ca. 0.06 V, which is common to most supported and unsupported Pt electrodes [42]. However, the internal and mass transfer resistances of the cell were found to be larger when C₃ and C₄ samples were used as the electrocatalyst at the cathode electrode compared to the commercial cathode. This might be caused by either a) the intrinsic properties of the synthesized electrocatalysts, mainly conductivity and pore structure, which are dominated by calcination conditions; or b) the properties of the catalyst layer determined by its preparation method and the ink composition. The ink solution is prepared by mixing carbon supported platinum nanoparticles, with an aqueous solution of perfluorosulfonic acid polymer and isopropyl alcohol, which serves as a binder and proton conductor. The structural distribution of the resulting mixture determines the effective Pt surface area of the catalyst ink. In order to discover which of these sources have the main impact on fuel cell performance, the same analysis, using equations (4.5) and (4.6), was done when C₃ and C₄ electrocatalysts are used

at the anode side, and the results are summarized in Table 4.4. The contribution of internal resistance and mass transfer losses to the overall fuel cell performance is quite comparable to the commercial electrode, where the C₃ and C₄ based electrodes are placed at the anode side. Therefore, larger internal and mass transfer resistances of the cell with cathode electrodes prepared from C₃ and C₄ electrocatalysts is mainly related to the catalyst layer properties. The impact of structure and composition of a catalyst layer on overall PEMFCs performances have been clarified both by experimental and theoretical means. Many experimental studies were focused on optimization of cell performance as a function of Nafion content [43,44]. Here, both the cathode and anode catalyst layers were prepared from the same ink solution, which seems to be quite efficient at the anode side but needed to be modified for the cathode side.

Table 4.4 Electrochemical parameters of the resulting MEAs for oxygen reduction reaction

MEA		E^0	b	R	m	n	R^2
Anode	Cathode	(V)	(V dec ⁻¹)	(Ω cm ²)	(V)	(cm ² A ⁻¹)	
commercial (BASF)	commercial (BASF)	0.772	0.062	0.354	1.09E-03	4.75	0.9984
commercial (BASF)	prepared from C ₃	0.799	0.060	0.714	6.63E-05	15.15	0.9993
commercial (BASF)	prepared from C ₄	0.778	0.056	0.864	5.96E-06	30.47	0.9976
commercial (BASF)	commercial (BASF)	0.772	0.062	0.354	1.09E-03	4.75	0.9984
prepared from C ₃	commercial (BASF)	0.798	0.058	0.389	3.93E-03	3.93	0.9993
prepared from C ₄	commercial (BASF)	0.787	0.045	0.397	7.66E-03	4.49	0.9947

4.4 Conclusion

An effective new approach toward preparing PEMFCs electrocatalysts was reported in which Pt containing MOF material was applied as the only precursor. Pt nanoparticles (7-10 nm) were produced by simple pyrolytic carbonization of Pt loaded MOF under flow of Ar. The electrocatalytic activities were tested in a single stack PEMFC. The results show that this rather simple technique allows producing electrocatalysts with performances comparable to the commercial materials. This new approach to preparing electrocatalysts is however prone to further improvement. In our work an inert atmosphere was used during MOF

carbonization. Changing this atmosphere to a reactive gas such as ethylene or acetylene may allow better preserving the original atomic dispersion of Pt in the MOF. Moreover starting with MOF containing other metals such as Fe or Co can address the most challenging issue of employing non-PGM ORR catalysts owing to their relatively low turn-over-frequency in comparison with Pt. The Fe or Co containing MOF precursors could also provide the highest possible volumetric density of evenly distributed active sites and so may lead to a simple, original method to synthesize new electrocatalysts [32-34].

4.5 Acknowledgments

The authors would like to thank the Fonds Québécois de Recherche sur la Nature et les Technologies (FQRNT) for financial support. The authors gratefully acknowledge the helpful comments by Prof. Jean-Pol Dodelet.

Chapter 4 References:

- [1] C. Song, Fuel processing for low-temperature and high-temperature fuel cells: Challenges, and opportunities for sustainable development in the 21st century, *Catalysis Today* 77 (2002) 17-49.
- [2] H. Gregor, *Fuel Cell Technology Handbook*, CRC Press, Birkenfeld, Germany (2002).
- [3] H.A. Gasteiger, S.S. Kocha, B. Sompalli, F.T. Wagner, Activity benchmarks and requirements for Pt, Pt-alloy, and non-Pt oxygen reduction catalysts for PEMFCs, *Applied Catalysis B: Environmental* 56 (2005) 9-35.
- [4] B.D. James, J.A. Kalinoski, *Mass Production Cost Estimation for Direct H₂ PEM Fuel Cell Systems for Automotive Applications*, Arlington, Virginia, 2008.
http://www.hydrogen.energy.gov/pdfs/review08/fc_7_james.pdf
- [5] K. Gong, F. Du, Z. Xia, M. Durstock, L. Dai, Nitrogen-Doped Carbon Nanotube Arrays with High Electrocatalytic Activity for Oxygen Reduction, *Science* 323 (2009) 760-764.
- [6] Y. Wang, Y. Shao, D.W. Matson, J. Li, Y. Lin, Nitrogen-Doped Graphene and Its Application in Electrochemical Biosensing, *ACS Nano* 4 (2010) 1790-1798.
- [7] B. Winther-Jensen, O. Winther-Jensen, M. Forsyth, D.R. MacFarlane, High Rates of Oxygen Reduction over a Vapor Phase-Polymerized PEDOT Electrode, *Science* 321 (2008) 671-674.
- [8] Y. Li, Q. Liu, W. Shen, Morphology-dependent nanocatalysis: metal particles, *Dalton Transactions* 40 (2011) 5811-5826.
- [9] A. Stein, Z. Wang, M.A. Fierke, Functionalization of Porous Carbon Materials with Designed Pore Architecture, *Advanced Materials* 21 (2009) 265-293.
- [10] Y. Xia, Y. Xiong, B. Lim, S.E. Skrabalak, Shape-Controlled Synthesis of Metal Nanocrystals: Simple Chemistry Meets Complex Physics?, *Angewandte Chemie International Edition* 48 (2009) 60-103.
- [11] C. Liu, C.-C. Wang, C.-C. Kei, Y.-C. Hsueh, T.-P. Perng, Atomic Layer Deposition of Platinum Nanoparticles on Carbon Nanotubes for Application in Proton-Exchange Membrane Fuel Cells, *Small* 5 (2009) 1535-1538.
- [12] S. Litster, G. McLean, PEM fuel cell electrodes, *Journal of Power Sources* 130 (2004) 61-76.
- [13] J.R. Long, O.M. Yaghi, The pervasive chemistry of metal-organic frameworks, *Chemical Society Reviews* 38 (2009) 1213-1214.
- [14] H.-C. Zhou, J.R. Long, O.M. Yaghi, Introduction to Metal-Organic Frameworks, *Chemical Reviews* 112 (2012) 673-674.
- [15] S. Ma, D. Sun, M. Ambrogio, J.A. Fillinger, S. Parkin, H.-C. Zhou, Framework-Catenation Isomerism in Metal-Organic Frameworks and Its Impact on Hydrogen Uptake, *Journal of the American Chemical Society* 129 (2007) 1858-1859.
- [16] B. Wang, A.P. Cote, H. Furukawa, M. O'Keeffe, O.M. Yaghi, Colossal cages in zeolitic imidazolate frameworks as selective carbon dioxide reservoirs, *Nature* 453 (2008) 207-211.
- [17] M. Park, D. Moon, J.W. Yoon, J.-S. Chang, M.S. Lah, A metal-organic framework based on an unprecedented nonanuclear cluster as a secondary building unit: structure and gas sorption behavior, *Chemical Communications* (2009) 2026-2028.
- [18] S. Ma, X.-S. Wang, D. Yuan, H.-C. Zhou, A Coordinatively Linked Yb Metal-Organic Framework Demonstrates High Thermal Stability and Uncommon Gas-Adsorption Selectivity, *Angewandte Chemie International Edition* 47 (2008) 4130-4133.
- [19] B. Chen, S. Ma, F. Zapata, F.R. Fronczek, E.B. Lobkovsky, H.-C. Zhou, Rationally Designed Micropores within a Metal-Organic Framework for Selective Sorption of Gas Molecules, *Inorganic Chemistry* 46 (2007) 1233-1236.

- [20] S. Bourrelly, P.L. Llewellyn, C. Serre, F. Millange, T. Loiseau, G. Férey, Different Adsorption Behaviors of Methane and Carbon Dioxide in the Isotypic Nanoporous Metal Terephthalates MIL-53 and MIL-47, *Journal of the American Chemical Society* 127 (2005) 13519-13521.
- [21] O.G. Nik, X.Y. Chen, S. Kaliaguine, Functionalized metal organic framework-polyimide mixed matrix membranes for CO₂/CH₄ separation, *Journal of Membrane Science* 413–414 (2012) 48-61.
- [22] H. Vinh-Thang, S. Kaliaguine in O.L. Ortiz, L.D. Ramírez (Eds.), *Coordination Polymers and Metal Organic Frameworks: Properties, Types and Applications*, Chemical Engineering Methods and Technology Series, Nova Science Publishers, Hauppauge, NY, USA (2011), Chapter 4, pp. 129–168.
- [23] P. Horcajada, T. Chalati, C. Serre, B. Gillet, C. Sebrie, T. Baati, J.F. Eubank, D. Heurtaux, P. Clayette, C. Kreuz, J.-S. Chang, Y.K. Hwang, V. Marsaud, P.-N. Bories, L. Cynober, S. Gil, G. Férey, P. Couvreur, R. Gref, Porous metal-organic-framework nanoscale carriers as a potential platform for drug delivery and imaging, *Nat Mater* 9 (2010) 172-178.
- [24] P. Horcajada, C. Serre, G. Maurin, N.A. Ramsahye, F. Balas, M. Vallet-Regí, M. Sebban, F. Taulelle, G. Férey, Flexible Porous Metal-Organic Frameworks for a Controlled Drug Delivery, *Journal of the American Chemical Society* 130 (2008) 6774-6780.
- [25] W.J. Rieter, K.M. Pott, K.M.L. Taylor, W. Lin, Nanoscale Coordination Polymers for Platinum-Based Anticancer Drug Delivery, *Journal of the American Chemical Society* 130 (2008) 11584-11585.
- [26] C. Zlotea, R. Campesi, F. Cuevas, E. Leroy, P. Dibandjo, C. Volkringer, T. Loiseau, G. Férey, M. Latroche, Pd Nanoparticles Embedded into a Metal-Organic Framework: Synthesis, Structural Characteristics, and Hydrogen Sorption Properties, *Journal of the American Chemical Society* 132 (2010) 2991-2997.
- [27] D. Dybtsev, C. Serre, B. Schmitz, B. Panella, M. Hirscher, M. Latroche, P.L. Llewellyn, S. Cordier, Y. Molard, M. Haouas, F. Taulelle, G. Férey, Influence of [Mo₆Br₈F₆]₂- Cluster Unit Inclusion within the Mesoporous Solid MIL-101 on Hydrogen Storage Performance, *Langmuir* 26 (2010) 11283-11290.
- [28] K.K. Tanabe, S.M. Cohen, Postsynthetic modification of metal-organic frameworks-a progress report, *Chemical Society Reviews* 40 (2011) 498-519.
- [29] B. Liu, H. Shioyama, T. Akita, Q. Xu, Metal-Organic Framework as a Template for Porous Carbon Synthesis, *Journal of the American Chemical Society* 130 (2008) 5390-5391.
- [30] B. Liu, H. Shioyama, H. Jiang, X. Zhang, Q. Xu, Metal-organic framework (MOF) as a template for syntheses of nanoporous carbons as electrode materials for supercapacitor, *Carbon* 48 (2010) 456-463.
- [31] J. Hu, H. Wang, Q. Gao, H. Guo, Porous carbons prepared by using metal-organic framework as the precursor for supercapacitors, *Carbon* 48 (2010) 3599-3606.
- [32] S. Ma, G.A. Goenaga, A.V. Call, D.-J. Liu, Cobalt Imidazolate Framework as Precursor for Oxygen Reduction Reaction Electrocatalysts, *Chemistry – A European Journal* 17 (2011) 2063-2067.
- [33] E. Proietti, F. Jaouen, M. Lefèvre, N. Larouche, J. Tian, J. Herranz, J.-P. Dodelet, Iron-based cathode catalyst with enhanced power density in polymer electrolyte membrane fuel cells, *Nat Commun* 2 (2011) 416.
- [34] D. Zhao, J.-L. Shui, C. Chen, X. Chen, B.M. Reprögle, D. Wang, D.-J. Liu, Iron imidazolate framework as precursor for electrocatalysts in polymer electrolyte membrane fuel cells, *Chemical Science* 3 (2012) 3200-3205.
- [35] E.D. Bloch, D. Britt, C. Lee, C.J. Doonan, F.J. Uribe-Romo, H. Furukawa, J.R. Long, O.M. Yaghi, Metal Insertion in a Microporous Metal-Organic Framework Lined with 2,2'-Bipyridine, *Journal of the American Chemical Society* 132 (2010) 14382-14384.
- [36] H. Darmstadt, C. Roy, S. Kaliaguine, S.J. Choi, R. Ryoo, Surface chemistry of ordered mesoporous carbons, *Carbon* 40 (2002) 2673-2683.
- [37] H. Darmstadt, C. Roy, S. Kaliaguine, T.-W. Kim, R. Ryoo, Surface and Pore Structures of CMK-5 Ordered Mesoporous Carbons by Adsorption and Surface Spectroscopy, *Chemistry of Materials* 15 (2003) 3300-3307.
- [38] B. Sakintuna, Y. Yürüm, Templated Porous Carbons: A Review Article, *Industrial & Engineering Chemistry Research* 44 (2005) 2893-2902.

- [39] D. Pantea, H. Darmstadt, S. Kaliaguine, L. Sümchen, C. Roy, Electrical conductivity of thermal carbon blacks: Influence of surface chemistry, *Carbon* 39 (2001) 1147-1158.
- [40] J.J. Van Der Klink, NMR Spectroscopy as a Probe of Surfaces of Supported Metal Catalysts, in: B.C.G. Werner O. Haag, K. Helmut (Editors), *Advances in Catalysis*, Academic Press, San Diego, USA (1999), pp. 1-117.
- [41] J. Kim, S.M. Lee, S. Srinivasan, C.E. Chamberlin, Modeling of Proton Exchange Membrane Fuel Cell Performance with an Empirical Equation, *Journal of The Electrochemical Society* 142 (1995) 2670-2674.
- [42] A. Parthasarathy, S. Srinivasan, A.J. Appleby, C.R. Martin, Electrode kinetics of oxygen reduction at carbon-supported and unsupported platinum microcrystallite/Nafion® interfaces, *Journal of Electroanalytical Chemistry* 339 (1992) 101-121.
- [43] G. Sasikumar, J.W. Ihm, H. Ryu, Dependence of optimum Nafion content in catalyst layer on platinum loading, *Journal of Power Sources* 132 (2004) 11-17.
- [44] Z. Qi, A. Kaufman, Low Pt loading high performance cathodes for PEM fuel cells, *Journal of Power Sources* 113 (2003) 37-43.

Chapter 5 Non-precious electrocatalyst synthesized from metal organic frameworks

Foroughazam Afsahi, Serge Kaliaguine*

Department of Chemical Engineering, Laval University, Québec (Québec), Canada, G1V 0A6

Published in Journal of Materials Chemistry A (2) 2014 12270-12279

Résumé

Les piles à combustible à membranes échangeuses de protons (PEMFCs) sont considérées comme des dispositifs propres et efficaces pour la conversion de l'énergie avec un grand potentiel pour le remplacement, dans un futur rapproché, des moteurs à combustion interne (MCI). Le développement d'électrocatalyseurs non-précieux, plus performants et moins coûteux est crucial pour la commercialisation à grande échelle des PEMFCs. Un MOF contenant du Fe a été employé comme le seul précurseur afin de préparer les électrocatalyseurs cathodiques. Le Fe-MOF a été synthétisé, soumis à une thermolyse sous atmosphère inerte, suivi d'une lixiviation acide et finalement d'un traitement thermique sous NH_3 à des températures se situant entre 700 et 1000 °C. Lors du processus de la pyrolyse du MOF, un complexe Fe-N est formé sur les sites actifs du carbone (Fe/N/C) en parallèle avec le développement d'un carbone électriquement conducteur. Les électrocatalyseurs synthétisés ont été caractérisés par DRX, physisorption d'azote, TEM et XPS. Dans une solution électrolytique de H_2SO_4 (pH = 1), un potentiel d'apparition de 0,915 V ORR, et un potentiel de demi-onde de 0,811 V sont obtenus en utilisant l'électrocatalyseur le plus prometteur (C700/950). Les assemblages membrane-électrode (MEA) de ces électrocatalyseurs ont également été testés en tant que cathode dans un élément de pile à combustible air/ H_2 . L'électrocatalyseur le plus prometteur (C700/950) a montré une tension en circuit ouvert de 0,945 V et une densité maximale de puissance de 0,302 W cm^{-2} atteinte à 0,391 V.

Abstract

Proton exchange membrane fuel cells (PEMFCs) are considered as clean and efficient energy conversion devices with great potential to replace currently used internal combustion engines (ICEs) in the near future. Developing high-performance and less expensive non-precious metal electrocatalysts for oxygen reduction reaction (ORR) at the cathode side is crucial for widespread application of PEMFCs. Herein an Fe-containing metal organic framework (MOF) was employed as the sole precursor for preparing a cathode electrocatalyst. Fe-MOF was synthesized and subsequently subjected to thermolysis under a non-reactive gas atmosphere followed by acid leaching and heat treatment under NH_3 at different temperatures between 700 and 1000 °C. Upon pyrolysis, iron-nitrogen containing carbon active sites (Fe/N/C) were formed in parallel with development of an electronically conductive carbon medium produced through pyrolytic carbonization of the organic component of the MOF material. The prepared electrocatalysts were characterized by XRD, N_2 physisorption, TEM and XPS. In H_2SO_4 (pH = 1) electrolyte, the ORR onset potential of 0.915 V, and the half-wave potential of 0.811 V are achieved using the most promising electrocatalyst (C700/950). The membrane electrode assemblies (MEAs) made of these electrocatalysts were also tested as a cathode in a H_2 /air single fuel cell. The most promising electrocatalyst (C700/950) demonstrated an open circuit voltage of 0.945 V and a maximum power density of 0.302 W cm^{-2} reached at 0.391 V.

5.1 Introduction

Polymer electrolyte membrane fuel cells (PEMFCs) are considered as the most promising alternative to internal combustion engines (ICEs). Unlike ICEs, PEMFCs provide high energy conversion efficiency and power density at relatively low operating temperatures with zero or low greenhouse gases emissions [1-3]. Large-scale commercialization of PEMFCs is hindered due to cost issues mostly related to platinum (Pt)-based electrocatalysts required to accomplish the sluggish oxygen reduction reaction (ORR) at the cathode [4,5].

During the past several decades, different approaches have been pursued to address the cost issue by reducing Pt content through employing Pt-M (M = Fe, Co, Ni, Pd, etc.) alloy catalysts or by developing effective non-platinum group metal (non-PGM) catalysts. The latter is persuaded by the Jasinski [6] discovery which demonstrated the capability of cobalt phthalocyanine macrocyclic structures to facilitate the ORR under alkaline conditions. Different types of non-PGM catalysts have been recognized: a) transition metal oxides [7,8], nitrides [9,10], carbides [11], chalcogenides [12,13], b) heteroatomic polymer/non-precious metal composites [14,15] and c) pyrolyzed transition metal-nitrogen-carbon catalysts (M/N/C) [16-19]. Among all, the M/N/C materials are known as the most promising category of non-PGM catalysts and different preparation methods have been investigated to develop electrocatalysts with ORR activities and operational stabilities, comparable to those achievable using Pt-based electrocatalysts under practical PEMFC conditions. ORR activity of non-PGM catalysts depends on turn-over-frequency (TOF), active site density and catalyst layer design. Since for non-PGM catalysts TOF is smaller in comparison with Pt [5], the other two parameters should be enhanced to provide efficient catalysts for PEMFC applications. In this regard metal organic frameworks (MOFs) can be considered as the potential precursors.

Metal-organic frameworks (MOFs) are porous materials in which metal ions or clusters are linked together by organic linkers to form well defined crystalline structures. They possess a set of unique characteristics such as high surface area and well-defined porous structures which provides them with a great potential to be applied for gas storage [20,21] and gas separation [22,23]. In addition, the mild synthesis conditions of MOFs allow the rational design of novel functional materials at the molecular level with promising catalytic

applications [24-26]. MOF materials have also been used as templates and/or carbon sources to synthesize nanoporous carbon (NPC) materials with high specific surface area [27,28]. As non-PGM electrocatalyst precursors, MOFs due to their three-dimensional crystalline structures can provide high density of active sites evenly distributed in the framework. In addition, the organic ligands can be transformed into a carbon support via thermolysis which allows the formation of active metal containing species and carbon support at the same time. The porosity of carbon derived from thermolysis of MOFs can assure the accessibility of the active sites to the reactants and products related to ORR such as O₂, H⁺ and water.

Employing MOFs as electrocatalyst precursors in PEMFCs is a quite novel approach. In our previous work, a Pt-based MOF was synthesized and applied as the only electrocatalyst precursor to produce Pt-based catalysts for both hydrogen oxidation reaction (HOR) and ORR [29]. These electrocatalysts demonstrated fuel cell performance comparable to that of the commercial Pt-based materials. Zeolitic imidazolate frameworks (ZIFs) as a subclass of MOFs have also been investigated as precursors for preparation of non-PGM electrocatalysts [30-32]. The most promising catalyst resulted from employing ZIF-8 (Zn(II) zeolitic imidazolate framework), with high nitrogen content and microporous surface area, as the support for Fe and N precursors [30]. In another approach [31,32] a MOF material is used as the sole precursor for electrocatalyst preparation. Co [31] and Fe [32] imidazolate frameworks, in which each metal atom is coordinated with four nitrogen atoms of imidazolate ligands to form Co (or Fe)N₄ moieties regularly dispersed in the framework, are used as ORR catalyst precursors. In both these approaches the MOF-based electrocatalyst precursors underwent two steps of thermolysis first under an inert gas to form the carbon support containing active site species and then under NH₃ to enhance the activity of the final product by increasing microporous surface area and N content [30]. While heat treatment was found necessary to produce Fe (Co)-based electrocatalysts from the MOF precursor, some electrocatalysts prepared from non-pyrolyzed MOF materials have also been reported [33]. Excluding the thermolysis step, a composite made from the assembly of Cu-based MOF and grapheme oxide (GO) was applied as an electrocatalyst in PEMFC.

Until now, only ZIF based MOFs have been used as electrocatalyst precursors. In this work, we explore the use of another type of Fe-containing MOF as the sole precursor for preparation of an ORR electrocatalyst. The nature of electrocatalysts prepared in this work is quite

different from the ones derived from ZIFs, which should indicate any significant effect of parent MOF chemistry on the electrocatalyst activity. Investigating other types of MOF materials with different chemistry and structure should provide more knowledge to develop non-PGM catalysts with higher ORR activity using MOFs. In addition, the PEMFC performance of those electrocatalysts which have been prepared by using only the synthesized Fe(Co)-containing ZIFs as the electrocatalyst precursors have not yet been reported in the open literature[31,32].

5.2 Experimental

5.2.1 Synthesis of the Fe-based MOF

The Fe-based MOF material was synthesized according to the reported procedure [34]. 4.72 mmol (608 mg) anhydrous ferrous chloride and 1.60 mmol (464 mg) of 1,3,5-Tris(2H-tetrazol-5-yl)benzene Hydrochloride ($H_3BTT \cdot 2HCl$), were stirred in a mixture of DMF (40 mL), and DMSO (40 mL) at 110 °C under an argon atmosphere. After 24 h the solid precipitated from the solution was filtered under an inert gas atmosphere and isolated as a pale yellow solid.

5.2.2 Preparation of electrocatalysts

To prepare the PEMFC electrocatalysts, the Fe-MOF materials were heat treated at temperatures ranging between 700 and 1000 °C. A quartz tube (6 mm diameter) containing about 300 mg of the sample was weighed and placed inside a furnace. The tube was purged with argon (Ar) for 1 h prior to the treatment. The materials were typically heated at the ramp rate of 1 °C min⁻¹ for 90 min under Ar flow at a rate of 20 mL min⁻¹. The yield after the heat treatment was normally about 40 wt%. The heat-treated samples were acid leached in H₂SO₄ (1 M) via 2 h sonication followed by 20 h of continuous agitation at 80 °C to remove unstable and inactive species. The acid leached samples were then thoroughly washed with de-ionized water until reaching a neutral pH. In the final step, the samples were heat treated under NH₃, at the same temperature as those used with Ar or at the constant temperature of 950 °C for 15 min. The nomenclature used for these electrocatalysts is as follows: C α / β where α and β are the temperatures (°C) of heat treatment under Ar and NH₃, respectively.

5.2.3 Characterization of the synthesized Fe-MOF and electrocatalysts

X-ray diffraction (XRD) patterns of the synthesized Fe-MOF and the prepared electrocatalysts were recorded with a SIEMENS D5000 diffractometer using a Cu $K\alpha$ radiation ($\lambda = 0.15406$ nm). Phase recognition was obtained by comparison to Joint Committee on Powder Diffraction Standards (JCPDS) files. Nitrogen adsorption-desorption measurements were performed at -196 °C using a Quantachrome Nova 2000 instrument. Before measurements, the Fe-based MOF material and the electrocatalyst samples were outgassed under a vacuum at 130 and 150 °C, respectively. The specific surface areas (S_{BET}) were calculated by Brunauer-Emmett-Teller (BET) method in the relative pressure range where a linear BET plot with a positive C constant was obtained. The total pore volumes were determined at $P/P_0 = 0.95$. The transmission electron microscopy (TEM) images were acquired using a Jeol JEM 1230 operated at 120kV. X-ray photoelectron spectroscopy (XPS) was carried out with a Kratos Axis Ultra spectrometer using a monochromatic Al $K\alpha$ source ($h\nu = 1486.6$ eV) operated at 300 W. Spectra were recorded applying pass energies of 160 eV for survey spectra or 20 eV and 40 eV for high-resolution spectra. The XPS spectra were taken after all binding energies were referenced to the C 1s carbon peak at 285 eV. The Fe content of the electrocatalysts was measured using atomic absorption spectroscopy. The analysis was performed using a Perkin-Elmer 1100B atomic absorption spectrometer. The carbon component was first removed by dry-ashing the catalysts in air at 900 °C. The ash residue was then digested in HCl and the resultant solution was diluted with de-ionized water to the appropriate concentration. The nitrogen content was measured using a Thermo Scientific Flash 2000 Series CHNS Analyzer.

5.2.4 Rotating disk electrode (RDE) measurements

The RDE experiments were performed at room temperature in a three-electrode electrochemical cell using an AFCBP1 Pine potentiostat controlled with Pine 2.8.0 software. A catalyst-coated glassy carbon electrode with a geometric area of 0.196 cm² was employed as the working electrode.

The catalyst ink was prepared by mixing 10 mg of catalyst, 95 μL of a 5 wt% Nafion solution and 350 μL of ethanol. A uniform catalyst layer containing 0.8 mg cm⁻² of catalyst was loaded

on the working electrode surface. The electrolyte was an aqueous solution of H₂SO₄ (pH = 1). A Pt wire and a saturated calomel electrode (SCE) were used as the counter and reference electrode, respectively. All potentials in this work were reported as referenced to the reversible hydrogen electrode (RHE). The change of scale was made by measuring the potential difference ΔE between the SCE and a Pt foil immersed in the electrolyte saturated in H₂ under atmospheric pressure. ΔE is ca. 304 mV at 20 °C.

The RDE with the catalyst layer was fixed and then dipped in the O₂ saturated electrolyte. The ORR polarization curves were recorded by scanning the disk potential from -0.25 to +0.75 vs. SCE (scan rate of 10 mV s⁻¹), using a rotation rate of 1500 rpm. The negative scan, from +0.75 to -0.25 vs. SCE data points were used for extraction of ORR activity. The capacitive current of each electrode was then measured by performing cyclic voltammetry in the N₂ saturated electrolyte (N₂ was bubbled in the electrolyte until all O₂ was removed) under the same above-mentioned conditions.

5.2.5 Performance tests of membrane-electrode assemblies (MEAs)

The catalyst ink was prepared by ultrasonic blending of the electrocatalysts with de-ionized water and ethanol for 15 min to disperse and homogenize the catalyst powder. Afterward the Nafion® solution (5 wt%, Sigma-Aldrich) was added and the catalyst ink was mixed in an ultrasonic bath (15 min) followed by agitation in a vortex mixer (30 min) and finally 15 min mixing in the ultrasonic bath. The catalyst to Nafion ionomer mass ratio was kept 1. To create the cathode, this ink was then applied to the commercial gas diffusion layer (SGL Sigracet 25BC) by successive deposition using a micropipette until the catalyst loading of ~ 4 mg cm⁻² was reached. To prepare the anode, the catalyst ink containing the platinum catalyst (47 wt% Pt/Vulcan from Tanaka Kikinzoku Kogyo) was deposited on the same type of GDL as for the cathode to reach the Pt loading of 0.5 mg cm⁻². In the latter case, the catalyst to ionomer mass ratio was 1.5.

The cathode and anode were then applied to a Nafion®NRE-211 membrane to fabricate the membrane electrode assembly (MEA) using the hot pressing technique. The geometric area of the MEA was 1.14 cm². Fuel cell testing was carried out in a single-cell test fuel cell using an in-house built fuel cell test bench and a Biologic SP150 Potentiostat equipped with a

VMP3B-20 Booster and EC-Lab V9.98 software. Hydrogen and air, humidified at 95 and 75 °C, respectively were supplied to the anode and cathode gas lines heated at 100 and 90 °C at a flow rate of 0.3 slpm. Both electrodes were maintained at the same backpressure of 15 psig. The cell was let at open circuit potential (OCP) for about 15 min until the OCP stabilized. The polarization experiments were then conducted at a cell temperature of 80 °C by scanning the cell potential down to 0.1 V at a scan rate of 0.5 mV s⁻¹.

5.3 Results and discussion

5.3.1 Characteristic properties

The principal building unit for the Fe-based MOF material is the truncated octahedron (Figure 5.1), which consists of six [Fe₄Cl]⁷⁺ squares and eight BTT³⁻ ligands. The adjacent cages of truncated octahedral, sodalite-like structures share square faces to create a cubic framework. In this MOF structure, each Fe²⁺ ion of the chloride-centered [Fe₄Cl]⁷⁺ clusters is bonded to four nitrogen atoms of tetrazolate rings from four different BTT³⁻ ligands, and each BTT³⁻ ligand is attached to three [Fe₄Cl]⁷⁺ squares to form a 3,8-network [35].

The XRD pattern of the synthesized Fe-MOF, which is consistent with the previously reported one [34], is shown in Figure 5.2a. To produce the PEMFC electrocatalysts, the Fe-MOF was first thermolyzed under Ar flow to form Fe/N/C active sites. It is expected that during thermolysis the organic part of the synthesized Fe-MOF would be carbonized to produce carbon, which would provide the required electronic conductivity. In order to study the effect of thermolysis temperature, the Fe-MOF thermolysis under Ar was performed at 700, 800, 900, and 1000 °C. The XRD patterns for the C700-C1000 samples (Figure 5.2b), show the characteristic diffraction peaks that can be assigned to different Fe containing crystallite phases such as cementite (Fe₃C), FeN_{0.0324}, metallic Fe (α-Fe) and iron oxide like magnetite (Fe₃O₄) phases. Pyrrhotite (Fe₇S₈) is also formed during thermolysis under Ar; the sulfur source in the Fe-MOF is from the DMSO solvent used during synthesis and trapped inside the pores. Decomposition of the Fe-MOF during heat-treatment is believed to be a complex process producing many species including metal-nitrogen species, metals in their metallic state and metal carbides. The same phenomenon is also observed using some other Fe containing precursors [36]. In addition it is observed that samples heat-treated at temperatures from 700 °C to 1000 °C have very similar patterns.

XRD patterns of the electrocatalysts having underwent acid leaching and second step heat-treatment under NH_3 (C700/700-C1000/1000, C700/950 and C900/950) are illustrated in Figure 5.2c. Comparing the diffraction patterns for these samples with C700-C1000 reveals that the acid leaching removes almost all of the unstable species such as iron oxide and pyrrhotite. The final electrocatalyst precursor mostly consists of iron, iron nitride and iron carbide. The diffraction peaks assigned to (110), (002), (111), (112), (300) and (113) planes of the Fe_2N phase were clearly appearing at $2\theta = 37.6, 40.8, 42.9, 56.6, 67.7$ and 75.7 , respectively. This implied that the well-crystallized Fe_2N phase was formed at temperatures over $700\text{ }^\circ\text{C}$. However, C900/900, C1000/1000, C700/950 and C900/950 in Figure 5.2c, established extra peaks that correspond to (101) and (110) reflections of the $\text{FeN}_{0.056}$ phase, which probably resulted from the transformation of the Fe_2N phase at higher temperatures [37].

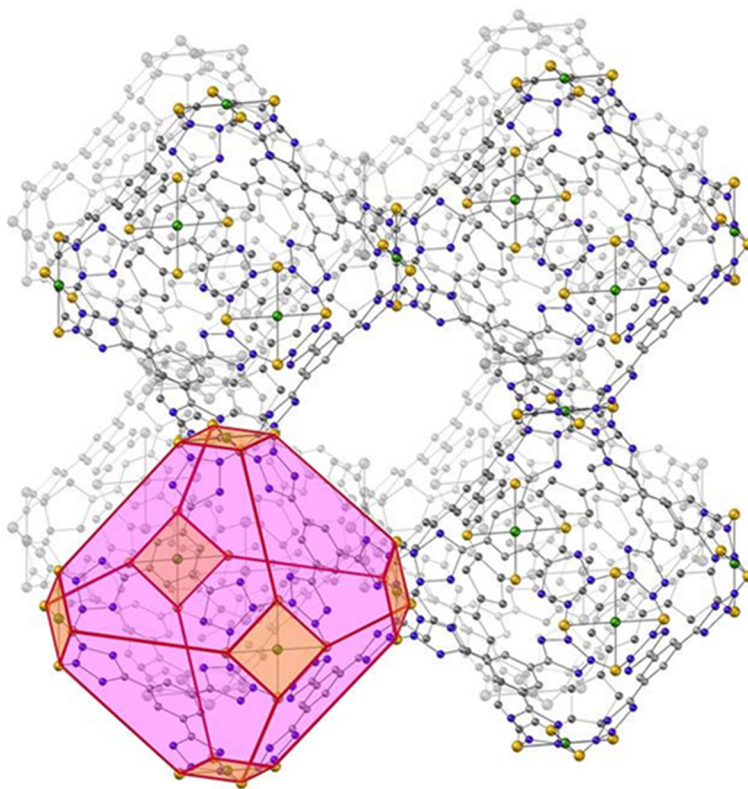


Figure 5.1 The crystal structure of Fe-MOF, A cube of eight sodalite-like truncated-octahedral cages sharing square faces.³⁵ Fe yellow, C gray, N blue and Cl green.

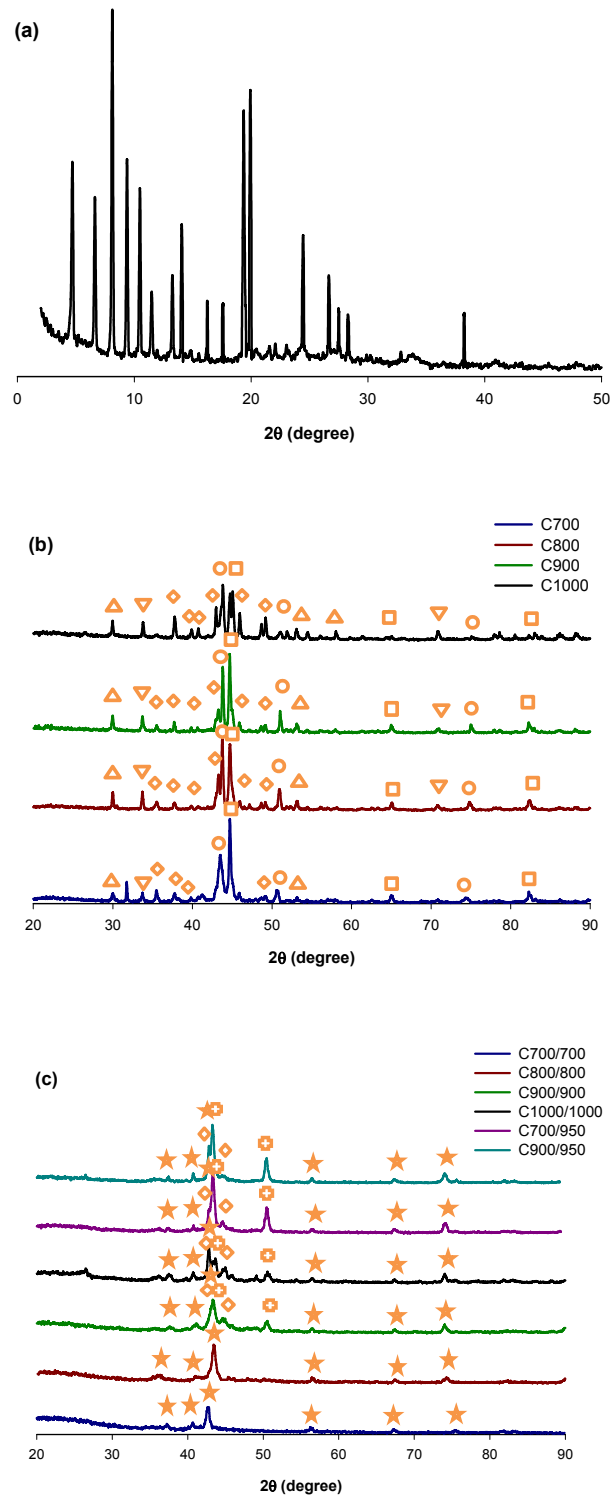


Figure 5.2 XRD patterns of (a) Fe-MOF (b) thermolized C700-C1000 samples and (c) electrocatalysts prepared upon acid leaching and NH_3 thermolysis (C700/700-C1000/1000, C700/950 and C900/950), \square , \diamond , \circ , \triangle , ∇ , \star , \oplus stand for metallic Fe, Fe_3C , $\text{FeN}_{0.0324}$, Fe_7S_8 , Fe_3O_4 , Fe_2N , $\text{FeN}_{0.056}$, respectively.

The nitrogen adsorption-desorption isotherm of the Fe-MOF (Figure 5.3a) reveals a type I adsorption isotherm characteristic of a microporous solid. Table 5.1 shows BET specific surface area and pore volume of the Fe-MOF. The shape of isotherms of the Fe-MOF thermolyzed under Ar (C700-C1000), shows the existence of both micropores and mesopores except for C1000 (Figure 5.3b). The steep knee at low relative pressure demonstrates the presence of micropores. The type IV isotherm with a capillary condensation step and a hysteresis loop near a relative pressure (P/P_0) of ~ 0.5 in the desorption branch indicates the presence of mesopores. The nonlocal density functional theory (NLDFT) method was employed to evaluate pore size distribution as shown in the inset of Figure 5.3b. The kernel of equilibrium NLDFT isotherms (desorption branch) with the carbon slit/cylindrical pore model was applied for pore width determination. All samples display similar pore size distribution with peaks centered at ca. 1.0, 2.0 and 5.0 nm. The presence of micropores (~ 10 Å equal to that of Fe-MOF) is reminiscent of the parent MOF structure. The mesopores have been developed during the thermolysis step and they correspond to those of nanoporous carbon formed in this step. As can be seen in Table 5.1, by increasing the thermolysis temperature from 700 to 900 °C, the specific surface areas and pore volumes are slightly increased; however, increasing the temperature from 900 to 1000 °C causes a remarkable decrease of both surface area and pore volume indicating a strong shrinkage of the microporosity accessible to N_2 .

The final electrocatalyst precursors C700/700-C1000/1000, show also the type IV isotherms similar to those of the C700-C1000 samples (Figure 5.3c); however, the surface area (microporous surface area) and pore volumes of all samples increased upon acid washing and NH_3 heat-treatment. The removal of Fe and/or other Fe-containing species during acid wash followed by second step heat treatment under NH_3 can cause this enhancement. The former is found to be mainly responsible for increasing the mesoporous surface area [31]; however, the latter contributes to developing microporous surface area [30]. Comparing C700/700 with C700/950 which has been treated under NH_3 at higher temperature indicates further development of micropores during second step heat-treatment. The similar trend can also be observed comparing C900/900 and C900/950; however, in this case the total surface area of the C900/950 is smaller compared to that of C900/900.

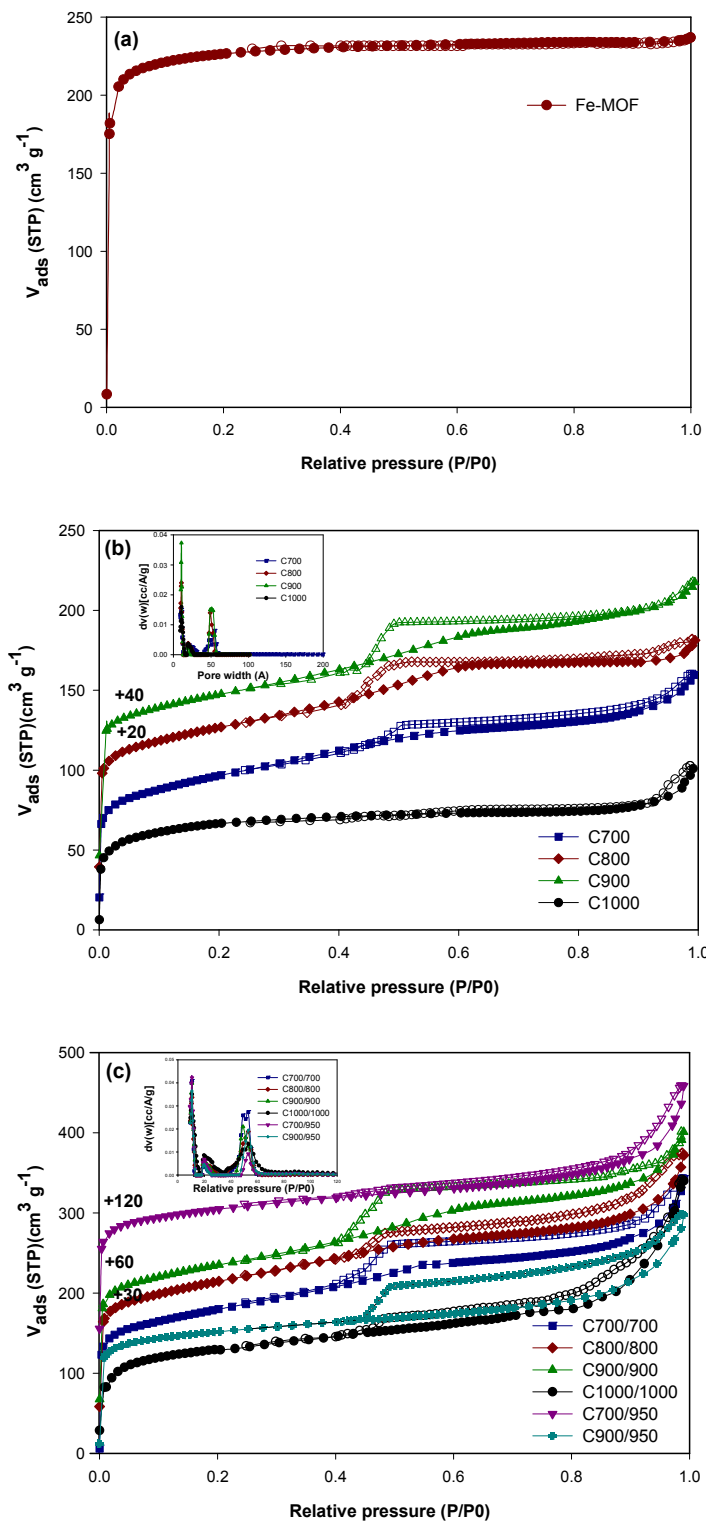


Figure 5.3 N_2 adsorption–desorption isotherms of (a) Fe-MOF (b) thermolized C700-C1000 samples and (c) electrocatalysts prepared upon acid leaching and NH_3 thermolysis (C700/700-C1000/1000, C700/950 and C900/950), closed: adsorption; open: desorption.

Table 5.1 BET specific surface area (S_{BET}), microporous surface area and pore volumes of the Fe-MOF and the samples thermolyzed under Ar, C700-C1000 and the final electrocatalyst samples C700/700-C1000/1000, C700/950, C900/950.

Sample	S_{BET} $\text{m}^2 \text{g}^{-1}$	Micropore surface area $\text{m}^2 \text{g}^{-1}$	V_{pore} $\text{cm}^3 \text{g}^{-1}$
Fe-MOF	901	–	0.36
C700	343	162	0.22
C800	386	192	0.23
C900	389	203	0.25
C1000	239	168	0.12
C700/700	647	309	0.46
C800/800	661	329	0.44
C900/900	628	278	0.45
C1000/1000	487	245	0.31
C700/950	687	516	0.41
C900/950	566	449	0.37

Figure 5.4 shows TEM micrographs of the electrocatalysts prepared by varying the thermolysis temperature from 700 °C to 1000 °C. The products mainly consist of spherical dark nanoparticles with sizes ranging between 10 and 60 nm diameter dispersed in some cube-shaped carbonaceous species. These dark sphericals are identified as iron containing particles (Fe_2N and Fe_3C) as indicated by XRD data. In addition to particles containing carbonaceous species, there are some empty carbonaceous cubes which are probably formed upon the removal of Fe containing species during acid leaching (Figure 5.4d).

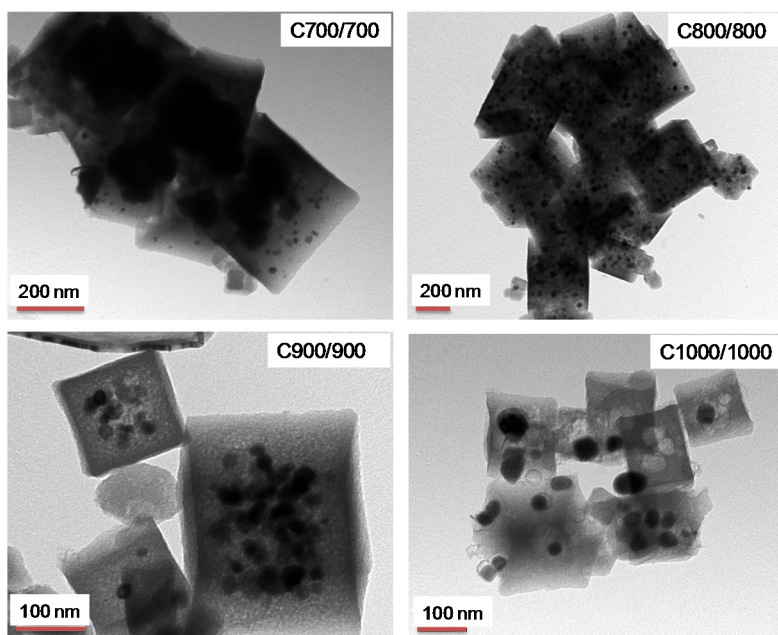


Figure 5.4 TEM images of C700/700-C1000/1000.

Nitrogen atoms at the surface of the M/N/C type catalysts are considered as part of the active sites and play a crucial role in catalyst activity [38,39]. The surface composition of the prepared electrocatalysts was characterized by XPS. The C 1s, N 1s, O 1s and Fe 2p regions were scanned and the respective contents of some samples (samples that demonstrate higher ORR activity) are reported in Table 5.2. The total nitrogen content decreased as the pyrolysis temperature was increased. This is due to the fact that the Fe metal drastically promotes the elimination of nitrogen during thermolysis at high temperature [40].

Table 5.2 Carbon, nitrogen, oxygen and Fe contents and relative ratio of N species.

Sample	Bulk content (%)		Surface content ^c (at.%)				Ratio of different nitrogen species ^d		
	Fe ^a	N ^b	C	N	O	Fe	Pyridinic-N	Quaternary-N	Oxidized-N
C700	40.4	3.6	82.9	5.6	6.8	4.4	42.6	41.4	15.9
C900	42.3	2.1	83.0	2.7	9.2	4.2	19.2	45.1	35.7
C700/700	7.4	8.2	89.7	7.9	1.6	0.7	48.6	34.1	17.2
C900/900	8.3	3.5	93.7	3.1	2.8	0.4	27.1	39.7	33.2
C700/950	5.3	3.6	96.4	2.6	0.7	0.3	31.2	34.5	34.3
C900/950	7.6	3.4	97.1	2.2	0.5	0.2	23.8	37.9	38.3

^a Fe content (wt.%) analyzed by atomic absorption, ^b obtained by elemental analysis, ^c & ^d determined from XPS analysis

To further illustrate the nitrogen speciation, the fitted N 1s spectra are plotted in Figure 5.5. The N1s XPS signal can be deconvoluted into three forms of nitrogen atoms associated with pyridinic-N type (398.6 ± 0.3 eV), quaternary-N (401.3 ± 0.3 eV) and pyridine N-oxide ($402 - 405$ eV). Pyridinic-N refers to nitrogen atoms on the edge of a carbon plane, each of which is bonded to two carbon atoms and donates one p-electron to the aromatic π system; quaternary-N is the type of nitrogen atom that bonds to three carbon atoms in the central or valley position of the graphene layer; pyridine-N-oxides are bonded to two carbon atoms and one oxygen atom. The actual electrocatalytically active sites are still controversial; in some studies, the electrocatalytic activity is attributed to pyridinic-N and/or pyrrolic-N [41-45]. Others found that catalysts containing larger amounts of quaternary-N lead to higher ORR activity [46-48]. Except for C700/700, the quantitative analysis demonstrates higher proportion of quaternary-N than that of pyridinic-N for all catalysts. Based on this observation alone, quaternary-N may be considered as the one involved in the active sites for ORR. However, since the total nitrogen content decreased, increasing the thermolysis temperature from 700 to 900 °C (Table 5.2), the absolute content of quaternary-N does not

actually increase. Therefore, correlating the ORR catalytic activity of the electrocatalysts with the quaternary-N content is not readily possible. It seems reasonable to assert that pyridinic-N and quaternary-N might contribute to the ORR catalytic activity of these catalysts [49].

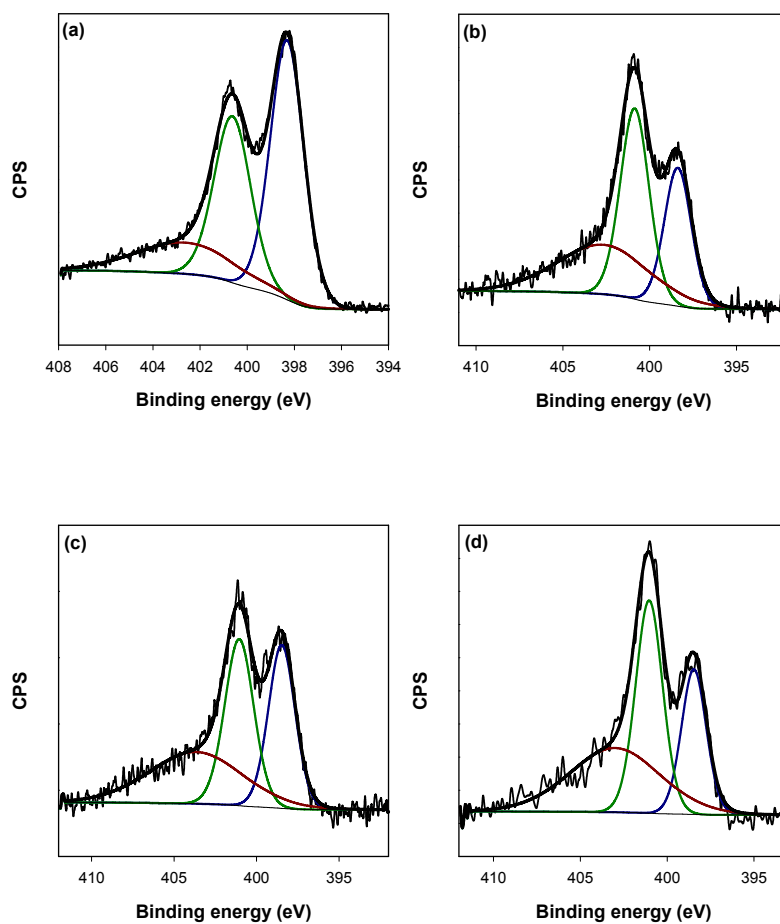
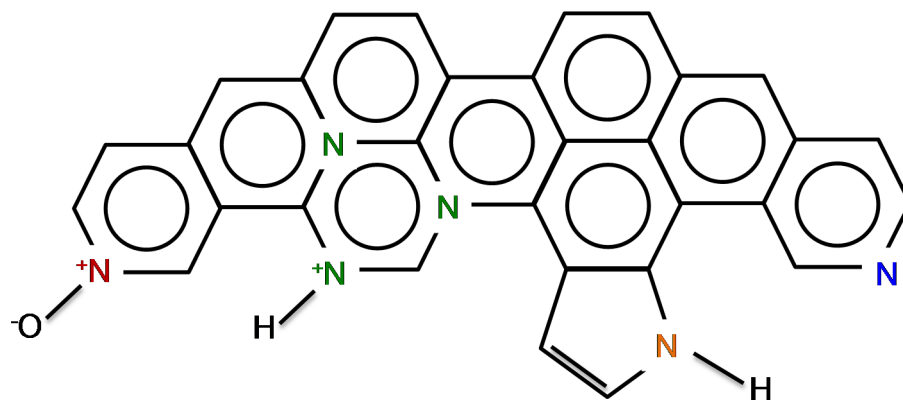


Figure 5.5 N 1s XPS spectra of (a) C700/700 and (b) C900/900, (c) C700/950 and (d) C900/950.

The C 1s XPS spectrum of the C700/700, C900/900, C700/950 and C900/950 samples (Figure 5.6) consist of a peak at ca. 284.6 eV, which could be attributed to the sp² graphitic carbon species. For C900/900, C700/950 and C900/950, this peak has full-width at half-maximum (FWHM) linewidths of 1.00, 0.93 and 0.90 eV, respectively, close to that reported for the graphitized carbon black (0.82 eV) [50,51], revealing a well-ordered packing of graphene layers. However, in the case of C700/700, this peak is broader with a (FWHM) linewidth of 1.14 eV, suggesting the presence of less ordered graphene layers compared to the graphitized carbon black.

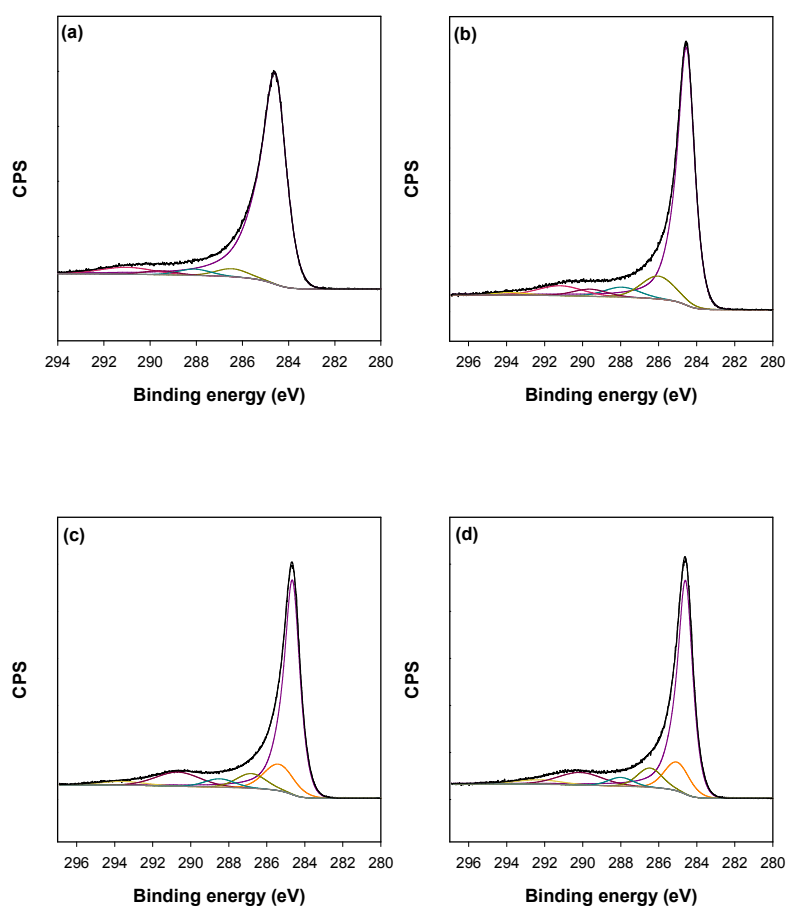


Figure 5.6 C 1s XPS spectra of (a) C700/700 and (b) C900/900, (c) C700/950 and (d) C900/950.

To quantify the Fe content in the catalysts before and after acid leaching, atomic absorption was carried out and the obtained values are reported in Table 5.2 (first column). These results indicate that most of the Fe is dissolved during the chemical leaching followed by the NH₃ heat-treatment process, in accordance with XRD results. The chemical leaching is essential for the application to fuel cells because unstable Fe containing species in the acidic

environment of fuel cells can cause the contamination of the proton exchanging membrane resulting in detrimental effects on the lifetime of fuel cells.

5.3.2 ORR activity measured with the RDE

Figure 5.7a shows the polarization curves obtained using C700/700-C1000/1000, C700/950 and C900/950 as electrocatalysts in an O₂-saturated H₂SO₄ (pH = 1) solution, after correction for capacitive current density. The electrocatalytic activity, as measured by the ORR onset and half-wave potentials ($E_{1/2}$) in the RDE polarization curves, increase upon raising the thermolysis temperature up to 900 °C and then drops for the catalyst synthesized at the maximum temperature (C1000/1000). Comparing C700/950 and C700/700 electrocatalysts demonstrates that increasing heat-treatment temperature under NH₃ increases the ORR activity slightly. The onset potential for C700/950 is about 0.1 V higher than that of C700/700, with a larger oxygen reduction current over the low overpotential range. The better catalytic activity is attributed to the higher active site density which resulted from increasing graphitization with temperature (consistent with C 1s XPS results). The ordered lattice of graphitized carbon can promote the formation of active sites derived from the nitrogen doping [52,53]. A similar trend is observed when comparing C900/900 and C900/950. The half-wave potential and onset potential of these electrocatalysts are summarized in Table 5.3.

Figure 5.7b demonstrates the mass transfer corrected Tafel plots of the ORR for the electrocatalysts prepared at different thermolysis temperatures. The kinetic current densities, j_k , and the mass activities, $j_{k,m}$, were calculated according to equations (5.1) and (5.2), respectively:

$$j_k = \frac{j_{lim} \times j_F}{j_{lim} - j_F} \quad (5.1)$$

$$j_{k,m} = \frac{-j_k}{m_{cat}} \quad (5.2)$$

where j_{lim} is the limiting current density obtained from the current plateau at low potentials of polarization curves (Figure 5.7a), j_F is the ORR current density after capacitive current correction and m_{cat} (mg cm⁻²) is the catalyst loading. Comparing the current density and the

mass activity at 0.8 V, at which non-precious metal catalysts are commonly compared, revealed that C700/950 has the highest kinetic current density and thus is the most active catalyst among all the electrocatalysts studied in this work. In order to be able to compare the ORR electrocatalytic activity of the samples prepared in this study with the one previously reported in literature and synthesized using the same approach, employing Fe-containing MOF as the sole electrocatalyst precursor [32], the current density and the mass activity at 0.8 V of this catalyst (FeIM-ZIF-8) is also reported in Table 5.3. More details regarding this catalyst are provided in the next section.

Table 5.3 Comparison of onset, half-wave potentials ($E_{1/2}$), kinetic currents (j_F), and mass activities ($j_{k,m}$) at 0.8 V vs. RHE of the electrocatalysts prepared in this work and the catalyst previously reported using Fe-containing ZIF as the electrocatalyst precursor [32].

Sample	E _{onset} (V)	E _{1/2} (V)	j _F @ 0.8 V (mA cm ⁻²)	j _{k,m} @ 0.8 V (A g ⁻¹)
C700/700	0.821	0.713	0.29	0.38
C800/800	0.844	0.729	0.36	0.48
C900/900	0.889	0.754	0.77	1.15
C1000/1000	0.833	0.667	0.14	0.18
C700/950	0.915	0.811	2.11	4.77
C900/950	0.894	0.795	1.53	2.93
FeIM-ZIF-8	0.915	0.755	1	2.6

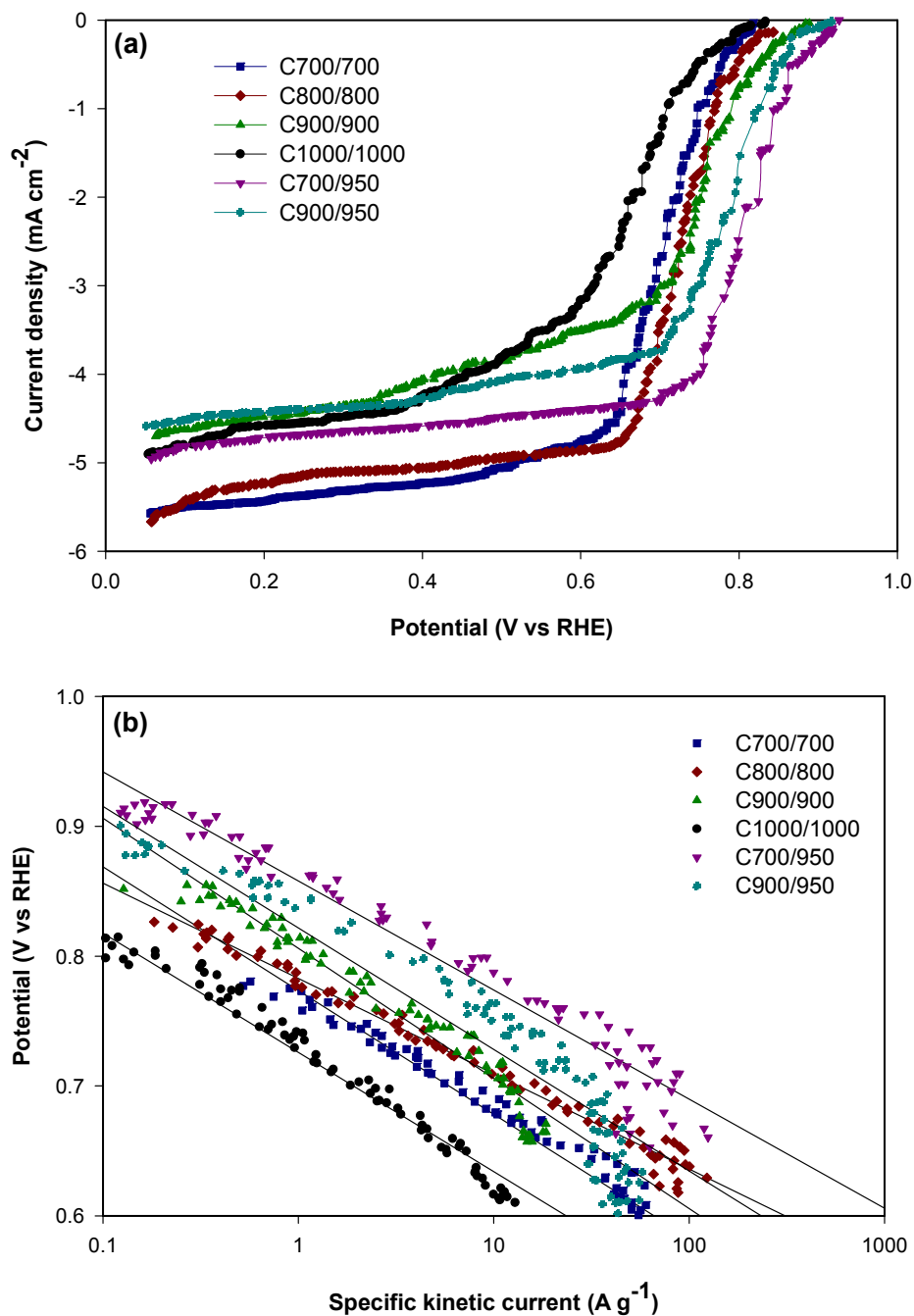


Figure 5.7 Faradaic current potential curves recorded on a rotating disk electrode coated with prepared electrocatalysts (a), Corresponding Tafel plot (b). Electrolyte: O₂ (N₂) saturated H₂SO₄ solution (pH=1); electrode rotation rate: 1500 rpm; potential scan rate: 10 mV s⁻¹; catalyst loading 0.8 mg cm⁻².

To further evaluate the ORR kinetic property of the electrocatalysts prepared at different temperatures, the kinetic parameters such as Tafel slope (b), exchange current density (j^0) and transfer coefficient (α_n), in the potential region > 0.7 V vs. RHE, were calculated using equation (5.3):

$$E = E^0 + \frac{2.303RT}{\alpha n_{\alpha} F} \log(j^0) - \frac{2.303RT}{\alpha n_{\alpha} F} \log(j_F) \quad (5.3)$$

where E is the electrode potential, E^0 is the thermodynamic electrode potential for the ORR (1.23 V vs. RHE), R is the universal gas constant (8.314 J mol⁻¹ K⁻¹), T is the working temperature (298.15 K), F is the Faraday constant (96,485 C mol⁻¹), n and α_n , the electron transfer number and coefficient, in the rate-determining step of the catalyzed ORR, respectively. j^0 is the exchange current density of the catalyzed ORR, and j_F has the meaning as defined above. According to equation (5.3), a plot of E vs. log(j_F) provides Tafel slope (b = 2.303RT/ $\alpha n_{\alpha} F$) and intercept ($E^0 + 2.303RT/\alpha n_{\alpha} F \log j^0$), from which the kinetic values are obtained and reported in Table 5.4. The exchange current densities of C700/950, C900/950 and C900/900 present higher values than those of other catalysts, demonstrating that these catalysts have better catalytic performance in the ORR; this is in agreement with Figure 5.7a. The Tafel slopes for the most active catalysts, C700/950, C900/950 and C900/900, are close to the theoretical value (120 mV dec⁻¹), indicating that the ORR on these catalysts is controlled by the first electron transfer process in the potential range measured [54,55].

Table 5.4 Electrochemical parameters of the prepared electrocatalysts for the ORR in H₂SO₄ solution (pH=1).

Sample	αn_{α}	-b (mV dec ⁻¹)	j^0 (mA cm ⁻²)
C700/700	0.81	73	2.42E-7
C800/800	0.66	90	6.64E-6
C900/900	0.59	100	3.24E-5
C1000/1000	0.77	77	2.68E-7
C700/950	0.47	127	6.59E-4
C900/950	0.48	122	3.68E-4

5.3.3 Performance in a fuel cell

The fuel cell polarization curves of the three promising electrocatalysts are shown in Figure 5.8a. In agreement with the RDE data in Figure 5.7a, C700/950 exhibits higher ORR activity than C900/900 and C900/950. The open circuit voltages (OCV) for C700/950, C900/950 and C900/900 are 0.945, 0.943 and 0.927 V, respectively. Comparing C900/900 and C900/950, the latter shows larger OCV and slightly higher ORR activity at low overpotential where ORR kinetic dominates, in agreement with RDE results (Figure 5.8a). At higher overpotential however, where mass transfer resistance plays a significant role, C900/900 provides better

ORR performance. This can be attributed to the higher porosity of C900/900 which can facilitate the mass transfer of O_2 , H^+ and water under fuel cell operation conditions. Figure 5.8b shows the power density curves of these electrocatalysts. Maximum power density values of 0.302, 0.223 and 0.209 $W\ cm^{-2}$ were achieved for C700/950, C900/950 and C900/900, respectively.

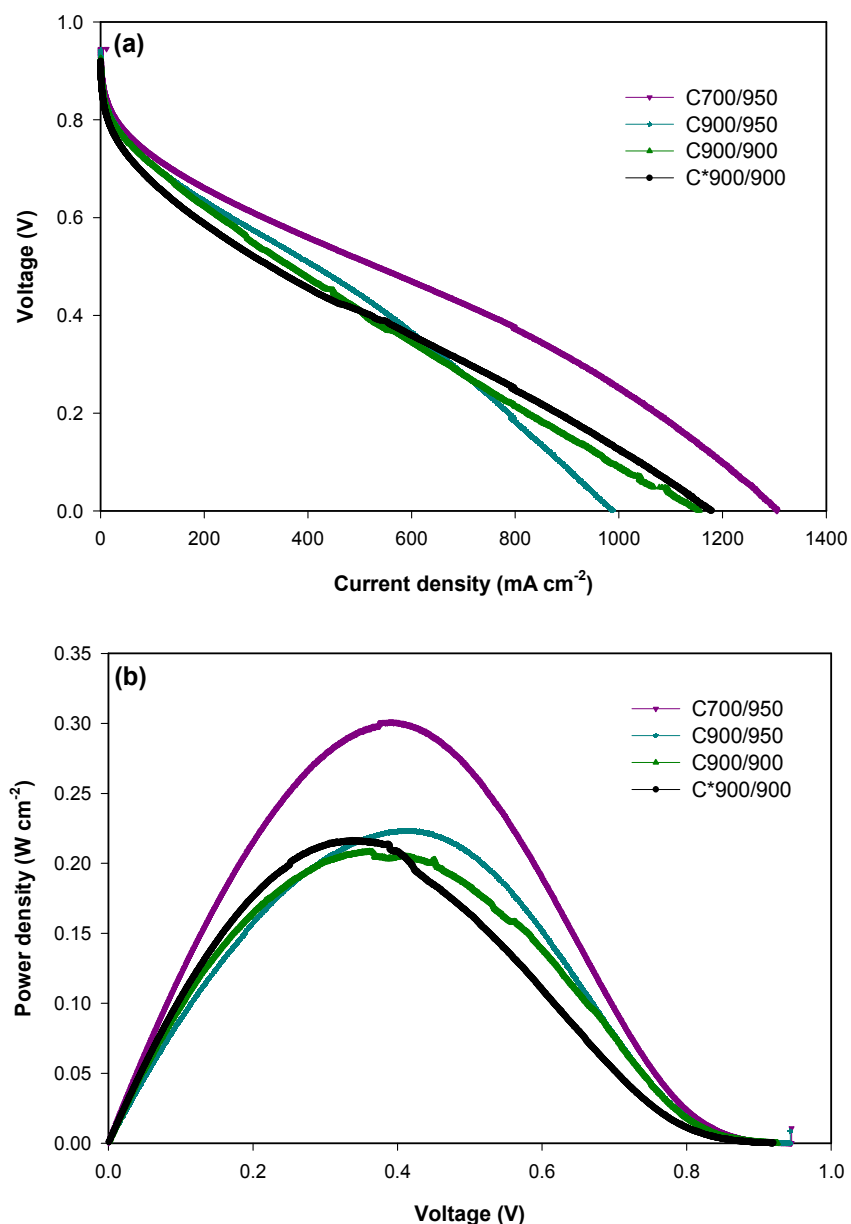


Figure 5.8 Polarization (a) and power density (b) curves at 80 °C for H_2 and air PEMFC with C700/950, C900/950, C900/900 and C*900/900 as the cathode catalysts. MEA active area 1 cm^2 , cathode catalyst loading 4 $mg\ cm^2$, anode catalyst loading 0.5 $mg\ cm^2$ 47wt % Pt/C, membrane was NRE 211. Hydrogen and air flow rate 0.3 slpm. Fuel cell operated at 100% relative humidity and 15 psig backpressure.

The electrocatalysts prepared in this study demonstrate better ORR activities compared to the ones reported previously in the literature employing the same approach, using Fe-containing ZIFs as the sole precursor for preparing PEMFC electrocatalysts [31,32]. In fact such PEMFC performance has not yet been reported using an Fe-MOF as the sole electrocatalyst precursor. Although FeIM (Fe containing ZIF) was previously synthesized and used as the sole electrocatalyst precursor [32], the PEMFC performance of these catalysts was not reported. Instead an FeIM/ZIF-8 electrocatalyst prepared upon pyrolysis of the ball-milled product of the FeIM and ZIF mixture is used as the cathode electrocatalyst under practical fuel cell conditions. The FC performance of our best electrocatalyst (C700/950; 5.3 wt% Fe content) was slightly better than that of FeIM/ZIF-8 containing 5.29 wt% of Fe. However, the performance of C700/950 is still far from the one reported previously by Dodelet's group [30]. In the latter work, the commercially available ZIF-8 (Basolite™ Z1200) with high nitrogen content and high micropore surface area was used as a support for Fe and N precursors. The optimized electrocatalyst was prepared from the pyrolysis of the electrocatalyst precursor obtained by low-energy planetary ball-milling of ZIF-8, 1,10-phenanthroline and ferrous acetate mixed in optimum ratios. The activity and power performance of the optimized catalyst (1 wt% Fe) were measured in H₂-O₂ PEMFC and yielded a current density of 1.2-1.3 A cm⁻² at 0.6 V and a maximum power density of 0.9 W cm⁻². This is 3.5-4 times higher than those of our most promising electrocatalyst (C700/950). The reason is most probably related to Fe content in our electrocatalysts which is higher than that in Dodelet's work. Indeed, using an Fe-containing MOF as the only electrocatalyst precursor, the final content of Fe in the electrocatalysts is determined by the chemistry of the MOF material. In our approach Fe is the only metal species which is inserted into the crystalline structure of the MOF during synthesis. When a MOF material such as Zn-based ZIF-8 is however used as the support and other Fe complexes are used as the Fe source to be dispersed uniformly in their porous structure via ball-milling [30,32], the Fe content in the final product is easily controlled. In their work Dodelet's group [30] optimized the ratio of ZIF-8, phenanthroline (N precursor) and ferrous acetate (Fe source) in their electrocatalyst precursor. The same procedure was also employed by Liu's group [32] to establish the optimum ratio between FeIM and ZIF-8.

In order to reduce the Fe content and hence enhance the performance of our electrocatalysts, we have tried two different approaches. First, employing additional carbon sources such as furfuryl alcohol (FA) and reactive gas precursors such as ethylene, this approach not only can enhance the electrocatalytic performance by increasing the carbon content (reducing the Fe content), but also may increase the electronic conductivity of the final electrocatalyst which plays a crucial role in electrocatalyst FC performance. Although these methods have successfully been used for preparing a porous carbon material using MOFs as the template [27,28,56], introducing even very small amount of FA through the incipient wetness method [57] to the synthesized Fe-MOF material before the first step thermolysis under Ar drastically reduced the performance of the electrocatalyst in a single fuel cell test (the results are not shown here). Using ethylene as the gas precursor, we thermolyzed the synthesized Fe-MOF in a mixture of Ar and ethylene gas flow instead of using only pure Ar during the first step heat treatment. Using only 0.5 % ethylene by volume balanced with Ar as a reactant gas results in a completely inactive electrocatalyst. This is mainly due to coverage of the active sites with coke, so that they are not any more accessible to the reactant species such as O₂ and H⁺.

In another approach, we tried to reduce the Fe content in a parent MOF by replacing 50 wt% of FeCl₂ with ZnCl₂ during MOF synthesis using a similar procedure reported previously for synthesis of Fe-MOFs. The synthesized Zn/Fe-containing MOF was then put through a similar electrocatalyst preparation procedure as those used for other electrocatalysts. This electrocatalyst was used as the cathode in a single fuel cell. The FC performance of the prototype electrocatalyst C*900/900 (Figure 5.8a) did not show considerable enhancement. The Fe content in this catalyst is found to be 3.9 wt%. This indicates that improving the catalyst performance may only be possible under special conditions in which the Fe content can reduce to very small values comparable to those used by Dodelet's groups [30], which means that other metal-containing MOFs (preferably Zn-based MOFs, due to their lower boiling temperatures ~ 907 °C) in which Fe instead of being used as the major constituent of the parent MOF was applied only as a minor component are promising as electrocatalyst precursors. Although this idea is currently under investigation by our research group, in a very recent work by Liu's group [58], a similar concept is utilized and bimetal ZIF materials (prepared via solid-state synthesis, using different type of imidazole linkers) containing Fe

as their minor part to form active sites were synthesized and employed as cathode electrocatalysts in PEMFC. These catalysts showed a substantial FC performance enhancement compared to those obtained using Fe-ZIF, previously reported by the same group [32].

5.4 Conclusions

PEMFC electrocatalysts with quite different chemistry and nature were synthesized using an Fe-containing MOF material as the only precursor. The Fe-MOF investigated in this work does not belong to the ZIF subclass of MOF which is the only class of MOF which till now has been used as the sole PEMFC electrocatalyst precursor. Although the electrocatalytic activities, tested in a single stack PEMFC, were not the best results reported in the literature using MOFs as the electrocatalyst precursor, they nevertheless provide the best performance by far reported employing only an Fe-based MOF as the electrocatalyst precursor. The results show that the chemistry of the parent Fe-MOF determines the final properties of the electrocatalysts. These results also confirm that using only an Fe-containing MOF does not lead to an optimized electrocatalyst, which is mainly related to the high concentration of Fe in the MOF precursor.

5.5 Acknowledgments

The authors gratefully acknowledge the constructive and insightful comments provided by Prof. Jean-Pol Dodelet. Furthermore, we would like to thank Dr Régis Chenitz for his expert help in running RDE and fuel cell measurements. We acknowledge the funding contributions of the Fonds de Recherche Nature et Technologie du Québec (FRNTQ).

Chapter 5 References:

- [1] R.M. Ormerod, Solid oxide fuel cells, *Chemical Society Reviews* 32 (2003) 17-28.
- [2] T. Norby, The promise of protonics, *Nature* 410 (2001) 877-878.
- [3] L. Carrette, K.A. Friedrich, U. Stimming, Fuel Cells: Principles, Types, Fuels, and Applications, *ChemPhysChem* 1 (2000) 162-193.
- [4] M.K. Debe, Electrocatalyst approaches and challenges for automotive fuel cells, *Nature* 486 (2012) 43-51.
- [5] H.A. Gasteiger, S.S. Kocha, B. Sompalli, F.T. Wagner, Activity benchmarks and requirements for Pt, Pt-alloy, and non-Pt oxygen reduction catalysts for PEMFCs, *Applied Catalysis B: Environmental* 56 (2005) 9-35.
- [6] R. Jasinski, A New Fuel Cell Cathode Catalyst, *Nature* 201 (1964) 1212-1213.
- [7] Y. Ohgi, A. Ishihara, K. Matsuzawa, S. Mitsushima, K. Ota, Zirconium Oxide-Based Compound as New Cathode Without Platinum Group Metals for PEFC, *Journal of The Electrochemical Society* 157 (2010) B885-B891.
- [8] A. Ishihara, M. Tamura, K. Matsuzawa, S. Mitsushima, K.-i. Ota, Tantalum oxide-based compounds as new non-noble cathodes for polymer electrolyte fuel cell, *Electrochimica Acta* 55 (2010) 7581-7589.
- [9] B. Avasarala, P. Haldar, Electrochemical oxidation behavior of titanium nitride based electrocatalysts under PEM fuel cell conditions, *Electrochimica Acta* 55 (2010) 9024-9034.
- [10] B. Avasarala, T. Murray, W. Li, P. Haldar, Titanium nitride nanoparticles based electrocatalysts for proton exchange membrane fuel cells, *Journal of Materials Chemistry* 19 (2009) 1803-1805.
- [11] Z. Yan, M. Cai, P.K. Shen, Nanosized tungsten carbide synthesized by a novel route at low temperature for high performance electrocatalysis, *Sci. Rep.* 3 (2013) 1646.
- [12] Y.J. Feng, T. He, N. Alonso-Vante, Carbon-Supported CoSe₂ Nanoparticles for Oxygen Reduction Reaction in Acid Medium, *Fuel Cells* 10 (2010) 77-83.
- [13] M.-R. Gao, J. Jiang, S.-H. Yu, Solution-Based Synthesis and Design of Late Transition Metal Chalcogenide Materials for Oxygen Reduction Reaction (ORR), *Small* 8 (2012) 13-27.
- [14] X. Yuan, X. Zeng, H.-J. Zhang, Z.-F. Ma, C.-Y. Wang, Improved Performance of Proton Exchange Membrane Fuel Cells with p-Toluenesulfonic Acid-Doped Co-PPy/C as Cathode Electrocatalyst, *Journal of the American Chemical Society* 132 (2010) 1754-1755.
- [15] G. Wu, K.L. More, C.M. Johnston, P. Zelenay, High-Performance Electrocatalysts for Oxygen Reduction Derived from Polyaniline, Iron, and Cobalt, *Science* 332 (2011) 443-447.
- [16] F. Jaouen, E. Proietti, M. Lefevre, R. Chenitz, J.-P. Dodelet, G. Wu, H.T. Chung, C.M. Johnston, P. Zelenay, Recent advances in non-precious metal catalysis for oxygen-reduction reaction in polymer electrolyte fuel cells, *Energy & Environmental Science* 4 (2011) 114-130.
- [17] M. Lefèvre, E. Proietti, F. Jaouen, J.-P. Dodelet, Iron-based Catalysts for Oxygen Reduction in PEM Fuel Cells: Expanded Study Using the Pore-filling Method, *ECS Transactions* 25 (2009) 105-115.
- [18] M. Lefèvre, E. Proietti, F. Jaouen, J.-P. Dodelet, Iron-Based Catalysts with Improved Oxygen Reduction Activity in Polymer Electrolyte Fuel Cells, *Science* 324 (2009) 71-74.
- [19] F. Charretre, F. Jaouen, S. Ruggeri, J.-P. Dodelet, Fe/N/C non-precious catalysts for PEM fuel cells: Influence of the structural parameters of pristine commercial carbon blacks on their activity for oxygen reduction, *Electrochimica Acta* 53 (2008) 2925-2938.
- [20] H. Wu, Y.S. Chua, V. Krungleviciute, M. Tyagi, P. Chen, T. Yildirim, W. Zhou, Unusual and Highly Tunable Missing-Linker Defects in Zirconium Metal–Organic Framework UiO-66 and Their Important Effects on Gas Adsorption, *Journal of the American Chemical Society* 135 (2013) 10525-10532.

- [21] R.D. Kennedy, V. Krungleviciute, D.J. Clingerman, J.E. Mondloch, Y. Peng, C.E. Wilmer, A.A. Sarjeant, R.Q. Snurr, J.T. Hupp, T. Yildirim, O.K. Farha, C.A. Mirkin, Carborane-Based Metal–Organic Framework with High Methane and Hydrogen Storage Capacities, *Chemistry of Materials* 25 (2013) 3539-3543.
- [22] O.G. Nik, X.Y. Chen, S. Kaliaguine, Functionalized metal organic framework-polyimide mixed matrix membranes for CO₂/CH₄ separation, *Journal of Membrane Science* 413–414 (2012) 48-61.
- [23] H. Vinh-Thang, S. Kaliaguine in O.L. Ortiz, L.D. Ramírez (Eds.), *Coordination Polymers and Metal Organic Frameworks: Properties, Types and Applications*, Chemical Engineering Methods and Technology Series, Nova Science Publishers, Hauppauge, NY, USA (2011), Chapter 4, pp. 129–168.
- [24] E.V. Ramos-Fernandez, C. Pieters, B. van der Linden, J. Juan-Alcañiz, P. Serra-Crespo, M.W.G.M. Verhoeven, H. Niemantsverdriet, J. Gascon, F. Kapteijn, Highly dispersed platinum in metal organic framework NH₂-MIL-101(Al) containing phosphotungstic acid – Characterization and catalytic performance, *Journal of Catalysis* 289 (2012) 42-52.
- [25] A. Arnanz, M. Pintado-Sierra, A. Corma, M. Iglesias, F. Sánchez, Bifunctional Metal Organic Framework Catalysts for Multistep Reactions: MOF-Cu(BTC)-[Pd] Catalyst for One-Pot Heteroannulation of Acetylenic Compounds, *Advanced Synthesis & Catalysis* 354 (2012) 1347-1355.
- [26] L. Bromberg, Y. Diao, H. Wu, S.A. Speakman, T.A. Hatton, Chromium(III) Terephthalate Metal Organic Framework (MIL-101): HF-Free Synthesis, Structure, Polyoxometalate Composites, and Catalytic Properties, *Chemistry of Materials* 24 (2012) 1664-1675.
- [27] S. Lim, K. Suh, Y. Kim, M. Yoon, H. Park, D.N. Dybtsev, K. Kim, Porous carbon materials with a controllable surface area synthesized from metal-organic frameworks, *Chemical Communications* 48 (2012) 7447-7449.
- [28] W. Xia, B. Qiu, D. Xia, R. Zou, Facile preparation of hierarchically porous carbons from metal-organic gels and their application in energy storage, *Sci. Rep.* 3 (2013) 1935.
- [29] F. Afsahi, H. Vinh-Thang, S. Mikhailenko, S. Kaliaguine, Electrocatalyst synthesized from metal organic frameworks, *Journal of Power Sources* 239 (2013) 415-423.
- [30] E. Proietti, F. Jaouen, M. Lefèvre, N. Larouche, J. Tian, J. Herranz, J.-P. Dodelet, Iron-based cathode catalyst with enhanced power density in polymer electrolyte membrane fuel cells, *Nature Communications* 2 (2011) 416.
- [31] S. Ma, G.A. Goenaga, A.V. Call, D.-J. Liu, Cobalt Imidazolate Framework as Precursor for Oxygen Reduction Reaction Electrocatalysts, *Chemistry – A European Journal* 17 (2011) 2063-2067.
- [32] D. Zhao, J.-L. Shui, C. Chen, X. Chen, B.M. Repragle, D. Wang, D.-J. Liu, Iron imidazolate framework as precursor for electrocatalysts in polymer electrolyte membrane fuel cells, *Chemical Science* 3 (2012) 3200-3205.
- [33] M. Jahan, Z. Liu, K.P. Loh, A Graphene Oxide and Copper-Centered Metal Organic Framework Composite as a Tri-Functional Catalyst for HER, OER, and ORR, *Advanced Functional Materials* 23 (2013) 5363-5372.
- [34] K. Sumida, S. Horike, S.S. Kaye, Z.R. Herm, W.L. Queen, C.M. Brown, F. Grandjean, G.J. Long, A. Dailly, J.R. Long, Hydrogen storage and carbon dioxide capture in an iron-based sodalite-type metal-organic framework (Fe-BTT) discovered via high-throughput methods, *Chemical Science* 1 (2010) 184-191.
- [35] M. Dincă, W.S. Han, Y. Liu, A. Dailly, C.M. Brown, J.R. Long, Observation of Cu²⁺–H₂ Interactions in a Fully Desolvated Sodalite-Type Metal–Organic Framework, *Angewandte Chemie International Edition* 46 (2007) 1419-1422.
- [36] C.W.B. Bezerra, L. Zhang, H. Liu, K. Lee, A.L.B. Marques, E.P. Marques, H. Wang, J. Zhang, A review of heat-treatment effects on activity and stability of PEM fuel cell catalysts for oxygen reduction reaction, *Journal of Power Sources* 173 (2007) 891-908.
- [37] U.I. Kramm, I. Herrmann-Geppert, P. Bogdanoff, S. Fiechter, Effect of an Ammonia Treatment on Structure, Composition, and Oxygen Reduction Reaction Activity of Fe–N–C Catalysts, *The Journal of Physical Chemistry C* 115 (2011) 23417-23427.

- [38] G. Lalande, R. Côté, D. Guay, J.P. Dodelet, L.T. Weng, P. Bertrand, Is nitrogen important in the formulation of Fe-based catalysts for oxygen reduction in solid polymer fuel cells?, *Electrochimica Acta* 42 (1997) 1379-1388.
- [39] F. Jaouen, S. Marcotte, J.-P. Dodelet, G. Lindbergh, Oxygen Reduction Catalysts for Polymer Electrolyte Fuel Cells from the Pyrolysis of Iron Acetate Adsorbed on Various Carbon Supports, *The Journal of Physical Chemistry B* 107 (2003) 1376-1386.
- [40] Y. Nabae, S. Moriya, K. Matsubayashi, S.M. Lyth, M. Malon, L. Wu, N.M. Islam, Y. Koshigoe, S. Kuroki, M.-a. Kakimoto, S. Miyata, J.-i. Ozaki, The role of Fe species in the pyrolysis of Fe phthalocyanine and phenolic resin for preparation of carbon-based cathode catalysts, *Carbon* 48 (2010) 2613-2624.
- [41] P.H. Matter, L. Zhang, U.S. Ozkan, The role of nanostructure in nitrogen-containing carbon catalysts for the oxygen reduction reaction, *Journal of Catalysis* 239 (2006) 83-96.
- [42] K. Gong, F. Du, Z. Xia, M. Durstock, L. Dai, Nitrogen-Doped Carbon Nanotube Arrays with High Electrocatalytic Activity for Oxygen Reduction, *Science* 323 (2009) 760-764.
- [43] S. Kundu, T.C. Nagaiah, W. Xia, Y. Wang, S.V. Dommele, J.H. Bitter, M. Santa, G. Grundmeier, M. Bron, W. Schuhmann, M. Muhler, Electrocatalytic Activity and Stability of Nitrogen-Containing Carbon Nanotubes in the Oxygen Reduction Reaction, *The Journal of Physical Chemistry C* 113 (2009) 14302-14310.
- [44] S. Maldonado, S. Morin, K.J. Stevenson, Structure, composition, and chemical reactivity of carbon nanotubes by selective nitrogen doping, *Carbon* 44 (2006) 1429-1437.
- [45] J.D. Wiggins-Camacho, K.J. Stevenson, Mechanistic Discussion of the Oxygen Reduction Reaction at Nitrogen-Doped Carbon Nanotubes, *The Journal of Physical Chemistry C* 115 (2011) 20002-20010.
- [46] R. Liu, D. Wu, X. Feng, K. Müllen, Nitrogen-Doped Ordered Mesoporous Graphitic Arrays with High Electrocatalytic Activity for Oxygen Reduction, *Angewandte Chemie International Edition* 49 (2010) 2565-2569.
- [47] Y.P. Wang, Y.J. Wang, Q.L. Ren, L. Li, L.F. Jiao, D.W. Song, G. Liu, Y. Han, H.T. Yuan, Ultrafine Amorphous Co-Fe-B Catalysts for the Hydrolysis of NaBH₄ Solution to Generate Hydrogen for PEMFC, *Fuel Cells* 10 (2010) 132-138.
- [48] L. Qu, Y. Liu, J.-B. Baek, L. Dai, Nitrogen-Doped Graphene as Efficient Metal-Free Electrocatalyst for Oxygen Reduction in Fuel Cells, *ACS Nano* 4 (2010) 1321-1326.
- [49] Y. Li, Z. Huang, K. Huang, D. Carnahan, Y. Xing, Hybrid Li-air battery cathodes with sparse carbon nanotube arrays directly grown on carbon fiber papers, *Energy & Environmental Science* 6 (2013) 3339-3345.
- [50] H. Darmstadt, C. Roy, S. Kaliaguine, T.-W. Kim, R. Ryoo, Surface and Pore Structures of CMK-5 Ordered Mesoporous Carbons by Adsorption and Surface Spectroscopy, *Chemistry of Materials* 15 (2003) 3300-3307.
- [51] B. Sakintuna, Y. Yürüm, Templated Porous Carbons: A Review Article, *Industrial & Engineering Chemistry Research* 44 (2005) 2893-2902.
- [52] H.R. Byon, J. Suntivich, Y. Shao-Horn, Graphene-Based Non-Noble-Metal Catalysts for Oxygen Reduction Reaction in Acid, *Chemistry of Materials* 23 (2011) 3421-3428.
- [53] C.V. Rao, C.R. Cabrera, Y. Ishikawa, In Search of the Active Site in Nitrogen-Doped Carbon Nanotube Electrodes for the Oxygen Reduction Reaction, *The Journal of Physical Chemistry Letters* 1 (2010) 2622-2627.
- [54] A. Kapałka, G. Fóti, C. Comninellis, Determination of the Tafel slope for oxygen evolution on boron-doped diamond electrodes, *Electrochemistry Communications* 10 (2008) 607-610.
- [55] A. Damjanovic, M.A. Genshaw, Dependence of the kinetics of O₂ dissolution at Pt on the conditions for adsorption of reaction intermediates, *Electrochimica Acta* 15 (1970) 1281-1283.
- [56] H.-K. Youn, J. Kim, W.-S. Ahn, MWCNT synthesis over Fe-BTC as a catalyst/carbon source via CVD, *Materials Letters* 65 (2011) 3055-3057.

[57] P. Pachfule, V.M. Dhavale, S. Kandambeth, S. Kurungot, R. Banerjee, Porous-Organic-Framework-Templated Nitrogen-Rich Porous Carbon as a More Proficient Electrocatalyst than Pt/C for the Electrochemical Reduction of Oxygen, *Chemistry – A European Journal* 19 (2013) 974-980.

[58] D. Zhao, J.L. Shui, L.R. Grabstanowicz, C. Chen, S.M. Commet, T. Xu, J. Lu, D.J. Liu, Highly Efficient Non-Precious Metal Electrocatalysts Prepared from One-Pot Synthesized Zeolitic Imidazolate Frameworks, *Advanced Materials* 26 (2014) 1093-1097.

Chapter 6 Impact of ionomer content on proton exchange membrane fuel cell performance

Foroughzham Afsahi¹, Francois Mathieu-Potvin², Serge Kaliaguine^{1*}

¹Department of Chemical Engineering, Laval University, Québec, G1V 0A6, Canada

²Department of Mechanical Engineering, Laval University, Québec, G1V0A6, Canada

Submitted to Journal of Fuel Cells, September 2015

Résumé

L'effet de la teneur en ionomère Nafion sur la performance d'une pile à combustible PEM à une seule cellule, fonctionnant avec des électrodes anodique et cathodiques fabriquées par nos soins à partir d'un électrocatalyseur au platine dérivé d'un MOF, a été étudié par simulation numérique et mesure expérimentale. Tout d'abord, l'étude de la sensibilité aux paramètres a été réalisée afin d'identifier les paramètres les plus influents du modèle. Ensuite, ces paramètres ont été calibrés pour différents types de piles à combustible considérés dans la présente étude, en utilisant les données expérimentales correspondantes. Le modèle calibré a été ensuite utilisé pour étudier l'impact de la teneur en ionomère Nafion dans la couche catalytique des électrodes-maison préalablement fabriquées. Enfin, la tendance qualitative prédite par ce modèle a été étudiée expérimentalement en faisant varier la teneur en ionomère Nafion entre 10 à 50 % en poids dans la couche catalytique des électrodes-maison. Du côté de l'anode, la performance de l'électrode-maison dans une pile à combustible PEM à une seule cellule s'est avérée dépendre légèrement de la teneur en ionomère Nafion. Pour l'électrode cathodique, la teneur en ionomère Nafion a démontré un fort impact sur la performance de la pile à combustible PEM à cellule unique. Bien que le modèle puisse capturer correctement l'impact de la teneur en ionomère Nafion sur les courbes de polarisation calculées, les valeurs optimales prédites par celui-ci dévient des résultats expérimentaux de façon significative. Ces écarts sont liés aux hypothèses simplificatrices faites dans le développement du modèle.

Abstract

The effect of Nafion ionomer content on performance of a single cell PEM fuel cell operated with home-made anodic and cathodic electrodes fabricated from a novel MOF derived Pt-based electrocatalyst was investigated via numerical simulation and experimental measurement. First, the parameter sensitivity analysis was performed to identify the most influential parameters of the model. Then, these parameters were calibrated for different fuel cell designs investigated in the current study by employing the corresponding experimental data. The calibrated model was subsequently used to investigate the impact of Nafion ionomer content in the catalyst layer of home-made electrodes. Finally, the qualitative trend predicted by this model was experimentally surveyed by varying the Nafion ionomer content between 10-50 wt% in the catalyst layer of home-made electrodes. At the anode side, the performance of home-made electrode in a single cell PEM fuel cell demonstrated small dependency on Nafion ionomer content. For the cathodic home-made electrode, Nafion ionomer content was found to affect the single cell PEM fuel cell performance more strongly. Although the model could correctly capture the impact of Nafion ionomer content on calculated polarization curves, the model predicted optimum values significantly deviate from the experimental results. This was related to the several simplifications made during model development.

6.1 Introduction

Proton exchange membrane fuel cells (PEMFCs) are considered a promising alternative to internal combustion engines. Unlike the latter one, PEMFCs can provide high energy conversion efficiency at relatively low operating temperatures with zero or low greenhouse gas emissions [1,2]. Large-scale commercialization of PEMFCs, however, is strongly impeded due to the cost issues mainly related to the use of platinum (Pt) electrocatalyst within catalyst layers [3,4].

During the past decades extensive efforts have been devoted toward developing effective non-platinum group metal (non-PGM) catalysts. However, non-PGM catalysts that could provide both high activity comparable to Pt and long-term stability under practical fuel cell operating conditions have not yet been achieved. Therefore, for the moment, Pt or Pt alloys are remaining as the only realistic choice at least until some phenomenal innovation occurs in the development of non-PGM catalysts [5-7]. In this context, it is vital to develop synthetic approaches toward producing more efficient Pt-based catalysts with a regular structure and controlled properties. In addition, optimizing the composition and structure of catalyst layers could enhance Pt utilization and hence, reduce the Pt content in the electrodes of PEMFCs.

Recently, new Pt-based electrocatalysts were prepared through a novel approach, i.e., by pyrolytic transformation of the Pt containing metal organic framework (MOF) [8]. To the best of authors' knowledge, this was the first report on employing MOF materials as the sole precursor to fabricate Pt-based electrocatalyst. These electrocatalysts were used to prepare ink solutions containing 20 wt% of Nafion ionomer (based on dry electrocatalyst) in their formulation. The catalytic performance of the anodic and cathodic electrodes prepared from such inks (home-made electrodes), were subsequently examined against a commercial electrode in a single PEM fuel cell. For the same Pt loading of 0.5 mg cm^{-2} , the home-made electrodes revealed performances comparable to the commercial electrode. However, the results demonstrate a potential to improve the performance via ink modification (varying Nafion ionomer content).

The effect of Nafion content in catalyst layers on the overall PEM fuel performance has been investigated through experimental and theoretical studies. Passalacqua et al. [9] studied the impact of the Nafion content (14 to 66 wt%) on the overall performance of a single cell PEM

fuel cell with low platinum loading (0.1 mg cm^{-2}). They found a dependency between PEM fuel cell performance and Nafion ionomer content in the electrodes, where a Nafion content of 33 wt% (with respect to the total solid content in a dried catalyst layer) resulted in the best performing electrode. Later, Sasikumar et al. [10] searched for a relationship between optimum Nafion content and Pt loading in the catalyst layer and found that the optimum Nafion content is determined by Pt loading. More specifically, they observed that larger Pt loadings require smaller amount of Nafion ionomer for the enhanced performance of the PEMFC. Different formulations have been applied to prepare the ink solution in PEMFCs throughout the literature. For instance, ratios between the masses of the catalyst and Nafion ionomer [11,12], Pt and Nafion ionomer [10,13] or carbon and Nafion [14,15] have been used to define the catalyst ink formulation. These formulations are mainly reported for standard Pt/C catalyst (20-40 wt% Pt supported on Vulcan XC72 carbon support), but some other works have investigated the optimum ink formulation for other types of electrocatalyst or carbon support [16-18].

Beside the experimental approach used to explore the optimum Nafion content in the catalyst layer, computational modeling has also been used to investigate the impact of Nafion ionomer content on the catalyst layer properties and Pt utilization. Various mathematical models have been developed to describe catalyst layers in PEMFCs including macro-homogeneous models [19,20], thin-film models [21,22], agglomerate models [23-29] and pore-scale models [30-32]. Employing the agglomerate model, Kamarajugadda and Mazumder [25] demonstrated the existence of an optimal fuel cell performance with changing ionomer volume fraction in the catalyst layer. Considering spherical agglomerate structure for the catalyst layer, Xing et al. [33] used a two dimensional, across the channel, two-phase flow model to optimize the initial dry ionomer content in the cathode catalyst layer for an enhanced PEM fuel performance. To improve the model accuracy, especially at higher current densities, they considered the effect of ionomer swelling on the catalyst layer porosity and oxygen mass transport resistance. According to their results, the best fuel cell performance could be achieved at initial dry ionomer volume fraction of 10%, corresponding to 0.3 mg cm^{-2} .

To summarize this literature review, earlier experimental measurements and numerical simulations both showed that Nafion content in catalyst layer has a significant impact on the

PEMFC performance and Pt electrocatalyst utilization. However, the impact of Nafion content on the performance of PEMFC operated with home-made electrodes prepared from the novel Pt-based MOF derived electrocatalysts presented in [8] has not yet been performed. Such study could lead to more effective electrodes that subsequently would improve the fuel cell performance.

Hence, in this paper, the main objective is to study the effect of Nafion ionomer content on the performance of a single cell PEM fuel cell operated with home-made electrodes fabricated from a novel MOF derived Pt-based electrocatalyst [8]. Such study could eventually enhance the fuel cell performance by providing higher currents densities (i) at a given operating voltage (V). The analyses presented in this paper are performed by comparing numerical simulations tools results and experimental measurements.

The paper is organized as follows: in Section 6.2, the general characteristics of the fuel cell design considered in this study are provided (geometry, materials, etc.), and the three fuel cell configurations investigated in this work are presented; in Section 6.3, the mathematical and numerical models are explained; in Section 6.4, the most influential parameters in the fuel cell model are identified by a sensitivity analysis; in Section 6.5, the numerical models of the three fuel cell configurations are calibrated by using experimental data; in Section 6.6, the existence of optimal ionomer content is predicted by using the calibrated numerical models; in Section 6.7, the presence of an optimal ionomer content is verified experimentally, and the optimal design obtained from experimental measurements and numerical simulations are compared. Then, in Sections 6.8, final discussions and conclusions are provided.

6.2 Description of the fuel cell device

The fuel cell device investigated in this paper is illustrated in Figure 6.1. More specifically, in Figure 6.1a it can be seen that two end plates enclose current collectors, bipolar plates, gasket layers, and a Membrane-Electrode Assembly (MEA). The end plates are used to maintain a compressive stress on the system, which provides good contacts between inner adjacent layers of the fuel cell. Collector plates allow the electrical current produced by the fuel cell to be directed toward external devices. Bipolar plates contain grooved channels in which the reactants and products can flow (see Figure 6.1b). Moreover, the end plates, current

collector and bipolar plates include internal pathways (not presented in Figure 6.1) in order to allow reactant gases and products to reach and leave the grooved channels. The gasket layers encase the MEA and are used to prevent gas leakage from the fuel cell. The different layers that constitute the MEA are illustrated in Figure 6.1c and are identified as layers II to VI. The MEA is made of a proton-conductive (ionomer) membrane (layer IV) bounded by two electrode layers (cathode and anode sides). These electrodes are made of a porous and electrically conductive medium (the diffuser, layers II and VI) on which a thin layer of electrocatalyst (layers III and V) is deposited. These electrocatalyst layers are in contact with the membrane, and are made of a mixture of Pt catalyst and Nafion ionomer, which allows transport of proton from the reaction sites (on Pt particles) to the membrane layer.

The exact geometry of channels grooved on the bipolar plates is presented in Figure 6.1b. The fluids flow within end plates, current collector and bipolar plates through internal pathways, then reach the grooved channels by the entry site “In” (see Figure 6.1b), and then leave the grooved channels by the exit site “Out” (see Figure 6.1b). Notice that the MEA is next to the channel on a well-defined effective area of size $1.4 \times 1.4 \text{ cm}^2$; in other words, the parts of the channel that are not directly adjacent to the MEA do not contribute to the electrochemical reactions (see Figure 6.1b).

Overall, in the fuel cell illustrated in Figure 6.1a, hydrogen (with water vapour) arrives via the end plate entry on the anode side, then it flows through the channels and diffuser, and finally it reacts in the catalyst layer to become protons and electrons. The protons generated move through the ionomer phase that is present in the catalyst layers and in the membrane, so as to reach the catalyst in the cathode. The electrons reach the anode collector and circulate in an external circuit so as to reach the cathode collector and then the cathode catalyst. On the other side of the fuel cell, oxygen (with water vapour) enters the fuel cell via the cathode end plate entry, then it flows through the cathode channels and diffuser, and it finally reacts with protons and electrons in the cathode catalyst layer, which produces water. To summarize, the fuel cell receives hydrogen, oxygen and water, and produces water, heat and electricity.

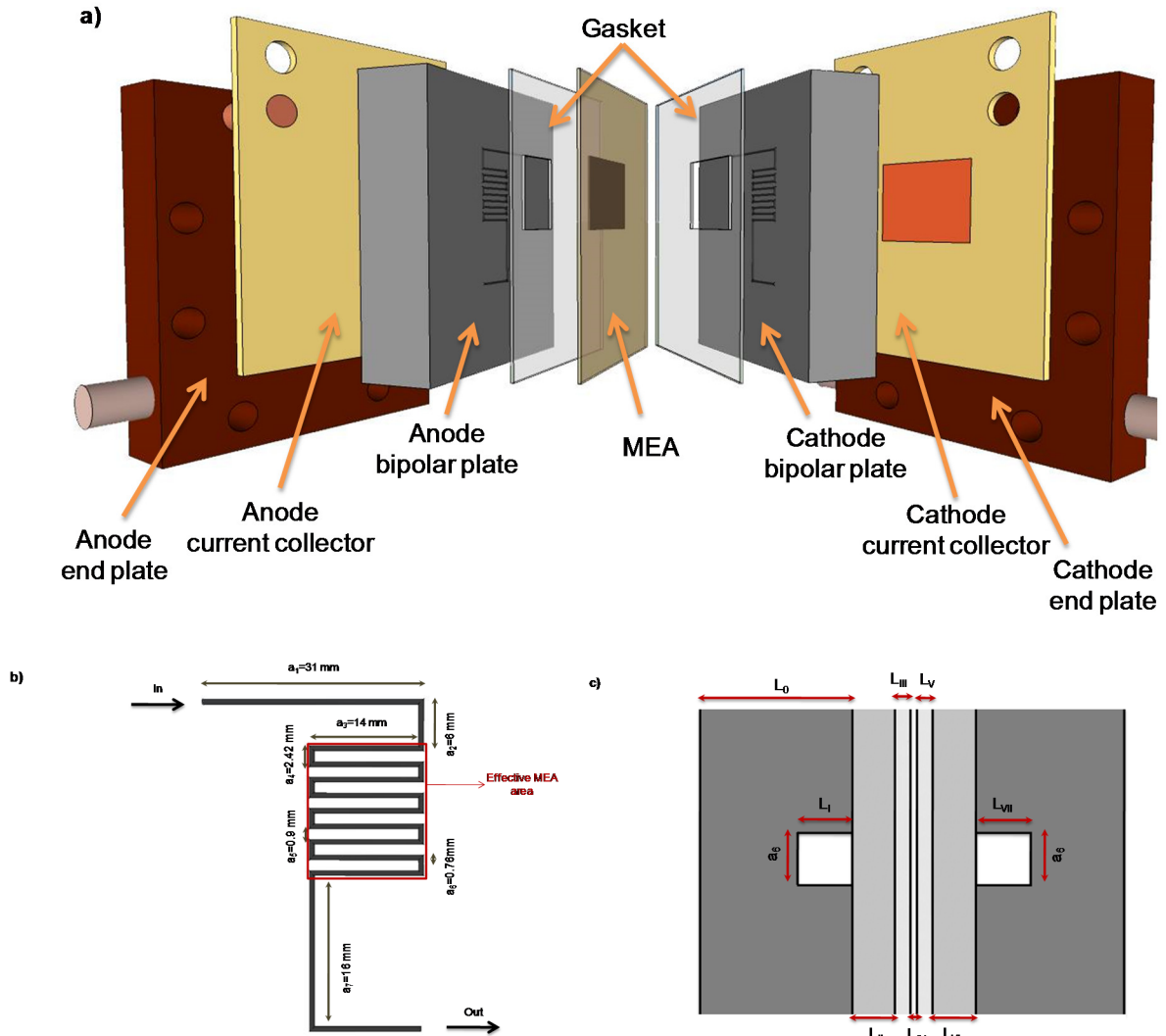


Figure 6.1 Schematic representation of the fuel cell device: (a) three dimensional exploded view, (b) channels pathways, and (c) two dimensional cross section of MEA and bipolar plates.

6.2.1 Description of the three designs of interest

In the current study, three variants of the general fuel cell design described above are investigated (see Figure 6.2). They correspond to: (i) a fuel cell including a commercial electrode for both the anode and cathode sides (Figure 6.2a); (ii) a fuel cell including a home-made electrode (Pt-based electrocatalyst derived from MOF precursor) at the anode side and the commercial electrode at the cathode side (Figure 6.2b); and (iii) a fuel cell including the commercial electrode at the anode side, while the home-made electrode is used at the cathode side (Figure 6.2c).

Notice that the overall design of these three variants are identical to that shown in Figure 6.1, i.e., the size and geometry of the end plates, collectors, bipolar plates, gasket and MEA effective area ($1.4 \times 1.4 \text{ cm}^2$) remain unchanged. The geometrical differences between these designs occur, however, in the thickness of the electrodes inner layers (L_{II} , L_{III} , L_V , and L_{VI}); the value of these parameters are reported for each design in Figure 6.2, and were obtained from the supplier (commercial electrodes) and from experimental measurement (home-made electrode).

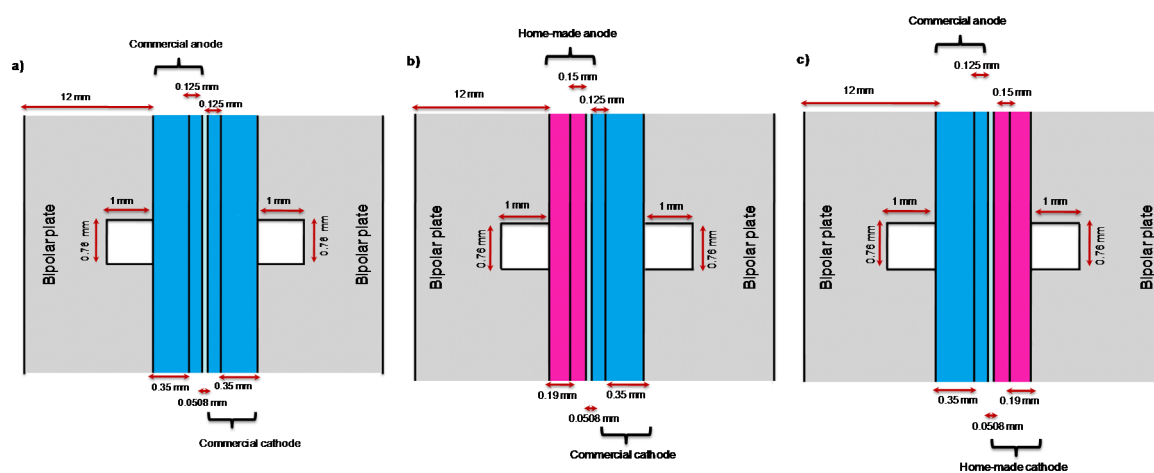


Figure 6.2 Illustration of the three fuel cell design: (a) commercial electrodes on both anode and cathode sides, (b) homemade electrode on the anode side, and (c) homemade electrode on the cathode side.

6.2.2 Description of the MEAs

MEAs that are used in the three designs described in Section 6.2.1 are assembled from commercial and/or home-made electrodes and a Nafion NRE-212 membrane. The commercial electrode (ELAT[®] V2.1, Single Sided Coating on TGPH-060, Pt loading (m_{Pt}) of 0.5 mg cm^{-2}) is provided by BASF and used at either anode or cathode side without any further processing.

The home-made electrodes are prepared by the author's research team [8]. The electrocatalyst used in the home-made electrodes were prepared through pyrolytic transformation of the Pt-based MOF precursor. More details on synthesis of the parent Pt-MOF and its pyrolytic transformation to the electrocatalyst precursor are reported in [8]. Previously, employing a range of thermolysis temperature (700-1050 °C), different electrocatalysts were prepared.

However, in the current study only the most promising electrocatalyst ($T_{\text{Thermolysis}} = 950 \text{ }^\circ\text{C}$) is considered.

The catalyst ink is prepared by ultrasonic blending of the electrocatalyst with Nafion solution (5 wt%, Sigma-Aldrich) in isopropyl alcohol for 2 h. This ink is then applied to a commercial GDL (Toray carbon paper, TGP-H-060, BASF) by successive brushing until the Pt loading (m_{Pt}) of $\sim 0.5 \text{ mg cm}^{-2}$ is reached.

6.2.3 Description of the operating condition

Experimental conditions under which the PEM fuel cell performance is conducted on a test station (Fideris TM Hydrogen Test Kit TM) to obtain the polarization curves, are provided in Table 6.1. Hydrogen and air, humidified at $80 \text{ }^\circ\text{C}$, are used as fuel and oxidant gasses at the anode and cathode, respectively. In addition, the parameters reported in Table 6.1 are the operational parameters used in the numerical model employed in the current study.

Table 6.1 Operating conditions of the fuel cell

Commercial (Home-made) electrode	
$V_{s,c}$	Operating parameter $\in [1.15 \text{ V}, 0.5 \text{ V}]$
ξ_a	3
ξ_c	3
$P_{a,out}$	15 psig
$P_{c,out}$	15 psig
$\varphi_{a,in}$	1
$\varphi_{c,in}$	1
T	$80 \text{ }^\circ\text{C}$

6.3 Mathematical modeling and numerical strategy

In upcoming sections of the paper, fuel cell performance is calculated by using numerical simulations. The mathematical model is presented in the Section 6.3.1, and the numerical tools are presented in Section 6.3.2.

6.3.1 Mathematical model

Strictly speaking, the fuel cell presented in Section 6.2 and illustrated in Figure 6.1 involves three-dimensional transport phenomena, temperature gradient, two-phase flow (liquid and vapour water) and complex water transport phenomena through the membrane. However, the purpose of this paper is not to obtain precise numerical data that represent exactly the physical fields throughout the fuel cell, but rather to highlight the main trends of the fuel cell performance with respect to several important variables. Therefore, a simplified mathematical model that was developed in a previous work [34] was adapted to the present work.

The model used in this work considers a two-dimensional (along the channels) section of the PEM fuel cell and consists of seven subdomains (layers I to VII) as shown in Figure 6.3. Two-dimensional “along the channel” geometry has often been used in the literature for fuel cell numerical modeling. The height H shown in Figure 6.3 corresponds to the total length of the serpentine shown in Figure 6.1b that is adjacent to the MEA (i.e., the length of the channel included in the $1.4 \times 1.4 \text{ cm}^2$ rectangle). The model implements: (i) a set of conservation equations for mass, momentum, species and charges, (ii) kinetic expressions for chemical reactions, (iii) expressions for calculating the required thermodynamic properties for ideal gases (iv) boundary conditions, (v) thermophysical properties, (vi) geometry of the domain, and (vii) operating conditions of the fuel cell. The places of these parameters in the model are described in a previous work [34].

The fuel cell is assumed to operate at steady-state with a uniform operating temperature (in the domain) and a uniform electric potential in the solid phase of each electrode. Electric potential varies within the ionomer phases that is present in the membrane (layer IV) and electrocatalyst layers (layer III and V), see Figure 6.3. More specifically, that potential drives

the motions of dissolved protons $H_{(d)}^+$ in the ionomer phase. The gas mixture in the gas channels is presumed to behave as an ideal gas and the flow is assumed to be laminar due to the small velocities involved. This model only considers the gaseous water transport and hence, it does not include the flooding effect and the resulting sharp potential drop that may happen at higher current densities ($i \geq 1 \text{ A cm}^{-2}$). Nonetheless, the presence of liquid water is taken into account implicitly and by applying an effective porosity value in the GDL (as proposed in Ref. [35]) which is smaller than its dry porosity value provided by the supplier. More details about that initial model may be found in [34].

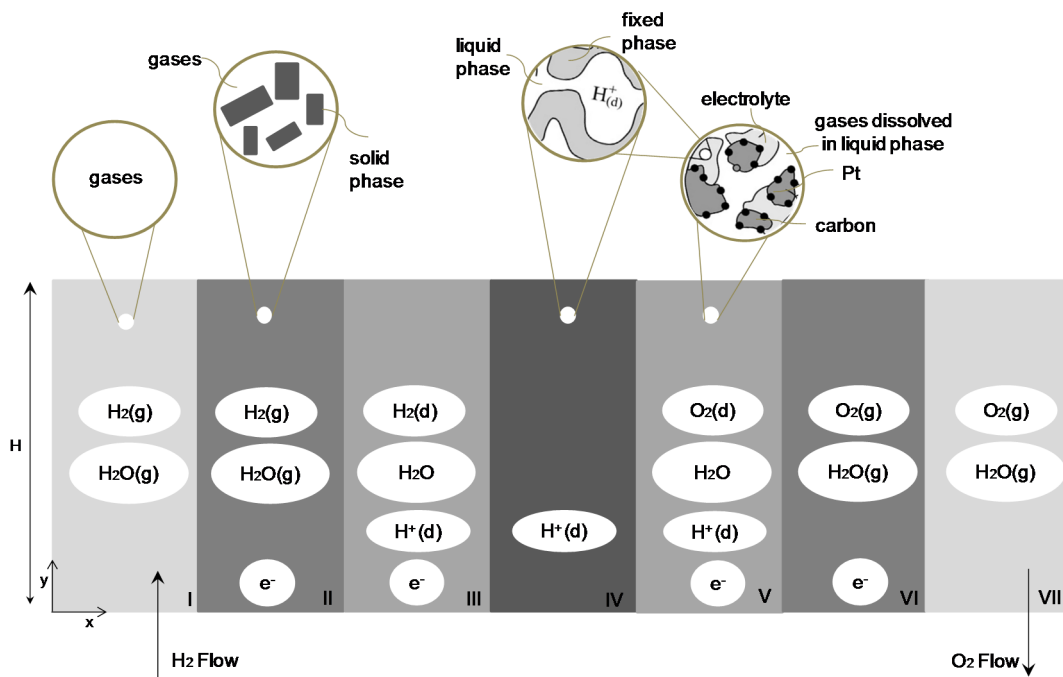


Figure 6.3 Two dimensional (along the channel) domain of the mathematical and numerical model.

In this paper, fuel cell performance has to be obtained for various Nafion content and operating conditions (i.e., various temperature and pressure values). As a consequence, the mathematical model described in [34] was improved in the following way:

- While in the previous study [34], the gas permeability in the catalyst layers (layers III and V) and gas diffusion layers (GDLs), layers II and VI, possessed a constant given value (K_{porous}), in the current study, the gas permeability in the gas diffusion layers (K_{GDL}) differs from the gas permeability in the catalyst layers (K_{CL}). The actual value for K_{GDL} is available from the supplier technical specifications (see Table 6.2). The

gas permeability in the catalyst layers is now calculated using the Kozeny-Carman equation [27,36] as follows:

$$K_{CL} = \beta \frac{\varepsilon_{CL}^3}{(1 - \varepsilon_{CL})^2} \quad (6.1)$$

where β is a constant determined from GDL properties and ε_{CL} is the porosity of catalyst layers.

- In the previous study [34], the porosity of the catalyst layers (layers III and V) and gas diffusion layers (layers II and VI) were assumed to possess a constant given value of ε_{porous} , however, in the current study, the porosity in the gas diffusion layers (ε_{GDL}) is different from the porosity of the catalyst layers (ε_{CL}). ε_{GDL} is provided by the supplier and is given in Table 6.2. The porosity of the catalyst layer (ε_{CL}) is now expressed as a function of the ε_{GDL} and catalyst layer properties, according to the following equation [37]:

$$\varepsilon_{CL} = \varepsilon_{GDL} \left(1 - \varepsilon_{m,catalyst}\right) - \frac{m_{Pt}}{L_{CL}f} \left(\frac{f}{\rho_{Pt}} + \frac{1-f}{\rho_C}\right) \quad (6.2)$$

where m_{Pt} is the Pt mass loading per unit area of the catalyst layer, L_{CL} is the catalyst layer thickness (either L_{III} or L_V), f represents the mass percentage of Pt in the Pt/C catalyst [8], ρ_{Pt} and ρ_C are the mass densities of the Pt and carbon black, respectively [37].

- Binary mutual diffusion coefficients between two species x and y are now expressed as functions of the operating temperature and pressure according to the following equation [38]:

$$D_{xy}(T, P) = D_{xy}^{ref}(T^{ref}, P^{ref}) \times (T/T^{ref})^{1.5} (P^{ref}/P) \quad (6.3)$$

- The open circuit potential $V_{o,c}$ at the cathode is now calculated according to the following equation [39]:

$$V_{OC} = 0.0025T + 0.2329 \quad (6.4)$$

where T is in kelvin and V_{OC} is in volts. It is worth mentioning that V_{OC} as appears in equation (6.4) is not the real open circuit potential of cathode which according to the Nernst equation is also a function of oxidant concentration. Indeed, V_{OC} only represents the constant term in the expression of the open circuit potential as a function of temperature. The concentration-dependent term of the open circuit potential that possesses a logarithmic form can then be extracted from the exponent in the Butler-Volmer equation and can then become the concentration term ($C_{O_2}/C_{O_2}^{ref}$) in front of the exponent in equation (6.7) (Section 6.4.1).

- Finally, the temperature dependency of the pre-exponential coefficient $a_{j_{0,c}}^{ref}(T)$ in the electrochemical expression of the cathode reaction is estimated from equation (6.5) [39]:

$$a_{j_{0,c}}^{ref}(T) = a_{j_{0,c}}^{ref}(353\text{ K}) \cdot \exp[0.014189(T - 353)] \quad (6.5)$$

By including equation (6.1) in the model, it is now possible to take into account the impact of the volume fraction available for gas flow in the catalyst layer (ε_{CL}) on the momentum equation via the gas permeability (K_{CL}). Furthermore, by adding equation (6.2) in the model, it is now possible to explicitly include the impact of Nafion content in the catalyst layer ($\varepsilon_{m,catalyst}$) on the volume fraction available for gas flow (ε_{CL}). In other words, the model is able to capture the impact of the Nafion content in the catalyst layer. Finally, including equations (6.3), (6.4) and (6.5) in the model allows to capture the impact of the operating pressure and temperature on the PEM fuel cell performance.

Table 6.2 Physical and electrochemical parameters with well-determined values used in the PEM fuel cell model

Parameter	Value
ε_{GDL}	0.3
K_{GDL}	$6.15 \times 10^{-12} \text{ m}^2$
$\varepsilon_{m,catalyst}$	0.05
ε_{CL}	0.2
$C_{H_2}^{ref}$	40.88 mol m^{-3}
$C_{O_2}^{ref}$	40.88 mol m^{-3}
$D_{H_2,H_2O}^{ref} (307 \text{ K}, 1 \text{ atm})$	$0.915 \times 10^{-4} \text{ m}^2 \text{ s}^{-1}$
$D_{O_2,H_2O}^{ref} (308 \text{ K}, 1 \text{ atm})$	$0.282 \times 10^{-4} \text{ m}^2 \text{ s}^{-1}$

6.3.2 Numerical methodology

The fuel cell geometry and modified mathematical method described in Section 6.3.1 have been implemented in a finite element software [40,41]. The domains were divided in a structured mesh of rectangular elements, and physical fields were calculated between nodes by using quadratic Lagrange interpolation.

The number of rectangular elements used in numerical simulations is defined by the number of nodes used along each of the boundaries illustrated in Figure 6.3. For the design using only commercial electrodes (introduced in Figure 6.2a), there were 50 nodes along the y-axis present in Figure 6.3; 20 nodes along the x-axis in subdomains I and VII; 35 nodes along the x-axis in subdomains II and VI; 63 nodes along the x-axis in subdomains III and V; and 20 nodes along the x-axis in subdomain IV. For the design that includes the home-made electrode on the anode side (introduced in Figure 6.2b), the number of nodes along the x-axis for subdomains of II and III was changed to 19 and 76, respectively. Similarly, for the design that includes the home-made electrode on the cathode side (introduced in Figure 6.2c), the

nodes number along the x-axis was changed to 76 and 19 for subdomains of V and VI, respectively.

Considering the dimensions of the domains, it should be noticed that the rectangular elements of the mesh are indeed extremely slender. Nevertheless, the commercial software used here has already proven its ability to handle such elements in previous studies [34,42]. A solver of the type “fully coupled” was selected in the finite element software [40], and convergence is declared when the relative error was smaller than 10^{-6} . With the meshes described above, it was verified that the value of the electric current density i changed by less than 0.5% when the number of elements was doubled in each direction. Hence, the meshes described above are considered adequate to declare mesh independence.

6.4 Sensitivity analysis

Mathematical PEM fuel cell models of different complexity involve different constants (usually called “parameters”) to calculate the polarization curves. These parameters can be classified as geometrical (design) parameters, operational parameters (temperature, pressure, humidity, flow rate, etc.), physical parameters (porosity, permeability, etc.) and electrochemical parameters (exchange current density, transfer coefficient, etc.) [43]. While some of these parameters can be measured directly [44,45] and used in numerical models, others could only be assumed or estimated with some degree of uncertainty. The values of these undetermined and therefore adjustable parameters may have negligible, moderate, or important impact on the simulations results. Hence, it is important to identify the most influential undetermined parameters and then obtain accurate values for them, in order to develop a numerical model that correctly predicts the performance of the fuel cell. The undetermined parameters of the model presented in this work will be investigated in the following section.

6.4.1 Description of the parameters

Tables 6.1-6.3 list the operational, physical and electrochemical and geometrical parameters of the mathematical PEM fuel cell model described in Section 6.3 which are considered to be accurately known. Other model parameters that remain undetermined and required to be

estimated for the fuel cell investigated in this paper are listed in the first column of Table 6.4. These parameters are: the exchange current density multiplied by the specific surface area ($aj_{0,a}^{ref}$) at the anode side, the transfer coefficient (α_a) at the anode side, exchange current density multiplied by the specific surface area ($aj_{0,c}^{ref}$ (353 K)) at the cathode side, the transfer coefficient (α_c) at the cathode side, and membrane protonic conductivity (σ_m).

The first four parameters listed above are related to the electrochemical reactions that occur in the catalyst layers; in other words, they appears in the kinetic expressions of the mathematical model, i.e.,

$$r_a = aj_{0,a}^{ref} (C_{H_2}/C_{H_2}^{ref})^{1/2} ((\alpha_a + \alpha_c)F\eta/RT) \quad (6.6)$$

$$r_c = -aj_{0,c}^{ref} (C_{O_2}/C_{O_2}^{ref}) (\exp(-\alpha_c F\eta/RT) - \exp(\alpha_c F\eta/RT)) \quad (6.7)$$

where the dependence of $aj_{0,c}^{ref}(T)$ with respect to temperature is developed in equation (6.5). These equations represent a simplified version of the general Butler-Volmer expression adopted in the model to determine the rate of oxidation (r_a) and reduction (r_c) reactions occurring at the anode and cathode electrodes [34]. The values of the four electrochemical parameters $aj_{0,a}^{ref}$, $aj_{0,c}^{ref}$ (353 K), α_a and α_c depend on the microscopic/nanosopic characteristics of the electrocatalyst, and as a consequence, they can only be obtained from experimental measurement. Finally, the membrane conductivity, σ_m , strongly depends on the average water content of the fuel cell investigated [46], and hence, on the global design of the fuel cell. Therefore, the membrane conductivity was identified as an undetermined parameter.

Table 6.3 Geometrical parameters of the fuel cell

	Commercial anode/ Commercial cathode	Commercial anode/ Home-made cathode	Home-made anode/ Commercial cathode
H [m]	126×10^{-3}	126×10^{-3}	126×10^{-3}
L_I [m]	1×10^{-3}	1×10^{-3}	1×10^{-3}
L_{II} [m]	3.5×10^{-4}	3.5×10^{-4}	1.9×10^{-4}
L_{III} [m]	1.25×10^{-4}	1.25×10^{-4}	1.5×10^{-4}
L_{IV} [m]	5.08×10^{-5}	5.08×10^{-5}	5.08×10^{-5}
L_V [m]	1.25×10^{-4}	1.5×10^{-4}	1.25×10^{-4}
L_{VI} [m]	3.5×10^{-4}	1.9×10^{-4}	3.5×10^{-4}
L_{VII} [m]	1×10^{-3}	1×10^{-3}	1×10^{-3}

Table 6.4 Undetermined model parameters used in the sensitivity analysis

Parameter	Base Value	Range
$a_{j_{0,a}}^{ref}$	$1 \times 10^9 \text{ A m}^{-3}$	$5 \times 10^7 - 5 \times 10^{11} \text{ A m}^{-3}$
$a_{j_{0,c}}^{ref} (353 \text{ K})$	$2.5 \times 10^3 \text{ A m}^{-3}$	$1 - 1 \times 10^4 \text{ A m}^{-3}$
α_a	1	0.25-1
α_c	1	0.25-1
σ_m	14 S m^{-1}	$6 - 14 \text{ S m}^{-1}$

6.4.2 Parametric analysis

Polarization curves are calculated by varying only one parameter at a time and keeping the rest of the parameters constant at their base values. These base values are reported in Table

6.4 and were used in our previous work [34] for fuel cell numerical simulations. The variation range of these parameters, also presented in Table 6.4, is selected based on their maximum and minimum values reported in literature.

Figures 6.4a and 6.4b display the effect of $a_{j_{0,a}}^{ref}$ and $a_{j_{0,c}}^{ref}$ (353 K) on the calculated polarization curves. As can be seen from these figures, while $a_{j_{0,c}}^{ref}$ (353 K) (Figure 6.4b) demonstrates significant impact on the predicted values of V-I in all the current density range, $a_{j_{0,a}}^{ref}$ (Figure 6.4a) mainly affects the model predictions in the medium current density range. In other words, at lower overpotentials, the activation resistance dominates the fuel cell performance, and the cathode exchange current density has more influence, which is expected due to the limiting effect of cathode reduction reaction. Indeed, the cathode oxygen reduction reaction (ORR) is several orders of magnitude slower than the anode hydrogen oxidation reaction (HOR), and is thus the limiting factor of the fuel cell performance [47] at low overpotential. In addition, Figure 6.4a reveals that at some point, increasing $a_{j_{0,a}}^{ref}$ values ($\geq 5 \times 10^{10} \text{ A m}^{-3}$) has negligible impact on the calculated values of the polarization curve; in other words, the limiting effect of the anode vanishes and the polarization becomes mainly dictated by other losses.

It should be noticed that the value of $a_{j_{0,c}}^{ref}$ (353 K) doesn't change the slope of the curves in the linear region of the polarization curves, dominated by internal resistance (see Figure 6.4b), which is in line with earlier works [48,49]. On the other hand, the value of $a_{j_{0,a}}^{ref}$ affects the slope of the linear portion of the polarization curves, especially for values $< 5 \times 10^9 \text{ A m}^{-3}$. Such a difference in behaviour between $a_{j_{0,a}}^{ref}$ and $a_{j_{0,c}}^{ref}$ (353 K) can be explained by comparing the form of equations (6.6) and (6.7). Indeed, a proportional dependence between the reaction rate and the overpotential η is used in the electrochemical expression of r_a in the anode (equation (6.6)), while an exponential dependence was used in equation (6.7) for r_c at the cathode, which explains the different trends of Figures 6.4a and 6.4b. Linear dependency for the anode side has been used in previous works [34,50]. Overall, it can be concluded that the values of $a_{j_{0,a}}^{ref}$ and $a_{j_{0,c}}^{ref}$ (353 K) have a strong influence on the calculated polarization curves.

The effect of transfer coefficients α_a and α_c on the calculated polarization curves are illustrated in Figures 6.4c and 6.4d, respectively. As can be seen from these figures, α_c has a significant effect on the polarization curves, whereas α_a has negligible impact. This is again related to the electrochemical expressions applied for r_a and r_c in the model.

The last parameter involved in the sensitivity analysis of the model is the membrane conductivity (σ_m). The protonic conductivity of a membrane is a function of membrane water content and temperature [46]. Since in this study the liquid water transport is however not explicitly considered, the electrolyte phase is postulated to have a constant and uniform conductivity. Assuming constant values for σ_m was found adequate to present a qualitative description of the fuel cell performance [48]. In Figure 6.4e, the parametric analysis reveals that variations of σ_m in the range of values typically found in the literature, yield important changes of the polarization curves. Moreover, it can be confirmed that larger values of membrane conductivity lead to higher potential values at a given current density, and hence to a better fuel cell performance [51].

To summarize this sensitivity analysis, it could first be stated that the influence of transfer coefficient of the anode reaction α_a on the polarization curves predicted by the model is very small. Hence, the base value reported in Table 6.4 will be assigned to this parameter for the rest of the analysis. However, the values of $aj_{0,a}^{ref}$, $aj_{0,c}^{ref}$ (353 K), α_c , and σ_m were shown to influence significantly the model predicted fuel cell performance over their respective range of accepted literature values. Therefore, these four parameters will be adjusted in the following steps for the model calibration.

Finally, it is informative to notice that most influential parameters identified by the sensitivity analysis in this paper are similar to those obtained previously [48]; however, the authors of this reference used a much more complex model involving three-dimensional, two-phase, non-isothermal simulations. Hence, the simplification used in the current model proved to correctly capture the essential phenomena in the fuel cell in order to predict overall trends with respect to undetermined parameters.

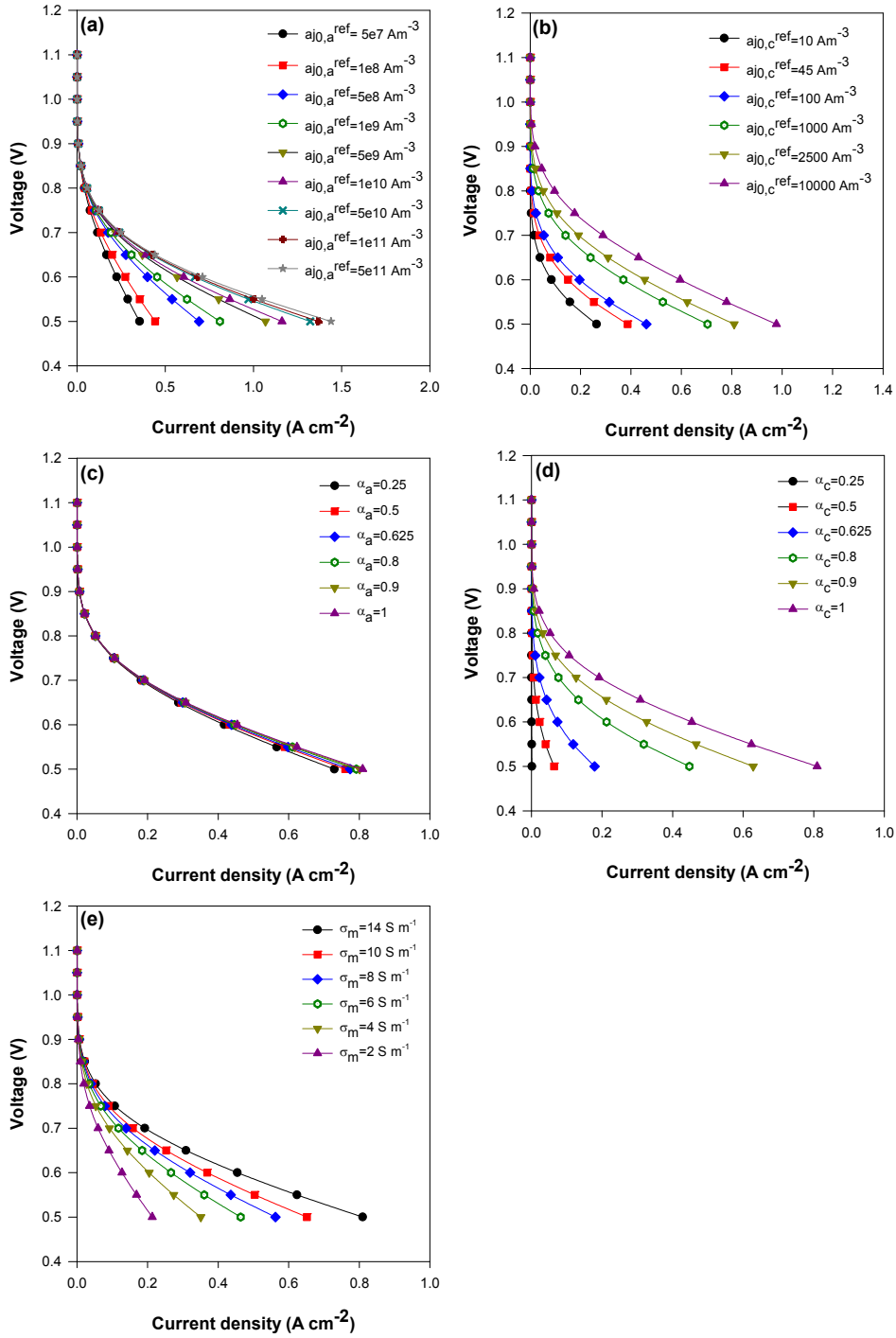


Figure 6.4 Polarization curves obtained from numerical simulations (solid lines) and experimental results, for the fuel cell design using the homemade electrode on the anode side.

6.5 Fuel cell model calibration

The objective in this section is to use experimental data to estimate the value of the four important adjustable parameters identified in the previous section. More precisely, the idea is to find the set of undetermined parameters values that provides the best match between numerical simulations results and experimental data.

Obtaining values for undetermined parameters of PEM fuel cell model has been done in recent literature. For example, Guo et al. [52] determined the model parameters including porosity, exchange current density and effective ionic conductivity of the electrolyte by least-squares fitting of experimental polarization curves measured at three different operating pressures. Dobson et al. [53], coupled a multi-dimensional model of PEM fuel cell MEA with a nonlinear least-squares parameter estimation algorithm to seek the micro-structural parameters of the catalyst layer. The results revealed that only a unique set of structural parameters could accurately predict the multiple polarization curves measured over a range of operating conditions.

Hu et al. [54], adjusted two electrochemical parameters (i.e., $a_{j_{0,a}}^{ref}$ and $a_{j_{0,c}}^{ref}$ (353 K)) while other geometric, operational and physical parameters were considered to be well determined or estimated. These two undetermined parameters were adjusted in such a way that the polarization curves obtained by numerical simulation were close to the experimental polarization curves obtained at various pressure and temperature. It is worth mentioning that the experimental data used in [54] were obtained from literature (i.e., by other research teams), and that some parameters values associated to the experimental fuel cell device had to be assumed. Utilization of experimental data that were measured by other groups and under conditions that do not specifically resemble the parameters used in those models were regularly found in literature [25, 55-57].

Similar to [52,53], the strategy used in this section will allow determining the values of the four adjustable parameters by best-fitting polarizations curves obtained at *various operating conditions*, hence, the model will be considered to be valid over a range of temperature and pressure. Moreover, the experimental data used for the best-fitting step will have been

generated *by the authors of this text*, hence, the operating conditions and all design parameters of the fuel cell are well determined and do not need to be guessed.

First, calibration of the model will be performed with the Commercial/Commercial fuel cell design (Figure 6.2a) in Section 6.5.1. Then, the parameters values obtained for the commercial electrodes will be used in Sections 6.5.2 and 6.5.3 for calibration of the remaining parameters for the Home-made/Commercial design (Figure 6.2b) and for the Commercial/Home-made design (Figure 6.2c), respectively.

6.5.1 Commercial/Commercial fuel cell model calibration

The fuel cell design made of commercial electrodes on both anode and cathode sides (see Figure 6.2a) is implemented in the numerical tools described in Section 6.3. The size of each layer of the 2D domain representing the fuel cell is given in Table 6.3. In the model, all parameters are well determined, except for the values of $a_{j_{0,a}}^{ref}$, $a_{j_{0,c}}^{ref}$ (353 K), α_c , and σ_m .

In addition to the numerical simulation, an experimental measurement of the polarization curve for this fuel cell design was also performed as discussed in Section 6.2.3. First, measurements were obtained under an initial operating condition ($T_{fuel\ cell} = 80^\circ\text{C}$ and electrode backpressure = 15 psig), and the corresponding data are illustrated on a V-I axis in Figure 6.5. Then, measurements were made at a different electrode backpressure (i.e., $T_{fuel\ cell} = 80^\circ\text{C}$ and electrode backpressure = 30 psig), and a different cell temperature (i.e., $T_{fuel\ cell} = 60^\circ\text{C}$ and electrode backpressure = 15 psig). The polarizations curves corresponding to these different operating conditions are reported in Figure 6.5.

To perform the calibration process, a suitable variation range is selected for each of the four undetermined parameters (i.e., $a_{j_{0,a}}^{ref}$, $a_{j_{0,c}}^{ref}$ (353 K), α_c , and σ_m). A finite group of values is selected within the range of each parameter. Then, different sets of model parameters are generated by considering all the possible permutations of the values of these four parameters (a total of 144 set of parameter values). Finally, the corresponding polarization curves are computed for each set of parameters values, for the three operating conditions described above. The polarization curves obtained by including each set of parameters in the numerical model are compared to the experimental data in order to find the parameter set that match the

experimental data more closely. The best set of parameters is defined as the set that provides the minimal value of total error (err_{tot}), where err_{tot} is defined as:

$$err_{tot} = \sum_{m=1}^3 \left[\sum_{n=1}^N \left(i_{num,m}(V_n) - i_{exp,m}(V_n) \right)^2 \right] / N \quad (6.8)$$

In equation (6.8), the subscript n is the identifier of the different electric potential values V_n at which the numerical and experimental current density (i.e., $i_{num,m}(V_n)$ and $i_{exp,m}(V_n)$) are compared. Furthermore, the subscript m identifies the operating conditions (pressure, temperature) at which the polarization curves were obtained (here, there are three operating conditions). Hence, the error variable err_{tot} represents the sum of squared differences between experimental and numerical current densities, considering all operating conditions tested.

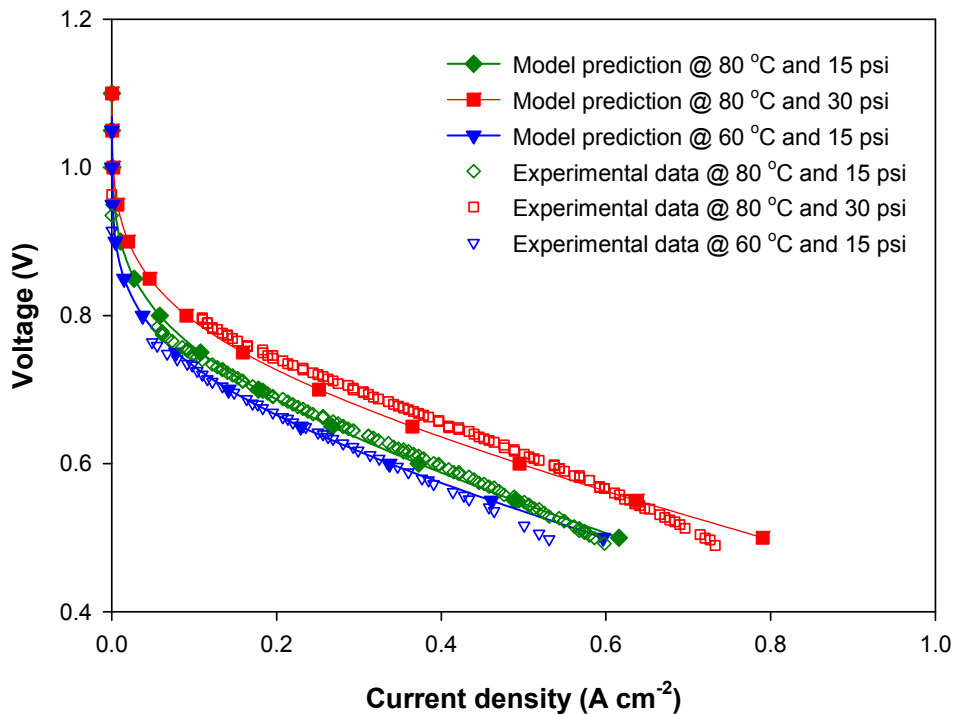


Figure 6.5 Polarization curves obtained from numerical simulations (solid lines) and experimental results, for the fuel cell design using commercial electrodes.

The best set of parameters for the Commercial/Commercial fuel cell model was identified by selecting the curves that provides the minimal value of err_{tot} . That optimal set is reported in Table 6.5, and the polarization curves obtained by using these parameters values in the numerical tools are presented in Figure 6.5. More specifically, the three polarization curves

obtained for the same three operating conditions through experimental measurements (i.e., $T_{\text{fuel cell}} = 80 \text{ }^\circ\text{C}$ and electrode backpressure = 15 psig, $T_{\text{fuel cell}} = 80 \text{ }^\circ\text{C}$ and electrode backpressure = 30 psig, and $T_{\text{fuel cell}} = 60 \text{ }^\circ\text{C}$ and electrode backpressure = 15 psig) are shown in Figure 6.5. First, it can be seen in Figure 6.5 that the impact of temperature and pressure are correctly represented by the model, i.e., the curves obtained by numerical simulations increases with the temperature, and increases with pressure. Moreover, the numerical curves follow correctly the trends of experimental curves with respect to temperature and pressure, i.e., they change with the good order of magnitude. This is possible due to the improvement of the model that were made in this work, i.e., by including equations (6.3), (6.4) and (6.5), which capture the temperature and pressure dependence of several parameters.

It should be observed in Figure 6.5 that the model does not match perfectly the experimental data. However, the intent here is not to develop a highly accurate model. Actually, the intent is to develop a model that captures the general behaviour of the fuel cell with respect to various parameters.

Table 6.5 Four series of adjusted parameters

	$aj_{0,a}^{ref} \text{ (A m}^{-3}\text{)}$	$aj_{0,c}^{ref} \text{ (353 K)(A m}^{-3}\text{)}$	α_c	$\sigma_m \text{ (S m}^{-1}\text{)}$
Commercial electrodes	5×10^8	5×10^3	1	10
Home-made anode	5×10^9	5×10^3	1	10
Home-made cathode	5×10^8	5×10^3	1	10

To summarize, a set of parameters values that allows numerical simulation of fuel cell design using commercial electrodes (see Figure 6.2a) was identified. This set of parameters represents the electrochemical behaviour of the commercial electrodes. Hence, these parameters values will be used in the following sections, where commercial electrodes are included in the modified fuel cell designs.

6.5.2 Home-made/Commercial fuel cell model calibration

The fuel cell investigated in this section is operated under similar conditions to those applied to the fuel cell design made only with commercial electrodes (Section 6.5.1). Therefore, most

of the parameters and governing equations are kept unchanged in the mathematical and numerical models. However, the geometrical parameters of the electrode on the anode side were modified according to the measured dimensions of the GDL (Toray carbon paper, TGP-H-060) and of the home-made electrode (see Figure 6.2 and Table 6.3). Moreover, the thermophysical properties of the GDL used for the home-made anodic electrode, such as porosity and permeability, are modified according to the available values from the technical data sheet of the suppliers.

The model associated to the fuel cell includes only one undetermined parameter, $a_{j_{0,a}}^{ref}$, which has to be found by best-fitting strategy. The other parameters ($a_{j_{0,c}}^{ref}$ (353 K), α_c and σ_m) are assigned the values reported in Table 6.5 (column “commercial/commercial”), because the same membrane (i.e., the same σ_m value) and the same commercial electrode on the cathode side (i.e., the same $a_{j_{0,c}}^{ref}$ (353 K) and α_c values) are used in the current design.

Figure 6.6 presents the experimental data obtained by using the home-made electrode at the anode side, along with the best-fitted curves obtained from numerical simulations. The best-fitted numerical curves were obtained by identifying the value of $a_{j_{0,a}}^{ref}$ that minimizes the error defined in equation (6.8). The experimental and numerical polarization curves were obtained under three operating conditions, i.e.,: (i) $T_{fuel\ cell} = 80\ ^\circ\text{C}$ and electrode backpressure = 15 psig, (ii) $T_{fuel\ cell} = 80\ ^\circ\text{C}$ and electrode backpressure = 30 psig, and, (iii) $T_{fuel\ cell} = 60\ ^\circ\text{C}$ and electrode backpressure = 15 psig. As can be noticed from this figure, there is some deviation between the numerical simulation results and the experimental data. The larger drop of voltage at higher current density observed for the experimental data in Figure 6.6 is typically associated to mass transfer limitations and flooding effects. However, the 2D, one-phase flow model used in this paper was not developed to capture such effects. Nonetheless, that simple model is clearly able to capture the trends of the polarization curve with respect to temperature and pressure.

The home-made and commercial anode can be compared by considering the $a_{j_{0,a}}^{ref}$ value. Typically, exchange current density based on the active surface area of the catalyst ($j_{0,a}^{ref}$, A m⁻²) is used to evaluate the catalyst activity. However, the electrochemical surface area of the MOF derived electrocatalyst could not be estimated as no cyclic voltammetry

measurements were available. Therefore, the term $aj_{0,a}^{ref}$, that appears in equation (6.6) and is defined as a model parameter, is applied for catalyst evaluation.

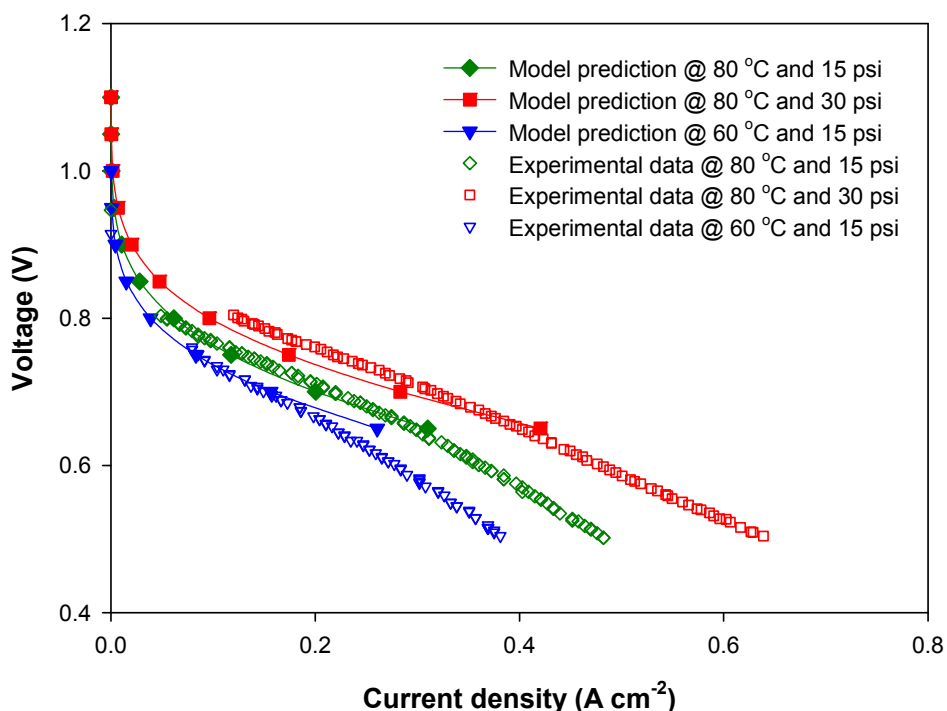


Figure 6.6 Polarization curves obtained from numerical simulations (solid lines) and experimental results, for the fuel cell design using the homemade electrode on the anode side.

Comparing the resulting $aj_{0,a}^{ref}$ value for the home-made anode with the one obtained for commercial anodic electrode (see Table 6.5) reveals a one order of magnitude larger $aj_{0,a}^{ref}$ in the case of the home-made anode. This can be attributed to either sufficient activity of MOF derived electrocatalyst for HOR or the effectiveness of the electrode structure. Considering the polarization curves measured with commercial and home-made anodic electrodes (Figures 6.5 and 6.6) it can be observed that while at low current densities the latter electrode provides slightly higher voltages, moving toward higher current densities, leads to an adverse trend and the former electrode reveals better performance (higher voltages at a given current density). Although at low current densities, the fuel cell performance is mainly limited by the kinetic of the oxidation, at medium current densities, proton (and oxygen) mass transport plays the dominant role. Therefore, it would be more reasonable to assume that performance deterioration results due to the incompetence of the home-made electrode's structure. Interactions between Nafion ionomer and catalyst particles in the ink

solution determine the structural properties of the electrode. Therefore, optimization of the Nafion ionomer content could provide a more effective home-made electrode and improve the fuel cell performance.

To summarize, by using the home-made electrode at the anode side only, it was possible to adjust the value of a single adjustable parameter ($aj_{0,a}^{ref}$) that characterizes the electrochemical behaviour of the home-made electrocatalyst. That value is reported in Table 6.5.

6.5.3 Commercial/Home-made fuel cell model calibration

The mathematical and numerical models are modified to take into account the size and the thermophysical properties of the GDL and the home-made cathode. The model associated to the fuel cell includes two adjustable parameters ($aj_{0,c}^{ref}(353 K)$, α_c), which have to be found by best-fitting strategy. Other parameters ($aj_{0,a}^{ref}$ and σ_m) are assigned to the values reported in Table 6.5 (column “commercial/commercial”), because the same membrane (i.e., the same σ_m value) and the same commercial electrode at the anode side (i.e., the same $aj_{0,a}^{ref}$ value) are used in the current design.

Figure 6.7 presents the experimental curves obtained for the MOF derived electrocatalyst at the cathode side, along with the best-fitted curves obtained from numerical simulations. The best-fitted numerical curves were obtained by identifying the value of $aj_{0,c}^{ref}(353 K)$ and α_c that minimizes the error defined in equation (6.8). These values are reported in Table 6.5. The experimental and numerical polarization curves were obtained at three operating conditions. Again, there is some deviation between the numerical simulation results and the experimental data. Nonetheless, that model is able to capture the trends of the polarization curve with respect to temperature and pressure.

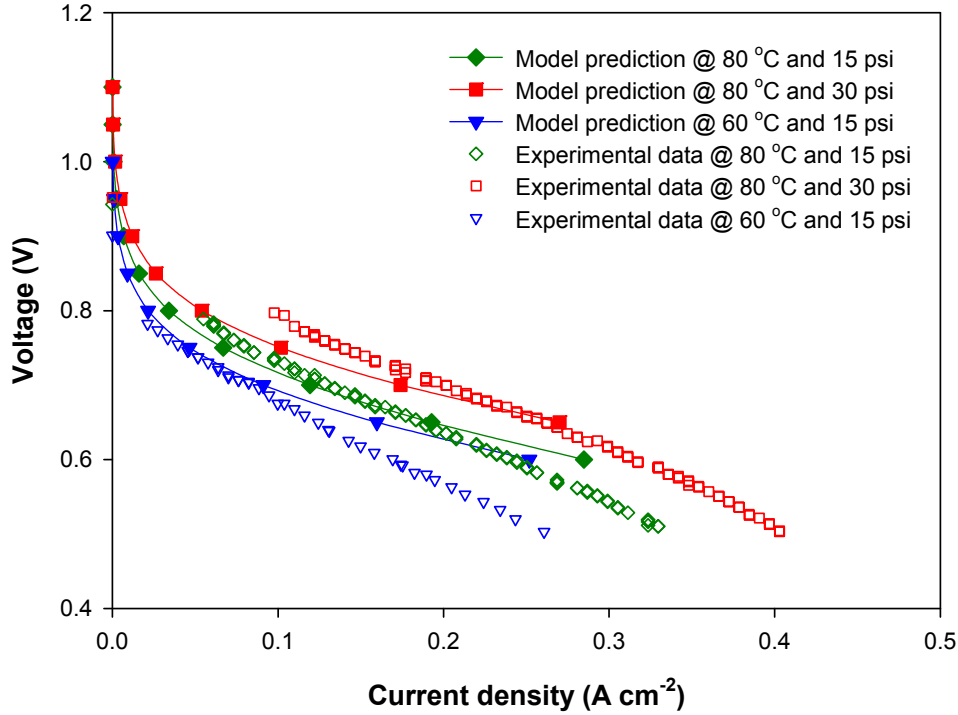


Figure 6.7 Polarization curves obtained from numerical simulations (solid lines) and experimental results, for the fuel cell design using the homemade electrode on the cathode side.

While a_j^{ref} (353 K) and α_c values obtained for the home-made cathode were found equal to those attained with commercial electrode (Table 6.5), the overall performance of the MEA prepared from home-made cathode is lower than the one prepared from the commercial electrode (Figures 6.5 and 6.7). More specifically, considering the linear region of their polarization curves home-made electrode demonstrates higher ionic resistance than the commercial electrode. This also implies the insufficiency of the ink solution regarding its composition as increasing the Nafion ionomer content in the catalyst layer can reduce ohmic losses which occur due to proton transfer resistance.

To summarize Section 6.5, by using best-fitting strategy, it was possible to obtain the value of the adjustable parameters that characterize the electrochemical behaviour of the commercial and home-made electrodes, either on the anode or cathode side (see Table 6.5). By using these parameters, the model is able to capture the general trend of the fuel performance with respect to various parameters and operating conditions. In the following section, the values of adjustable parameters found in this section are included in the numerical model in order to identify optimization opportunities for the home-made electrocatalyst.

6.6 Predicted impact of Nafion content

Recent literature has shown that the performance of Pt-based electrodes can be improved by optimizing the content and distribution of Nafion in fuel cell catalyst layers. However, such studies have not yet been performed for the home-made electrodes fabricated from the MOF derived Pt-based electrocatalysts developed by the authors [8]. Hence, in this section, the numerical tools developed in the current work will be used to reveal if there are opportunities to improve the performance of home-made electrodes by optimizing their Nafion content. To do so, the parameters (a_j^{ref} , a_j^{ref} (353 K), α_c , and σ_m) calibrated in previous sections for commercial and home-made electrodes are included in the model.

6.6.1 Home-made/Commercial fuel cell numerical optimization

Parametric study of the current density is performed with respect to the Nafion content, $\varepsilon_{m,catalyst}$, in the catalyst layer in order to determine its impact on the overall performance of PEM fuel cell using home-made electrodes at the anode side. It is worth mentioning that during this study, $\varepsilon_{m,catalyst}$ was varied only at the electrode side in which home-made electrode is applied. The operating conditions used in the simulations are $T_{fuel\ cell} = 80\text{ }^\circ\text{C}$ and electrode backpressure = 15 psig.

Figure 6.8 exhibits the calculated current densities as a function of $\varepsilon_{m,catalyst}$ for three different electric potentials (0.6, 0.4 and 0.2 V). As can be observed from this figure, according to the model, there is an optimal value of the Nafion content at each electric potential investigated. Moreover, the impact of the Nafion ionomer content on fuel cell performance looks very similar at three electric potential values investigated. In addition, the optimal value of Nafion ionomer is quite similar (average ~ 0.67) for the various electric potential investigated: it is 0.74 for 0.6 V, 0.68 for 0.4 V and 0.6 for 0.2 V. In other words, according to the numerical simulations the optimal Nafion content is robust, and should provide good fuel cell performance over a wide range of electric potential.

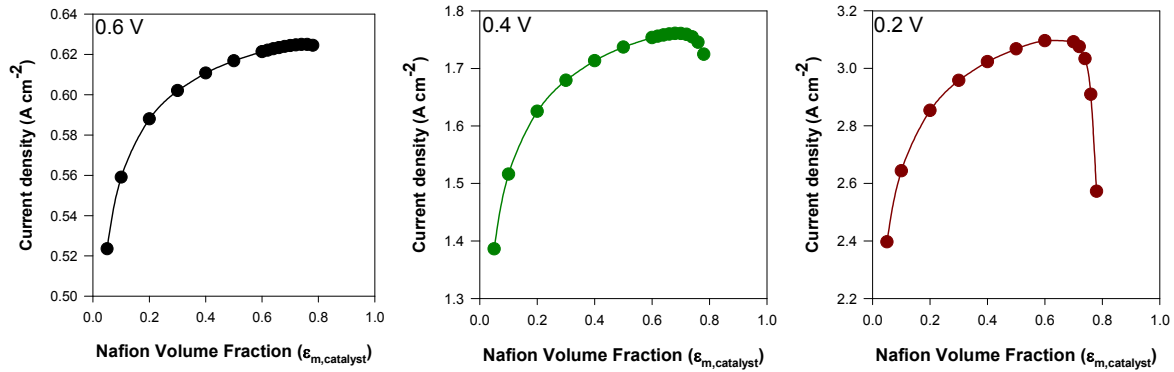


Figure 6.8 Numerical prediction of the impact of Nafion content on the current density, for the fuel cell design using home-made electrode on the anode side. (a) Fixed electrical potential of 0.6 V, (b) 0.4 V, and (c) 0.2 V.

6.6.2 Commercial/Home-made fuel cell numerical optimization

A parametric study of the current density was also performed with respect to the Nafion content, $\epsilon_{m,catalyst}$, in the catalyst layer for the PEM fuel cell using home-made electrode on the cathode side. Again, $\epsilon_{m,catalyst}$ is varied only at the electrode side in which home-made electrode is applied. The operating conditions used in the simulations are $T_{fuel\ cell} = 80\ ^\circ C$ and electrode backpressure = 15 psig.

The impact of Nafion content on the calculated current densities is shown for three different electric potentials (0.6, 0.4 and 0.2 V) in Figure 6.9. It can be observed in this figure that there is again an optimal value of the Nafion content at each electric potential investigated. The optimal value of Nafion ionomer is also found to be robust (i.e., optimal value of 0.7 at 0.6 V, 0.7 at 0.4 V, and 0.6 at 0.2 V). This robustness is an important characteristic if the fuel cell is to be used in transient condition (various electrical potential values).

To verify the trend predicted by the model (i.e., the presence of optimal Nafion content values) for the home-made anode and cathode electrodes, experimental measurements were performed as reported in the next section.

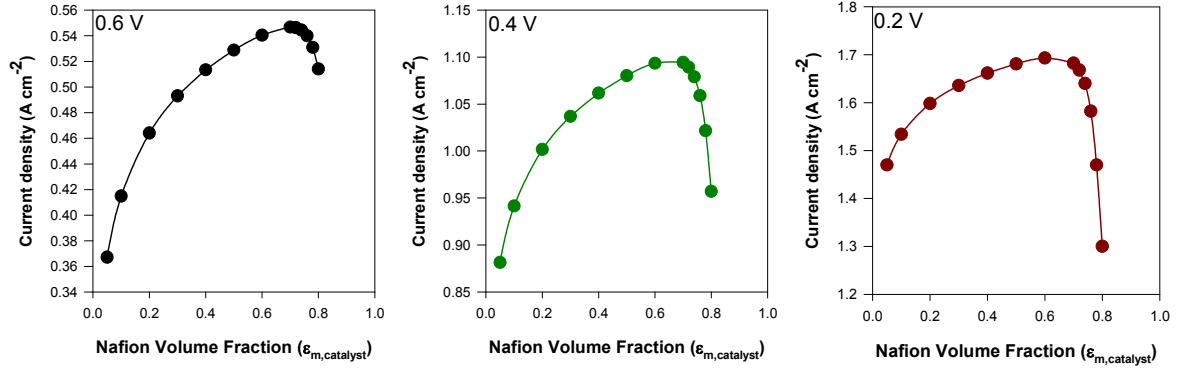


Figure 6.9 Numerical prediction of the impact of Nafion content on the current density, for the fuel cell design using home-made electrode on the cathode side. (a) Fixed electrical potential of 0.6 V, (b) 0.4 V, and (c) 0.2 V.

6.7 Experimental measurement of Nafion content impact

The two electrodes investigated numerically in Section 6.6 were fabricated and the PEM fuel cell polarization curves of the corresponding MEAs were experimentally measured for various values of Nafion content.

Catalyst ink solutions containing 10, 20, 25, 30, 35, 40 and 50 wt% of Nafion were prepared. The weight percentage of Nafion ionomer in the catalyst layer is defined as:

$$N(\text{wt}\%) = \frac{w_{Nafion}}{w_{Nafion} + w_{catalyst}} \times 100 \quad (6.9)$$

where, w_{Nafion} is the weight of dry ionomer and $w_{catalyst}$ is the weight of MOF-derived catalyst. Hence, knowing the desired values of Nafion content N (wt%), it was possible to choose appropriate values for w_{Nafion} and $w_{catalyst}$ during the ink preparation, by virtue of equation (6.9). The volume fraction of the electrolyte phase in the catalyst layers ($\epsilon_{m,catalyst}$) is related to Nafion content N (wt%) and can be calculated using the following expression [37]:

$$\epsilon_{m,catalyst} = \frac{N(\text{wt}\%) \times (1/f) \times (m_{Pt}/L_{Cl})}{\rho_N \times (1 - N(\text{wt}\%))} \quad (6.10)$$

where all the parameters have the same definition as before.

6.7.1 Home-made/Commercial fuel cell experimental measurement

First, the MEAs using home-made electrode at the anode side (illustrated in Figure 6.1 and 6.2b) were fabricated with the various Nafion content (N (wt%)) values listed above. These MEAs were included in the fuel cell test bench, one at a time, and the corresponding polarization curves are reported in Figure 6.10. In that figure, it can be seen that the Nafion content has an impact on the performance of the fuel cell (i.e., on the current density generated at a given voltage).

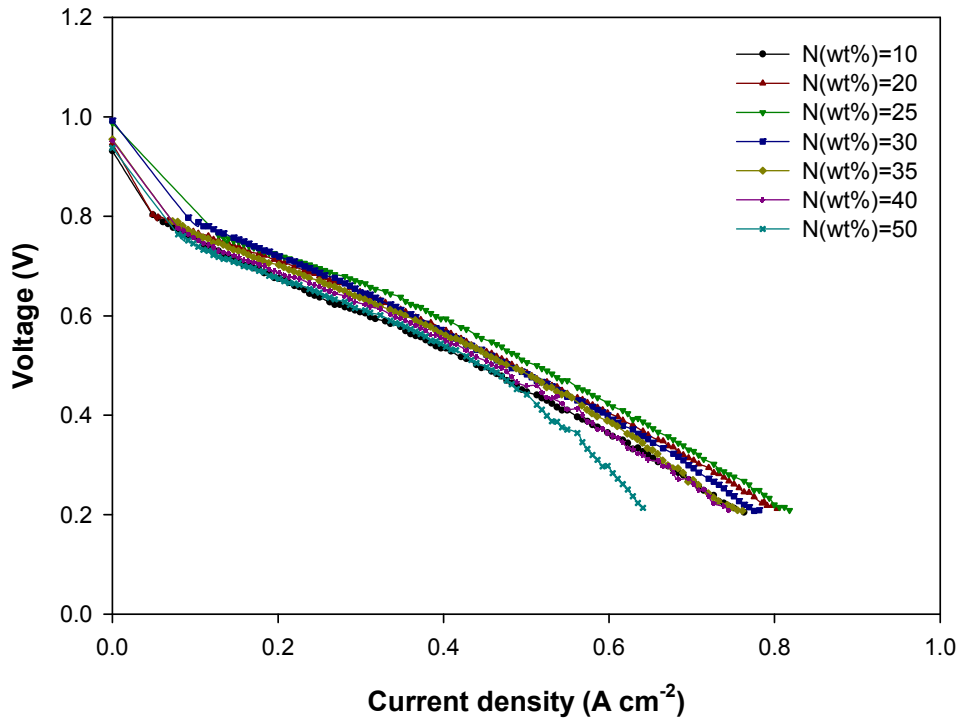


Figure 6.10 Measured polarization curves of the fuel cell design using homemade electrode on the anode side, for various Nafion content.

Furthermore, the values of the current density at three specific voltages were taken from this data and were reported in Figure 6.11. More specifically, Figures 6.11a, 6.11b and 6.11c depict the current density with respect to the Nafion content for 0.6, 0.4 and 0.2 V, respectively. In these three cases, a maximum current density and an optimal value of Nafion content are clearly observed. The optimal value of Nafion volume fraction ($\varepsilon_{m,catalyst}$) is 0.04, corresponded to $N(\text{wt}\%) = 25 \text{ wt}\%$, at 0.6 V, 0.4 V and 0.2 V, hence, the optimal values for that fuel cell design are similar for a wide range of electric potential. That robustness characteristic was also predicted by the numerical analysis.

It can be noticed that the optimal values of Nafion volume fraction at the three selected voltages from experimental measurements (~ 0.04) are not equal to those predicted by numerical simulation (~ 0.67). This is expected because the model neglects several transport phenomena. Nonetheless, the *trends* observed in Figure 6.11 are equivalent to those observed with the numerical analysis (Figure 6.8), i.e.,: (i) the presence of an optimal Nafion content, (ii) the optimal Nafion content is almost independent of the fuel cell voltage, and (iii) the dependency of the current density with respect to the Nafion content is similar at various voltage value.

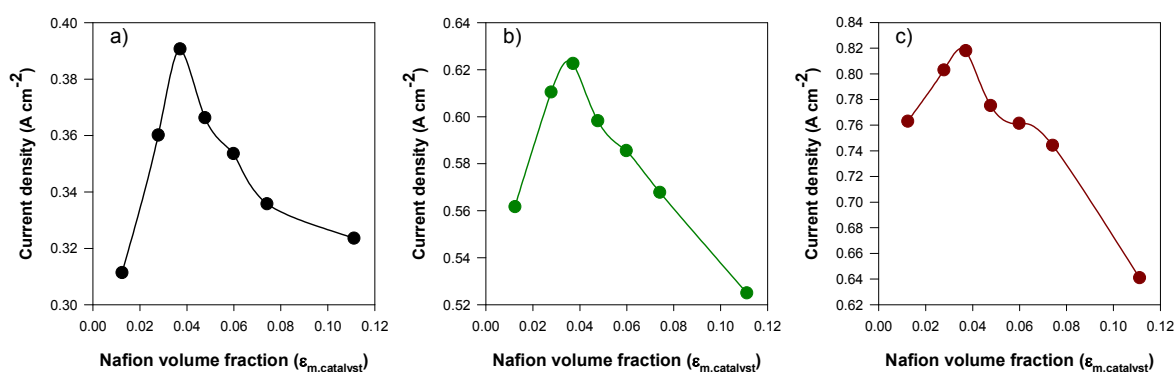


Figure 6.11 Measurement of the impact of Nafion content on the current density, for the fuel cell design using home-made electrode on the anode side. (a) Fixed electrical potential of 0.6 V, (b) 0.4 V, and (c) 0.2 V.

6.7.2 Commercial/homemade fuel cell experimental measurement

The MEAs using home-made electrode at the cathode side (illustrated in Figure 6.1 and 6.2c) were also fabricated with the various Nafion content values listed above. The corresponding polarization curves are reported in Figure 6.12. In that figure, it can be seen that the Nafion content at the cathode side has a larger impact on the performance of the fuel cell (i.e., on the current density generated at a given voltage), than on the anode side (Figure 6.10).

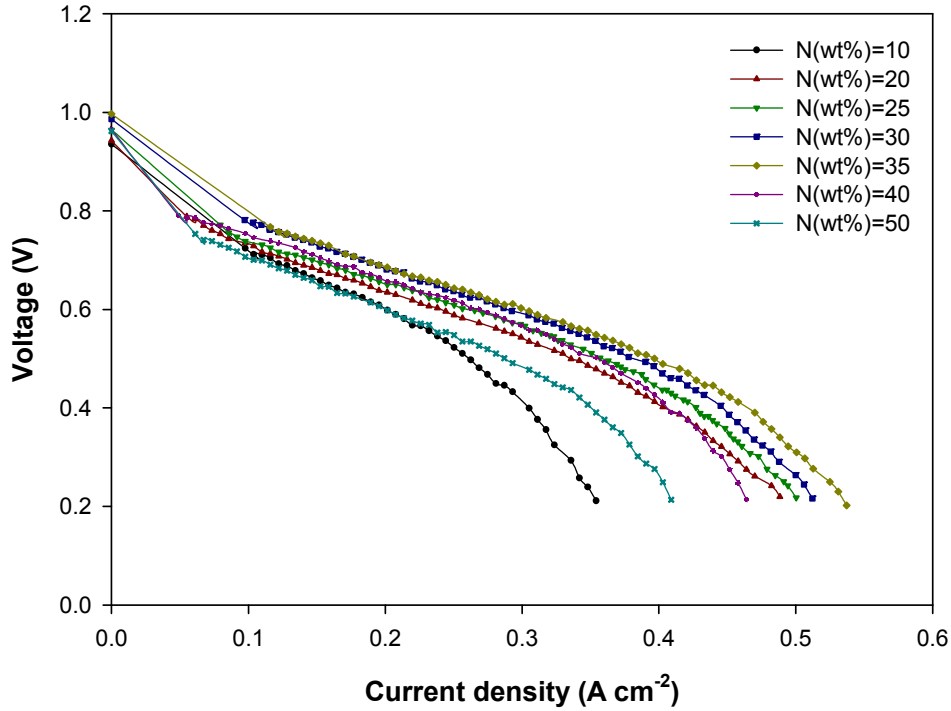


Figure 6.12 Measured polarization curves of the fuel cell design using homemade electrode on the cathode side, for various Nafion content.

Values of the current density at 0.6, 0.4 and 0.2 V were taken from these data and reported in Figure 6.13a, 6.13b and 6.13c, respectively. Again, several *trends* may be observed: there is an optimal Nafion content at all voltages; optimal values of Nafion volume fraction ($\epsilon_{m,catalyst}$) ~ 0.06 corresponded to $N(wt\%) = 35$ wt%, is almost independent of the fuel cell voltage, and (iii) the dependency of the current density with respect to the Nafion content is roughly similar at various voltage values. These trends were clearly predicted by the numerical model, even if the optimal values of Nafion volume fraction obtained experimentally (~ 0.06 from Figure 6.13) do not match those obtained numerically (~ 0.67 from Figure 6.9).

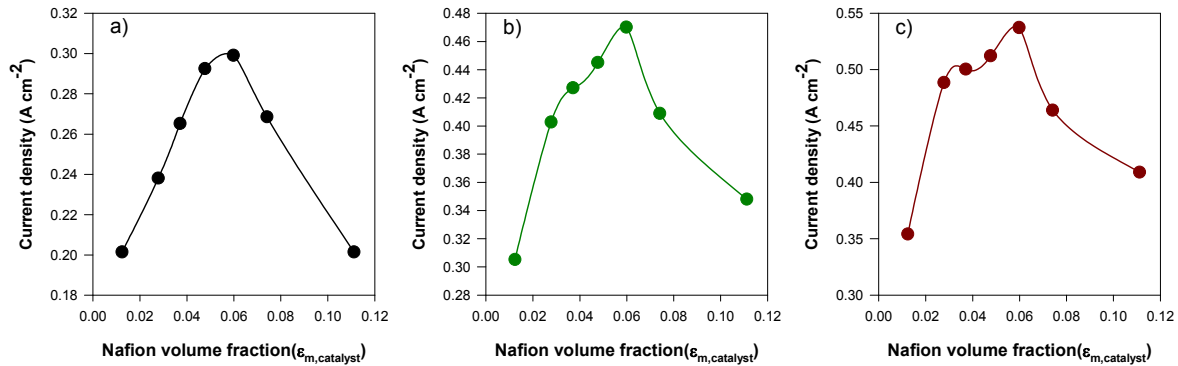


Figure 6.13 Measurement of the impact of Nafion content on the current density, for the fuel cell design using home-made electrode on the cathode side. (a) Fixed electrical potential of 0.6 V, (b) 0.4 V, and (c) 0.2 V.

6.7.3 Discussion of the results

As mentioned earlier, Nafion is needed in the catalyst layer to improve the contact between different phases and subsequently, increase the probability of electrochemical reaction occurrence. While low Nafion contents provide submissive protonic conductivity and lead to poor connection of the catalyst particles to the electrolyte solution, excess Nafion loading, prevents the efficient gas transfer to the catalytic active sites. At high current density region, the increase in water content causes even more resistance to gas transfer whilst promotes the flooding. The numerical and experimental results obtained in this study demonstrated the existence of an optimum Nafion ionomer content for anodic and cathodic home-made electrodes, however, this parameter was found to possess different values. Moreover, both numerical and experimental studies revealed that the impact of Nafion ionomer content on the fuel cell performance is more tangible at the cathode side. As mentioned before, the practical optimum values of Nafion content are different from the model estimations mainly due to the simplifications made during model development.

According to the *numerical* results, for the home-made anode operating at low overpotentials, after a certain point, increasing the Nafion content in the catalyst layer has a very small impact on the fuel cell performance (see Figure 6.8a). However, at larger overpotentials, the impact of Nafion content in catalyst layer ($\epsilon_{m,catalyst}$) demonstrates a more considerable impact (Figure 6.8b and 6.8c). The numerical results demonstrated that unlike the anode side, for the home-made cathode, at all overpotential ranges Nafion ionomer content ($\epsilon_{m,catalyst}$)

affect the calculated current density values (see Figure 6.9). Moreover, at low and medium overpotentials, minimum computed value for current density is found for minimum electrolyte content. At high overpotentials however the minimum current density value calculated from the model corresponds to a maximum Nafion ionomer content. This indicates that too much ionomer in the catalyst layer can lead to significant mass transfer limitations especially at higher current densities and hence diminishes the fuel cell performance.

Based on the *experimental* results, varying Nafion ionomer content between 10 to 50 wt% at the anode side results in a very small reduction in the fuel cell performance (Figure 6.10), while 25 wt% Nafion content was found to be optimum. At the cathode side, Nafion ionomer content shows a larger impact on the overall performance of the PEM fuel cell compared to the anodic electrodes of different composition (Figure 6.12). Increasing the Nafion content from 10 % up to 35 wt% in the cathode catalyst layer improves the fuel cell performance, however, further increment of Nafion causes performance reduction. This reduction can mostly be realized at high current density region. At this region, MEA containing 35 wt% Nafion at the cathodic catalyst layer demonstrates the highest potential.

6.8 Conclusions

In spite of its well recognized impact on PEM fuel cell performance, previous studies did not reveal a uniform optimum value for Nafion ionomer content as it is found to be determined by various factors such as Pt loading in the Pt/C catalyst and type of electrocatalyst or carbon support. Therefore, it is essential to survey the effect of Nafion ionomer content in the catalyst layer of home-made electrodes fabricated from a MOF derived Pt-based electrocatalyst previously synthesized by the author's research group [8].

The effect of model parameters on calculated fuel cell polarization curves was investigated via sensitivity analyses. Among the five undetermined model parameters: $aj_{0,a}^{ref}$, $aj_{0,c}^{ref}(353 K)$, α_a , α_c and σ_m , only α_a was found to be insignificant. This was in accordance with the results previously obtained with a more complex model [37] and confirms the adequacy of the model in predicting overall trends with respect to the parameters.

Excluding α_a , the four remaining adjustable parameters were estimated via model calibration using experimental data obtained for three different MEA designs investigated in the current study: i) commercial electrode at both anode and cathode sides, ii) home-made anodic and commercial cathodic electrodes and iii) commercial anode and home-made cathode electrodes.

Various operating conditions (two different cell temperatures and two different electrode backpressures) were considered to estimate undetermined model parameters by best-fitting several polarization curves obtained over a range of temperature and pressure.

The calibrated model was then used to survey the effect of Nafion ionomer content on the performance of home-made electrodes fabricated from a new MOF-derived Pt-based electrocatalyst at different electrical potentials (0.6, 0.4 and 0.2 V). The model predicted a robust optimal Nafion ionomer content for each of these potentials at which maximum current density was attained for home-made anodic and cathodic electrodes.

Finally, the qualitative trend predicted by the model regarding the optimal Nafion content was verified via experimental measurements. Electrodes containing a range of Nafion ionomer (10-50 wt%) in their catalyst layers were fabricated and used in a single PEM fuel cell. According to the experimental measurements at the anode side 25 wt% Nafion ionomer in the catalyst layer of home-made electrode resulted the best performing fuel cell, however, at the cathode side optimal Nafion content of 35 wt% was observed. Although these optimal values were different from those obtained by numerical simulation, the model predicted trends with respect to the optimal Nafion content were similar to the experimental results. This discrepancy was related to several simplifications made during model development.

Therefore, in future works improvement of the current model to consider the three-dimensional transport phenomena, temperature gradient and two-phase flow will be attempted.

6.9 Nomenclature

Variables

aj_0^{ref} : exchange current density multiplied by specific surface area, $A\ m^{-3}$

C: molar concentration, $mol\ m^{-3}$

D: diffusivity, $\text{m}^2 \text{s}^{-1}$
 err_{tot} : total fitting error
f: mass percentage of platinum
F: Faraday constant, C mol^{-1}
H: channel height, m
i: current density, A cm^{-2}
K: permeability, m^2
 L_I to L_{VII} : thickness of layers I to VII, m
 m_{Pt} : Platinum mass loading, mg cm^{-2}
N: Nafion content, weight percentage
P: pressure, psig
r: electrochemical reaction rate, A m^{-3}
R: universal gas constant, $\text{J mol}^{-1} \text{K}^{-1}$
T: temperature, K
V: electrical potential, V
w: weight of catalyst or Nafion ionomer, mg
x and y: two gas species

Greek symbols

α : transfer coefficient
 β : Kozeny-Carman constant
 ε : porosity
 $\varepsilon_{m,catalyst}$: Nafion volume fraction
 ρ_{Pt} : mass density of platinum, g cm^{-3}
 ρ_C : mass density of carbon black, g cm^{-3}
 η : overpotential, V
 ξ : stoichiometric ratio
 φ : relative humidity
 σ_m : electrolyte phase electrical conductivity, S m^{-1}

Subscripts

a: anode
c: cathode
CL: in catalyst layer

exp: experimental
GDL: in gas diffusion layer
H₂: hydrogen fuel
in: inlet
m: operating conditions identifier
n: electrical potential identifier
num: numerical
O₂: oxygen oxidant
OC: open circuit
out: outlet
Pt: platinum catalyst
porous: in porous medium
s: in solid phase

Superscripts

ref: reference value

Abbreviations

GDL: Gas diffusion layer
HOR: hydrogen oxidation reaction
MOF: metal organic framework
MEA: membrane-electrode assembly
non-PGM: non-platinum group metal
ORR: oxygen reduction reaction
PEMFCs: proton exchange membrane fuel cells
Pt: platinum

6.10 Acknowledgments

The authors would like to thank the Fonds Québécois de Recherche sur la Nature et les Technologies (FQRNT) for financial support.

Chapter 6 References:

- [1] C. Song, Fuel processing for low-temperature and high-temperature fuel cells: Challenges, and opportunities for sustainable development in the 21st century, *Catalysis Today* 77 (2002) 17-49.
- [2] H. Gregor, *Fuel Cell Technology Handbook*, CRC Press, Birkenfeld, Germany (2002).
- [3] H.A. Gasteiger, S.S. Kocha, B. Sompalli, F.T. Wagner, Activity benchmarks and requirements for Pt, Pt-alloy, and non-Pt oxygen reduction catalysts for PEMFCs, *Applied Catalysis B: Environmental* 56 (2005) 9-35.
- [4] B.D. James, J.A. Kalinoski, Mass Production Cost Estimation for Direct H₂ PEM Fuel Cell Systems for Automotive Applications, Arlington, VA, USA (2008).
http://www.hydrogen.energy.gov/pdfs/review08/fc_7_james.pdf
- [5] K. Gong, F. Du, Z. Xia, M. Durstock, L. Dai, Nitrogen-Doped Carbon Nanotube Arrays with High Electrocatalytic Activity for Oxygen Reduction, *Science* 323 (2009) 760-764.
- [6] Y. Wang, Y. Shao, D.W. Matson, J. Li, Y. Lin, Nitrogen-Doped Graphene and Its Application in Electrochemical Biosensing, *ACS Nano* 4 (2010) 1790-1798.
- [7] B. Winther-Jensen, O. Winther-Jensen, M. Forsyth, D.R. MacFarlane, High Rates of Oxygen Reduction over a Vapor Phase-Polymerized PEDOT Electrode, *Science* 321 (2008) 671-674.
- [8] F. Afsahi, H. Vinh-Thang, S. Mikhailenko, S. Kaliaguine, Electrocatalyst synthesized from metal organic frameworks, *Journal of Power Sources* 239 (2013) 415-423.
- [9] E. Passalacqua, F. Lufrano, G. Squadrito, A. Patti, L. Giorgi, Nafion content in the catalyst layer of polymer electrolyte fuel cells: effects on structure and performance, *Electrochimica Acta* 46 (2001) 799-805.
- [10] G. Sasikumar, J.W. Ihm, H. Ryu, Dependence of optimum Nafion content in catalyst layer on platinum loading, *Journal of Power Sources* 132 (2004) 11-17.
- [11] A.M. Chaparro, B. Gallardo, M.A. Folgado, A.J. Martín, L. Daza, PEMFC electrode preparation by electrospray: Optimization of catalyst load and ionomer content, *Catalysis Today* 143 (2009) 237-241.
- [12] C.-N. Sun, K.L. More, G.M. Veith, T.A. Zawodzinski, Composition Dependence of the Pore Structure and Water Transport of Composite Catalyst Layers for Polymer Electrolyte Fuel Cells, *Journal of The Electrochemical Society* 160 (2013) F1000-F1005.
- [13] G. Sasikumar, J.W. Ihm, H. Ryu, Optimum Nafion content in PEM fuel cell electrodes, *Electrochimica Acta* 50 (2004) 601-605.
- [14] S. Jeon, J. Lee, G.M. Rios, H.-J. Kim, S.-Y. Lee, E. Cho, T.-H. Lim, J. Hyun Jang, Effect of ionomer content and relative humidity on polymer electrolyte membrane fuel cell (PEMFC) performance of membrane-electrode assemblies (MEAs) prepared by decal transfer method, *International Journal of Hydrogen Energy* 35 (2010) 9678-9686.
- [15] P. Gode, F. Jaouen, G. Lindbergh, A. Lundblad, G. Sundholm, Influence of the composition on the structure and electrochemical characteristics of the PEFC cathode, *Electrochimica Acta* 48 (2003) 4175-4187.
- [16] Q. Zheng, X. Cheng, T.-C. Jao, F.-B. Weng, A. Su, Y.-C. Chiang, Fuel cell performances at optimized Nafion and Ru₈₅Se₁₅ loadings in cathode catalyst layer, *Journal of Power Sources* 201 (2012) 151-158.
- [17] C.-Y. Ahn, J.-Y. Cheon, S.-H. Joo, J. Kim, Effects of ionomer content on Pt catalyst/ordered mesoporous carbon support in polymer electrolyte membrane fuel cells, *Journal of Power Sources* 222 (2013) 477-482.
- [18] M. Eguchi, K. Baba, T. Onuma, K. Yoshida, K. Iwasawa, Y. Kobayashi, K. Uno, K. Komatsu, M. Kobori, M. Nishitani-Gamo, T. Ando, Influence of Ionomer/Carbon Ratio on the Performance of a Polymer Electrolyte Fuel Cell, *Polymers* 4 (2012) 1645-1656.
- [19] D. Harvey, J.G. Pharoah, K. Karan, A comparison of different approaches to modelling the PEMFC catalyst layer, *Journal of Power Sources* 179 (2008) 209-219.

- [20] Q. Wang, M. Eikerling, D. Song, Z. Liu, T. Navessin, Z. Xie, S. Holdcroft, Functionally Graded Cathode Catalyst Layers for Polymer Electrolyte Fuel Cells: I. Theoretical Modeling, *Journal of The Electrochemical Society* 151 (2004) A950-A957.
- [21] C. Marr, X. Li, Composition and performance modelling of catalyst layer in a proton exchange membrane fuel cell, *Journal of Power Sources* 77 (1999) 17-27.
- [22] D. Song, Q. Wang, Z. Liu, T. Navessin, M. Eikerling, S. Holdcroft, Numerical optimization study of the catalyst layer of PEM fuel cell cathode, *Journal of Power Sources* 126 (2004) 104-111.
- [23] N.P. Siegel, M.W. Ellis, D.J. Nelson, M.R. von Spakovsky, Single domain PEMFC model based on agglomerate catalyst geometry, *Journal of Power Sources* 115 (2003) 81-89.
- [24] D.H. Schwarz, N. Djilali, 3D Modeling of Catalyst Layers in PEM Fuel Cells: Effects of Transport Limitations, *Journal of The Electrochemical Society* 154 (2007) B1167-B1178.
- [25] S. Kamarajugadda, S. Mazumder, Numerical investigation of the effect of cathode catalyst layer structure and composition on polymer electrolyte membrane fuel cell performance, *Journal of Power Sources* 183 (2008) 629-642.
- [26] M. Srinivasarao, D. Bhattacharyya, R. Rengaswamy, S. Narasimhan, Multivariable optimization studies of cathode catalyst layer of a polymer electrolyte membrane fuel cell, *Chemical Engineering Research and Design* 89 (2011) 10-22.
- [27] S. Obut, E. Alper, Numerical assessment of dependence of polymer electrolyte membrane fuel cell performance on cathode catalyst layer parameters, *Journal of Power Sources* 196 (2011) 1920-1931.
- [28] W.K. Epting, S. Litster, Effects of an agglomerate size distribution on the PEFC agglomerate model, *International Journal of Hydrogen Energy* 37 (2012) 8505-8511.
- [29] F.C. Cetinbas, S.G. Advani, A.K. Prasad, A Modified Agglomerate Model with Discrete Catalyst Particles for the PEM Fuel Cell Catalyst Layer, *Journal of The Electrochemical Society* 160 (2013) F750-F756.
- [30] L. Pisani, M. Valentini, G. Murgia Analytical Pore Scale Modeling of the Reactive Regions of Polymer Electrolyte Fuel Cells, *Journal of The Electrochemical Society* 150 (2003) A1549-A1559.
- [31] G. Wang, P.P. Mukherjee, C.-Y. Wang, Direct numerical simulation (DNS) modeling of PEFC electrodes: Part I. Regular microstructure, *Electrochimica Acta* 51 (2006) 3139-3150.
- [32] P.P. Mukherjee, C.-Y. Wang, Stochastic Microstructure Reconstruction and Direct Numerical Simulation of the PEFC Catalyst Layer, *Journal of The Electrochemical Society* 153 (2006) A840-A849.
- [33] L. Xing, M. Mamlouk, R. Kumar, K. Scott, Numerical investigation of the optimal Nafion® ionomer content in cathode catalyst layer: An agglomerate two-phase flow modelling, *International Journal of Hydrogen Energy* 39 (2014) 9087-9104.
- [34] F. Mathieu-Potvin, L. Gosselin, Optimal topology and distribution of catalyst in PEMFC, *International Journal of Hydrogen Energy* 39 (2014) 7382-7401.
- [35] H. Ju, C.-Y. Wang, Experimental Validation of a PEM Fuel Cell Model by Current Distribution Data, *Journal of The Electrochemical Society* 151 (2004) A1954-A1960.
- [36] N. Zamel, X. Li, Effective transport properties for polymer electrolyte membrane fuel cells – With a focus on the gas diffusion layer, *Progress in Energy and Combustion Science* 39 (2013) 111-146.
- [37] D. Cheddie, N. Munroe, Parametric model of an intermediate temperature PEMFC, *Journal of Power Sources* 156 (2006) 414-423.
- [38] E.L. Cussler, *Diffusion–Mass Transfer in Fluid Systems*, Cambridge University Press, Cambridge, 1984.
- [39] A. Parthasarathy, S. Srinivasan, A.J. Appleby, C.R. Martin, Temperature Dependence of the Electrode Kinetics of Oxygen Reduction at the Platinum/Nafion® Interface—A Microelectrode Investigation, *Journal of The Electrochemical Society* 139 (1992) 2530-2537.
- [40] COMSOL Multiphysics, COMSOL AB Inc.

- [41] G. Dhatt, E. Lefrançois, G. Touzot, Finite Element Method, John Wiley & Sons, Inc. New York, N.Y. USA (1984).
- [42] F. Mathieu-Potvin, L. Gosselin, A.K. da Silva, Optimal geometry of catalytic microreactors: Maximal reaction rate density with fixed amount of catalyst and pressure drop, *Chemical Engineering Science* 73 (2012) 249-260.
- [43] W.Q. Tao, C.H. Min, X.L. Liu, Y.L. He, B.H. Yin, W. Jiang, Parameter sensitivity examination and discussion of PEM fuel cell simulation model validation: Part I. Current status of modeling research and model development, *Journal of Power Sources* 160 (2006) 359-373.
- [44] M. Acosta, C. Merten, G. Eigenberger, H. Class, R. Helmig, B. Thoben, H. Müller-Steinhagen, Modeling non-isothermal two-phase multicomponent flow in the cathode of PEM fuel cells, *Journal of Power Sources* 159 (2006) 1123-1141.
- [45] N.P. Siegel, M.W. Ellis, D.J. Nelson, M.R. von Spakovsky, A two-dimensional computational model of a PEMFC with liquid water transport, *Journal of Power Sources* 128 (2004) 173-184.
- [46] T.E. Springer, T.A. Zawodzinski, S. Gottesfeld, Polymer Electrolyte Fuel Cell Model, *Journal of The Electrochemical Society* 138 (1991) 2334-2342.
- [47] M.K. Debe, Electrocatalyst approaches and challenges for automotive fuel cells, *Nature* 486 (2012) 43-51.
- [48] C.H. Min, Y.L. He, X.L. Liu, B.H. Yin, W. Jiang, W.Q. Tao, Parameter sensitivity examination and discussion of PEM fuel cell simulation model validation: Part II: Results of sensitivity analysis and validation of the model, *Journal of Power Sources* 160 (2006) 374-385.
- [49] M. Wöhr, K. Bolwin, W. Schnurnberger, M. Fischer, W. Neubrand, G. Eigenberger, Dynamic modeling and simulation of a polymer membrane fuel cell including mass transport limitation, *International Journal of Hydrogen Energy* 23 (1998) 213-218.
- [50] Y.A. Cengel, M. Boles, Thermodynamics: an engineering approach, 4th edition, McGraw-Hill, New York, NY, USA (2001).
- [51] F. Gao, B. Blunier, A. Miraoui, Proton Exchange Membrane Fuel Cell Modeling, Wiley & Sons, Inc. (2012).
- [52] Q. Guo, V.A. Sethuraman, R.E. White, Parameter Estimates for a PEMFC Cathode, *Journal of The Electrochemical Society* 151 (2004) A983-A993.
- [53] P. Dobson, C. Lei, T. Navessin, M. Secanell, Characterization of the PEM Fuel Cell Catalyst Layer Microstructure by Nonlinear Least-Squares Parameter Estimation, *Journal of The Electrochemical Society* 159 (2012) B514-B523.
- [54] M. Hu, A. Gu, M. Wang, X. Zhu, L. Yu, Three dimensional, two phase flow mathematical model for PEM fuel cell: Part I. Model development, *Energy Conversion and Management* 45 (2004) 1861-1882.
- [55] B.R. Sivertsen, N. Djilali, CFD-based modelling of proton exchange membrane fuel cells, *Journal of Power Sources* 141 (2005) 65-78.
- [56] S. Um, C.Y. Wang, K.S. Chen, Computational Fluid Dynamics Modeling of Proton Exchange Membrane Fuel Cells, *Journal of The Electrochemical Society* 147 (2000) 4485-4493.
- [57] F. Hashemi, S. Rowshanzamir, M. Rezakazemi, CFD simulation of PEM fuel cell performance: Effect of straight and serpentine flow fields, *Mathematical and Computer Modelling* 55 (2012) 1540-1557.

Chapter 7 Complex impedance spectroscopy study of the thermolysis products of metal organic frameworks

Serguei D. Mikhailenko, Foroughazam Afsahi, Serge Kaliaguine*

Department of Chemical Engineering, Laval University, Québec (Québec), Canada, G1V 0A6

Published in Journal of physical Chemistry C (118) 2014 9165-9175

Résumé

La spectroscopie d'impédance a permis d'étudier les produits de la transformation thermique des MOF-253 qui contiennent d'Al auquel on a ajouté du platine pour produire un électrocatalyseur supporté sur noir de carbone. La thermolyse est effectuée à des températures se situant entre 700 et 1050 °C sous atmosphère inerte. Les produits résultants ont démontré diverses propriétés électriques révélées par des réponses très différentes en spectroscopie d'impédance. Le MOF initial est un isolant qui présente une très faible conductivité électrique de $\sigma = 1.3 \times 10^{-11} \text{ S cm}^{-1}$. Les produits obtenus suite à une transformation thermique à 700-800 °C se comportent comme des semi-conducteurs avec une faible conductivité de $\sigma \approx 10^{-6}$ - $10^{-5} \text{ S cm}^{-1}$ à température ambiante. De plus, ils ont une forte dépendance thermique et leur conductibilité électrique augmente à $\sigma \approx 10^{-3} \text{ S cm}^{-1}$ à 200 °C. Les réponses d'impédance sont complexes, et peuvent être interprétées comme correspondant à une conduction mixte où le comportement du semi-conducteur est accompagné d'un transfert de charge ionique. Le produit final obtenu suite à une décomposition à 1050 °C démontre la particularité d'une conductance similaire à celle des métaux avec une dépendance à la température positive, mais faible et une conductivité à température ambiante de $\sigma = 9.0 \times 10^{-2} \text{ S cm}^{-1}$. Les propriétés des électrocatalyseurs de Pt à base de noir de carbone obtenus à 950 °C semblent être intermédiaires entre les deux derniers états de conduction. La thermolyse initiale du MOF-253 s'effectue à des températures inférieures. La conductivité du produit final de la pyrolyse à 1050 °C du MOF-253 initial était inférieure à celle de Pt-MOF avec $\sigma_{25^\circ\text{C}} = 1.0 \times 10^{-2} \text{ S cm}^{-1}$. Un essai d'interprétation des résultats est présenté.

Abstract

The products of thermal transformation of MOF-253 (Al containing MOF) and its Pt-based derivative, into carbon-black-based electrocatalyst were studied using a.c. impedance spectroscopy. The thermolysis was carried out at 700-1050 °C under an inert atmosphere. The resulting products were found to possess diverse electrical properties, revealed through very different impedance responses. As-synthesized MOF material was an insulator with a conductivity of $\sigma = 1.3 \times 10^{-11} \text{ S cm}^{-1}$. Products obtained at 700-800 °C behaved as semiconductors with low room temperature conductivity of ca. $\sigma \approx 10^{-6}$ - $10^{-5} \text{ S cm}^{-1}$ and strong thermal dependence ($\sigma \approx 10^{-3} \text{ S cm}^{-1}$ at 200 °C). They exhibited complex impedance responses, which may be interpreted as mixed conduction, where semiconducting behaviour was accompanied by ionic charge transfer. The final product obtained at 1050 °C exhibited a particular metal-like conductance with positive but weak temperature dependence and ambient conductivity of $\sigma = 9.0 \times 10^{-2} \text{ S cm}^{-1}$. The properties of Pt/carbon-based material obtained at 950 °C seem to be transient between the latter two conduction states. Thermolysis of initial MOF-253 is less hindered and occurs at lower temperatures. The conductivity of the final product of pyrolysis at 1050 °C of initial MOF-253 was inferior to that of Pt-MOF with $\sigma_{25^\circ\text{C}} = 1.0 \times 10^{-2} \text{ S cm}^{-1}$. A tentative interpretation of the results is presented.

7.1 Introduction

It was recently attempted to use metal organic frameworks (MOFs) as precursors in preparation of electrocatalysts for the hydrogen/oxygen fuel cells (FC) [1-3]. This approach is based on the idea to transform the organic ligands linking metal ions, or clusters of the highly crystalline MOF structures, into carbon support for the catalytically active metal particles. The transformation is supposed to be carried out through thermolysis of MOF which purportedly allowed formation of active metal particles simultaneously with the carbon support. This could be beneficial for fine dispersion of the metal and consequently could result in electrocatalysts with high specific surface area, high conductivity and enhanced activity. In a recent paper this approach was tested, and the conditions, required for obtaining a metal/carbon material with good electrical conductivity, were investigated [4]. It should be noted that the efficiency of FCs strongly depends on the catalysts activity as well as their electrical conductivity.

It was observed that during thermolysis in an inert gas flow a MOF sample being initially an insulator transforms into a conductor only after treatment at very high temperature typically above 1000 °C [4]. It is therefore of interest to trace the development of electrical properties of these materials in the course of converting the metal-organic structure (insulator) into a metal-carbon product (electrical conductor). The systematic investigation of the process of thermal transformation of MOFs can give a better understanding of the electrochemical potential of carbon-based materials and enlarge their field of application, as the transitional products of this process may possess useful properties for practical purposes. Generally, adjustable electrical conductivity of carbon-based materials ensure their wide applications as structural and functional components of thermistors, electrical screening materials, self-limited electrical heaters, sensors and so forth [5-7].

In this work, the investigation of the conduction mechanism of the Pt-based MOF was carried out using a.c. impedance spectroscopy, which is a valuable tool for studying the bulk transport properties of materials. This technique seems to be particularly appropriate for investigation of electrophysical characteristics of powdered materials, such as the products of MOF thermolysis which represent heterogeneous disperse systems with unknown contribution of ionic and electronic components to the total conductivity.

The Pt-containing MOF studied in this work was produced by grafting of Pt complexes to the nitrogens of bipyridine ligands of Al-based MOF-253. Despite the fact that MOF-253 itself obviously cannot be used as an electrocatalyst precursor, the electrophysical and some other properties of thermolysis products of this MOF were also studied and compared with those of Pt-MOF in order to present a more comprehensive report on the effects of thermal treatment of MOF materials.

7.2 Experimental

The two-step synthesis of Pt-based MOF-253 material is described elsewhere [4]. Essentially in the first step Al-based MOF-253 was obtained where Al atoms were linked by bipyridine-dicarboxylic ligands to form a 3-dimensional metal-organic lattice. Then in the second step dichloro-bis(acetonitrile) Pt complexes were inserted into bipyridine links, following the procedure described previously for the preparation of Pd-containing MOF [8]. After washing and drying, the Pt-MOF was ready to be tested or/and further treated at higher temperature. From the initial Pt-MOF, four carbon black samples were prepared by pyrolysis at 700, 800, 950 and 1050 °C, further referred to as C700-C1050 with the initial Pt-MOF designated as C0. In a similar fashion the initial Al-containing MOF (MOF-253) was designated as A0 and samples treated at 580-1050 °C as A580-A1050.

Thermolysis was carried out in a quartz tube containing 150 mg of the sample. The sample containing tube was purged with argon for 1 h prior to heating at 1 °C min⁻¹ for 4 h under argon flow of 20 mL min⁻¹. The yield after heat treatment was normally about 50 wt% of black powder, which was slightly sticky after thermolysis at 700 °C, however less so after heating at higher temperatures.

The a.c. impedance measurements were conducted using a Solartron 1260 gain phase analyzer connected to a cell, where the specimens were clamped within a 6 mm glass tube between two stainless steel pistons used as electrodes. Two springs produced a mechanical pressure of 10 atm per sample. The cell was placed in an oven where the impedance measurements were carried out at 25-200 °C. The acquired impedance data were corrected for the contribution from the empty and short circuited cell.

Pt-MOF materials were characterized by X-ray diffraction (XRD) using a SIEMENS D5000 diffractometer with Cu $K\alpha$ radiation. A Perkin Elmer Pyris Diamond TG/DTA thermogravimetric analyzer was employed to study the thermal properties of MOF samples. In these experiments samples were heated under nitrogen flow from room temperature to 800 °C at 10 °C min⁻¹.

7.3 Results and discussion

7.3.1 Unthermolized Pt-MOF (sample C0)

As can be seen from Figure 7.1, where a.c. impedance response is presented as a Nyquist plot, freshly prepared Pt-MOF behaves as an insulator. Only a part of the semicircle is observed at higher frequencies, while at lower frequencies with the decrease of the phase angle the response signal reduces below sensitivity level of the apparatus (picoamperes) even at very high perturbation voltage of 2 V. This produces a cloud of random values below 100 Hz. They are shown in Figure 7.1b but omitted in Figure 7.1a for sake of clarity.

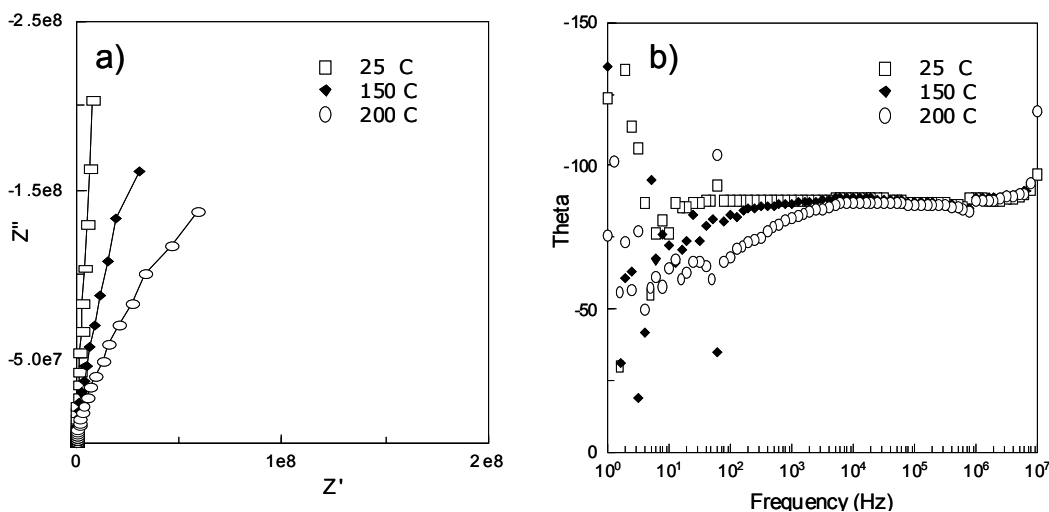


Figure 7.1 A.c. impedance responses obtained at different temperatures for untreated Pt-MOF sample (C0); (a) Nyquist plot, the signal below 100 Hz is not shown, (b) Phase angle as a function of frequency. Conductivity evaluation is $\sigma_{25}=1.3 \times 10^{-11} \text{ S cm}^{-1}$ and $\sigma_{200}=4.9 \times 10^{-10} \text{ S cm}^{-1}$.

Fitting of the Z'' vs. Z' plots with semicircles (Figure 7.2), was made on the assumption that the circuit under study corresponds to a capacitor (electrodes of the cell) in parallel with a very high resistance (the sample). It allowed to tentatively evaluate the conductivity of the sample as calculated from the value of Z' in the low-frequency end of the semicircle, where

Z'' would supposedly reach the abscissa axis ($Z'' = 0$). The conductivity of MOF increased from $1.3 \times 10^{-11} \text{ S cm}^{-1}$ at room temperature to $4.9 \times 10^{-10} \text{ S cm}^{-1}$ with heating to $200 \text{ }^\circ\text{C}$ due to the higher mobility of charge carriers. These data are reported in Table 7.1.

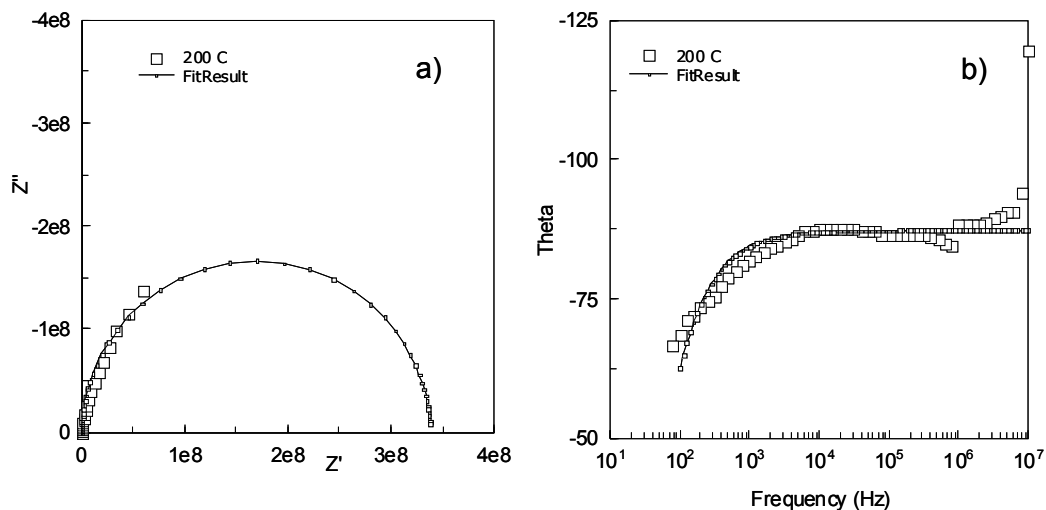


Figure 7.2 Fitting of impedance response for C0 sample acquired at $200 \text{ }^\circ\text{C}$ with an $-RC-$ circuit.

A very similar response was observed for A0 sample of untreated MOF-253 (Al-containing MOF). It also behaves as an insulator with conductivity on the order of $10^{-10} \text{ S cm}^{-1}$ (Table 7.1) over the temperature range from room to $200 \text{ }^\circ\text{C}$.

7.3.2 Pt-MOF and Al-MOF thermolyzed at $700 \text{ }^\circ\text{C}$ (sample C700 and A700)

The product of Pt-MOF thermolysis at $700 \text{ }^\circ\text{C}$ exhibited a response where two depressed semicircles were observed in the complex plane (Figure 7.3a). The large one corresponds to the low-frequency plateau in the Bode plot of the real part of the conductance (Figure 7.3c). The phase angle Θ (Figure 7.3d) at these frequencies is reducing to zero, which means that the impedance is dominated by the d.c. bulk resistance of the sample. The small semicircle in Figure 7.3a corresponds to the frequency range of 10^5 - 10^7 Hz where phase angle has a minimum and the plateau in Bode plot is distorted.

The fitting model for room temperature response of this sample comprised a series of two RC circuits, where the capacitances were replaced by constant phase elements (CPE). This substitution is stipulated by the shape of the responses that differs from perfect semicircles (particularly so in the case of the small one at high frequencies), reflecting the fact that the

sample material is not uniform and its microscopic bulk properties are space distributed due to local inhomogeneities, phase interfaces, defects, and so forth. This may provoke the depression of RC semicircle, the degree of which is roughly expressed through the parameter φ varying from 1 to 0, where $\varphi = 1$ corresponds to perfectly capacitive behaviour.

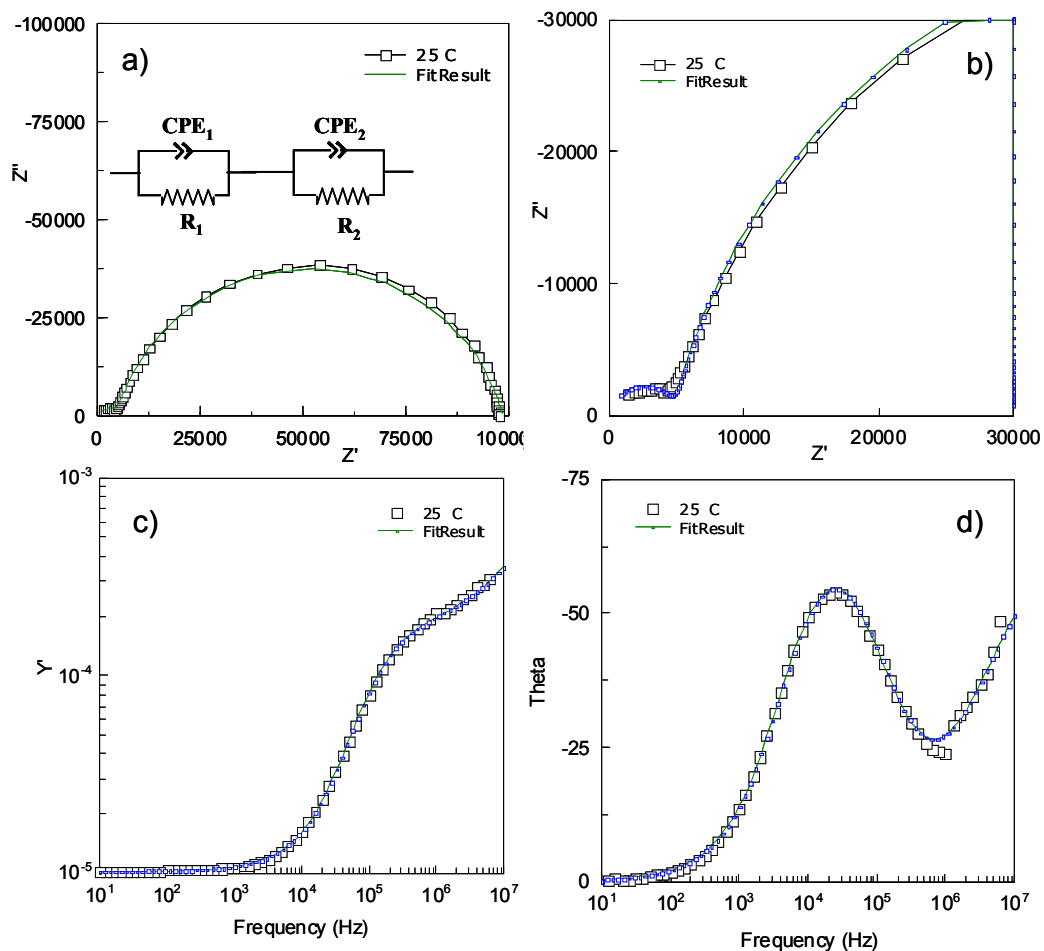


Figure 7.3 Room temperature a.c. impedance spectra of C700, a) Nyquist plot with a model circuit; b) High frequency part of the same plot; c) Real part of conductance vs. frequency; d) Phase angle vs. frequency. Symbols – experimental data, dotted line – fitting results.

The φ values obtained as a result of fitting the data acquired at various temperatures for this and other samples are gathered in Table 7.1. The high frequency part of the response is more strongly distorted (with $\varphi_2 = 0.74$ compared to $\varphi_1 = 0.86$ of low frequency) and corresponds to a resistance of about 5 kohm, which is nearly 20 times less than the low frequency part of the spectrum. Heating this sample caused a strong continuous decrease of the resistances in both parts of the spectra as illustrated by Figures 7.4, 7.5 and Table 7.1. One can see that the

high frequency signal degraded as φ_2 decreased to 0.53 at 100 °C, and above this temperature the high frequency part of the response became unsuitable for fitting. The low frequency range dominated by d.c. bulk resistance was enlarged from 10 to 10^4 up to 10^6 Hz (Figure 7.4b). Measurements at 200 °C revealed only one semicircle in the full frequency range 1- 10^7 , which however had characteristic half tear-drop shape (Figure 7.5). The presence of such feature (response shaped as half tear-drop in the Nyquist plot) is regarded as a key characteristic of the impedance spectra collected from mixed ionic and electronic conductors placed between two metal electrodes [9]. In case of thermolyzed MOF material, it is quite probable that residues of organic ligands may participate in charge transfer, particularly at elevated temperature.

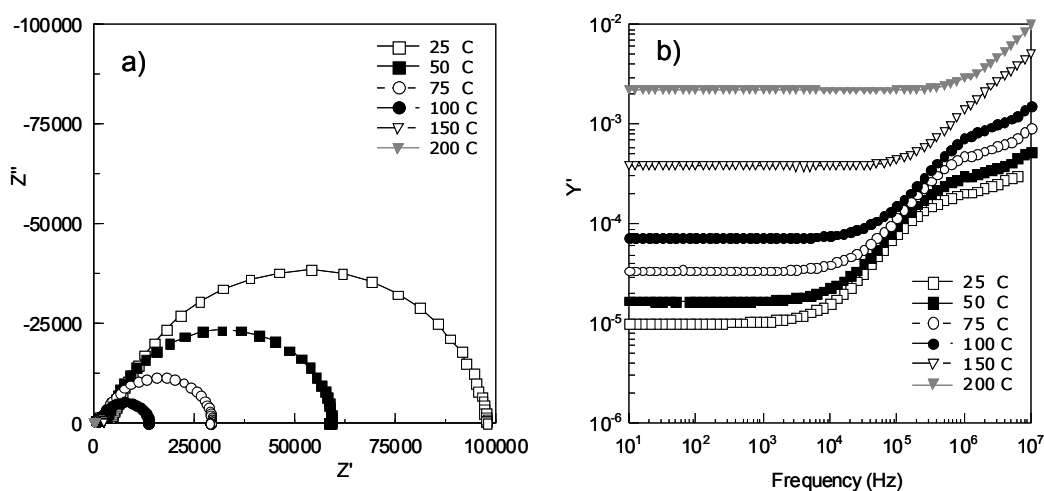


Figure 7.4 A.c. impedance spectra of C700 acquired at 25-200 °C. a) Nyquist plot; b) real part conductance vs. frequency.

In Figure 7.5, the equivalent circuit model is depicted as finite-length Warburg element W_1 which is usually attributed to diffusion-limited processes and produces in Nyquist representation a straight line with a 45° slope at the high-frequency side and a semicircular arc at its low-frequency side, similar to the shape of the signal shown in Figure 7.5c. However, finite-length Warburg type of response applies to a supporting electrolyte placed between kinetically reversible electrodes [10], which is more appropriate for liquid electrolytes rather than for a solid where apparently electrons are major charge carriers. So, the W_1 element is used here to denote the case of mixed electronic/ionic conductivity, in

contrast with the other data obtained with the same material where this behaviour was not revealed.

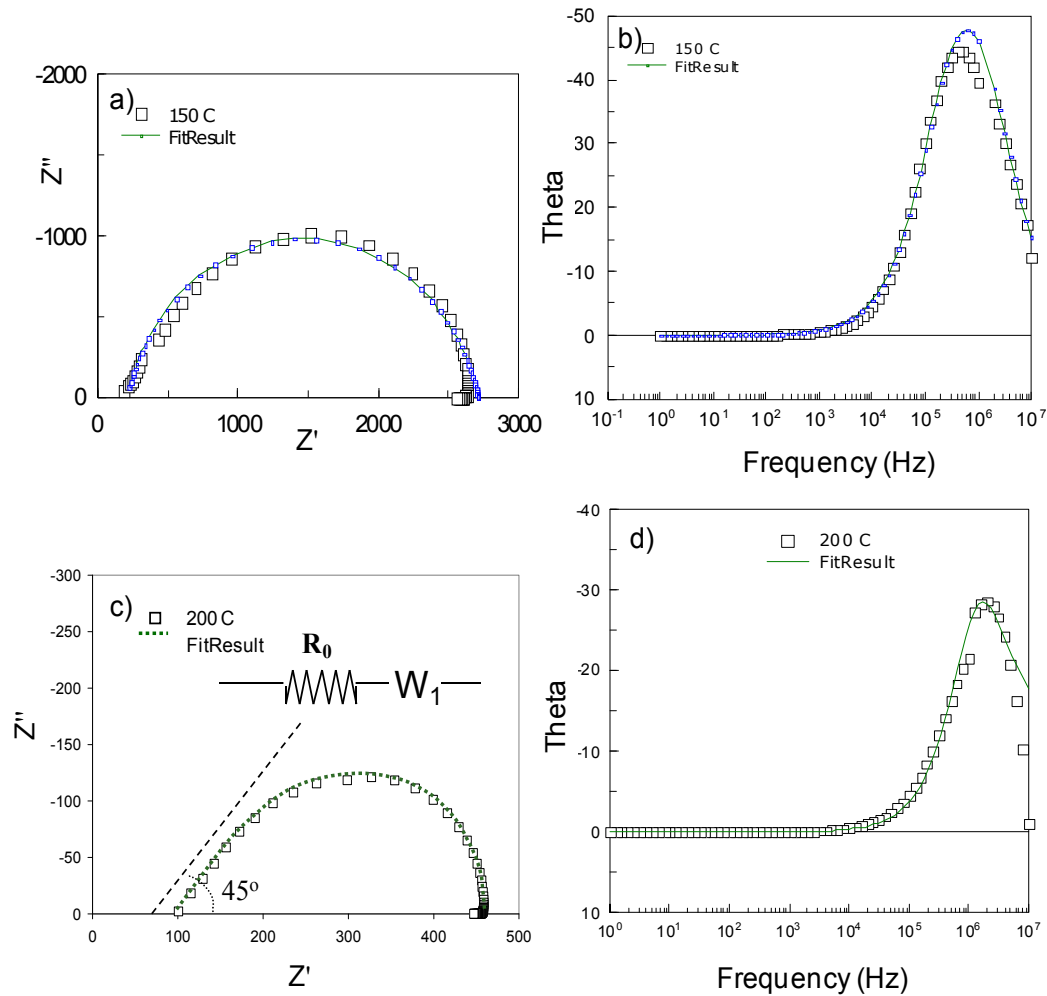


Figure 7.5 A.c. impedance spectra of C700 acquired at 150 and 200 °C. a) Nyquist plot, 150 °C; b) Phase angle vs. frequency, 150 °C. c) Nyquist plot, 200 °C; d) Phase angle vs. frequency, 200 °C. Symbols – experimental data, dotted line – fitting results.

Room temperature data for instance evidence the presence of two circuits in series (Figure 7.3a), most probably attributable to the bulk resistance of the material and electrode/specimen interface properties. Heating reduced the resistance of both components (see Table 7.1), but the interface related high frequency signal was more affected and disappeared above 150 °C. The resulting spectra might be read as corresponding to a solid where conductance of both holes and electrons became significant.

A quite different response was observed for A700 sample (Figure 7.6 and Table 7.1). Having resistance of 30-180 ohm at 25-200 °C, it possesses a conductivity about 1000 times higher than C700 of Pt-MOF. The conductance plateau in Figure 7.6b spans almost the whole range of frequencies, indicating that the response of the circuit is under control of the bulk conductivity of A700 sample. In the case of Pt-MOF that kind of behaviour was observed only on the products obtained at much higher temperatures. The properties of the Al-MOF thermolysis products will therefore be discussed in Sections 7.3.4-7.3.6 along with the results obtained for Pt-MOF samples.

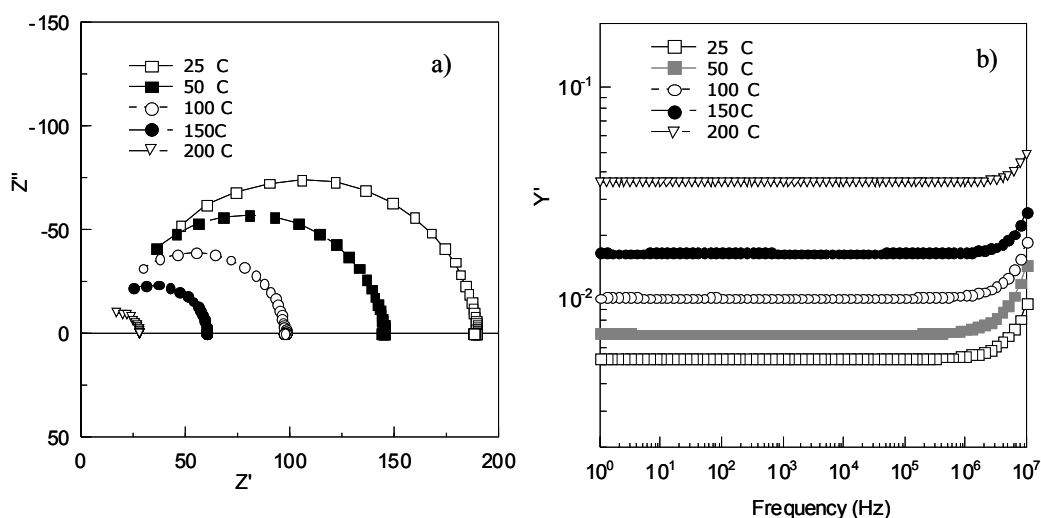


Figure 7.6 A.c. impedance spectra of A700 (Al-MOF sample) acquired at 25-200 °C. a) Nyquist plot; b) Phase angle vs. frequency.

7.3.3 Pt-MOF thermolyzed at 800 °C (sample C800)

Qualitatively, the behaviour of this material is essentially the same as the one obtained at 700 °C (Figure 7.7). It also exhibited a low frequency semicircle attributable to bulk resistance, which was initially 3.6 times smaller than in the case of C700 and which continually lowered with temperature (Table 7.1). However, the high frequency part of response is more distorted, and only resistance of this component can be determined. Above 150 °C again only finite-length Warburg element is observed on the spectrum of C800 similar to the one shown in Figure 7.5c for C700 sample. It can be supposed that agglomerates of carbon black particles grow with temperature; their surfaces become less imperfect, resulting in lesser resistance

and charge accumulation on the interface with the electrodes and between agglomerates within the bulk of the material.

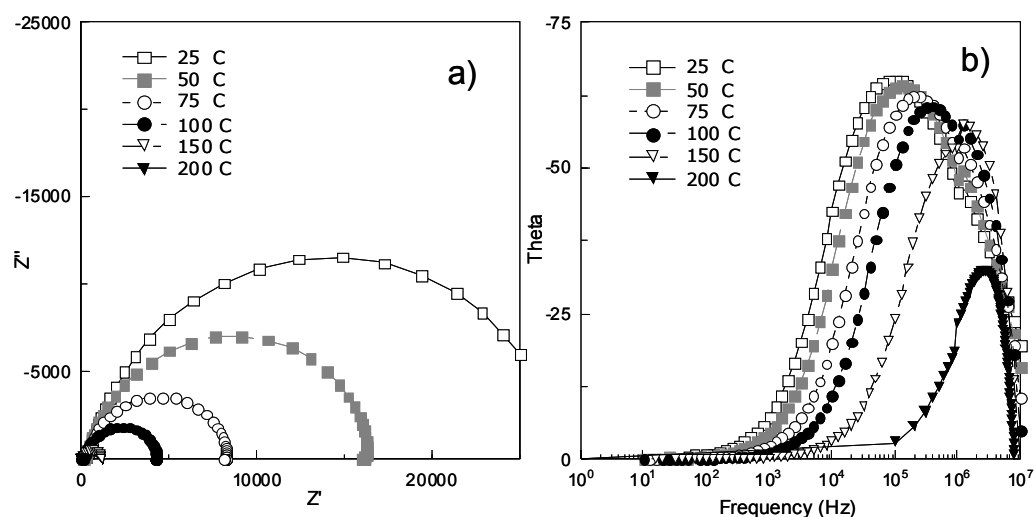


Figure 7.7 A.c. impedance spectra of C800 acquired at 25-200 °C. a) Nyquist plot; b) Phase angle vs. frequency.

7.3.4 MOF pyrolyzed at 950 °C (sample C950 compared with A700)

Sample C950 obtained by thermolysis of Pt-MOF at 950 °C revealed impedance responses, illustrated by Figure 7.8. The impedance curves in the complex plane are incomplete semicircles due to the limited range of frequency available with the setup used in the work. It is however reasonable to suggest that again mixed electron/ion (vacancy) conductance occurs in this Pt/carbon black material, similar to C700 measured at 200 °C (Figure 7.5c).

Formally the best fitting results were obtained with a single finite-length Warburg element as a model circuit. From Table 7.1 it is seen that the capacitance of the system constantly decreased with temperature. This might be attributed to the decrease in dielectric constant of the material which is generally caused by heat provoked misalignment of dipoles within the bulk of carbon black agglomerates.

For evaluation of the material conductivity, however, the model used is of no importance because the graphical analysis of the spectra takes into account the low frequency intercept with the real axis, which corresponds to the electrical resistance of the whole system. In this case the response is dominated by only one component- the bulk conductivity of the material.

As mentioned in Section 7.3.2, Al-MOF-based sample A700 behaves similarly showing to some extent more depressed semicircles, corresponding to slightly higher resistance and lower capacitance than those of C950 (Table 7.1). The capacitance of A700 was also gradually decreasing with temperature. These observations might be accounted for by a higher disorder in A700 structure which similarly to C950 was aggravated by heating to 200 °C.

It seems that the formation of metal/carbon black conductive structure occurs more readily in absence of Pt complexes in MOF precursors. However, in both cases of C950 and A700 the conduction is still of mixed nature where electron displacement is accompanied by ion/vacancy migration.

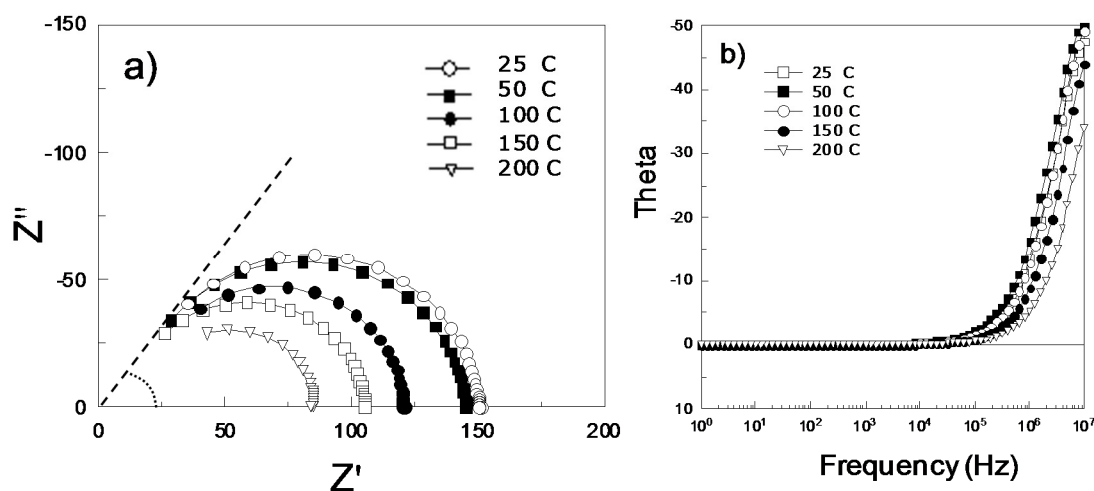


Figure 7.8 a.c. impedance spectra of C950 acquired at 25-200 °C. a) Nyquist plot; b) Phase angle vs. frequency.

7.3.5 Pt-MOF and Al-MOF pyrolyzed at 1050 °C (samples C1050 and A1050)

A completely different a.c. impedance response was observed for both Pt- and Al-MOF pyrolyzed at 1050 °C, as shown in Figure 7.9. It is seen that the responses at all temperatures represent small clouds of points dispersed around a value of the resistance of the samples under the chosen conditions. It should be noticed that A1050 sample has significantly higher resistance than C1050 (compare $R = 21$ ohm and $R = 2.8$ ohm both at 25 °C, Table 7.1). In both cases there is no imaginary component in the response and at any frequency phase angle

$\Theta=0$. Obviously, these materials exhibit purely electronic conductance where RC circuit is reduced to pure R.

It evidently has lost its dielectric properties because its dipole structure does not exist anymore and its orientational polarizability vanished. It may be suggested that defects, impurities, and other unknown substances, previously largely present at the interfaces between metal particles and polarizable nanoformations of carbon black material, were reduced to such a degree that much bigger agglomerates became as a whole electronic conductors. These agglomerates are not susceptible to reorientational displacement. However, the temperature dependence of the conductivity of this metal/carbon black sample remains positive, as can be seen from Figure 7.9 and from the resistance values reported in Table 7.1. Therefore, this conductance is not entirely of metal type for which resistance would increase with temperature. The temperature dependence of the conductivity for all the products of MOF pyrolysis is discussed below.

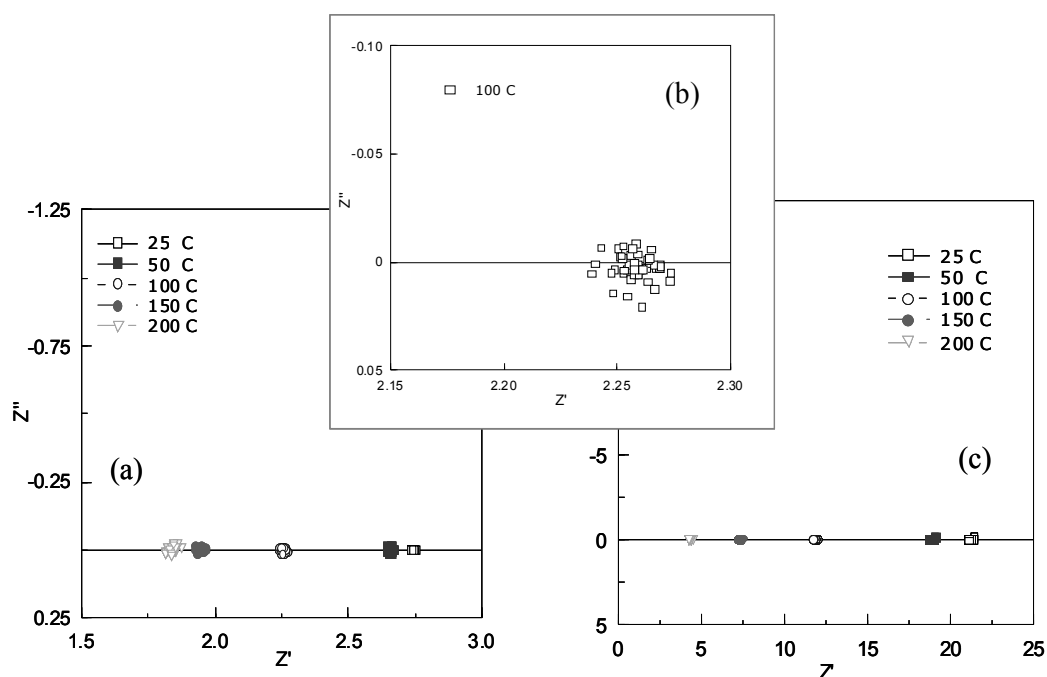


Figure 7.9 Complex impedance representation of the responses obtained at 25-200 °C from MOF pyrolyzed at 1050 °C. a) Nyquist plot acquired at selected temperatures for C1050; b) same as a), enlarged; c) Nyquist plot for A1050.

Table 7.1 Parameters of equivalent circuits evaluated from simulation of a.c. impedance data.

T _{measurement} °C	Circuit parameter	Thermolysis product										
		C0	C700		C800		C950	C1050	A0	A580	A700	A1050
		(initial)	Frequency domain		Frequency domain				(initial)			
		Low	High	Low	High							
25	R, ohm	1.8×10 ¹⁰	97800	4950	27100	200	155	2.8	1.4×10 ¹⁰	2.4×10 ⁶	179	21.1
	C, F	1.1×10 ⁻¹¹	1.59×10 ⁻⁹	7.85×10 ⁻¹⁰	3.6×10 ⁻⁹		1.6×10 ⁻⁷		1.2×10 ⁻¹¹	1.3×10 ⁻¹¹	3.8×10 ⁻⁸	
	φ	- ^b	0.86	0.74	0.86		0.48		- ^b	- ^b	0.41	
50	R, ohm		58500	3050	16470	170	140	2.7		1.8×10 ⁶	151	18.7
	C, F	-	1.81×10 ⁻⁹	3.9×10 ⁻¹⁰	3.6×10 ⁻⁹		1.3×10 ⁻⁷		-	2.3×10 ⁻¹¹	1.2×10 ⁻⁸	
	φ		0.86	0.71	0.88		0.49			- ^b	0.44	
100	R, ohm		13800	1200	4360	110	129	2.3	8.5×10 ⁹	1.1×10 ⁶	79	11.8
	C, F	-	1.83×10 ⁻⁹	7×10 ⁻⁸	2.9×10 ⁻⁹		8.9×10 ⁻⁸		1.1×10 ⁻¹¹	1.3×10 ⁻¹⁰	5.9×10 ⁻⁹	
	φ		0.89	0.53	0.89		0.49		- ^b	- ^b	0.46	
150	R, ohm	1.5×10 ⁹	2245	210	900	50	97	2		440×10 ³	49	7.3
	C, F	1.1×10 ⁻¹¹	3.7×10 ⁻⁹		1.4×10 ⁻⁹		7.3×10 ⁻⁸		-	3.9×10 ⁻¹⁰	3.4×10 ⁻⁹	
	φ	- ^b	0.90		0.90		0.51			0.69	0.47	
200	R, ohm	4.7×10 ⁸	410		210		68	1.8	3.9×10 ⁹	209×10 ³	36	4.3
	C, F	1.2×10 ⁻¹¹	4.3×10 ⁻⁹		1.2×10 ⁻⁹		5.1×10 ⁻⁸		1.3×10 ⁻¹¹	3.8×10 ⁻¹⁰	1.1×10 ⁻⁹	
	φ	- ^b	0.50		0.49		0.52		- ^b	0.71	0.50	

^a The model shown in Figure 7.3a was used for simulation of the response where it was appropriate. ^b Depression angle could not be determined due to partial distortions of the response. ^c Impedance response corresponded to pure electronic conductivity with unique circuit element R.

7.3.6 Temperature dependence of the conductivity

The results of resistance evaluation discussed above are gathered in Figure 7.10, where they are reported as conductivity σ vs. temperature curves. Conductivity was calculated according to $\sigma = d/S \times R_{bulk}$, where d and S are distance between electrodes and their surface area, respectively. The difference between room temperature conductivity of the C-series amounts to almost 5 orders of magnitude, while at 200 °C it reduces until about 2 orders. The temperature sensitivity of C700 and C800 samples differs significantly from that of C1050, where heating caused less than a 2-fold conductivity increase.

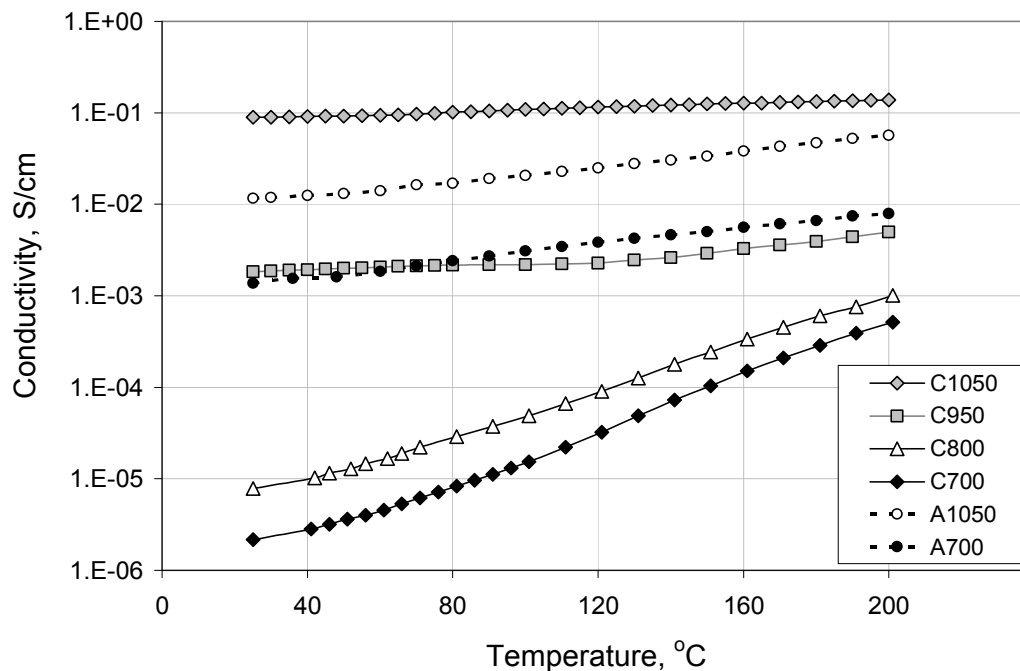


Figure 7.10 Conductivity of thermolysis products of Pt-MOF (C700-C1050) and Al-MOF (A700-A1050) as a function of temperature.

Contrary to that, the conductivities of Al-MOF based products A700 and A1050 exhibit same slope in this plot which means that their temperature sensitivities are identical. The closeness of curves for A700 and C950 in the figure evidences that initial Al-MOF more readily transforms into conductive material.

For a better understanding of that difference in susceptibility to restructuring under the thermal treatment, the TGA experiment may be helpful. Figure 7.11 illustrates the weight

loss and its temperature derivative for Al-MOF and Pt-MOF materials. It is evident that a major weight loss occurs in both cases at 350-380 °C and then at 480-560 °C where products lose 35-45 wt%. This can be apparently associated with degradation of bipyridine-dicarboxylic ligands of MOF. This latter stage seems to be the final step of thermolysis. Thereafter weight decreases gradually with the rate of about $\sim 2\%/100\text{ }^\circ\text{C}$ and reduces to 45-50% of the initial value at 1000 °C. The presence of heat-resisting Pt diminishes the relative weight loss of MOF (Figure 7.11a). Another major difference between the two materials is a sharp maximum at 240 °C corresponding to a 4% weight loss characterizing DTG curve of Pt-MOF (Figure 7.11b). The most plausible origin of this loss is the cleavage of chlorine atoms from Pt complexes attached to bipyridine linkages. A most significant structure transformation affecting conductivity takes place in both MOFs above 700 °C, beyond the temperature range where major mass losses occur. However, the materials behave rather differently in the process of thermolysis. Al-MOF more easily degrades into metal/carbon material and already after thermolysis at 700 °C exhibits rather high conductivity. Treatment at 500 and 580 °C (the temperature of ending of weight loss process) resulted in an insulator with impedance responses corresponding to resistances on the order of megaohms. Data for 580°C are shown in Table 7.1. Graphically the spectra of A0, A500 and A580 were similar to the untreated initial Pt-MOF spectrum shown in Figure 7.1 and are not presented here. This indicates that the degradation of MOF structure below 580 °C does not bring about any major changes in electrochemical properties of MOF. Apparently, the formation of an electronically conductive medium suitable for electrochemical applications occurs through diffusion processes taking place at higher temperatures, in succession to weight loss observed in TGA below 580 °C. Therefore, the transformation of MOF from insulator to electronic conductor may be generally considered as a process where first metal-organic complexes are destroyed accompanied by major weight losses followed by metal-carbon structures gradually forming with conductivity rising proportionally to the thermolysis temperature. Note that in Pt-MOF the second stage is more constrained due to strong Pt-N links, but the final product is 10 times more conductive owing to presence of Pt particles.

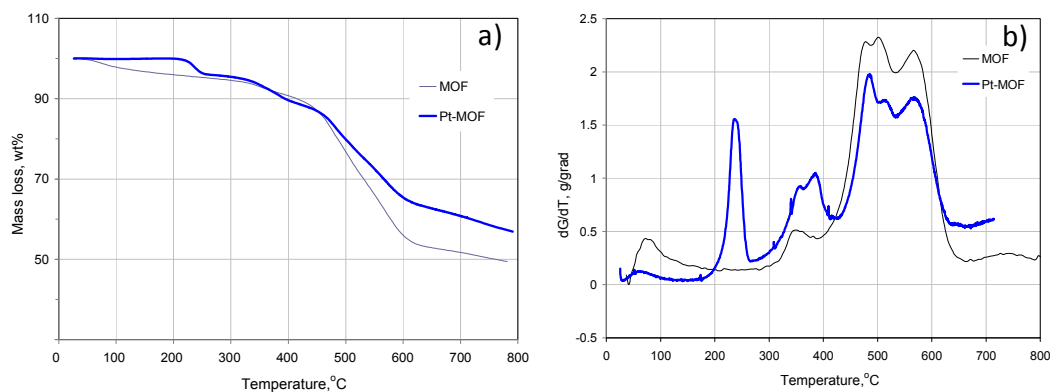


Figure 7.11 TGA and DTG plots of Al-MOF and Pt-MOF samples.

The conductivity of products of MOF thermolysis most strongly depends on the properties of the carbon component supporting metal particles. Its large resistance in series with that of good conductors determines the resistance of the whole system. Pt particles of about 7 nm size were indeed formed in C700-C1050 as was observed previously [4]. The metal content was not large in the MOF products. This content was 5 wt% Pt and about same for Al [4]. Despite the low percentage and much higher conductivity of pure metals their influence on electrical properties of the metal/carbon system seems however to be significant. Indeed, the Pt containing material is more conductive than that produced from Al-MOF at 1050 °C (Table 7.1). The reason might be that the material is approaching the concentrational threshold where electrodes are almost short-circuited by metal pathways going in parallel to some segments of larger carbon resistance.

It might be instructive to compare the electrical conductivity of pyrolytic products of MOF with data for carbon blacks reported in the literature. It should be mentioned that there are great varieties of carbon blacks differing in conductivity by orders of magnitude. For example, the thermal carbon black may be not conductive at all [11] or have conductivity varying from 0.02 to about 0.2 S cm⁻¹ when it is produced from natural gas and up to 0.9 S cm⁻¹ with oil as the feedstock [12]. Naturally, specialty furnace blacks, such as Vulcan XC-72 and alike, possess higher conductivity of 4-8 S cm⁻¹ [13]. As seen from Figure 7.10, the materials studied in this work have a maximum conductivity of 0.09 S cm⁻¹ (sample C1050) which placed them among thermal carbon blacks produced from natural gas. It should be mentioned that this kind of conductivity is high enough for the material to be applied as electrocatalyst in gas diffusion electrodes because this value is of the same order as the

conductivity of electrolyte membranes used in fuel cells. The catalytic layer is however much thinner, resulting in a smaller resistance and less significant Ohmic loss.

Despite the well-known fact that carbon black is a semiconductor, there are not many studies of electrical properties of carbon blacks as a function of temperature. It is however a most illustrative phenomenon allowing to distinguish metals from semiconductors and other types of conductors. It is known that the conductivity of metals decreases with temperature due to scattering of conduction electrons on the phonons (oscillations of the crystal lattice) according to Bloch–Grüneisen formula $\sigma \sim T^{-5}$ up to a certain temperature (corresponding to Debye frequency), and above this point σ decreases linearly. At the same time the charge carrier density in metals is nearly independent of temperature because of the Fermi distribution. Contrary to this, the concentration of electrons and holes in semiconductors is temperature dependent since they are formed by thermal activation. The concentration of charge carriers n is expressed as $n \approx \exp(-E_g/2kT)$, where E_g is gap energy between edges of the conduction band and the valence band. The conductivity can be expressed as a function of mobility and concentration of all charge carriers $\sigma \approx \sum n_i \mu_i$. However, it is known that the mobility of charge carriers in semiconductors decreases with temperature as $\mu \approx T^{-(3/2)}$ due to scattering with phonons and has rather limited influence on conductivity compared with the much more significant effect of concentration.

Arrhenius plots for samples A700, A1050 and C700-C1050 are presented in Figure 7.12, where from one can see that above a certain temperature the $\log(\sigma \times T^{(3/2)})$ vs. $1/T$ curves takes a linear shape. Activation energies which can be calculated from the slopes of these curves are also shown in the figure.

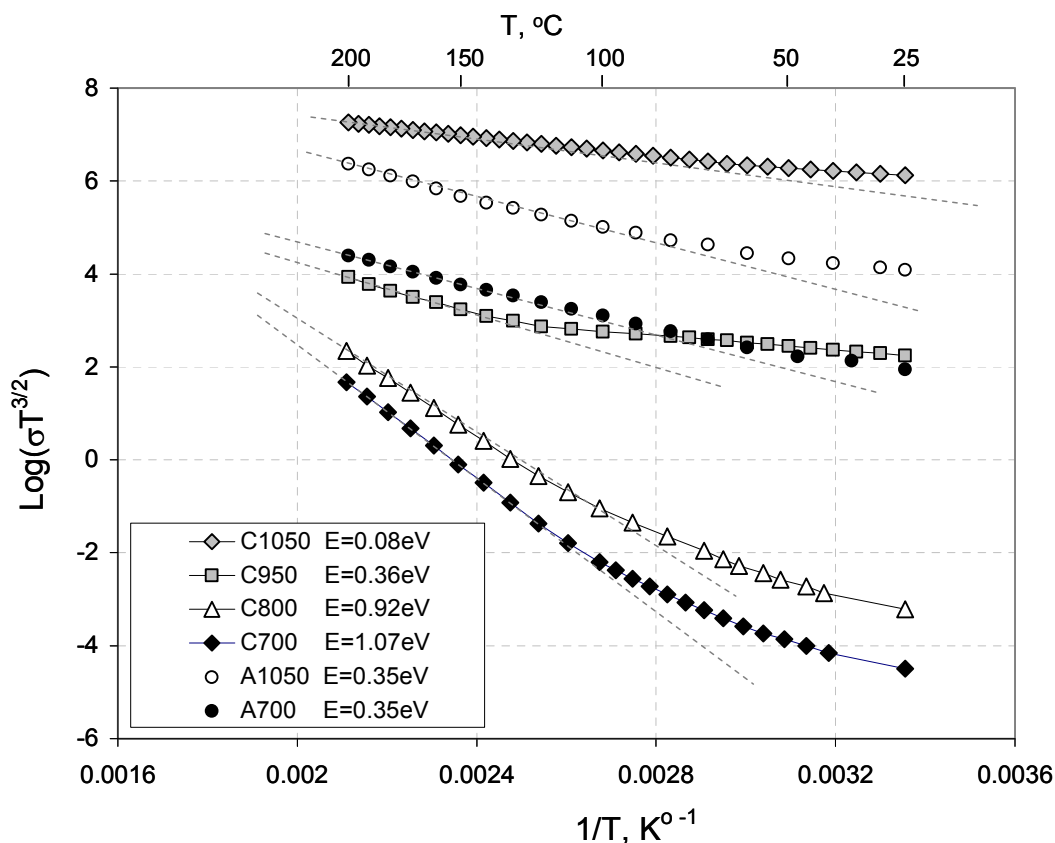


Figure 7.12 Arrhenius plot of conductivity of Pt-MOF pyrolysis products.

The potential barrier associated with the exponent in this plot might have different physical meaning. For instance, if the conductance is controlled by excitation of valence electrons across the band gap, then the plot is reflecting semiconductive behaviour. However, the calculated activation energies associated with the straight lines in the figure have values that can be related to semiconductors only in the cases of C700 and C800, while in the cases of C950, A700, A1050 and particularly for C1050 these values are too small for true semiconductors. Besides, the latter exhibited a response in impedance experiment (Figure 7.9), which is not typical for a semiconductor, where normally the spectrum has an imaginary component in complex plane [14,15]. The response shown in Figure 7.9 is more often associated with metallic conductivity where the response is purely resistive. However, this resistance decreases upon heating, so it seems reasonable to speculate that such a low potential barrier in sample C1050 is related to boundaries of carbon black agglomerates, which are partially shunted by metal particles formed on the carbon support. The samples C700-C950 and A700 are less well formed, and their conductance is more hindered by

imperfections on the grain boundaries and less promoted by metal particles on the interfaces between carbon agglomerates. The conduction mechanism in these materials possibly involves not only electrons and holes but also ionized electron donors or acceptors. This is being reflected in their a.c. impedance spectra most probably revealing mixed conductivity with participation of positive and negative charge carriers. It is of interest that A1050 showed the same E_g as A700 but exhibited a much higher conductivity. This may indicate that carbon agglomerates did not change their nature upon heating from 700 to 1050 °C; however, their dimensions were enlarged with the size of Al particles, in all probability reducing the extent of the interfaces and diminishing the resistance.

7.3.7 MOF shelf stability

It was noticed that when the thermolysis was undertaken more than 3 month after synthesis of Pt-MOF, the obtained products remained insulators even after pyrolysis at 1050 °C. The impedance spectra of these materials closely resembled the responses of nontreated initial MOFs shown in Figure 7.1 and corresponded to apparent conductivity as low as 10^{-10} - 10^{-11} S cm⁻¹. Hence, the thermolysis of the freshly prepared MOF and MOF after storage produced very different substances with completely different electrical properties. Such dissimilar properties of products derived from the same material at different postsynthesis periods most probably reflect the degradation of MOF during storage and cast some doubt on the stability of the MOF under storage conditions. It might be noted that the physical appearance of the nonconductive powder was similar to that of the regular C1050, and the weight loss during thermal treatment remained at 50%, which is typical for fresh samples.

X-ray diffraction patterns of the freshly prepared and aged MOFs revealed a broadening of the main diffraction line at $d=14.43$ Å (FWHM increased from 0.392 to 0.481, Figure 7.13). Taking into account the fact that measurement conditions and line position are the same, this may be provoked whether by a decrease of the mean size (D) of coherent crystal domains or by an increase in lattice distortions (ε) in the MOF. Both parameters are dependent on the line broadening (Δ) [16]: $D = \lambda / (\Delta \cos \theta)$ and $\varepsilon = \Delta / (4 \tan \theta)$, where λ is irradiation wavelength and θ is a diffraction angle. In fact, appropriate analysis of the XRD line profile could yield information such as mean size of coherent crystalline domain and the nature and

extent of lattice imperfections [17]. However, this holds true only when Fourier analysis of XRD profiles can be performed on the pattern with good resolution over a large range of angles. This was not the case for the pyrolyzed MOF where only the mentioned diffraction at $d=14.43 \text{ \AA}$ was well shaped and the rest of the pattern at higher angles had low resolution. It is however possible to evaluate the limits in which sizes of crystals and their defects can affect widening of FWHM. From the above formulas it follows that if widening was only due to a decrease in domain sizes, this decrease would be ca. 40 \AA . On the other hand, the same widening could be produced by an increase in lattice distortion by ca. 0.7% .

It can be assumed that the observed broadening of the diffraction line by 23% is due to both MOF lattice distortion and partial collapse of framework domains during aging. Apparently, that sort of degradation was critical for the precursor structure, and further thermo treatment could not result in formation of hexagonal graphitic layers but rather brought about amorphous carbon black with very poor electrical conductivity.

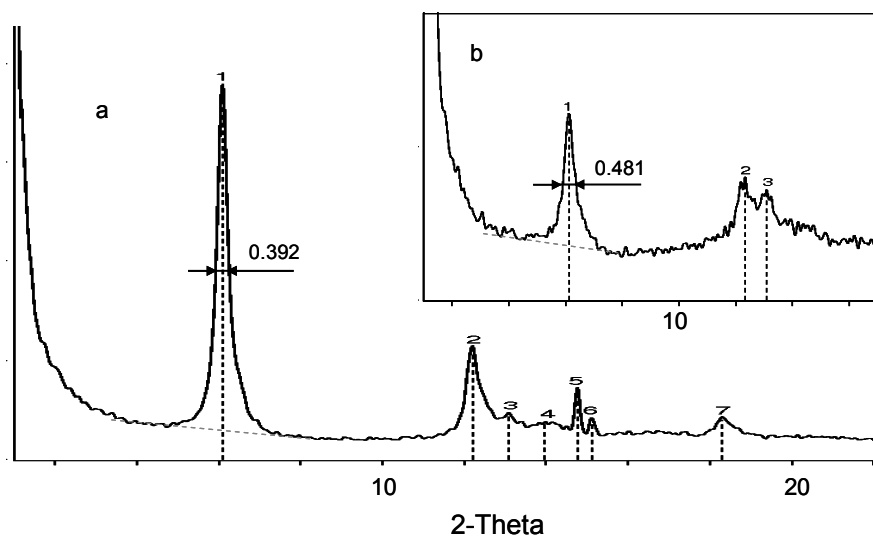


Figure 7.13 (a) XRD patterns of freshly prepared Pt-MOF and (b) Pt-MOF after storage for 3 months.

Al-MOF proved to be stable under the same conditions, and the products of thermolysis of fresh and aged Al-MOF did not differ in conductivity. Some ground for speculation on this fact may be taken from TGA experiment, which shows that the degradation of Pt-MOF starts more readily than in the case of Al-MOF and the first mass loss sets up just above $200 \text{ }^\circ\text{C}$ (Figure 7.11). Evidently, a lack of stability of Pt ligands produced from dichlorobis(acetonitrile) complexes provokes this instability of Pt-MOF material, which

however can be easily circumvented by using simple precautions and working with freshly prepared materials.

7.4 Conclusion

The study of the products of thermal transformation of Al-MOF and Pt-MOF into carbon-black-based electrocatalysts was carried out using a.c. impedance analysis. It was observed that the materials subjected to thermolysis at increasing temperatures pass through different conduction states starting from insulator with $\sigma = 1.3 \times 10^{-11} \text{ S cm}^{-1}$ and ending up with a particular metal-like conductance with positive temperature dependence and high ambient conductivity.

Intermediate products of the thermolysis exhibited complex impedance responses, which may be interpreted as mixed conduction by electrons accompanied by ionic drift. The temperature dependence of conductivity of these materials was also positive with the rise of σ by about 250 times upon heating from 25 to 200 °C. Thermolysis of initial Al-MOF is less hindered and occurs at lower temperatures. However, the conductivity of the final product of pyrolysis at 1050 °C was higher for Pt-MOF ($\sigma_{25^\circ\text{C}} = 9.0 \times 10^{-2} \text{ S cm}^{-1}$) while it was $\sigma_{25^\circ\text{C}} = 1.0 \times 10^{-2} \text{ S cm}^{-1}$ for the MOF-253. The shelf stability of Pt-modified MOF was found to be inadequate, making impossible electrocatalyst manufacturing after storage of Pt-MOF for 3 months. Only freshly prepared Pt-MOF is suitable for Pt/C catalyst preparation.

7.5 Acknowledgments

The authors thank the Fonds Québécois de Recherche sur la Nature et les Technologies (FQRNT) for financial support.

Chapter 7 References:

- [1] S. Ma, G.A. Goenaga, A.V. Call, D.-J. Liu, Cobalt Imidazolate Framework as Precursor for Oxygen Reduction Reaction Electrocatalysts, *Chemistry – A European Journal* 17 (2011) 2063-2067.
- [2] E. Proietti, F. Jaouen, M. Lefèvre, N. Larouche, J. Tian, J. Herranz, J.-P. Dodelet, Iron-based cathode catalyst with enhanced power density in polymer electrolyte membrane fuel cells, *Nat Commun* 2 (2011) 416.
- [3] D. Zhao, J.-L. Shui, C. Chen, X. Chen, B.M. Repragle, D. Wang, D.-J. Liu, Iron imidazolate framework as precursor for electrocatalysts in polymer electrolyte membrane fuel cells, *Chemical Science* 3 (2012) 3200-3205.
- [4] F. Afsahi, H. Vinh-Thang, S. Mikhailenko, S. Kaliaguine, Electrocatalyst synthesized from metal organic frameworks, *Journal of Power Sources* 239 (2013) 415-423.
- [5] C. Klason, J. Kubát, The Conductivity Distribution in Injection Moulded LDPE and HDPE Filled with Carbon Black, *International Journal of Polymeric Materials and Polymeric Biomaterials* 10 (1984) 259-280.
- [6] K. Miyasaka, K. Watanabe, E. Jojima, H. Aida, M. Sumita, K. Ishikawa, Electrical conductivity of carbon-polymer composites as a function of carbon content, *Journal of Materials Science* 17 (1982) 1610-1616.
- [7] Y.-J. Wang, Y. Pan, X.-W. Zhang, K. Tan, Impedance spectra of carbon black filled high-density polyethylene composites, *Journal of Applied Polymer Science* 98 (2005) 1344-1350.
- [8] E.D. Bloch, D. Britt, C. Lee, C.J. Doonan, F.J. Uribe-Romo, H. Furukawa, J.R. Long, O.M. Yaghi, Metal Insertion in a Microporous Metal–Organic Framework Lined with 2,2'-Bipyridine, *Journal of the American Chemical Society* 132 (2010) 14382-14384.
- [9] W. Lai, S.M. Haile, Impedance Spectroscopy as a Tool for Chemical and Electrochemical Analysis of Mixed Conductors: A Case Study of Ceria, *Journal of the American Ceramic Society* 88 (2005) 2979-2997.
- [10] D.R. Franceschetti, J.R. Macdonald, R.P. Buck, Interpretation of Finite-Length-Warburg-Type Impedances in Supported and Unsupported Electrochemical Cells with Kinetically Reversible Electrodes, *Journal of The Electrochemical Society* 138 (1991) 1368-1371.
- [11] D. Pantea, H. Darmstadt, S. Kaliaguine, C. Roy, Electrical conductivity of conductive carbon blacks: influence of surface chemistry and topology, *Applied Surface Science* 217 (2003) 181-193.
- [12] D. Pantea, H. Darmstadt, S. Kaliaguine, L. Sümmechen, C. Roy, Electrical conductivity of thermal carbon blacks: Influence of surface chemistry, *Carbon* 39 (2001) 1147-1158.
- [13] H.S. Katz, J.V. Mileski, *Handbook of Fillers for Plastics*, Kluwer Academic Publishers, Dordrecht, Netherlands (1987).
- [14] M.E. Orazem, B. Tribollet, *Electrochemical Impedance Spectroscopy*, Wiley-Blackwell, Chichester, West Sussex, UK (2008).
- [15] M.E. Orazem, *The Impedance Response of Semiconductors: An Electrochemical Engineering Perspective*, *Chemical Engineering Education* 24 (1990) 48-55.
- [16] B.D. Cullity, S.R. Stock, *Elements of X-Ray Diffraction*, 3rd ed., Prentice Hall, Upper Saddle River, NJ, USA (2001).
- [17] B. Lanson, B. Kubler, Experimental determinations of the coherent scattering domain size distribution of natural mica-like phases with the Warren-Averbach technique, *Clays and clay minerals* 42 (1994) 489-494.

Chapter 8 Conclusions and outlook

8.1 Conclusions

The overall objective of this research study was to put the great potential of metal organic framework (MOF) materials as electrocatalyst precursor in practice and prepare well performing precious and non-precious electrocatalysts for PEM fuel cells employing only MOF as the precursor. MOFs can be potentially used for wide ranging technological applications such as gas storage and gas separation, drug delivery and catalysis. MOFs have also been used as a template and/or carbon source to synthesize nanoporous carbon materials with high surface area.

This thesis has covered the synthesis and characterization of Pt containing MOF-253 and a Fe-based MOF synthesized using 1,3,5-tris(2H-tetrazol-5-yl)benzene hydrochloride ($H_3BTT.2HCl$) as an organic ligand. The as-synthesized MOF materials were found to act as insulators therefore heat treatment at high temperatures under inert (or reactive) atmosphere was applied to produce electronically conductive materials that were subsequently used as the electrocatalyst precursor.

Employing a Pt containing MOF as an electrocatalyst precursor could provide potential to benefit from high and uniform intrinsic distribution of Pt species throughout the 3D, crystalline structure of parent MOF-253. This could eventually lead to an efficient electrocatalyst precursor as in its structure the precious Pt nanoparticles are being used effectively. Although this was the goal, the necessity to apply high temperature pyrolysis limited the extent of achieving it. Transmission electron microscopy (TEM) and X-ray diffraction (XRD) for the electrocatalysts prepared through pyrolysis of Pt containing MOF-253 in the temperature range of 700 to 1050 °C, showed average Pt particle and crystal domain sizes of 5.5 and 8 nm, respectively. Similar Pt nanoparticle sizes were observed when highly porous supports materials such as CNTs were employed for electrocatalyst preparation. Furthermore, these results demonstrated that the pyrolytic transformation of parent Pt-based MOF-253 to electrocatalyst precursors results in the formation of germinal Pt nanoparticles at relatively lower temperatures ~ 800 °C followed by coalescence of these nanoparticles to form larger ones above this temperature. While the Pt phase properties

demonstrated dependency on pyrolysis temperature, the carbon support showed minor structural changes due to temperature variations. This could be rationalized considering the changes which occurred to specific surface area and pore size distribution of the electrocatalysts over such pyrolysis temperature span. Indeed, the specific surface area and pore size distribution did not vary too much with pyrolysis temperature. XPS analysis illustrated the formation of higher amounts of ordered graphene layers in the electrocatalyst structure upon heat-treatment at higher pyrolysis temperature. This could also be related to the higher electronic conductivity obtained for electrocatalyst precursor treated at higher temperatures. In addition, according to XPS analysis results, pyrolysis at higher temperatures facilitates the reductive formation of metallic Pt(0) as Pt 4*f* XPS spectrum demonstrated only those peaks which were attributable to the metallic Pt and not its oxidized form. The above presented properties for the obtained electrocatalyst precursors raise our interest to study the performance of these samples as HOR and ORR electrocatalysts; therefore, those two samples that provided the purely electronic type of conductivity were tested in a single PEM fuel cell. To assist surveying the electrocatalyst performance, they were only applied to one of the electrodes whilst at the other side commercially available electrodes were used. For the same Pt loading, the MOF derived Pt-based electrocatalyst prepared at a pyrolysis temperature of 1050 °C (the most promising electrocatalyst), at the anode side demonstrated performances comparable to the commercial electrode. At the cathode side however the same electrocatalyst's performance deviated from the commercial electrode. Different reasons could contribute to this deviation namely the catalyst properties and the electrode structure.

A similar concept was also employed in the current research to develop a non-precious (Fe-based) electrocatalyst for ORR. The most challenging issue regarding the application of non-PGM catalysts is related to their relatively low turn-over-frequency compared with Pt. This necessitates excessive amounts of non-PGM catalyst in the corresponding catalyst layer to compensate for their low electrochemical activity which could lead to thicker electrodes with higher mass transport resistance. Therefore, MOFs are expected to be a superior choice as electrocatalyst precursor and provide the potential for high volumetric density of active sites distributed evenly throughout the catalyst structure.

Unlike the previous reports which merely used ZIFs as a support for Fe and N or only as Fe and N sources, this study employed a new class of MOF material as the only electrocatalyst

precursor. Using the Fe-BTT MOF synthesized in this work which possesses quite different chemistry compared to ZIF-based precursors, revealed that the MOF chemistry determines the final properties of the electrocatalyst. The as-synthesized MOF material underwent two steps of heat-treatment first under inert gas condition followed by acid leaching and finally pyrolysis under NH_3 . The pyrolysis temperature range for both of the heat-treatment processes was between 700 to 1000 °C. XRD analysis demonstrated the presence of different crystalline phases in the final electrocatalyst precursor including mostly Fe_2N and $\text{FeN}_{0.056}$. Electrocatalysts obtained at higher pyrolysis temperature, contained Fe_3C as well. Although, all the prepared electrocatalyst precursors provide mixed micro-meso porous structure, the samples which underwent heat-treatment under NH_3 at higher temperatures showed a larger contribution of microporosity within their porous structure. XPS analysis demonstrated the presence of three different nitrogen species including quaternary-N, pyridinic-N and pyridine N-oxide in the Fe-BTT MOF derived electrocatalysts which were also found in almost all the non-precious (Fe/N/C) type of ORR electrocatalysts reported in the literature. Although our quantitative analysis demonstrates higher proportion of quaternary-N than that of pyridinic-N for almost all the electrocatalyst precursors, the absolute content of quaternary-N could not be determined accurately as the total nitrogen content was found to decrease upon increasing the thermolysis temperature. Hence, correlating the ORR catalytic activity of these electrocatalysts with the quaternary-N content was not readily possible and both pyridinic-N and quaternary could be assumed contributing to the ORR catalytic activity. Acid leaching after the initial pyrolysis is supposed to remove the excess metal in the sample, leading to better ink dispersion and higher stability. The ORR activity of these electrocatalysts, as measured with the RDE, demonstrates dependency on the heat-treatment temperature. It increases upon raising the thermolysis temperature up to 900 °C and then drops for the catalyst synthesized at the maximum temperature. The most promising electrocatalysts prepared in this study showed Tafel slopes close to that of the theoretical value (120 mV dec^{-1}), indicating that in the potential range measured, the ORR on these catalysts is controlled by the first electron transfer process. The most promising electrocatalysts were also tested in a single cell PEM fuel cell operating under H_2/air and provide the best performances by far reported employing only an Fe-based MOF as the

electrocatalyst precursor. This indeed was not the best result reported in the literature using MOFs as the electrocatalyst precursor.

In the catalyst layer, Nafion ionomer serves as a physical binder for the electrocatalyst/carbon particles and facilitates the contact between electrocatalysts, electrolyte, and dissolved reactant gases and hence the occurrence of electrochemical reactions. The Nafion content used in the ink solution can determine the effectiveness of the catalyst layer toward proceeding of reactions and therefore affect the catalyst utilization and PEM fuel cell performance. In this study the effect of Nafion content on the PEM fuel cell performance was investigated through numerical modeling. To do so first, a sensitivity analysis was performed to identify the most influential parameters of the model which subsequently were calibrated using experimental data. The results obtained during sensitivity analysis were in accordance with those reported previously in the literature for more sophisticated models. This confirms the capability of this model in capturing the essential phenomena in the fuel cell in order to predict the overall trends with respect to undetermined model parameters. The calibrated model was employed in the next step to investigate the impact of Nafion ionomer content. Although the model could not accurately predict the optimum values of Nafion ionomer content measured experimentally, it could provide a qualitative trend that could also be observed through experiments. The experimental study considered a relatively large span of Nafion ionomer content in the ink solution between 10 to 50 wt% (based on dry electrocatalyst). The experimental results demonstrated that slightly increasing the Nafion content in both anodic and cathodic electrodes compared to those electrodes prepared previously with only 20 wt% of Nafion (the results were reported chapter 4 of this dissertation), could enhance the fuel cell performance to some extent. In addition the results showed the existence of two different optimum formulations for anodic and cathodic electrodes prepared based on electrocatalyst derived from Pt containing MOF-253 precursor.

This dissertation was ended with reporting the results obtained from impedance spectroscopy analysis performed on the thermolysis products of Pt containing MOF-253 as well as MOF-253 itself. The results demonstrated the dependency of the conduction of these products to the thermolysis temperature used for their preparation (700 to 1050 °C). While the thermolysis temperature corresponding to the minimum value of this range results in the formation of completely insulating material, the one prepared at the maximum temperature

revealed metal-like conductance. For the products in between complex impedance responses were obtained which indicate the presence of mixed electronic and ionic type of conduction. To conclude, this study has demonstrated a successful synthesis of precious and non-precious metal containing electrocatalysts derived from MOF precursors. Characterization results showed that the properties of these electrocatalysts such as surface area, conductivity and electrochemical properties depend on the pyrolysis conditions. Based on the findings in this thesis, some areas for future investigations are highlighted below.

8.2 Outlook

One possible avenue for the future work regarding the Pt-based electrocatalyst is to study the effect of additional carbon source. This can allow better preserving the original atomic dispersion of Pt in the MOF. Additional carbon source can also affect the porosity and electronic conductivity of the final electrocatalyst. Increasing electronic conductivity and mesoporosity within the electrocatalyst products could improve their performances in a PEM fuel cell. One way to apply additional carbon source is to impregnate the porous Pt-MOF precursor with carbon sources such as furfuryl alcohol (FA) before the pyrolysis step. In another approach, the pyrolysis atmosphere can be switched from pure inert gas to a mixture of inert and reactive gas (with controllable amount of reactive gases such as ethylene or acetylene). Another fascinating area for future work is to use nanoscale MOF materials as the electrocatalyst precursor. Compared with bulk materials, the nanoscale ones are found to provide more capability to resist drastic structural and/or morphological damage caused by high temperature pyrolysis. In addition, the larger surface-to-volume ratio would also be beneficial if the size of pyrolysis products could be kept in the nanometer scale. The long-term stability of these electrocatalysts under PEM fuel cell operating conditions needs to be investigated as well.

Regarding the non-precious electrocatalysts, using MOF precursor, especially a MOF which contains only Fe as the metal species as the sole precursor, doesn't seem to be an efficient approach. Indeed, although in the parent Fe-MOF precursor, there are sufficient Fe-N coordination that have potential to be converted to active sites, upon pyrolysis which destroys the MOF structure, most of these active sites seems to be inaccessible to take part in ORR.

Therefore, one interesting avenue for the future work is synthesizing bi-metal, especially Zn-Fe, MOF precursors. Although Fe containing MOF precursors alone are not great candidates for electrocatalyst preparation, their composite with carbon conductive materials such as graphene have great potential to be applied as prototype electrocatalysts. Using these composite materials there would be no need to apply high temperature pyrolysis to prepare the conductive medium and the Fe-N coordination, which is believed to play active site role, can remain intact and assist in understanding the mechanism of ORR reaction on such active sites. The mechanism of ORR reaction on this type of catalyst remained an unanswered question for the past decades and resolving this question could result in producing more active catalyst materials.

The numerical model used in this study has also great potential to be improved in future works through considering i) the liquid water transport to capture the flooding effect, ii) non-uniform temperature profiles, and a three-dimensional geometry.